

# MOCVD Growth of InGaP-based Heterostructures for Light Emitting Devices

by

Lisa Megan McGill

B.A. with Honors in Geological Sciences  
Cornell University, 1997

Submitted to the Department of Materials Science and Engineering in Partial Fulfillment  
of the Requirements for the Degree of

Doctor of Philosophy in Electronic Materials  
at the  
Massachusetts Institute of Technology

February 2004

**ARCHIVES**

© 2004 Massachusetts Institute of Technology. All rights reserved.

Signature of Author: \_\_\_\_\_

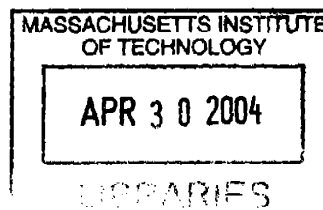
Department of Materials Science and Engineering  
October 29<sup>th</sup>, 2003

Certified by: \_\_\_\_\_

Eugene A. Fitzgerald  
Merton C. Flemings-SMA Professor of Materials Science and Engineering  
Thesis Supervisor

Accepted by: \_\_\_\_\_

Harry L. Tuller  
Professor of Ceramics and Electronic Materials  
Chair, Departmental Committee on Graduate Students



# MOCVD Growth of InGaP-based Heterostructures for Light Emitting Devices

by

Lisa Megan McGill

Submitted to the Department of Materials Science and Engineering on October 29<sup>th</sup>, 2003, in Partial Fulfillment of the Requirements for the Degree of Doctor of Philosophy in Electronic Materials

## ABSTRACT

In this work, we examine fundamental materials processes in the growth of indium gallium phosphide (InGaP) via metalorganic chemical vapor deposition (MOCVD). In particular, we realize improvements in the epitaxial integration of high-quality InGaP device materials on non-standard platforms, such as GeSi graded buffers on Si substrates, and InGaP or indium aluminum gallium phosphide (InAlGaP) graded buffers on GaP substrates. We apply these improvements to the design and implementation of strained-InGaP quantum-well light emitting diodes (LEDs) operating in the yellow-green region of the visible spectrum. The innovative use of these traditional materials is intended to provide a solution for bright green solid-state light emitters.

Initial modes of InGaP lattice-matched epitaxy on GeSi were studied. Three-dimensional growth was observed over a wide range of deposition temperatures and V/III ratios. Pre-growth thermal cycling in a H<sub>2</sub> plus PH<sub>3</sub> ambient led to a large increase in surface roughness and the formation of surface mesas. Thermodynamic simulations suggest that these mesas may be P clusters or GeP solid complexes. They may also be surface oxides formed in conjunction with water vapor in the deposition chamber. Such surface degradation prior to the initiation of epitaxy is unfavorable for monolayer growth.

The development and evolution of defect microstructures in relaxed, compositionally graded InGaP buffers deposited on GaP were examined. In particular, the properties of branch defects in InGaP graded buffers were examined for a large number of growth and annealing conditions. These studies confirm that branch defect formation is driven by surface, not bulk, processes. Branch defects in the bulk arise from surface features that are metastably "frozen" in place by subsequent deposition and propagate through the thickness of the sample. We conclude that branch defects comprise a local compositional fluctuation resulting from the clustering of In atoms. This identification is supported by the suppression of branch defect formation under conditions of reduced adatom mobility, including low growth temperature and high V/III ratio. In addition, we demonstrate that dislocations gliding in the [1 $\bar{1}$ 0] direction are preferentially blocked by strain fields arising from nearly-[110]-oriented branch defects. This is further evidence for the link between branch defects and In clustering.

A relaxed InAlGaP graded buffer platform was utilized in the design and fabrication of a novel strained-InGaP quantum-well epitaxial-transparent-substrate LED (ETS-LED). The best devices exhibited yellow-green emission with a primary wavelength of 590 nm and a secondary wavelength of 560 nm. These devices had  $\rho_{TD} = 7 \times 10^6 \text{ cm}^{-2}$  and an  $\text{In}_{0.32}\text{Ga}_{0.68}\text{P}$  quantum well active region, and operated at 0.18  $\mu\text{W}$  per facet at 20 mA, corresponding to a luminous efficacy of approximately 0.01 lm/W. Transmission electron diffraction indicates that the observed spectral lineshape is the result of emission from ordered and disordered domains in the quantum well. Devices with  $\rho_{TD} = 5 \times 10^7 \text{ cm}^{-2}$  and an  $\text{In}_{0.32}\text{Ga}_{0.68}\text{P}$  quantum well active region operated at 0.08  $\mu\text{W}$  per facet, and exhibited a similar bimodal emission lineshape. Devices with  $\rho_{TD} = 5 \times 10^7 \text{ cm}^{-2}$  and an  $\text{In}_{0.37}\text{Ga}_{0.63}\text{P}$  quantum well operated at 0.06  $\mu\text{W}$  per facet at single peak wavelength of 588 nm. The degree of ordering in the  $\text{In}_{0.37}\text{Ga}_{0.63}\text{P}$  quantum well was reduced due to an increase in V/III ratio during deposition; this decrease in ordering leads to a large overlap between ordered and disordered emission peaks.

Thesis Supervisor: Eugene A. Fitzgerald

Title: Merton C. Flemings-SMA Professor of Materials Science and Engineering

## Table of Contents

<b>List of Figures</b>	<b>7</b>
<b>List of Tables</b>	<b>12</b>
<b>Acknowledgements</b>	<b>13</b>
<b>1 Motivation for and Organization of Thesis</b>	<b>15</b>
1.1 Motivation	15
1.2 Organization of Thesis	19
<b>2 Overview of MOCVD Growth</b>	<b>21</b>
2.1 Motivation for MOCVD	21
2.2 MOCVD Process	21
2.2.1 Precursor Materials	22
2.2.2 Source Purity and Film Contamination	26
2.2.3 Doping	27
2.3 Deposition Parameters	28
2.3.1 Thermal Regimes	29
2.3.2 Mass Transport-Limited Growth	30
2.4 Reaction Mechanisms	32
2.5 Summary	33
<b>3 Mismatched Epitaxy of InGaP and InAlGaP for Optical Devices</b>	<b>35</b>
3.1 Physical Properties of InGaP and InAlGaP	35
3.2 Dislocation Systems	39
3.3 Lattice-mismatched epitaxy	42
3.4 Relaxed Graded Buffer Growth	47
3.5 Modes of Epitaxy	50
3.6 Surface Morphology	52
3.7 Deviations from Randomness	53
3.7.1 Macroscopic Deviations	55
3.7.2 Microscopic Deviations	61
3.8 Device and Material Design Goals	63
3.8.1 Quantum Efficiency and Device Performance	63
3.8.2 Emitter Designs	65
3.9 Summary	67
<b>4 MOCVD Conditions and Characterization Methods</b>	<b>69</b>
4.1 Introduction	69
4.2 MOCVD Reactor System	69
4.2.1 Substrate Preparation	70
4.3 Characterization	72
4.3.1 Composition	72
4.3.2 Microstructure and Defect Density	79
4.3.3 Surface Morphology	81
4.3.4 Optical Performance	81
<b>5 InGaP Heteroepitaxial Integration with GeSi</b>	<b>83</b>
5.1 Introduction	83
5.2 Justification	83
5.3 Early Growth Schemes	84

5.4	Barriers to Heteroepitaxy	85
5.4.1	Lattice Mismatch	85
5.4.2	Thermal Mismatch	86
5.4.3	Heterovalent-on-Homovalent Epitaxy	86
5.5	The Device Material	88
5.6	Growth Conditions	89
5.7	Results and Discussion	90
5.7.1	Initiation Studies	91
5.7.2	Substrate Studies	93
5.7.3	Luminescence Studies	104
5.8	Conclusions	106
<b>6</b>	<b>Mechanisms of Branch Defect Formation</b>	<b>109</b>
6.1	Introduction	109
6.2	Branch Defects in InGaP	110
6.3	InGaP Graded Buffers Produced using an Industrial MOCVD Reactor	112
6.3.1	Background	112
6.3.2	Threading Dislocation Density and Surface Structure	114
6.3.3	Branch Defects	116
6.3.4	Summary	122
6.4	<i>In-situ</i> Annealing and Branch Defect Evolution	123
6.4.1	Uncapped Anneals	125
6.4.2	Capped Anneals	128
6.4.3	Post-growth Annealing	130
6.5	Defect Formation Mechanism	130
6.5.1	Spinodal Decomposition	131
6.5.2	Nucleation and Growth	132
6.5.3	Relaxation Anisotropy	134
6.6	Conclusions	137
<b>7</b>	<b>Yellow-green Strained-InGaP Quantum Well LEDs</b>	<b>139</b>
7.1	Introduction	139
7.2	Materials Issues in Device Design	140
7.2.1	Relaxed Graded Buffer Epitaxial Transparent Substrate	142
7.2.2	Device Structure	143
7.2.3	Thermal Expansion	146
7.2.4	Quantum Well Emission Model	147
7.3	Initial Results	151
7.4	Device Performance	155
7.4.1	Performance Variation with Threading Dislocation Density	156
7.4.2	Performance Variation with Quantum Well Composition	159
7.4.3	Performance Variation with Quantum Well Growth Temperature	160
7.4.4	Longer-Wavelength Operation	162
7.5	Non-idealities in Device Performance	163
7.5.1	Doping Control	163
7.5.2	Ordering	165
7.6	Conclusions	166

<b>8</b>	<b>Summary of Results and Suggestions for Future Work</b>	<b>169</b>
8.1	Overview	169
8.2	Summary of Results	170
8.2.1	InGaP Monolithic Integration with GeSi	170
8.2.2	Microstructural Studies	170
8.2.3	Strained-InGaP Quantum Well ETS-LEDs	172
8.3	Suggestions for Future Work	173
8.3.1	InGaP Monolithic Integration with GeSi	173
8.3.2	Microstructural Studies	173
8.3.3	Strained-InGaP Quantum Well ETS-LEDs	174
<b>Appendix A.</b>	<b>Critical Thickness Calculation</b>	<b>177</b>
<b>Appendix B.</b>	<b>Sample MOCVD Growth Sheets</b>	<b>179</b>
<b>Appendix C.</b>	<b>Calculation of Figure 7.1: InAlGaP Properties</b>	<b>183</b>
<b>Appendix D.</b>	<b>Calculation of Predicted InGaP Strained Quantum Well Emission</b>	<b>185</b>
<b>References</b>		<b>199</b>

## List of Figures

Figure 1.1. Evolution of visible LED performance with time (reproduced from Craford <sup>2</sup> ).	16
Figure 1.2. Device performance compared to eye sensitivity (reproduced from Kish <sup>4</sup> ). The solid line represents the CIE Eye Response function, $V(\lambda)$ .	17
Figure 1.3. Performance of typical visible LEDs (from the OIDA 2002 Technology Roadmap <sup>9</sup> ).	18
Figure 2.1. Molecular structure of trimethyl-Group III sources.	23
Figure 2.2. Molecular structure of phosphine.	24
Figure 2.3. Molecular structure of silane.	25
Figure 2.4. Molecular structure of dimethylzinc.	26
Figure 2.5. Dopant and unintentional impurity incorporation in MOCVD-grown $\text{In}_{0.22}(\text{Al}_{0.2}\text{Ga}_{0.8})_{0.78}\text{P}$ .	28
Figure 2.6. Group-V terminated III-V semiconductor surface.	29
Figure 2.7. Thermal regimes of growth rate in MOCVD.	29
Figure 2.8. Boundary layer thickness over the substrate for laminar flow conditions.	30
Figure 3.1. Zincblende crystal structure (reproduced from Stringfellow <sup>13</sup> ).	36
Figure 3.2. Schematic energy vs. momentum band structure for a) direct bandgap semiconductor, and b) indirect bandgap semiconductor.	36
Figure 3.3. Relationship between bandgap/emission wavelength and lattice constant in the AlP-GaP-InP system.	38
Figure 3.4. Common dislocation configurations. a) Origination from the substrate, b) termination at the edge of the crystal, c) dislocation half-loop nucleation, d) heterogeneous dislocation nucleation at a point source.	40
Figure 3.5. Burger's vector components of a dislocation in the $\frac{1}{2}a[101]$ (111) slip system.	41
Figure 3.6. a) $\alpha$ and b) $\beta$ dislocations in compressively strained III-V epitaxy (reproduced from Matagrano <sup>31</sup> ).	42
Figure 3.7. a) Schematic of fully-strained epitaxy ( $h < h_c$ ), and b) schematic of partially-relaxed epitaxy ( $h \geq h_c$ ).	44
Figure 3.8. Variation of epilayer critical thickness with lattice mismatch.	45
Figure 3.9. Termination of a misfit dislocation in two threading segments.	47
Figure 3.10. Misfit dislocation arrays for a) direct mismatched deposition, and b) relaxed graded buffer deposition.	48
Figure 3.11. Dislocation glide and misfit recycling during graded buffer growth.	49
Figure 3.12. a) PVTEM and b) XTEM of an InGaP graded buffer misfit dislocation array.	49
Figure 3.13. Misfit array geometry for a) on-axis substrates, b) substrates misoriented toward the nearest $\langle 111 \rangle$ , and c) substrates misoriented toward the nearest $\langle 110 \rangle$ .	50
Figure 3.14. Initial modes of epitaxy <sup>45</sup> .	51
Figure 3.15. Surface sites for adatom attachment during epitaxy: a) terrace, b) ledge, and c) kink.	51

Figure 3.16. AFM images of a) step-flow growth and b) step-bunching (reproduced from Shinohara <sup>47</sup> ).	52
Figure 3.17. Schematic pseudobinary T-x phase diagram (reproduced from Stringfellow <sup>13</sup> ).	56
Figure 3.18. Calculated InP-GaP T-x phase diagram (reproduced from Zunger and Mahajan <sup>49</sup> ).	56
Figure 3.19. CuPt-B ordering in InGaP (reproduced from Zunger and Mahajan <sup>49</sup> ).	58
Figure 3.20. Diffraction superspots arising from CuPt-B ordering ([110] pole figure).	59
Figure 3.21. P-rich 2x1 surface reconstruction in InGaP (reproduced from Zunger and Mahajan <sup>49</sup> ).	59
Figure 3.22. Variation of internal quantum efficiency with In fraction in In <sub>x</sub> Ga <sub>1-x</sub> P.	64
Figure 3.23. Light escape cones in a transparent substrate device (reproduced from Kish <sup>4</sup> ).	65
Figure 3.24. Energy band diagrams for a homojunction LED a) flat band, b) thermal equilibrium.	66
Figure 3.25. Energy band diagrams for a single heterojunction LED a) flat band, b) thermal equilibrium.	66
Figure 3.26. Energy band diagrams for a double heterojunction LED a) flat band, b) thermal equilibrium.	67
Figure 4.1. Thomas Swan MOCVD reactor chamber used to produce the samples in this study.	69
Figure 4.2. Orientation of (004) planes relative to the sample surface for 10° misorientation toward the nearest <110>; n <sub>s</sub> refers to the sample surface normal.	71
Figure 4.3. Illustration of the single-crystal diffraction condition a) prior to alignment and b) with the plane normal of interest, g, aligned along the diffraction vector, q.	73
Figure 4.4. Axes of rotation available for sample alignment in TAXRD.	74
Figure 4.5. Resolution of substrate offcut into the perpendicular in-plane <110> directions. g <sub>004</sub> is the (004) plane normal; n <sub>s</sub> is the sample surface normal.	74
Figure 4.6. Tilt of epilayer (001) planes during growth on a misoriented substrate.	75
Figure 4.7. In the case of a tilted epilayer and <110> sample alignment, the epitaxial plane normal of interest, g <sub>epi</sub> , does not lie completely in the dispersion plane.	75
Figure 4.8. The 004 diffraction condition.	76
Figure 4.9. The 224 diffraction condition.	77
Figure 4.10. Predicted transmission electron diffraction patterns for a zincblende crystal. a) <110> pole figure; b) <100> pole figure.	80
Figure 4.11. Schematic illustration of SEM beam shape variation with accelerating voltage (reproduced from Leon, <i>et al.</i> <sup>79</sup> )	81
Figure 5.1. Anti-Phase Boundary ([110] projection) <sup>95</sup> .	87
Figure 5.2. Double-atomic-step surface ([110] projection).	87
Figure 5.3. APB annihilation ([110] projection).	88
Figure 5.4. Bandgap vs. lattice constant of common III-V and IV semiconductors. (—: Direct bandgap; ---: Indirect bandgap)	89
Figure 5.5. a) PV-AFM image of In <sub>0.3</sub> Ga <sub>0.7</sub> P on Ge <sub>0.7</sub> Si <sub>0.3</sub> , initiated at T=700°C and V/III = 1000. Target InGaP thickness = 500Å. Maximum island height = 300 nm; b) PV-AFM image of In <sub>0.3</sub> Ga <sub>0.7</sub> P on Ge <sub>0.7</sub> Si <sub>0.3</sub> , initiated at T=500°C and V/III = 1000. Target InGaP thickness = 500Å. Maximum island height = 675 nm.	92



Figure 5.6. PV-AFM image of $\text{In}_{0.3}\text{Ga}_{0.7}\text{P}$ on $\text{Ge}_{0.7}\text{Si}_{0.3}$ , initiated at $T=500^\circ\text{C}$ and $V/\text{III} = 1000$ . Target InGaP thickness = 500nm, RMS = 167 nm.	92
Figure 5.7. PV-AFM images of $\text{In}_{0.3}\text{Ga}_{0.7}\text{P}$ on $\text{Ge}_{0.7}\text{Si}_{0.3}$ , initiated at $T=700^\circ\text{C}$ and $V/\text{III} = 1000$ . Target InGaP thickness = 300nm. a) 5 min Piranha clean; RMS = 28 nm, and b) 10 min Piranha clean; RMS = 32 nm.	93
Figure 5.8. $\text{In}_{0.22}\text{Ga}_{0.78}\text{P}$ on $\text{Ge}_{0.5}\text{Si}_{0.5}$ , initiated at $T=700^\circ\text{C}$ and $V/\text{III} = 1000$ . Target InGaP thickness = 800nm; RMS = 58nm. a) PV-AFM; b) Nomarski; c) cross-section SEM.	94
Figure 5.9. SIMS analysis of $\text{In}_{0.22}\text{Ga}_{0.78}\text{P}$ on $\text{Ge}_{0.5}\text{Si}_{0.5}$ ; images of this sample shown in Figure 5.8.	95
Figure 5.10. PV-AFM images of $\text{Ge}_{0.7}\text{Si}_{0.3}$ before and after thermal cycling in MOCVD hydride ambient. a) Before thermal cycling, RMS ~ 0.17 nm, b) After cycling in $\text{N}_2$ only, RMS ~ 0.2 nm (note change in image scale), c) After cycling in $\text{H}_2$ only, RMS = 0.25 nm and d) After cycling in $\text{H}_2$ plus $\text{PH}_3$ , RMS = 0.88 nm.	96
Figure 5.11. Thermodynamically predicted gas-phase etch products for $\text{H}_2(\text{g})$ over $\text{Ge}_{0.7}\text{Si}_{0.3}$ .	98
Figure 5.12. Thermodynamically predicted gas- and solid-phase etch products for $\text{H}_2(\text{g})$ over $\text{Ge}_{0.7}\text{Si}_{0.3}$ .	99
Figure 5.13. Thermodynamically predicted gas-phase etch products for $\text{H}_2(\text{g})$ plus $\text{PH}_3(\text{g})$ over $\text{Ge}_{0.7}\text{Si}_{0.3}$ .	100
Figure 5.14. Variation of $\text{SiP}_2(\text{g})$ production with temperature and P for $\text{H}_2(\text{g})$ plus $\text{PH}_3(\text{g})$ over $\text{Ge}_{0.7}\text{Si}_{0.3}$ .	101
Figure 5.15. Thermodynamically predicted gas- and solid-phase etch products for $\text{H}_2(\text{g})$ plus $\text{PH}_3(\text{g})$ over $\text{Ge}_{0.7}\text{Si}_{0.3}$ .	102
Figure 5.16. Thermodynamically predicted $\text{GeP}(\text{s})$ formation for $\text{H}_2(\text{g})$ plus $\text{PH}_3(\text{g})$ over $\text{Ge}_{0.7}\text{Si}_{0.3}$ , illustrating complete consumption of available P.	103
Figure 5.17. CL emission from a) InGaP islands and b) bare GeSi substrate.	105
Figure 5.18. XTEM of $\text{In}_{0.42}\text{Ga}_{0.58}\text{P}$ islands on $\text{Ge}_{0.7}\text{Si}_{0.3}$ , initiated at $T=500^\circ\text{C}$ and $V/\text{III} = 1000$ .	106
Figure 6.1. Schematic of the InGaP relaxed, graded buffer deposited via MOCVD.	110
Figure 6.2. Branch defect formation regimes for MOCVD grown InGaP <sup>41</sup> . Note that the direct bandgap to indirect bandgap crossover for InGaP lies within the branch defect regime.	111
Figure 6.3. Threading dislocations pinned on a branch defect.	112
Figure 6.4. AFM of Lumileds samples: a) LL5, b) LL11, c) LL2, d) LL8.	115
Figure 6.5. PVTEM of Lumileds samples: a) LL5, b) LL11, c) LL2, d) LL8.	117
Figure 6.6. PVTEM of sample LL8.	118
Figure 6.7. PVTEM of sample LL8, $g \cdot R \approx 0$ .	119
Figure 6.8. XTEM of sample LL8.	119
Figure 6.9. PVTEM of sample LL8.	120
Figure 6.10. PVTEM of sample LL8, in the same area as Figure 6.9. Note misfit dislocations that underlie regions of branch defect contrast in Figure 6.9.	120
Figure 6.11. HRTEM lattice image of a branch defect region: a) plan view and b) cross section.	121
Figure 6.12. Fast Fourier transforms of plan view lattice images from a) a bright fringe and b) a dark fringe of a branch defect.	122

Figure 6.13. Uncapped <i>in-situ</i> annealing procedure for InGaP graded buffer. Dashed lines indicate an interruption in 725°C growth to perform a 10 minute anneal at 775°C in a PH <sub>3</sub> ambient. _____	124
Figure 6.14. Capped <i>in-situ</i> annealing procedure for InGaP graded buffer. Dashed lines indicate an interruption in 725°C growth to perform a 10 minute anneal at 775°C in a PH <sub>3</sub> ambient. _____	124
Figure 6.15. TEM of a) unannealed and b) <i>in-situ</i> annealed $\nabla_x[\text{In}_x\text{Ga}_{1-x}\text{P}]$ graded buffer, where $x_{\text{In}} = 0.21$ in the cap layer. Typical branch defects indicated by $\blacktriangle$ . _____	126
Figure 6.16. TEM of <i>in-situ</i> annealed $\nabla_x[\text{In}_x\text{Ga}_{1-x}\text{P}]$ graded buffers with a) $x_{\text{In}} = 0.08$ , b) $x_{\text{In}} = 0.13$ , and c) $x_{\text{In}} = 0.19$ in the cap layer. Typical branch defects indicated by $\blacktriangle$ . _____	127
Figure 6.17. PVTEM of annealed samples with $x_{\text{In}} = 0.10$ , deposited with V/III ratio of a) 50, and b) 150. Typical branch defects indicated by $\blacktriangle$ . Note the lack of branch defect development in b). _____	128
Figure 6.18. XTEM of $\nabla_x[\text{In}_x\text{Ga}_{1-x}\text{P}]$ graded buffers a) unannealed, $x_{\text{In}} = 0.12$ , b) capped anneal, $x_{\text{In}} = 0.12$ , and c) capped anneal, $x_{\text{In}} = 0.15$ . Typical branch defects are denoted by $\blacktriangle$ . V/III=150 for all. _____	129
Figure 6.19. Surface degradation in sample 10-2 (see Figure 6.15) after post-growth annealing. _____	130
Figure 6.20. Schematic crystallographic geometry of branch defects and dislocation blocking. _____	137
Figure 7.1. $E_g$ , $E_o$ and lattice constant contours for the InAlGaP system. $\Gamma$ refers to direct ( $k=0$ ) transitions, while X refers to indirect ( $k\neq 0$ ) transitions from the conduction band. _____	141
Figure 7.2. Decline in internal quantum efficiency with increasing Al fraction in $\text{In}_{0.5}(\text{Al}_x\text{Ga}_{1-x})_{0.5}\text{P}$ (reproduced from Cao, <i>et al</i> <sup>10</sup> ). _____	142
Figure 7.3. Schematic of a) the device structure, b) $E_c$ , $E_v$ , and refractive index variation in the device structure, c) the device energy levels in thermal equilibrium (not to scale). _____	145
Figure 7.4. Predicted emission for sub-critical-thickness quantum well devices with $\text{In}_{0.22}(\text{Al}_{0.2}\text{Ga}_{0.8})_{0.78}\text{P}$ clads and an aluminum-free strained quantum well. _____	146
Figure 7.5. Strain contributed by thermal expansion mismatch between GaP and $\text{In}_x(\text{Al}_{0.2}\text{Ga}_{0.8})_{1-x}\text{P}$ , and between GaP and $\text{In}_{0.32}\text{Ga}_{0.68}\text{P}$ . _____	147
Figure 7.6. Predicted emission for sub-critical-thickness quantum well devices with a) $\text{In}_{0.2}(\text{Al}_{0.2}\text{Ga}_{0.8})_{0.8}\text{P}$ clads and an aluminum-free strained quantum well, and b) $\text{In}_{0.26}(\text{Al}_{0.2}\text{Ga}_{0.8})_{0.74}\text{P}$ clads and an aluminum-free strained quantum well. _____	150
Figure 7.7. Predicted emission for sub-critical-thickness quantum well devices with $\text{In}_{0.32}(\text{Al}_{0.2}\text{Ga}_{0.8})_{0.78}\text{P}$ clads and an aluminum-free strained quantum well. _____	150
Figure 7.8. a) XTEM of a device structure with an undoped $\text{In}_{0.4}\text{Ga}_{0.6}\text{P}$ active layer and undoped $\text{In}_{0.27}\text{Ga}_{0.73}\text{P}$ clads. b) Cathodoluminescence emission from the active layer, at 612 nm, and from the clads, at 575 nm. _____	151
Figure 7.9. Cathodoluminescence emission from undoped, strained $\text{In}_{0.35}\text{Ga}_{0.65}\text{P}$ quantum well device structures. —: $\text{In}_{0.24}(\text{Al}_{0.2}\text{Ga}_{0.8})_{0.76}\text{P}$ clads and $\text{In}_{0.24}\text{Ga}_{0.76}\text{P}$ SCH. - - -: $\text{In}_{0.24}\text{Ga}_{0.76}\text{P}$ clads and no SCH. _____	152
Figure 7.10. Cathodoluminescence emission from undoped device structure with $\text{In}_{0.24}(\text{Al}_{0.2}\text{Ga}_{0.8})_{0.76}\text{P}$ clads and $\text{In}_{0.24}\text{Ga}_{0.76}\text{P}$ SCH, but no quantum well. _____	153

Figure 7.11. —: CL emission from sample shown in Figure 7.10, ...: Sum of Gaussian functions defined below in Table 7.1.	153
Figure 7.12. —: CL emission from sample shown in Figure 7.9, ...: Sum of Gaussian functions representing all emission sources.	154
Figure 7.13. XTEM of device structure with $\text{In}_{0.24}(\text{Al}_{0.2}\text{Ga}_{0.8})_{0.76}\text{P}$ clads, $\text{In}_{0.24}\text{Ga}_{0.76}\text{P}$ SCH, and $\text{In}_{0.35}\text{Ga}_{0.65}\text{P}$ quantum well. Emission from this structure is shown in Figure 7.9.	155
Figure 7.14. Schematic of the processed LED.	156
Figure 7.15. Spectral and optical power per facet characteristics of devices with the structure illustrated in Figure 7.14, grown at $650^\circ\text{C}$ with an $\text{In}_{0.32}\text{Ga}_{0.68}\text{P}$ quantum well active region and varying $\rho_{\text{TD}}$ .	157
Figure 7.16. XTEM of a device with an $\text{In}_{0.32}\text{Ga}_{0.68}\text{P}$ quantum well. Electron diffraction of the quantum well (center) shows ordering superspots, while the clad (right) does not.	158
Figure 7.17. Spectral and optical power per facet characteristics of devices grown at $650^\circ\text{C}$ with $\rho_{\text{TD}} = 5 \times 10^7 \text{ cm}^{-2}$ and varying $x_{\text{In}}$ in the quantum well.	159
Figure 7.18. XTEM of a device with an $\text{In}_{0.37}\text{Ga}_{0.63}\text{P}$ quantum well and $\rho_{\text{TD}} = 5 \times 10^7 \text{ cm}^{-2}$ . a) $650^\circ\text{C}$ quantum well growth, b) $575^\circ\text{C}$ quantum well growth. The ripple pattern in b) is an artifact of TEM foil preparation.	160
Figure 7.19. Spectral and optical power per facet characteristics of devices grown with an $\text{In}_{0.37}\text{Ga}_{0.63}\text{P}$ active layer, $\rho_{\text{TD}} = 5 \times 10^7 \text{ cm}^{-2}$ , and varying quantum well growth temperatures.	161
Figure 7.20. Spectral and optical power per facet characteristics of devices grown at $650^\circ\text{C}$ with $\rho_{\text{TD}} = 5 \times 10^7 \text{ cm}^{-2}$ and varying $x_{\text{In}}$ in the quantum well.	162
Figure 7.21. Doping fluctuations via SIMS analysis of three quantum well device structures. a) and b) were deposited 2 months apart, while b) and c) were deposited one week apart.	164
Figure 7.22. [110] Transmission Electron Diffraction of InGaP for V/III = 85 and a) Growth Rate = $131 \text{ \AA}/\text{min}$ , b) Growth Rate = $515 \text{ \AA}/\text{min}$ .	166
Figure 8.1. Schematic of a) insulator-stripe contacts; b) double top contacts.	175

## List of Tables

Table 2.1. Physical properties of MOCVD precursor materials. _____	22
Table 3.1. Physical properties of AlP, GaP, and InP. _____	37
Table 3.2. Nonrandom atomic arrangements identified in III-V semiconductors. _____	53
Table 3.3. Constants used in Figure 3.21. _____	64
Table 5.1. Lattice parameters and bandgaps of semiconductors of interest. _____	85
Table 5.2. Nucleation of $\text{In}_{0.3}\text{Ga}_{0.7}\text{P}$ on $\text{Ge}_{0.7}\text{Si}_{0.3}$ by MOCVD. _____	91
Table 5.3. Thermodynamically predicted etch rates for $\text{H}_2$ over $\text{Ge}_{0.7}\text{Si}_{0.3}$ . _____	99
Table 6.1. Description of samples provided by Lumileds Lighting. _____	112
Table 6.2. Data from Lumileds $\text{V}_x[\text{In}_x\text{Ga}_{1-x}\text{P}]$ MOCVD samples. _____	113
Table 6.3. Data from MIT $\text{V}_x[\text{In}_x\text{Ga}_{1-x}\text{P}]$ MOCVD samples <sup>11</sup> (compare to LL5 and LL11). _____	113
Table 6.4. Energy dispersive x-ray (EDX) measurements of lateral fluctuations in indium fraction within a branch defect. _____	121
Table 6.5. Summary of Samples in Annealing Series _____	125
Table 6.6. Strain relaxation for uncapped, annealed samples compared to strain relaxation for standard relaxed, graded buffers grown at $725^\circ\text{C}$ . _____	135
Table 7.1. Coefficients of Gaussian functions in Figure 7.11. $I_1$ represents $\Gamma$ emission from the SCH, $I_2$ represents $\Gamma$ emission from the clad, and $I_3$ is a broad background. _____	154
Table 7.2. Summary of LED results. _____	162
Table 7.3. Summary of growth conditions for $\text{In}_{0.32}\text{Ga}_{0.68}\text{P}$ samples in the ordering study. _____	165

## Acknowledgements

First and foremost, I would like to thank my advisor, Prof. Gene Fitzgerald. Gene has the energy and enthusiasm of three people and dreams enough for ten or more. He gave me the opportunity not just to study InGaP and defects and MOCVD, but also to become a materials scientist. Gene's ideas were of course the genesis of this project, and his feedback and faith helped to see it through.

Professors Klavs Jensen, Caroline Ross, and Michael Rubner graciously brought their various areas of expertise to bear on my work. Their contributions improved and enriched my defense, my dissertation, and most of all my understanding.

When I first joined the Fitzgerald Group, Gene joked that I was on the one-year plan. This was perhaps karmically disadvantageous. However, my slow and steady course of graduate research has allowed me to interact with many exceptional Fitzgerald Group members, including Jeev Makan, Mayank Bulsara, Steve Ting, Andy Kim, Tom Langdo, Matt Currie, Chris Leitz, Vicky Yang, Mike Groenert, Gianni Taraschi, Larry Lee, Arthur Pitera, Nate Quitoriano, Nava Ariel, Juwell Wu, Mike Mori, Carl Dohrman, Saurabh Gupta, and David Isaacson. They have made innumerable positive contributions to my research and to my experience as a graduate student. Anabela Afonso keeps our administrative wheels turning and can always make me laugh. Special thanks to Andy Kim, who introduced me to many useful techniques and concepts, and whose work laid the foundation for my branch defect studies; Juwell Wu, who processed my wafer pieces into real, live LEDs; and to Mike Mori, Gianni Taraschi, and Sajan Saini, for reading and commenting on parts of this thesis.

I can't emphasize enough the value of the help I received from Mike Frongillo, who runs a tight ship in the electron microscopy lab. Thanks also to Libby Shaw, who does the same in the AFM lab. Peter Kloumann, Joe Adario, Tony Garratt-Reed, Jurgen Michel, and Sajan Saini provided frequent assistance with wrangling microscopes, diffractometers, photodetectors, and even data. Finally, I could not have made the LED measurements in Chapter 7 without the help and patience of Harry Lee, from the lab of Prof. Rajeev Ram, MIT.

I was fortunate to have in my life many good friends who moved to Boston or who were dedicated to staying in touch by e-mail, including Jamileh Jemison, Shane Detweiler, John Beaber, Erik and Stephanie Leavitt, and Sajan Saini. We're all moving to the same place after this, right? Right?! Guys?? Dawn Metcalf helped me to understand myself and MIT a bit better. I have also had Isshinryu Karate-do at MIT to keep me healthy and happy and driven. The club members were first my classmates and then my students, but always my friends.

My family means the world to me. They have always supported my interests, even when they don't know what the heck I'm talking about. First, the family that raised me: my dad, Stephen McGill; my maternal grandparents, Keith and Muriel Milgate; my uncle, Larry Milgate; and my cousins, Mike, Angel, Evan, and Riley Greenleaf. My mother, Karen Milgate McGill; my aunt, Sandra Milgate Greenleaf; my cousin, Doug Greenleaf; and my paternal grandparents, Homer and Helen McGill, are always in my heart, although my time with them was cut short. I am also very fortunate in my family-in-law: Bill, Arlene, and Jane Borthwick. Regardless of my career, I will always be rich.

My husband, Matt Borthwick, helped to keep me sane throughout my time at MIT. As a physics Ph.D. student (who conveniently works three floors below me) he has all too much empathy for the ups and downs of graduate life. He pushed when I needed pushing, and left me alone when I was best ignored, and I would not want to experience life—graduate or otherwise—without him. He also reviewed this entire dissertation, which was a generous feat in itself.

Finally, I would like to dedicate this thesis to my grandmother, Muriel Milgate. She taught me, by example, that I can figure out a way to accomplish just about anything I want to, regardless of things like training or previous experience. That thinking got me into MIT; fortunately, it also got me out. Gram very much wanted to see me graduate, and I very much wanted her to see me graduate, but she warned me—with unhappy and uncanny accuracy, as it turned out—that she was only holding on until June. I hope that, somewhere, she's watching.

# 1 Motivation for and Organization of Thesis

## 1.1 Motivation

In the field of semiconductor devices, compound semiconductor materials are uniquely suited for the production of efficient light emitting devices. Optimal materials for light emitters have a high radiative recombination efficiency; that is, a large proportion of injected electrical carriers are converted to photons. Several binary compound semiconductors, including gallium arsenide (GaAs) and indium phosphide (InP), possess the direct bandgap required for efficient conversion of carriers to photons. In addition, ternary alloys of a direct bandgap compound semiconductor with an indirect, such as GaP or AlP, often exhibit a direct bandgap over a large composition range. This provides a great deal of flexibility in tailoring the wavelength and operation of compound semiconductor light emitting diodes (LEDs). However, the development of solid-state lighting depends on economics in addition to science. To penetrate the lighting market, LEDs must compete in terms of cost as well as performance. This work examines and expands upon a dominant materials system that satisfies both of these requirements: indium gallium phosphide (InGaP) and indium aluminum gallium phosphide (InAlGaP) alloys produced by metal organic chemical vapor deposition (MOCVD).

Commercial III-V semiconductor LEDs first appeared in 1962 with the introduction by General Electric of red gallium arsenide phosphide (GaAsP) devices<sup>1,2</sup>. These were followed in the late 1960s by improved devices from Monsanto and Hewlett-Packard<sup>3</sup>. These early GaAsP devices were produced in high volumes using vapor phase epitaxy (VPE). Because III-V materials that emit visible light generally consist of alloys, and often utilize thin-film layer structures, they cannot be produced using bulk techniques. Therefore, epitaxial methods such as VPE were developed. GaAsP red LEDs were joined by GaP:Zn,O and aluminum gallium arsenide (AlGaAs) red-emitting devices produced via liquid phase epitaxy (LPE). In the mid-1980s, AlGaAs double-heterostructure (DH) LEDs achieved luminous efficiency levels on par with red-filtered incandescent lamps<sup>4</sup>. Each of these new technologies represented a substantial increase in performance, as illustrated in Figure 1.1. Attempts to access more of the visible

spectrum led to isoelectronically N-doped GaP:N and GaAsP:N devices, which emit green and red-yellow light, respectively.

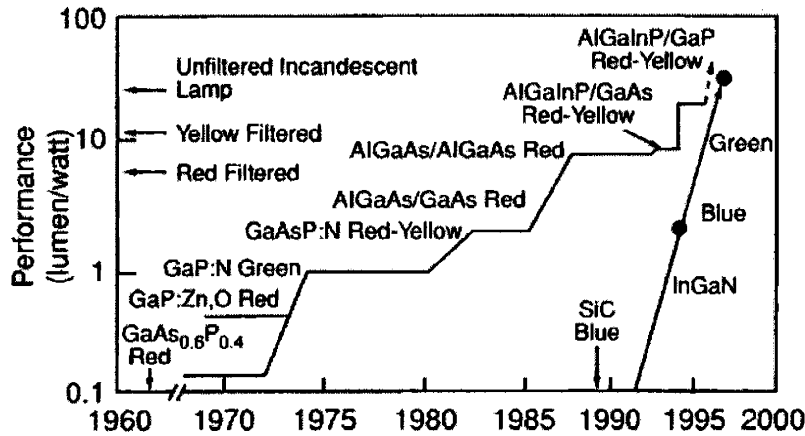


Figure 1.1. Evolution of visible LED performance with time (reproduced from Craford<sup>2</sup>).

In the early 1990s, MOCVD was applied to the commercial production of InAlGaP LEDs operating in the red through yellow-green region of the spectrum<sup>5,6</sup>. Conventional VPE and LPE techniques are not suitable for InAlGaP production, due to Al-precursor incompatibility and Al melt segregation, respectively<sup>4</sup>. On the other hand, MOCVD is well-suited to the growth of InAlGaP devices, and MOCVD has produced the highest efficiency InAlGaP LEDs to date<sup>7</sup>. Traditionally, InAlGaP devices consist solely of  $\text{In}_{0.5}(\text{Al}_y\text{Ga}_{1-y})_{0.5}\text{P}$  layers that are lattice-matched to a GaAs substrate. The device emission wavelength is determined by the fraction of aluminum present in the active layer. The best yellow-to-red LEDs utilize a transparent GaP substrate, which is implemented by etching away the original GaAs substrate and wafer-bonding the device stack to GaP<sup>7</sup>. Through the use of chip-shaping to reduce internal absorption losses, peak efficiencies of more than 100 lumens/watt have been achieved for 610 nm emission, with a direct current external efficiency of 55%<sup>8</sup>.

Our interest in InGaP and InAlGaP as materials for light emitting devices stems from the desire to produce solid-state lasers and high-brightness LEDs operating in the green region of the spectrum, particularly near 555 nm where the eye is most sensitive. None of the materials that currently dominate the LED market has demonstrated



exceptional performance in this part of the spectrum, as illustrated in Figure 1.2. This problem is colloquially known as the “green gap”. Also illustrated in Figure 1.2 is the CIE Eye Response function,  $V(\lambda)$ , which gives a quantitative measure of the sensitivity of the human eye across the visible spectrum.

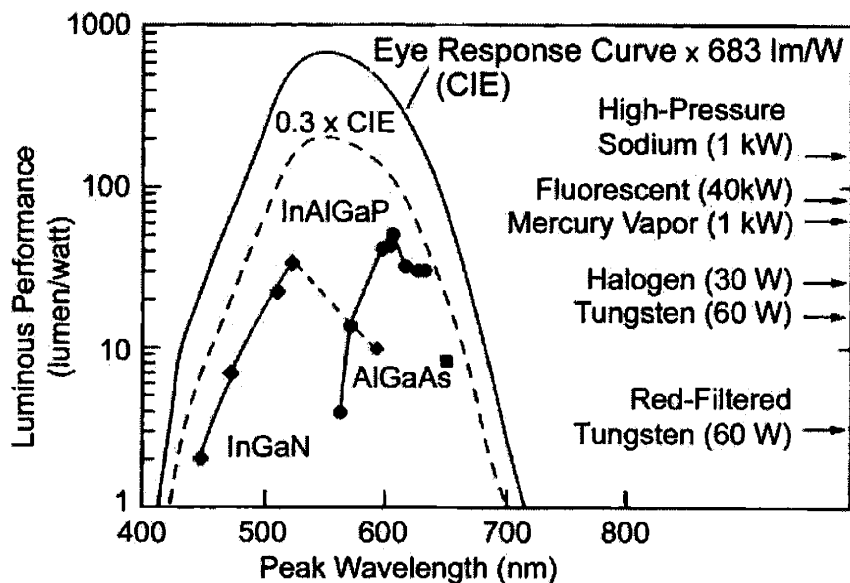


Figure 1.2. Device performance compared to eye sensitivity (reproduced from Kish<sup>4</sup>). The solid line represents the CIE Eye Response function,  $V(\lambda)$ .

From the short wavelength side, the longest-wavelength InGaN devices operate between 520 nm and 540 nm. Pronounced In segregation at higher In fractions has limited the ability to produce high quality longer wavelength devices. From the long wavelength side, green InAlGaP devices have poor internal quantum efficiency due to the proximity of the indirect bandgap-direct bandgap crossover at the compositions of interest, as well as to oxygen-related defects. The shortest wavelength bright InAlGaP devices operate in the range of 590 nm to 600 nm. These 500 nm-600 nm devices often have very poor color purity, leading to an undersaturated appearance. This is a particular problem in the green region, where a deviation of as little as 2 nm is discernable to the human eye.

Based on the OIDA 2002 solid state lighting roadmap<sup>9</sup>, a white LED performance target of 150 lm/W requires a consistent 50% power conversion efficiency for the

constituent RGB devices. Power conversion efficiency is also known as “wall-plug” efficiency and is defined as the ratio of output optical power to input electrical power. It is clear from Figure 1.3 that the majority of visible wavelengths lag far behind this goal. Furthermore, devices in the range of 500 nm-600 nm do not yet even approach the 10%-20% power conversion efficiencies available at longer and shorter wavelengths.

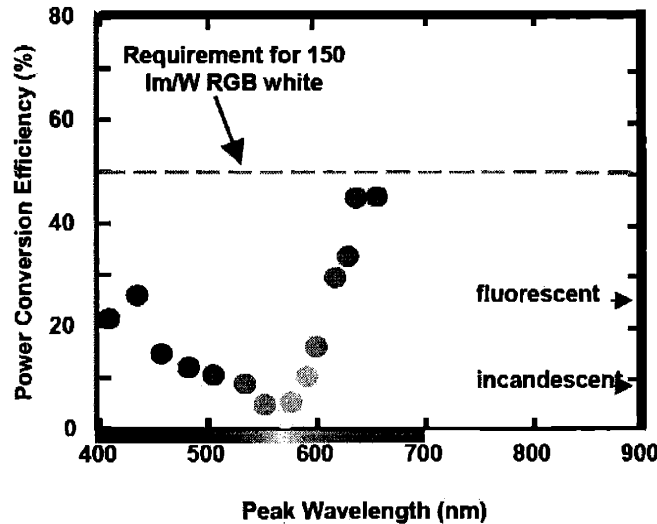


Figure 1.3. Performance of typical visible LEDs (from the OIDA 2002 Technology Roadmap<sup>9</sup>).

The development of a solid state RGB lighting system with a large color gamut demands an intense, efficient device with a narrow spectral linewidth. Until the green gap problem is solved, full-color mixing with flexible color temperature will remain difficult to achieve. In addition, no laser operating at these wavelengths can be produced until a truly efficient material is found.

The goal of this work is to examine fundamental materials processes in the InGaP system as they pertain to the integration of InGaP and InAlGaP on non-standard platforms such as GeSi graded buffers ( $\nabla_x[\text{Ge}_x\text{Si}_{1-x}]$ ) on Si and InGaP or InAlGaP graded buffers ( $\nabla_x[\text{In}_x\text{Ga}_{1-x}\text{P}]$  or  $\nabla_x[\text{In}_x(\text{Al}_y\text{Ga}_{1-y})_{1-x}\text{P}]$ ) on GaP. This improved understanding of InGaP and InAlGaP properties and microstructural development is applied to the design and implementation of novel InGaP epitaxial transparent substrate light emitting diode devices (ETS-LEDs) operating in the yellow-green region of the visible spectrum.

The use of low-defect-density graded buffer virtual substrates provides access to a range of alloy compositions and lattice constants not frequently utilized in optical devices. In addition, these novel substrates enable the use of Al-free active regions. This is desirable because the affinity of Al for oxygen often leads to detrimental defect states in the active region and a related decrease in device performance<sup>10</sup>. Through the use of heterostructure and graded buffer technologies, enabled by lattice-mismatched MOCVD, we can access the entire red to green emission range using Al-free InGaP active regions.

Ultimately, InGaP can be a flexible, effective device material when it is integrated on novel platforms that provide access to a range of lattice constants and wavelengths long neglected by traditional lattice-matched epitaxy. In this work, we examine the initial heteroepitaxy of InGaP on GeSi virtual substrates, for application to future optoelectronic integration. We also address significant materials issues in the growth of high-quality InGaP graded buffer virtual substrates; specifically, we examine the origin and evolution of branch defects, the presence of which has been found to degrade device performance<sup>11</sup>. Finally, we demonstrate a novel strained-InGaP quantum-well LED epitaxially integrated on a transparent, graded-InGaP/GaP substrate. This device design incorporates indirect-bandgap InAlGaP clads and an indirect-bandgap InGaP separate confinement heterostructure, and is theoretically capable of 540 nm to 600 nm emission. We have achieved forward current LED operation of processed device structures, with fully transparent, yellow-green emission clearly visible to the unaided eye in ambient room light. We believe that these device structures will serve as the basis for improved, bright green and yellow LEDs to fill the green gap, and potentially for yellow laser diodes.

## **1.2 Organization of Thesis**

This work utilizes the versatile MOCVD growth technique to fabricate and characterize a range of InGaP- and InAlGaP-based heterostructures for optical device applications. The approach taken in this study unites basic materials research with novel device design and applications. Each experimental path seeks to identify new or improved platforms for the integration of InGaP alloy compositions that are not lattice-

matched to any common substrate materials. Of primary interest are materials properties that influence device performance, including dislocations and other microstructural defects, ordering and other deviations from randomness, and the efficient conversion of electrical carriers to visible light. The thesis is grouped into two major sections:

- *Review of MOCVD and the Properties of InGaP and InAlGaP*

Chapter 2 provides a detailed overview of the MOCVD process. Chapter 3 is an introduction to the crystallographic, mechanical, chemical, and optical properties of InGaP and InAlGaP. Chapter 4 describes the growth conditions and characterization methods employed throughout this study.

- *Original Research*

Chapter 5 presents progress in initial modes of epitaxy during monolithic InGaP heterointegration on GeSi substrates. Chapter 6 details an examination of the nucleation and evolution of the branch defect microstructure found in InGaP, and identifies the mechanism by which these defects form. Chapter 7 reports the development of an epitaxial-transparent-substrate light emitting diode (ETS-LED) that incorporates a separate confinement heterostructure and a strained-InGaP quantum well active region integrated on GaP via an InAlGaP graded buffer. Device operation with 560 nm and 590 nm emission is demonstrated, while theoretical models predict accessible wavelengths as short as 540 nm. The best device has a power of 0.18  $\mu\text{W}/\text{facet}$  at 20 mA, corresponding to a luminous efficacy of approximately 0.01 lm/W. Finally, Chapter 8 summarizes the results of this work and contemplates future directions for and applications of these studies.

## 2 Overview of MOCVD Growth

### 2.1 Motivation for MOCVD

In general, compound semiconductor materials that emit visible light comprise layer structures and alloy compositions that cannot be produced by the bulk growth procedures, such as Czochralski growth, favored for infrared GaAs and InP devices<sup>12</sup>. The earliest compound-semiconductor-alloy visible LEDs to appear on the market were red GaAsP devices grown via vapor phase epitaxy (VPE) and red AlGaAs emitters grown via liquid phase epitaxy (LPE)<sup>2,12</sup>. However, the large thermodynamic stability of AlP relative to InP impedes compositional control during equilibrium growth. This necessitated the development of non-equilibrium deposition methods to produce high-quality InAlGaP materials. The technique that has come to dominate in both commercial and research settings is metalorganic chemical vapor deposition (MOCVD), also known as organometallic chemical vapor deposition (OMCVD), metalorganic vapor phase epitaxy (MOVPE), and organometallic vapor phase epitaxy (OMVPE). MOCVD is a complex process; however, it is also extremely flexible and has been applied to nearly the entire range of compound semiconductor materials.

### 2.2 MOCVD Process

The specific parameters used in the MOCVD growth of compound semiconductors tend to vary as widely as the specific reactor systems used; however, Stringfellow<sup>13</sup> offers an excellent treatment of the key issues. MOCVD growth of epitaxial films is a non-equilibrium process that proceeds by flowing gaseous precursors—in ratios calibrated to yield the desired film composition—over a heated, single-crystal substrate. In the elevated temperature environment of the reactor chamber, the gases undergo a complicated series of homogeneous and heterogeneous pyrolysis reactions that cause the precursors to dissociate or “crack” and deposit their Group III or V elements on the substrate surface.

### 2.2.1 Precursor Materials

The choice of source gases for III-V growth is critical to the design of the MOCVD growth process, as well as to the ultimate film quality. In this study, III-V growth was carried out in a Thomas Swan MOCVD reactor using H<sub>2</sub>-bubbled trimethylindium (TMIn), H<sub>2</sub>-bubbled trimethylgallium (TMGa), H<sub>2</sub>-bubbled trimethylaluminum (TMAI), and phosphine (PH<sub>3</sub>) as gaseous precursors carried in a H<sub>2</sub> ambient. Silane (SiH<sub>4</sub>) and H<sub>2</sub>-bubbled dimethylzinc (DMZn) were used as n- and p-type dopants, respectively. Because the organometallic sources are liquid at room temperature, they are held in constant-temperature baths and delivered to the reactor chamber dissolved in H<sub>2</sub> gas piped, or “bubbled”, through the source. Physical properties of the precursors are given in Table 2.1<sup>13</sup>. Key issues for each of these materials are presented below.

Element	Source	Melting Point (°C)	Boiling Point (°C)	Vapor Pressure (torr)	Bubbler Temperature, T <sub>b</sub> (°C)
In, group III	TMIn	88	135.8	$\log p = 10.52 - 3014/T_b(K)$	25.1
Ga, group III	TMGa	-15.8	55.8	$\log p = 8.07 - 1703/T_b(K)$	2.0
Al, group III	TMAI	15	126	$\log p = 8.224 - 2135/T_b(K)$	16.9
P, group V	PH <sub>3</sub>	--	-87.8	Undiluted gas	--
Si, n-dopant	SiH <sub>4</sub>	--	-111.4	Undiluted gas	--
Zn, p-dopant	DMZn	-42	46	$\log p = 7.802 - 1560/T_b(K)$	-9.9

Table 2.1. Physical properties of MOCVD precursor materials.

#### 2.2.1.1 Trimethylindium

TMIn consists of one In atom bonded to three CH<sub>3</sub> groups. Indium, with atomic number 49, has unfilled 5s<sup>2</sup> and 5p<sup>1</sup> electron states. Based on the valence-shell electron pair repulsion (VSEPR) theory, these bonds hybridize to form a planar, trigonal sp<sup>2</sup> configuration. One methyl radical is attached to each sp<sup>2</sup> orbital, with a bond angle of

120°, leading to the configuration shown in Figure 2.1. TMIn is typically chosen because of its bond stability and resistance to parasitic decomposition reactions. Such reactions tend to deplete reactants in the vapor and lead to nonuniformities in growth. However, TMIn is a solid at room temperature, making it difficult to maintain a consistent vapor pressure as the surface area of the solid changes. To avoid this issue, solution TMIn is used. Because the TMIn bubbler temperature is greater than room temperature, care must be taken to heat the gas line downstream from the bubbler to prevent condensation.

TMIn pyrolysis in H<sub>2</sub> proceeds via a large number of intermediate reactions, leading ultimately to the release of atomic In, with CH<sub>4</sub> and—to a lesser extent—C<sub>2</sub>H<sub>6</sub> gaseous byproducts. TMIn pyrolysis is catalyzed in a H<sub>2</sub> ambient; in this case it is expected to significantly decompose above 350°C. At high growth temperatures, In tends to desorb more readily from the growth surface<sup>14</sup>. This is typically referred to as a decrease in the In sticking coefficient, a general term accounting for the chemical factors that lead to diminished In adsorption and incorporation. Extremely high film quality has been achieved using TMIn<sup>13</sup>.

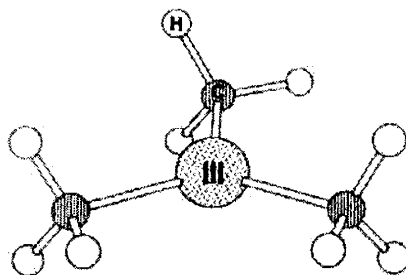


Figure 2.1. Molecular structure of trimethyl-Group III sources.

#### 2.2.1.2 Trimethylgallium

TMGa, similar to TMIn, consists of one Ga atom bonded to three CH<sub>3</sub> groups. Gallium lies one row above In in the periodic table and has unfilled 4s<sup>2</sup> and 4p<sup>1</sup> states. Thus, it will also be an sp<sup>2</sup> hybrid with the structure shown in Figure 2.1. The vapor pressure of TMGa is relatively high, and the bubbler temperature quite low, leading to a large partial pressure in the gas stream. The pyrolysis of TMGa is similar to that of

TMI<sub>n</sub>, yielding CH<sub>4</sub> and C<sub>2</sub>H<sub>6</sub> byproducts. However, the larger bond strength of TMGa means that substantial decomposition occurs only above 450°C.

#### 2.2.1.3 Trimethylaluminum

TMAI is also sp<sup>2</sup> hybridized with one Al atom bonded to three CH<sub>3</sub> molecules. Its vapor pressure is intermediate between that of TMGa and TMI<sub>n</sub>. The choice of Al precursor has a large impact on the ultimate film quality, as Al is highly reactive and easily forms complexes with oxygen and carbon, which are extremely detrimental contaminants. In fact, TMAI is a dimer in the gas phase, and has been observed to pyrolyze heterogeneously, forming aluminum carbide<sup>13</sup>. This leads to increased levels of carbon contamination relative to other possible Al precursors. Indeed, carbon contamination from all organometallic sources is a problem that must be carefully monitored.

#### 2.2.1.4 Phosphine

PH<sub>3</sub> consists of one P atom bonded to three hydrogens in a tetrahedral sp<sup>3</sup> configuration with one unbonded lone pair, shown in Figure 2.2. PH<sub>3</sub> is a gas at room temperature and is delivered via a compressed gas cylinder. The pyrolysis behavior of the Group V source is an important determinant of its usefulness for MOCVD. PH<sub>3</sub> has a relatively large bond strength, and its homogeneous decomposition proceeds only at high temperatures. This can be misleading, however, as the introduction of H<sub>2</sub> and organometallic precursors to the gas stream will catalyze PH<sub>3</sub> decomposition at much lower temperatures. For our purposes, adequate decomposition of PH<sub>3</sub> is assumed to occur only above 500°C.

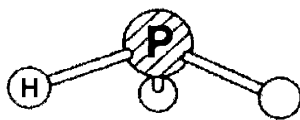


**Figure 2.2. Molecular structure of phosphine.**



A significant trade-off to the maturity of  $\text{PH}_3$  as a source is its toxicity. The threshold limit value for toxic exposure to  $\text{PH}_3$  is 0.3 ppm. In addition, highly reactive phosphorous compounds tend to form downstream throughout the reactor system, leading to the release of toxic byproducts and frequently to small fires. For this reason, stringent safety measures are employed in MOCVD growth using  $\text{PH}_3$ . The laboratory is maintained at negative pressure relative to its surroundings, and gas cylinders are chained in bunkered gas cabinets that vent directly to the roof. Toxic gas levels are redundantly monitored in the glove box and at several points throughout the room. Finally, self-contained breathing apparatus is frequently employed when carrying out reactor maintenance. Clearly, these issues can be a hindrance to the implementation of MOCVD growth. Less toxic precursor alternatives such as tertiarybutylphosphine are being explored, but at present  $\text{PH}_3$  remains the source of choice.

#### 2.2.1.5 Silane

$\text{SiH}_4$  consists of a Si atom covalently bonded to four hydrogen atoms, shown in Figure 2.3. A group IV atom, Si enters the III-V crystal on the Group III sublattice, donating its extra electron and acting as an n-type dopant. Because dopant levels are usually in the ppt to ppm range, 1%  $\text{SiH}_4$  diluted in  $\text{H}_2$  is used. Efficient pyrolysis of  $\text{SiH}_4$ , similar to  $\text{PH}_3$ , occurs at high temperatures above about  $600^\circ\text{C}$ .  $\text{SiH}_4$  decomposition remains reaction-limited over a large temperature range, making its incorporation into the film temperature dependent. As a hydride gas,  $\text{SiH}_4$  possesses many of the same safety issues discussed above for  $\text{PH}_3$ .

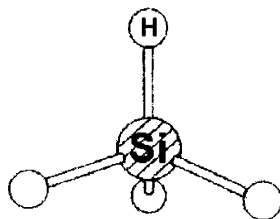


**Figure 2.3. Molecular structure of silane.**

### 2.2.1.6 Dimethylzinc

DMZn consists of an  $sp$  hybridized Zn atom linearly bonded to two  $CH_3$  molecules, shown in Figure 2.4. Its vapor pressure is on the order of the vapor pressure of TMGa, and it begins to pyrolyze at a low temperature, around  $200^\circ C$ . A group II atom, Zn also substitutes on the Group III sublattice and acts as a p-type dopant. Doping control will be discussed further below.

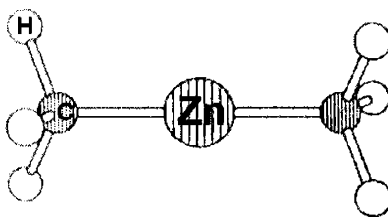


Figure 2.4. Molecular structure of dimethylzinc.

### 2.2.2 Source Purity and Film Contamination

Assuming careful system maintenance and leak checking, the primary source of contamination in MOCVD-grown films is the precursor materials themselves. The unintentional incorporation of oxygen, particularly in Al-containing films, has a pronounced detrimental effect. It forms a deep trap state in the film, making it both absorptive and highly resistive<sup>13,15</sup>. The anomalous performance decrease in InAlGaP LEDs with large Al fractions has been attributed to nonradiative recombination at oxygen traps<sup>4</sup>. In sufficient concentrations, oxygen contamination can lead to the formation of alumina compounds, disrupting epitaxy and leading to essentially polycrystalline film deposition. High-purity sources and further  $H_2$  carrier purification via a palladium diffuser may be employed to minimize oxygen contamination. Oxygen incorporation has also been shown<sup>16</sup> to vary inversely with growth temperature, as alumina complexes sublime at high temperatures. For this reason, temperatures above  $700^\circ C$  are desirable for InAlGaP film growth.

As noted above, carbon contamination is prevalent in MOCVD films, though the effect seems to be suppressed in phosphides relative to arsenides. Because carbon is an

intrinsic component of the organometallic precursors, the primary strategies to limit incorporation include careful selection of growth conditions and the use of hydride precursors to catalyze the conversion of  $\text{CH}_3$  molecules to  $\text{CH}_4$  gas.

### 2.2.3 Doping

Due to the volatility of the Group V precursor, MOCVD growth is typically carried out in a V-saturated regime. This suppresses V desorption from the surface and limits vacancy defect formation. As a result, film composition and growth rate are governed by the volumes of Group III precursors. For this reason, we select dopant atoms that incorporate substitutionally on the Group III sublattice, leading to improved doping control.

The stability of  $\text{SiH}_4$  is discussed above, and its low vapor pressure makes it a relatively straightforward dopant. Doping levels are proportional to the flow of  $\text{SiH}_4$  in the gas stream, and inversely proportional to growth rate. However, as noted above, the pyrolysis of  $\text{SiH}_4$  is temperature-dependent under typical MOCVD conditions. Si incorporation in the film will have an associated temperature dependence and must be calibrated for various growth temperatures. Si n-type doping with activated carrier concentrations up to  $10^{19} \text{ cm}^{-3}$  have been achieved<sup>12,17</sup>, and Si shows little memory effect in InAlGaP compounds.

Doping with Zn proves to be more difficult. The high vapor pressure of DMZn limits Zn incorporation; while incorporation increases with DMZn flow, it decreases at higher temperatures<sup>13</sup>. In addition to incorporation obstacles, the Zn acceptors are easily compensated in wide bandgap films by impurity states, especially oxygen. This becomes an issue in high-Al InAlGaP films, where it can be difficult to activate more than  $10^{17} \text{ cm}^{-3}$  carriers<sup>17</sup>. Finally, Zn diffuses very quickly in InAlGaP, making it extremely difficult to achieve abrupt p-type interfaces. Secondary ion mass spectroscopy (SIMS) analysis of Si and Zn doping increments during typical InAlGaP growth, along with O and C contamination levels, is given in Figure 2.5. Well-defined doping steps are visible in the Si curve, while Zn diffusion has produced a smooth Zn profile. Unintentional impurity levels are well below the dopant levels.

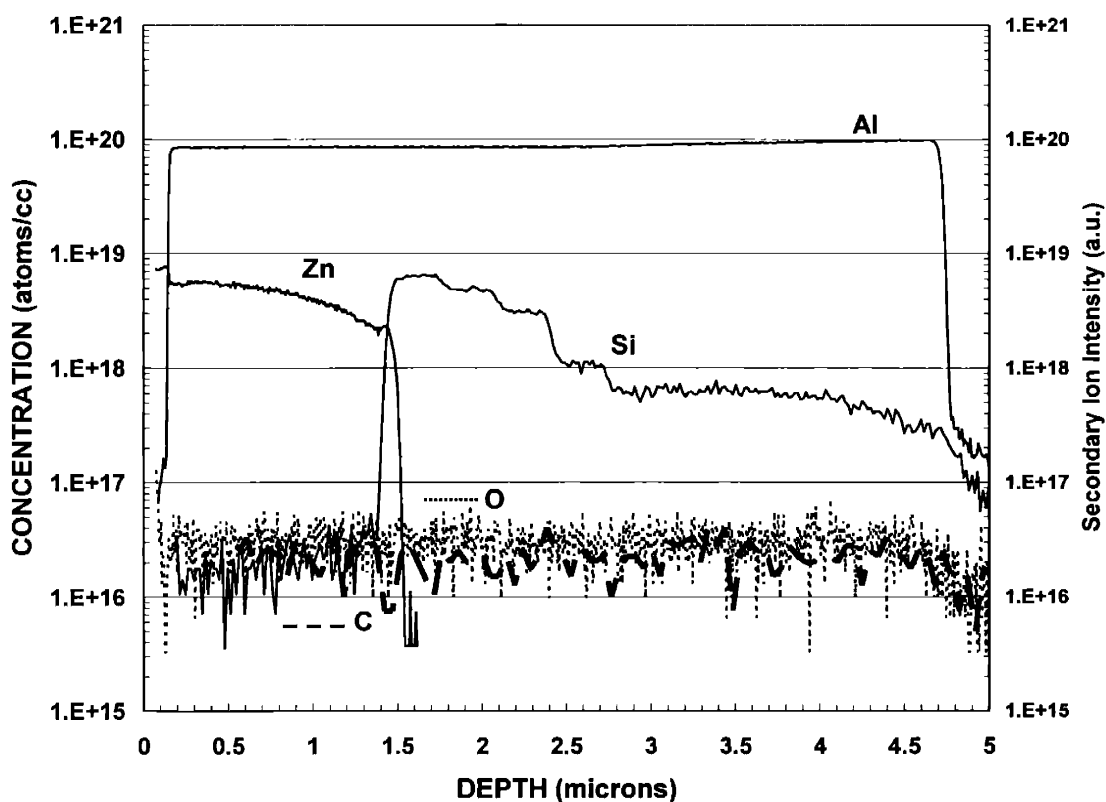


Figure 2.5. Dopant and unintentional impurity incorporation in MOCVD-grown  $\text{In}_{0.22}(\text{Al}_{0.2}\text{Ga}_{0.8})_{0.78}\text{P}$ .

### 2.3 Deposition Parameters

Perhaps the two most important factors in MOCVD film growth are growth temperature and V/III ratio. V/III ratio is generally taken to be the molar ratio of Group V source gases to Group III source gases. There is some conflict in the literature as to the precise definition of V/III ratio, so care must be taken when comparing reported growth conditions. In general, high Group V overpressures are required to prevent Group V desorption from the growth surface, and high V/III ratios are found to promote quality film growth and suppress vacancy formation on the Group V sublattice. In the presence of a high V/III ratio, the semiconductor surface will tend to be V-terminated, as shown in Figure 2.6. For the case of InGaP, it is believed that the P-dimer surface reconstruction may be 2x1 or 2x4, depending on the growth conditions<sup>18</sup>. More recently, however, the 2x1 reconstruction alone has been attributed to the P-rich condition<sup>19</sup>.

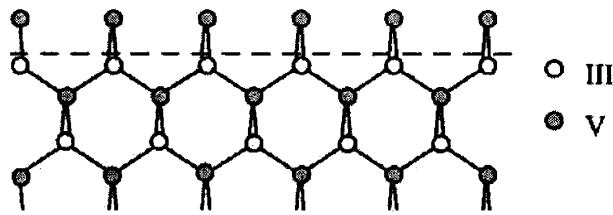


Figure 2.6. Group-V terminated III-V semiconductor surface.

As noted above, the supersaturation of V in the reactor chamber causes the film composition and growth rate to be independent of  $\text{PH}_3$  flow; therefore,  $\text{PH}_3$  flow can be adjusted at will to produce different V/III ratios. Group III precursors flows should not be changed to vary the V/III ratio, as this will alter the growth rate and possibly the film composition.

### 2.3.1 Thermal Regimes

Early in the development of MOCVD, Shaw<sup>20</sup> divided the dependence of growth rate on temperature into three general regimes, illustrated schematically in Figure 2.7.

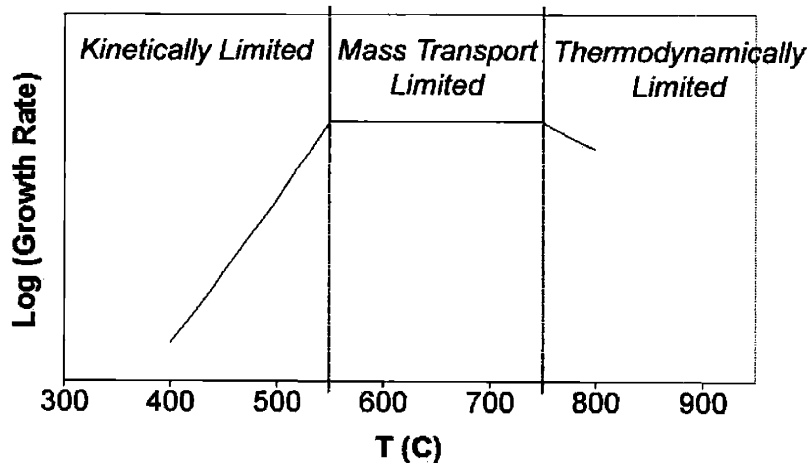


Figure 2.7. Thermal regimes of growth rate in MOCVD.

At low temperatures, growth rate is controlled by thermal activation of kinetic surface reactions, and varies exponentially with temperature. Likewise, substrate orientation will

impact the growth rate in this surface reaction limited case. In the intermediate temperature range, from about 550°C to 750°C, growth rate is limited by the mass transport of constituents through a boundary layer to the substrate surface. As diffusion through the boundary layer is only weakly dependent on temperature, growth rate remains relatively constant in this regime. On the other hand, total laminar flow velocity is a key factor in determining the boundary layer thickness, discussed below, and hence the rates of mass transport. In the mass transport regime, growth rate varies directly with flow velocity, as a thinner boundary layer leads to more rapid diffusion. Finally, at the highest temperatures, growth rate decreases with increasing temperature. This is believed to be the result of thermodynamic effects, or of reactant depletion due to upstream reactions<sup>13</sup>. Because extremely stable and reproducible substrate temperatures are difficult to achieve, growth is carried out in the Group III mass transport-limited thermal regime.

### 2.3.2 Mass Transport-Limited Growth

For a stationary sample in a horizontal reactor, gas flow over the substrate surface creates a boundary layer of thickness,  $\delta$ , in which reactants are depleted from the gas stream, shown in Figure 2.8. To be precise,  $\delta$  is defined as the coordinate above the substrate surface at which the gas flow velocity parallel to the substrate reaches 99% of its free velocity in the chamber<sup>13</sup>.

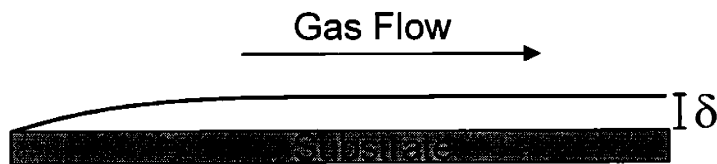


Figure 2.8. Boundary layer thickness over the substrate for laminar flow conditions.

Although growth in the mass transport-limited regime is a nonequilibrium process and therefore not governed by thermodynamics, an adequate first-order model of deposition may be developed using a distribution coefficient,  $k_i$ , to relate the solid and vapor-phase mole fractions of a given species  $i$ :

$$x_{i,s} = k_i x_{i,v} \quad \text{Equation 2.1}$$

where  $x_{i,s}$  is the solid-phase mole fraction of species  $i$  and  $x_{i,v}$  is the vapor-phase mole fraction of species  $i$ . Assuming linear concentration gradients and first-order reaction kinetics, the flux through the boundary layer,  $J_i$ , of species  $i$  is given by:

$$J_i = -D_i \frac{\partial c_{i,v}}{\partial z} K_i = \left( \frac{D_i K_i}{\delta_i} \right) c_{i,v} \quad \text{Equation 2.2}$$

where  $D_i$  is the diffusivity through the boundary layer,  $K_i$  is a general reaction coefficient accounting for precursor depletion, sticking coefficient, and other factors,  $\delta_i$  is the boundary layer thickness, and  $c_{i,v}$  is the species concentration in the vapor phase. A detailed model for mass transport-limited growth in our system has been derived by Kim<sup>11</sup>. Salient points include the use of a modified distribution coefficient,  $R$ , which is the ratio of each Group III distribution coefficient to  $k_{Ga}$ :

$$R_{In/Ga} = \frac{x_{In,s}}{x_{In,v}} \div \frac{x_{Ga,s}}{x_{Ga,v}} = \frac{k_{In}}{k_{Ga}} \quad \text{Equation 2.3}$$

$$R_{Al/Ga} = \frac{x_{Al,s}}{x_{Al,v}} \div \frac{x_{Ga,s}}{x_{Ga,v}} = \frac{k_{Al}}{k_{Ga}} \quad \text{Equation 2.4}$$

For  $\text{In}_x(\text{Al}_y\text{Ga}_{1-y})_{1-x}\text{P}$  alloys grown in this study, composition may be expressed as:

$$x_{Ga,s} = \frac{x_{Ga,v}}{R_{Al/Ga} x_{Al,v} + R_{In/Ga} x_{In,v} + x_{Ga,v}} \quad \text{Equation 2.5}$$

$$x_{In,s} = \frac{R_{In/Ga} x_{In,v}}{R_{Al/Ga} x_{Al,v} + R_{In/Ga} x_{In,v} + x_{Ga,v}} \quad \text{Equation 2.6}$$

$$x_{Al,s} = \frac{R_{Al/Ga} x_{Al,v}}{R_{Al/Ga} x_{Al,v} + R_{In/Ga} x_{In,v} + x_{Ga,v}} \quad \text{Equation 2.7}$$

and growth rate,  $G$ , as:

$$G = \underline{V}C_g [p_{Ga} + R_{In/Ga}p_{In} + R_{Al/Ga}p_{Al}] \quad \text{Equation 2.8}$$

where  $\underline{V}$  is the molar volume of the alloy,  $C_g$  is a constant calibration factor, and  $p_i$  is the partial pressure of species  $i$ . With this formulation, the deposition of ternary and quaternary alloys can be fully calibrated by determining composition and growth rate for deposition of the related binary components under the conditions of interest. In general, growth rate is calibrated via cross-section transmission electron microscopy, and R-factors are determined via x-ray diffraction. The best results are achieved when separate calibrations are obtained for disparate growth temperatures and alloy compositions, though small extrapolations are valid.

## 2.4 Reaction Mechanisms

As alluded to above, MOCVD proceeds via a complicated series of homogenous and heterogeneous pyrolysis reactions among the precursor gases at elevated temperatures. In general, the presence of both Group III and Group V precursors in the gas stream leads to accelerated pyrolysis<sup>13</sup>. For the “simplified” case of InP deposition, the pyrolysis temperatures of both PH<sub>3</sub> and TMIIn are lowered by as much as 100°C. Two models are presented to account for this effect. In the first model, PH<sub>3</sub> interacts with TMIIn before any homogeneous decomposition of TMIIn occurs. During this interaction, an adduct is formed, either in the vapor phase or on the surface. An initial transition state yields a CH<sub>4</sub> and a strongly bonded PH<sub>2</sub>-In(CH<sub>3</sub>)<sub>2</sub> complex. Subsequent heterogeneous reactions remove the two remaining CH<sub>4</sub> molecules, leaving In and P to incorporate on the substrate surface. In the second model, a short-lived (CH<sub>3</sub>)<sub>3</sub>In-PH<sub>3</sub> complex forms via the gas-phase collision of TMIIn and PH<sub>3</sub> in the boundary layer at high temperatures. Subsequent dissociation leads to the elimination of CH<sub>4</sub> and the deposition of In and P on the substrate. It is believed that at low temperature the same mechanism may occur entirely on the substrate surface<sup>13</sup>.

Due to the evident complexity of MOCVD pyrolysis reactions, which is only augmented by the introduction of additional precursor types, no single pyrolysis mechanism has been identified. It in fact seems likely that different mechanisms may



dominate in different regimes of pressure and temperature. To a certain extent, MOCVD has been treated as a “black box”, wherein appropriate precursor flows and growth conditions for the desired film are empirically determined and optimized. However, the chemical and hydrodynamic principles outlined above, in conjunction with ongoing research into MOCVD theory<sup>21-23</sup>, sheds some light on this intricate but powerful process.

## 2.5 Summary

The MOCVD growth technique is well-suited for the thin-film epitaxy of compound semiconductors used in optical emitter applications. While the film growth rate is lower than in near-equilibrium techniques such as LPE or VPE, a wide range of high-quality films with metastable alloy compositions can be produced. Presented above are key issues related to precursor selection and chemistry, impurity incorporation, growth regimes, and reaction kinetics. Deposition is carried out in the mass transport-limited regime, in order to optimize reproducibility and uniformity. One of the primary drawbacks of MOCVD is the toxicity of many common precursors, such as PH<sub>3</sub>. It is likely that in the coming years a great deal of effort will be applied to the development of alternative Group V sources such as tertiarybutylphosphine, both for their decreased toxicity and increased flexibility in terms of growth conditions.

Through the use of MOCVD in this study, we are able to produce a wide range of InGaP and InAlGaP structures with relative ease. Various permutations of growth conditions may be conveniently accessed, giving us the ability to establish well-defined bounds for high-quality film growth. The economy and flexibility of MOCVD has earned it a dominant position in LED research and development.



### 3 Mismatched Epitaxy of InGaP and InAlGaP for Optical Devices

In this section, we present a review of the properties of InGaP and InAlGaP alloys as they pertain to the fabrication of interesting optical and electronic device materials.

The major properties of interest in this study are:

- The nature of the alloy bandgap, in particular the transition from indirect bandgap to direct bandgap, and its impact on device efficiency;
- The formation and behavior of dislocations during mismatched epitaxy, specifically the reduction of threading dislocation density;
- The occurrence of ordering and In clustering during MOCVD, and their detrimental effects on device performance; and
- Intrinsic requirements for a high-brightness LED that will fill the green gap, and pertinent design parameters.

#### 3.1 Physical Properties of InGaP and InAlGaP

Indium aluminum gallium phosphide (InAlGaP) is a compound semiconductor composed of an equal proportion of atoms from Group III and Group V of the periodic table. III-V semiconductors have a zincblende structure, shown in Figure 3.1. In this structure with unit cell size  $a$ , the Group III and Group V atoms are situated on independent, interpenetrating FCC sublattices that are offset by  $a/4$  along the body diagonal. The zincblende structure mimics a diamond lattice, but has a slightly polar nature because the Group III atom must “borrow” a bond from the Group V atom to produce the observed tetrahedral covalent hybridization.  $\text{In}_x\text{Al}_y\text{Ga}_z\text{P}$  alloys having nearly any combination of In, Al, and Ga fractions on the Group III sublattice may be produced using non-equilibrium growth techniques, subject to the constraint that  $x+y+z=1$ .

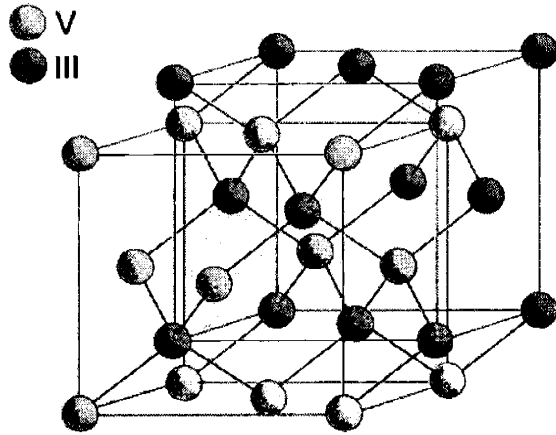


Figure 3.1. Zinblende crystal structure (reproduced from Stringfellow<sup>13</sup>).

InAlGaP is of particular interest for light emitter applications because many of its alloys have a direct bandgap. A direct bandgap material is one in which the lowest energy gap between conduction band and valence band is located at  $k=0$ ; that is, carriers may recombine to produce a photon without coupling to a phonon. Direct transitions are much more probable than indirect, phonon-assisted transitions; therefore, a direct bandgap material will more efficiently convert carriers to photons. Schematic band structures for direct and indirect bandgap III-V materials are presented in Figure 3.2.

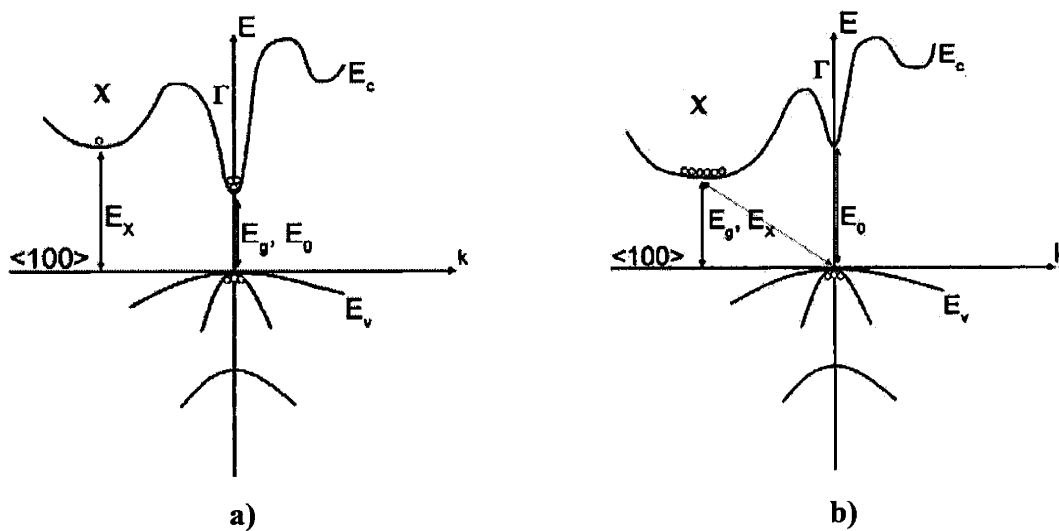


Figure 3.2. Schematic energy vs. momentum band structure for a) direct bandgap semiconductor, and b) indirect bandgap semiconductor.

The  $k=0$  point is commonly referred to as the  $\Gamma$  point, while the transition is termed  $E_0$  or sometimes  $E_\Gamma$ . For InAlGaP, the next lowest conduction band minimum is located along  $\langle 100 \rangle$ , at the  $X$  point. In order to inhibit the thermal spillover of carriers from  $\Gamma$  to  $X$ ,  $E_X - E_0$  must be greater than several  $kT$ . In the event that thermal energy is sufficient to promote carriers from  $\Gamma$  to  $X$ , the efficiency of carrier-to-photon conversion will be greatly reduced. Because the density of states at  $X$  is large, any carrier spillover is likely to be catastrophic for light emission.

Pertinent materials properties for the AlP-GaP-InP alloy system are given in Table 3.1.

	<b>AlP</b>	<b>GaP</b>	<b>InP</b>
<b>a</b> (Å)	5.4672 <sup>[24]</sup>	5.4512 <sup>[17,25]</sup>	5.8697 <sup>[24]</sup>
	5.4511 <sup>[17]</sup>	5.4505 <sup>[24,26]</sup>	5.8687 <sup>[26]</sup>
<b>E<sub>g</sub></b> (eV)	2.52 <sup>[24]</sup>	2.26 <sup>[26]</sup>	1.35 <sup>[25]</sup>
<b>E<sub>0</sub></b> (eV)	3.63 <sup>[24]</sup>	2.78 <sup>[26]</sup>	1.35 <sup>[25]</sup>
<b>n</b>	2.8 <sup>[27]</sup>	3.02 <sup>[26]</sup>	3.1 <sup>[26]</sup>
<b>α</b> (°C <sup>-1</sup> )	4.50 x 10 <sup>-6</sup> <sup>[17]</sup>	5.91 x 10 <sup>-6</sup> <sup>[17]</sup>	4.75 x 10 <sup>-6</sup> <sup>[17]</sup>

**Table 3.1. Physical properties of AlP, GaP, and InP.**

By convention, atomic fractions for InGaP and InAlGaP alloys will be defined as  $\text{In}_x\text{Ga}_{1-x}\text{P}$  and  $\text{In}_x(\text{Al}_y\text{Ga}_{1-y})_{1-x}\text{P}$ . A physical property,  $a$ , of any InGaP or InAlP ternary may be determined by linear interpolation from the corresponding binary values:

$$a(\text{In}_x\text{Al}_{1-x}\text{P}) = x \cdot a(\text{InP}) + (1-x) \cdot a(\text{AlP}), \quad \text{Equation 3.1}$$

$$a(\text{In}_x\text{Ga}_{1-x}\text{P}) = x \cdot a(\text{InP}) + (1-x) \cdot a(\text{GaP}). \quad \text{Equation 3.2}$$

Similarly, for the quaternary:

$$a[\text{In}_x(\text{Al}_y\text{Ga}_{1-y})_{1-x}\text{P}] = y \cdot a(\text{In}_x\text{Al}_{1-x}\text{P}) + (1-y) \cdot a(\text{In}_x\text{Ga}_{1-x}\text{P}). \quad \text{Equation 3.3}$$

The behavior of the semiconductor bandgap is integral to any device structure. Bandgap ( $E_g$ ) decreases as  $x$  increases in the  $\text{In}_x(\text{Al}_y\text{Ga}_{1-y})_{1-x}\text{P}$  alloy, rendering layers with lower indium fraction transparent to emission from a layer with a higher indium fraction. Additionally, AlP and GaP are indirect bandgap semiconductors; only InP possesses the direct bandgap required for efficient light emission.  $\text{In}_x\text{Al}_{1-x}\text{P}$  will remain indirect<sup>24</sup> for  $x \leq 0.56$ , while  $\text{In}_x\text{Ga}_{1-x}\text{P}$  will remain indirect<sup>28</sup> for  $x \leq 0.27$ . The direct energy gaps of the ternaries have been modeled as follows<sup>28,29</sup>:

$$E_0(\text{In}_x\text{Al}_{1-x}\text{P}) = 1.351 + 1.83 \cdot (1-x) + 0.38 \cdot (1-x)^2, \text{ and} \quad \text{Equation 3.4}$$

$$E_0(\text{In}_x\text{Ga}_{1-x}\text{P}) = 1.351 + 0.643 \cdot (1-x) + 0.786 \cdot (1-x)^2, \quad \text{Equation 3.5}$$

The relationship between bandgap and lattice constant for InAlGaP is summarized in Figure 3.3.

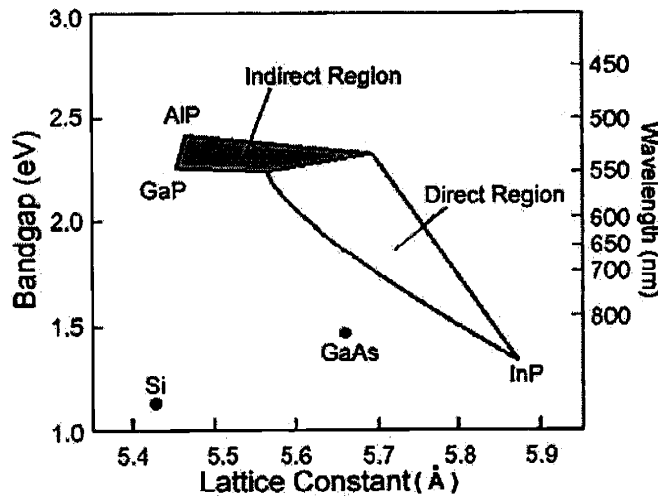


**Figure 3.3. Relationship between bandgap/emission wavelength and lattice constant in the AlP-GaP-InP system.**

The transition from direct bandgap to indirect bandgap materials properties is not an abrupt one. Rather, the value of  $E_x - E_0$ —and hence the efficiency of photon production—decreases smoothly with decreasing In fraction. This is an inherent difficulty with short-wavelength InAlGaP emitters, as will be discussed below.

Figure 3.3 illustrates that a wide range of InGaP and InAlGaP alloys have a direct bandgap; however, the only available lattice-matched substrate is GaAs. GaAs has a narrow bandgap that will absorb a large portion of the emitted light. In addition, InAlGaP emitters lattice-matched to GaAs must contain a relatively large fraction of Al to operate at the shortest wavelengths. While this solution has been widely employed in the industry to achieve yellow and green InAlGaP devices, the presence of Al in large quantities in the active region is known to be detrimental to device performance<sup>4</sup>. As discussed in Chapter 2, Al complexes readily with O, introducing non-radiative defect levels to the active region. An anomalously rapid decrease in efficiency with decreasing wavelength in InAlGaP devices has been attributed to O-related defect levels<sup>4</sup>. We wish, therefore, to minimize or eliminate Al from the device active region without losing access to the full range of visible wavelengths. To do this, we will clearly need to develop an appropriate lattice-mismatched substrate for the device active region.

## 3.2 Dislocation Systems

Optical device production has historically been confined to the realm of lattice-matched epitaxy because of defects associated with lattice-mismatched epitaxy. In particular, strain-relieving dislocations may lead to non-radiative carrier recombination and poor internal efficiency. The epitaxial growth of a single-crystal thin film having a different lattice constant than the substrate produces strain in the film, as will be discussed below. This strain can be relieved by misfit dislocations at the mismatched interface. A single misfit dislocation can relieve strain across its entire length by gliding along the interface. A dislocation with line direction,  $\xi$ , parallel to its Burger's vector,  $\mathbf{b}$ , is known as a screw dislocation, while a dislocation with line direction perpendicular to its Burger's vector is known as an edge dislocation. Only edge-type dislocations contribute to strain relief.

Figure 3.4 illustrates common ways in which misfit dislocations form. Dislocations cannot terminate within the crystal, so they must originate from and terminate at a free surface. The most important sources of misfit dislocations for the purposes of mismatched epitaxy are threading dislocations from the substrate that bend to form misfits at the interface, and dislocation nucleation on heterogeneous sources such as

particles or defects. Interactions among dislocations can lead to dislocation multiplication, particularly if a gliding dislocation is pinned by an interaction and can therefore provide no further strain relief. Dislocations with proper Burger's vectors may also annihilate one another.

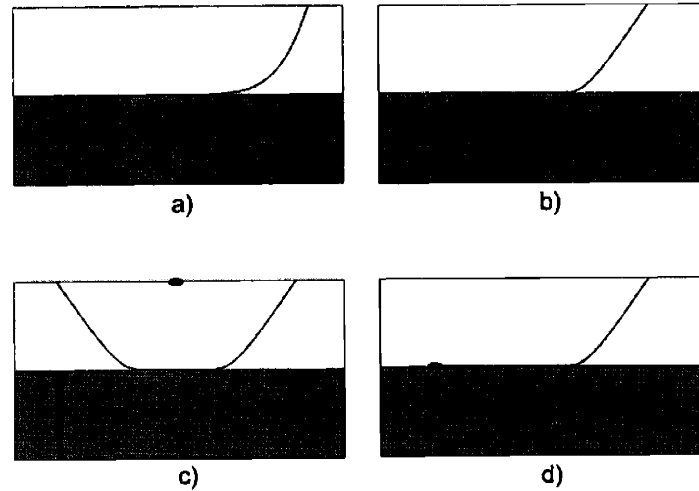


**Figure 3.4. Common dislocation configurations. a) Origination from the substrate, b) termination at the edge of the crystal, c) dislocation half-loop nucleation, d) heterogeneous dislocation nucleation at a point source.**

In the zincblende crystal system, glissile dislocations are of the type  $\frac{1}{2}a\langle 110 \rangle \{111\}$ . This refers to a dislocation with Burger's vector,  $\mathbf{b}$ , of  $\frac{1}{2}a\langle 110 \rangle$  that glides in a  $\{111\}$  plane. Crystallographically, this produces 24 unique slip systems, comprising twelve  $\langle 110 \rangle$  Burger's vector directions each associated with two possible  $\{111\}$  glide planes. For strain relief in the (001) plane, eight of the slip systems are eliminated because they are purely screw-type. Dislocations in the remaining systems are of mixed character, as they are neither purely edge- nor screw-type, as illustrated in Figure 3.5.



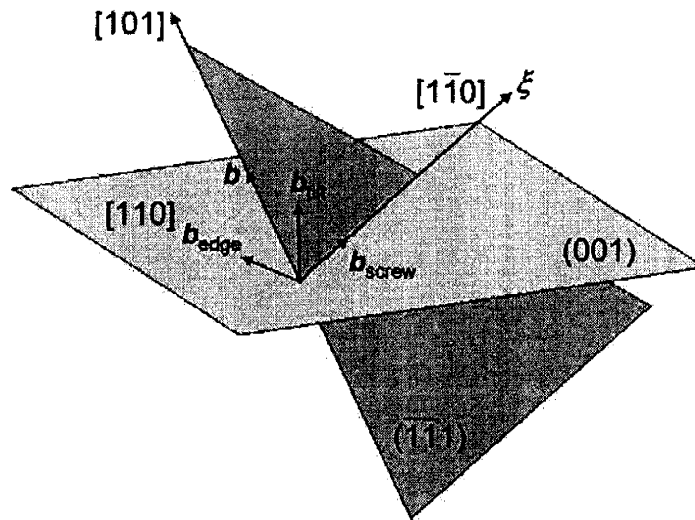


**Figure 3.5. Burger's vector components of a dislocation in the  $\frac{1}{2}a[101](\bar{1}\bar{1}\bar{1})$  slip system.**

These dislocations are referred to as  $60^\circ$  dislocations, based on the angle between  $\mathbf{b}$  and  $\xi$ . Of the sixteen remaining systems, half will have Burger's vector directions that relieve tensile strain, while the other half will relieve compressive strain. This leaves eight  $\frac{1}{2}a\langle 110\rangle\{111\}$  dislocation systems that relieve compressive strain in mismatched epitaxy, the configuration of interest in this study. Due to the mixed nature of the III-V lattice, four of these systems have Group III atoms at their core; these are termed  $\alpha$  dislocations. The other four systems have Group V atoms at their core and are known as  $\beta$  dislocations.  $\alpha$  and  $\beta$  dislocations can have very different glide velocities, and therefore may contribute unequally to strain relief<sup>30</sup>. This will lead to a relaxation anisotropy in the film along the two perpendicular in-plane  $\langle 110\rangle$  directions.  $\alpha$  and  $\beta$  dislocation types are illustrated in Figure 3.6 for the case of compressive strain in the film.

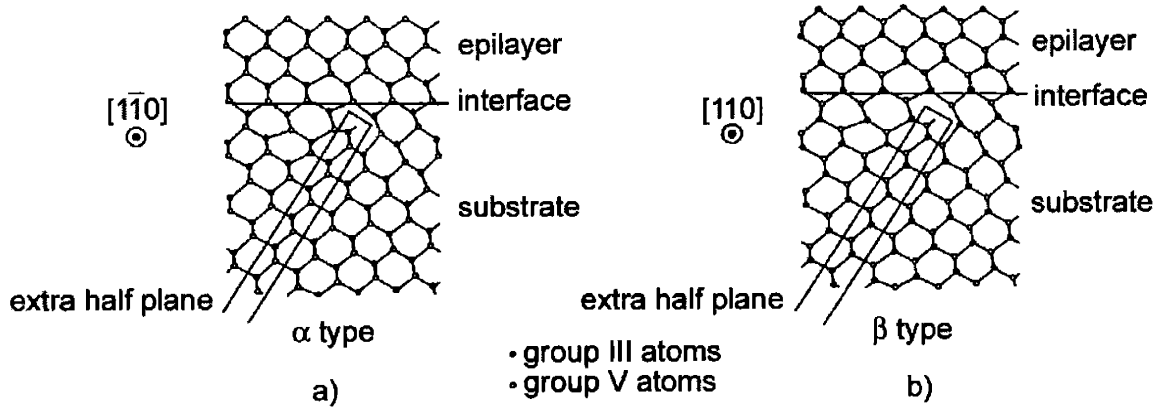


Figure 3.6. a)  $\alpha$  and b)  $\beta$  dislocations in compressively strained III-V epitaxy (reproduced from Matagrano<sup>30</sup>).

Dislocations in this system are glissile because the Burger's vector and line direction lie in a glide plane,  $\{111\}$ . A purely edge dislocation would relieve more strain but would be sessile, since the glide plane for the edge dislocation is  $\{100\}$ , a higher energy slip system. The Burger's vector components of the  $60^\circ$  dislocation are illustrated in Figure 3.5.  $\mathbf{b}_{\text{edge}}$ , which is perpendicular to  $\xi$ , relieves strain in the (001) plane. From basic trigonometry, we can determine that  $|\mathbf{b}_{\text{edge}}| = \frac{a}{2\sqrt{2}}$ ; this value is used to determine the critical thickness of the epitaxial overlayer, as described below.  $\mathbf{b}_{\text{screw}}$ , which is parallel to  $\xi$ , leads to rotation of the film in the (001) plane, while  $\mathbf{b}_{\text{tilt}}$  causes the epilayer to tilt relative to the substrate.  $\mathbf{b}_{\text{tilt}}$  becomes important in the case of substrates misoriented from the (001). It is energetically favorable for epilayers deposited on such substrates to tilt in order to recover an (001) orientation. This can lead to the nucleation of dislocations with the proper Burger's vector to produce this tilt, even when the sense of the Burgers vector is wrong for strain relief<sup>30</sup>. This would cause a detrimental increase in dislocation density while detracting from strain relief.

### 3.3 Lattice-mismatched epitaxy

We have chosen to focus on GaP as our lattice-mismatched substrate material. While they can be expensive, high-quality GaP wafers are readily available. In addition, GaP has the advantage of being transparent to most InGaP emission wavelengths; that is,

it has a larger bandgap than any InGaP alloy that could be deposited upon it. To bridge the difference in lattice constant between the GaP substrate and any device layers, we will employ optimized, relaxed graded buffer technology.

Lattice mismatch,  $f$ , is defined<sup>31</sup> as:

$$f = \frac{a_s - a_f}{a_f} \quad \text{Equation 3.6}$$

where  $a_s$  is the lattice parameter of the substrate and  $a_f$  is the lattice parameter of the film. Mismatch may be positive or negative, depending on the relative magnitudes of the lattice parameters, and is indicative of the resulting sense of stress in the film (tensile and compressive, respectively). Furthermore, the accommodation of lattice mismatch in the system may be expressed as:

$$f = \varepsilon + \delta, \quad \text{Equation 3.7}$$

where  $\varepsilon$  represents mismatch accommodation through elastic strain of the film, and  $\delta$  represents accommodation through plastic strain of the film (i.e. dislocation nucleation). Below a certain critical thickness,  $h_c$ ,  $\delta$  will be equal to zero and the epitaxially grown film will completely strain to match the lattice parameter of the substrate, leading to a tetragonal distortion, illustrated in Figure 3.7a. Above  $h_c$ , the film will begin to deform plastically to relieve this strain, through the introduction of misfit dislocations along the film/substrate interface<sup>32,33</sup>, illustrated in Figure 3.7b.

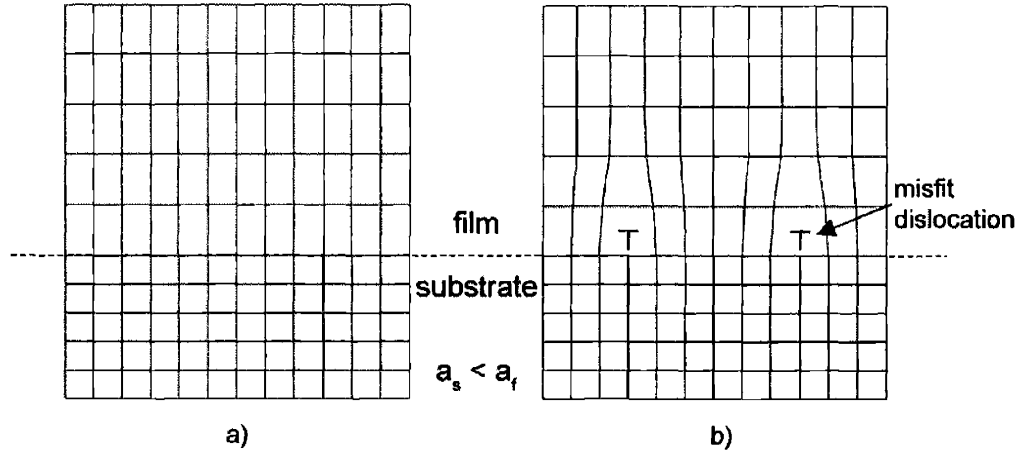


Figure 3.7. a) Schematic of fully-strained epitaxy ( $h < h_c$ ), and b) schematic of partially-relaxed epitaxy ( $h \geq h_c$ ).

The critical thickness is determined thermodynamically from a minimization of elastic strain energy and dislocation energy; plastic deformation begins when dislocation energy becomes less than that of continued strain accumulation. The thermodynamic critical thickness is defined by Matthews, *et al*<sup>34</sup> to be the transcendental equation:

$$h_c = \frac{D(1 - \nu \cos^2 \alpha)(\ln \frac{h_c}{b} + 1)}{Yf} \quad \text{Equation 3.8}$$

for the case of  $60^\circ$  dislocations, where

$$D = \frac{G_o G_s b}{\pi(G_o + G_s)(1 - \nu)}, \quad \text{Equation 3.9}$$

$$G = C_{44} - \frac{2C_{44} + C_{12} - C_{11}}{2}, \quad \text{Equation 3.10}$$

$$\nu = \frac{C_{12}}{C_{12} + C_{11}}, \quad \text{Equation 3.11}$$

$$Y = C_{11} + C_{12} - \frac{2C_{12}^2}{C_{11}}, \quad \text{Equation 3.12}$$

and  $\alpha$  is the angle between the Burger's vector and the dislocation line direction,  $b$  is the magnitude of the strain-relieving component of the Burger's vector,  $\nu$  is Poisson's Ratio of the film,  $Y$  is the Young's modulus of the film,  $G_o$  and  $G_s$  refer to the shear moduli of the film and substrate, respectively, and  $C_{11}$ ,  $C_{12}$ , and  $C_{44}$  are mechanical constants. Details for the solution of this transcendental are presented in Appendix A; the functional form is shown in Figure 3.8. Because dislocation nucleation and motion are kinetically controlled, the actual critical thickness will almost always be greater than that calculated from thermodynamic considerations<sup>35</sup>.

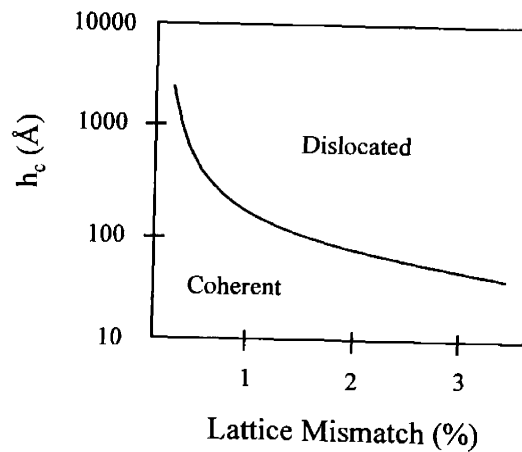


**Figure 3.8. Variation of epilayer critical thickness with lattice mismatch.**

The determination of critical thickness is somewhat more complicated for epitaxy on a misoriented substrate. Changing the orientation of the substrate surface relative to the pertinent Burger's vectors breaks the degeneracy among the slip systems, causing the critical thickness to vary based on the active slip system. A complete treatment of this issue is presented by Kim<sup>11</sup>.

As mentioned above, dislocation glide kinetics will tend to metastably extend the critical thickness above its thermodynamic value by controlling strain relaxation. Above the critical thickness, dislocations from the substrate can glide to relieve strain at the mismatched interface. In this case, plastic strain,  $\delta$ , is taken to be<sup>36</sup>:

$$\delta = \frac{\rho_{\text{misfit}} b_{\text{edge}}}{2}$$

Equation 3.13

where  $\rho_{\text{misfit}}$  is the linear misfit dislocation density and  $b_{\text{edge}}$  is the magnitude of the strain-relieving component of the Burger's vector. The factor of  $\frac{1}{2}$  arises due to the two orthogonal  $\langle 110 \rangle$  misfit arrays discussed above. The misfit density can be related to the threading dislocation density,  $\rho_{TD}$ , as:

$$\rho_{TD} = \frac{2\rho_{\text{misfit}}}{L}$$

Equation 3.14

where  $L$  is the mean misfit dislocation length.

When the plastic strain rate is fast enough to maintain a low elastic strain, then relaxation will occur primarily through the glide of existing dislocations<sup>35</sup>. In this case, the dislocation glide velocity—and therefore the mean dislocation length,  $L$ —are kinetically limited by the activation energy for dislocation glide. In general, however, the dislocation density arising from the substrate is insufficient to fully relieve mismatch strain, necessitating the nucleation of additional dislocations<sup>11</sup>. Of the dislocation nucleation mechanisms presented above, dislocation multiplication probably results from heterogeneous nucleation on defects or from dislocation-dislocation interactions. In general, the activation energy for dislocation nucleation is inversely proportional to the strain in the epitaxial film. Thus, dislocation multiplication will proceed until  $\rho_{\text{misfit}}$  is sufficient to maintain a low enough level of elastic strain that further multiplication is unfavorable.

Because a dislocation cannot terminate within a crystal, most dislocations will propagate through the film to its surface, forming threading dislocation segments as shown in Figure 3.9.

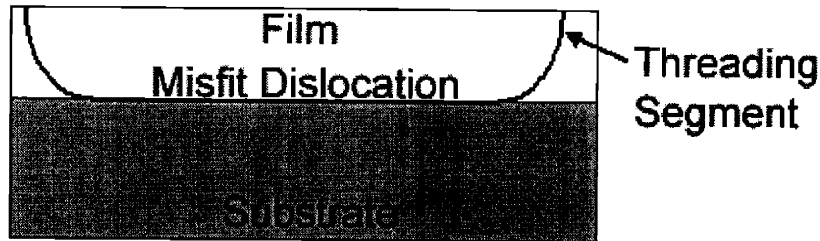


**Figure 3.9. Termination of a misfit dislocation in two threading segments.**

These threads, which act as non-radiative recombination centers, must inevitably pass through the active region of the film on their way to the surface, and may degrade device quality unacceptably. Threading dislocation densities on the order of  $10^6 \text{ cm}^{-2}$  or less are required for good quality optical device performance. Ideally, threading dislocations should be eliminated or at least controlled. For this reason, the behavior of misfit dislocations during mismatched epitaxy is critically important for device performance.

### **3.4 Relaxed Graded Buffer Growth**

When a large lattice mismatch is accommodated at a single interface, a dense array of misfit dislocations forms, as shown in Figure 3.10a. This increases the likelihood that a gliding dislocation will be pinned by a misfit from a perpendicular slip system, necessitating multiplication. (As noted, it is also possible for dislocations with the appropriate Burger's vectors to meet and annihilate one another.) An alternative method of strain accommodation is to distribute the mismatch among several epilayer interfaces, as shown in Figure 3.10b. This will reduce dislocation interactions, leading to enhanced glide and more efficient strain relief, which in turn minimizes the ultimate threading dislocation density.

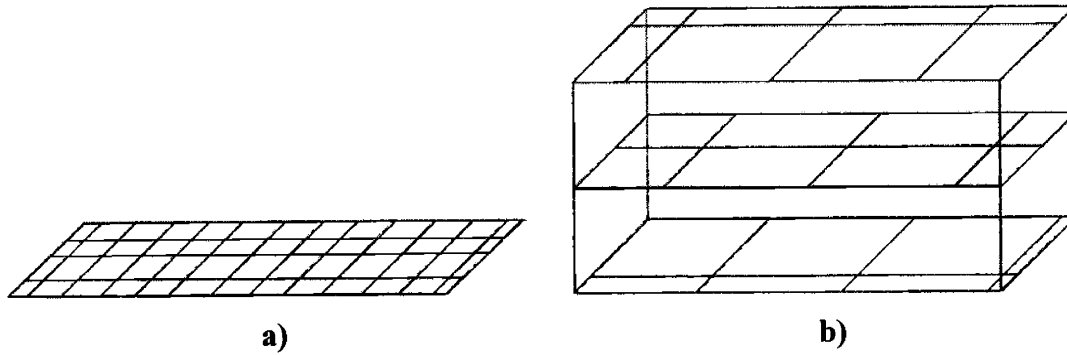


**Figure 3.10. Misfit dislocation arrays for a) direct mismatched deposition, and b) relaxed graded buffer deposition.**

This structure, in which composition is varied incrementally from the substrate to the thick cap film in order to maximize efficient strain relief, is known as an optimized, relaxed, graded buffer. It has been extensively researched in the field of GeSi epitaxy<sup>35,37-39</sup>, and has also been applied to the InGaP/GaP system<sup>40,41</sup>. Abrahams, *et al.*<sup>42</sup> described the properties of dislocations in the graded buffer and proposed a phenomenological model relating dislocation spacing to the average glide length. Implicit in this is a relation between dislocation interaction and glide length, as described above. Subsequent work studied the role of dislocation kinetics in graded buffer growth. This ultimately led to two possible models for dislocation formation during graded buffer growth<sup>43</sup>. The first is a kinetic nucleation mechanism, in which misfit (and therefore threading) density is expected to increase linearly with grading and exponentially with temperature. The second is a kinetic glide model, in which threading density is independent of grading and decreases exponentially with increasing temperature, as dislocation glide is thermally enhanced. Recent studies have demonstrated the validity of the kinetic glide model<sup>39</sup>.

During relaxed graded buffer growth, preexisting substrate dislocations bend to form misfits at the mismatched interface. The misfits glide along the interface to relieve strain, while their threading segments turn up to terminate at the nearest free surface, usually the surface of the film. Upon subsequent deposition, these threads can also bend to become misfits at the new interface, effectively recycling dislocations throughout the graded buffer while minimizing the need for additional dislocation nucleation and leading to a steady-state dislocation density in the graded buffer and cap film. This is illustrated



schematically in Figure 3.11. TEM images of a typical graded buffer are shown in Figure 3.12.

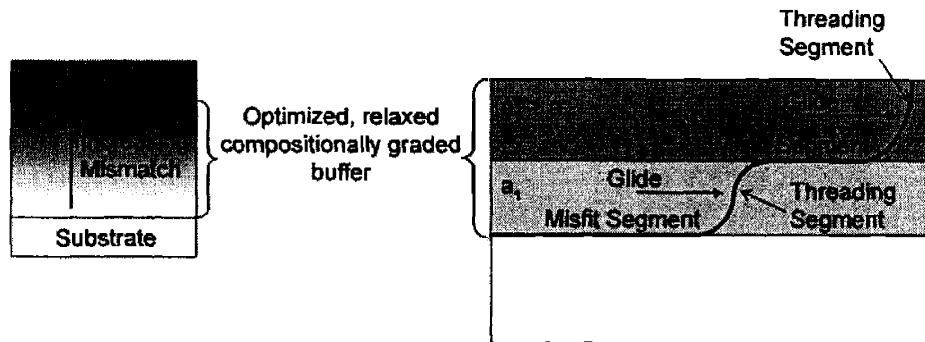


Figure 3.11. Dislocation glide and misfit recycling during graded buffer growth.

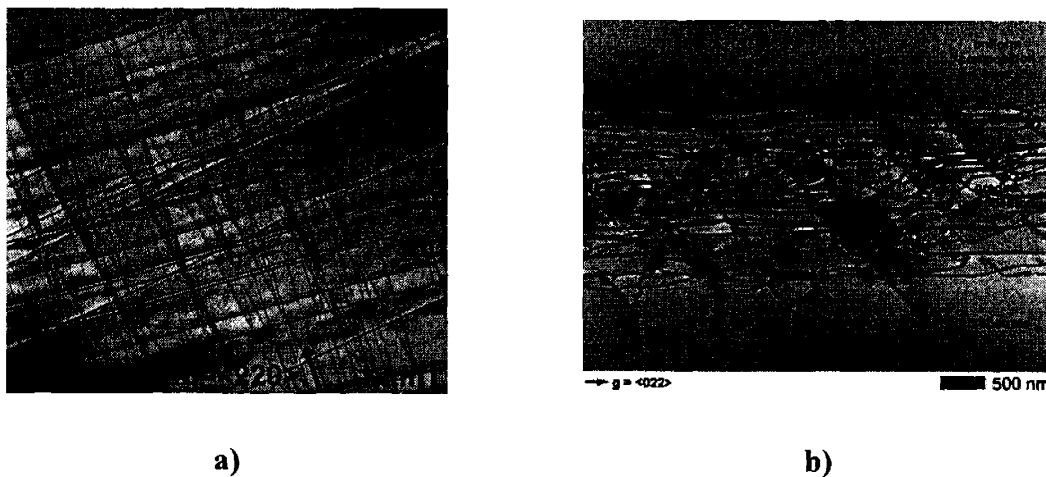
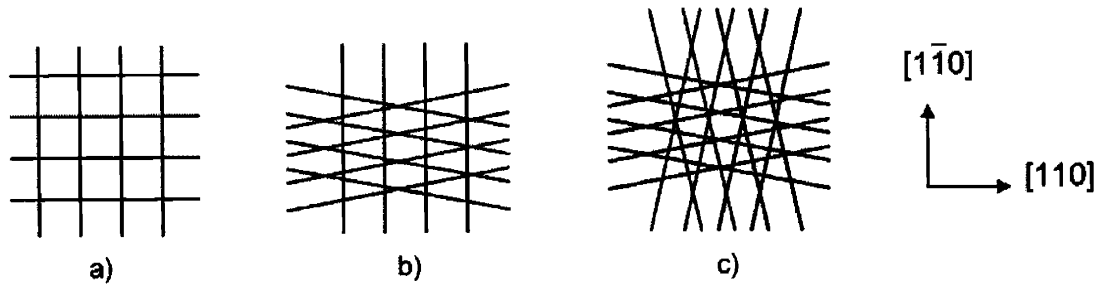


Figure 3.12. a) PVTEM and b) XTEM of an InGaP graded buffer misfit dislocation array.

Substrate offcut has been observed to affect the temperature dependence of dislocation glide kinetics, with higher threading dislocation densities present in misoriented samples. This has been attributed to a saturation in annihilation reactions in the case of substrate misorientation<sup>39</sup>. The symmetry of the misfit array is broken by the substrate misorientation, as shown in Figure 3.13.



**Figure 3.13. Misfit array geometry for a) on-axis substrates, b) substrates misoriented toward the nearest  $\langle 111 \rangle$ , and c) substrates misoriented toward the nearest  $\langle 110 \rangle$ .**

Finally, feedback among the strain fields associated with misfit dislocations can lead to what is termed a “pileup”, a cluster of threading dislocations that have become pinned at the same site. Such pileups can account for a large fraction of the total threading dislocation density, and their presence in the active region would be extremely detrimental.

The MOCVD growth model outlined in Chapter 2 breaks down somewhat for graded buffer growth. A modified graded buffer process model based on mass transport-limited deposition is described by Kim<sup>11</sup>, and is used for all samples produced in this work. A sample graded buffer worksheet is presented in Appendix B.

### 3.5 Modes of Epitaxy

Initial modes of epitaxy, illustrated in Figure 3.14, are also affected by lattice mismatch, as well as the relative bond energies of film and substrate species<sup>44</sup>. When substrate-film bonds are favored, initial film growth will proceed two-dimensionally (Frank-van der Merwe growth). When film-film bonds are favored, epitaxial growth will not initiate in a two-dimensional mode, but rather as discrete islands, leading to a poor quality film that would be unlikely to support a thin-film optical device (Volmer-Weber growth). The intermediate case is Stranski-Krastanov growth, in which energetic factors such as lattice-mismatch strain cause a disruption in initial two-dimensional growth, leading to an undulated, roughened surface.

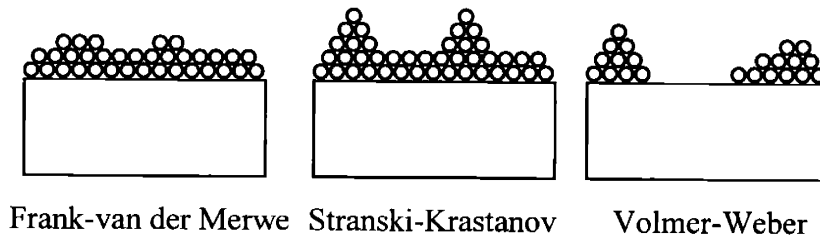


**Figure 3.14. Initial modes of epitaxy<sup>44</sup>.**

Ideally, epitaxial film growth will proceed in Frank-van der Merwe—or monolayer-by-monolayer—fashion, leading to the highest film quality. When an adatom arrives at the semiconductor surface, there are three typical sites to which it may attach, illustrated in Figure 3.15.

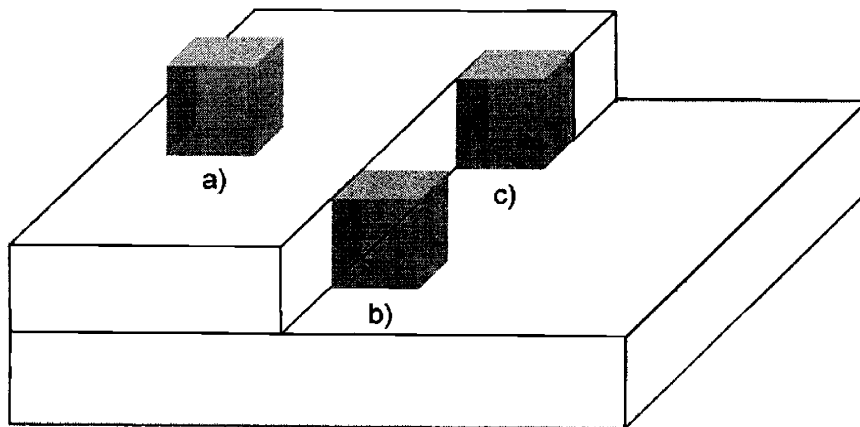


**Figure 3.15. Surface sites for adatom attachment during epitaxy: a) terrace, b) ledge, and c) kink.**

Of these, deposition at kinks is energetically most favorable, as it completes the largest number of dangling bonds. Adatom attachment at kinks will progressively increase the width of the associated terrace, leading to a characteristic structure shown in Figure 3.16a. However, under certain conditions, terrace growth will not proceed in such an orderly fashion, and the steps will crowd—or bunch—together<sup>45</sup>. These features are referred to as step bunches or supersteps, and are illustrated in Figure 3.16b. Superstep formation tends to be augmented at low growth temperatures and weakly suppressed at

low V/III ratios<sup>11,45</sup>. Misoriented substrates, such as those used in this study, have a large surface step density, which increases the number of ledge and kink sites.

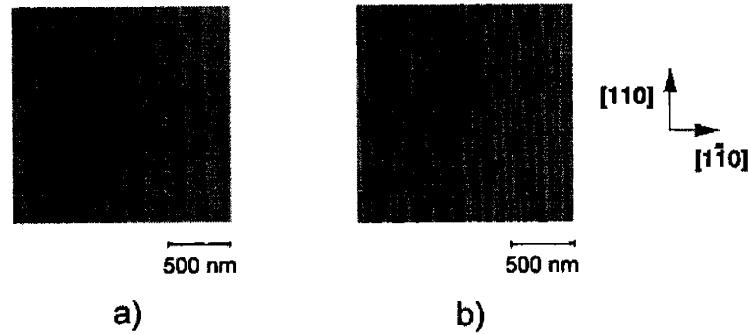


**Figure 3.16.** AFM images of a) step-flow growth and b) step-bunching (reproduced from Shinohara<sup>46</sup>).

### 3.6 Surface Morphology

Good surface morphology is important in the growth of device-quality films, particularly in the case of multiple layer growth or regrowth after cleaning. Surface roughening during growth may be a reflection of poor quality initial surfaces, leading to a semi-coherent or even polycrystalline film. Surface morphology may also degrade as film thickness increases, as in the Stranski-Krastanov growth mode, or as a result of step-bunching. Roughness in epitaxially grown films may be suppressed by initiating the film growth at low temperatures, which limits the adatom mobility and leads to two-dimensional growth. However, low-temperature growth may not produce the highest crystalline perfection throughout the film.

Even “good-quality” graded-buffer films may exhibit a certain characteristic type of surface roughness, known as crosshatch. This crosshatch pattern on the surface is believed to arise from strain fields produced by the misfit dislocation network that relieves strain at the mismatched interface. When thick layers are grown, pronounced crosshatch and dislocation multiplication may develop due to dislocation pinning on surface topography. In this case, intermediate planarization steps may be used to reduce roughening<sup>38</sup>.

### 3.7 Deviations from Randomness

The final microstructural topics pertinent to this study relate to the miscibility gap that is present in the InP-GaP system, and more specifically to associated fluctuations in In fraction throughout the sample. An excellent treatment of this topic is provided by Zunger and Mahajan<sup>18</sup>, and their formulation is generally followed below.

The structure of a ternary III-V semiconductor is idealized as a zincblende structure with random mixing among Group III and Group V atoms on their respective sublattices, in proportion to the binary constituents. In reality, size-mismatched alloys such as InGaP will exhibit both chemical and positional deviations from the ideal random structure. (“Size mismatch” for an alloy refers to the differing lattice constants of the binary end members, and should not be confused with epitaxial “lattice mismatch”.) Chemical deviation refers to the correlated occupation of lattice sites; that is, the occupation of a site by a given type of atom is more or less likely than random chance would predict. Positional deviation refers to the relaxation of an atom to a location displaced from its coordinate in an ideal zincblende structure. For the case of InGaP, the In-P (Ga-P) bonds are locally compressed (dilated) relative to their natural lengths in the pure binary. In the ternary, the atoms will “relax” their positions to produce bond lengths closer to those in their respective binaries. These deviations can have a marked impact on the optical and electronic properties of the ternary, and generally invalidate a linear interpolation of such properties from those of the binary end members. Even in a random alloy, fluctuations about the ideal configuration can lead to scattering, absorption tails, and optical bowing<sup>47,48</sup>. Deviations from randomness are categorized in Table 3.2.

	<b>Like atoms attract</b>	<b>Unlike atoms attract</b>
<b>“Macroscopic” Length Scale</b> ( $> 10$ bond distances)	Phase Separation	Ordering
<b>“Microscopic” Length Scale</b> (1 or a few bond distances)	Clustering	Anticlustering

**Table 3.2. Nonrandom atomic arrangements identified in III-V semiconductors.**

These phenomena may be driven by thermodynamic or kinetic factors. While MOCVD is a two-dimensional, nonequilibrium process, the factors that lead to

equilibrium nonrandomness still exist and may drive local variations in In fraction during thin film growth. However, for the case of epitaxy, processes that lead to nonrandomness tend to occur at or near the surface, not in the bulk. Special epitaxial considerations will be discussed below.

From a thermodynamic standpoint, we can define the sum of the energies,  $E_i$ , of the unmixed binaries to be the zero of energy. For the case of an ordered  $A_{1-x}B_x$  alloy of ordering type  $\sigma$  versus a random alloy, the pertinent excess energies are:

$$\Delta E_f(\sigma_x) = E_\sigma(\text{ordered}) - [(1-x)E_A - xE_B], \text{ and} \quad \text{Equation 3.15}$$

$$\Delta E_{mix}(x) = E(\text{random}) - [(1-x)E_A - xE_B]. \quad \text{Equation 3.16}$$

The ordering energy is then defined as:

$$\delta E_{ord}(\sigma_x) = \Delta E_f(\sigma_x) - \Delta E_{mix}(x) = E_\sigma(\text{ordered}) - E(\text{random}). \quad \text{Equation 3.17}$$

Historically,  $\Delta E_{mix}(x)$  for III alloys fits well to a regular solution model of the form  $\Omega x(1-x)$ , where  $\Omega$  is found to always be positive. This corresponds to attraction between like atoms and at first glance appears to rule out the possibility of ordering in III-Vs. However, Equation 3.17 illustrates that the total mixing enthalpy for ordering must also include  $\Delta E_f(\sigma_x)$ . This allows for the thermodynamic coexistence of phase separation and ordering. Based on these energetic considerations, semiconductor alloys may be grouped as follows:

1. Type-I:  $\Delta E_f(\sigma_x) < 0$ ,  $\delta E_{ord}(\sigma_x) < 0$ ; Long-range: ordering, Short-range: anticlustering.
2. Type-II:  $\Delta E_f(\sigma_x) > 0$ ,  $\delta E_{ord}(\sigma_x) < 0$ ; Long-range: phase separation, Short-range: anticlustering.
3. Type-III:  $\Delta E_f(\sigma_x) > 0$ ,  $\delta E_{ord}(\sigma_x) > 0$ ; Long-range: phase separation, Short-range: clustering

Most semiconductors, including InGaP, are type-II; however, it should be noted for consideration of quaternary alloys that InAlP is most likely type-I and AlGaP is most likely type-III<sup>18</sup>.

### 3.7.1 Macroscopic Deviations

As noted in Table 3.2, macroscopic nonrandomness may take the form of phase separation or ordering. The excess energies may be redefined as:

$$\Delta E_f(\sigma_x) = \Delta E_{VD}(x) + \Delta E_{CT}(ord) + \Delta E_{REL}(ord), \text{ and} \quad \text{Equation 3.18}$$

$$\Delta E_{mix}(x) = \Delta E_{VD}(x) + \Delta E_{CT}(random) + \Delta E_{REL}(random). \quad \text{Equation 3.19}$$

where  $\Delta E_{VD}$  is the volume deformation energy,  $\Delta E_{CT}$  accounts for charge transfer and other band-structure effects, and  $\Delta E_{REL}$  accounts for positional relaxations. The volume deformation energy depends only on alloy composition and to first-order is independent of structure<sup>49</sup>, and is always positive. Charge transfer and relaxation depend upon the configuration of the mixed structure; relaxation energy is always negative, while charge transfer may be positive or negative. It is specifically the charge transfer and relaxation terms of  $\Delta E_f(\sigma_x)$  that do not conform to  $\Omega x(1-x)$  and can give rise to ordering.

For size-mismatched alloys such as InGaP,  $\Delta E_f(\sigma_x) > 0$  and phase separation is predicted. This is shown in the schematic pseudobinary phase diagram in Figure 3.17.

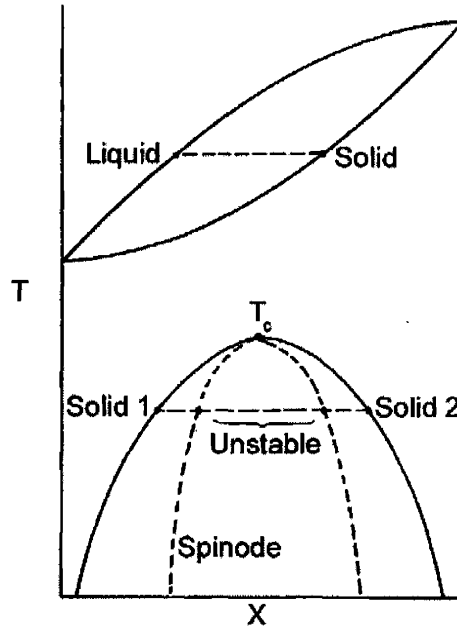


Figure 3.17. Schematic pseudobinary T-x phase diagram (reproduced from Stringfellow<sup>13</sup>).

Volume deformation dominates over any potential mitigation from charge transfer or relaxation, and a miscibility gap arises as a result of strain energy from the different InP and GaP bond lengths<sup>50,51</sup>. An InGaP phase diagram calculated from first principles is shown in Figure 3.18.

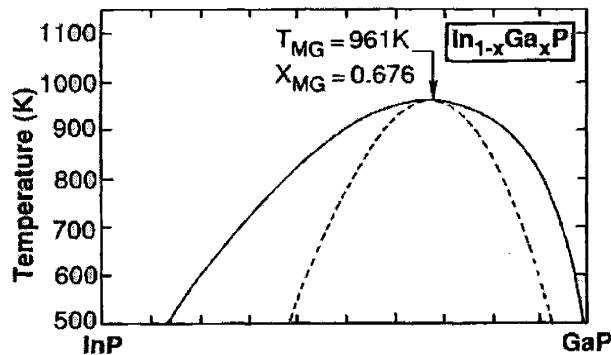


Figure 3.18. Calculated InP-GaP T-x phase diagram (reproduced from Zunger and Mahajan<sup>48</sup>).

The form of the InP-GaP miscibility gap can be dramatically altered under epitaxial conditions<sup>48</sup>. Among other factors, surface adatom diffusivity is orders of



magnitude higher than bulk diffusivity, favoring the formation of structures that would effectively never arise in the bulk. Furthermore, coherent phase separated regions will have a different lattice-mismatch with respect to the substrate than that of a random film. In the case of InGaP mismatched epitaxy on GaP, Ga-enriched regions will experience relatively less mismatch strain than average, while In-enriched regions will experience more strain. On the other hand, in the case of lattice-matched epitaxy, the magnitude of strain for both cluster types will be higher than average. Qualitatively, in this case, phase separation is suppressed and the miscibility gap temperature is lowered<sup>48</sup>. The impact of local coherency strains on phase separation in mismatched epitaxy is less straightforward. Additionally, phase separated regions on the growth surface are likely to be partially incoherent.

#### 3.7.1.1 Ordering

Phase separation is treated extensively in the literature<sup>52-55</sup>; for our purposes, ordering is the macroscopic phenomenon of interest. Order-disorder transformations can have important and undesirable effects on the properties of InGaP device materials. The problem of ordering in InGaP was first recognized by Gomyo, *et al.*, and referred to as the “50 meV” problem, due to the observed anomalous 50 meV decrease in energy gap<sup>56</sup>. Bulk thermodynamic considerations favor the occurrence of the chalcopyrite ordered structure in InGaP, as it best accommodates disparate bond lengths<sup>48,51</sup>. However, this structure is never observed. On the other hand, CuPt-B type ordering, shown in Figure 3.19, is predicted to arise at a free surface. CuPt-B ordering is commonly observed in epitaxial InGaP, further evidence that nonrandom materials properties are determined by surface—not bulk—effects.

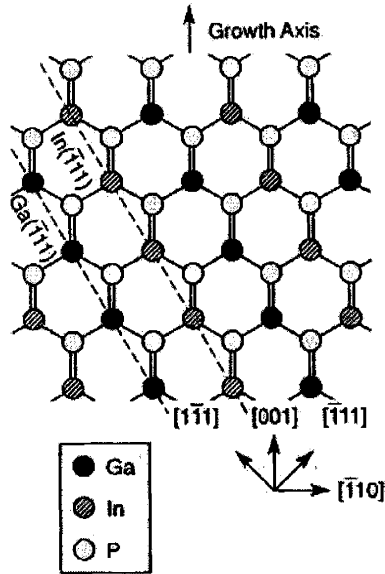
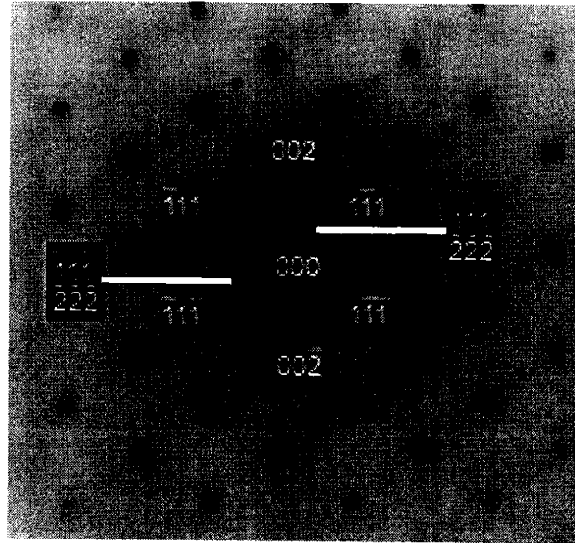


Figure 3.19. CuPt-B ordering in InGaP (reproduced from Zunger and Mahajan<sup>48</sup>).

In the CuPt-B structure, In and Ga atoms are arrayed on alternating (111) planes of the Group III sublattice, creating a new periodicity at  $2d_{(111)}$ . This leads to the presence of electron diffraction “superspots”, shown in Figure 3.20. Because ordering in InGaP occurs on the Group III sublattice, only two of the four possible CuPt ordering variants, (111) and  $(\bar{1}\bar{1}1)$ , will be present. Therefore, electron diffraction superspots will appear only in the [110] cross-section pole figure. For [110] surface steps, only the  $(\bar{1}\bar{1}1)$  subvariant is observed, as in Figure 3.20. From a practical standpoint, this may be used to unambiguously identify crystallographic directions in the sample. The reduction in symmetry arising from CuPt-B ordering leads to a decrease in the semiconductor bandgap of as much as 160 meV<sup>17</sup>. Photoluminescence polarization<sup>57</sup> and spectral broadening<sup>58</sup> are also observed. These effects are clearly undesirable when short-wavelength emission is desired.



**Figure 3.20. Diffraction superspots arising from CuPt-B ordering ([110] pole figure).**

Several mechanisms for surface driven ordering have been proposed, and the dependence of ordering on growth conditions is found to be extremely complicated. The occurrence of CuPt-B ordering is driven primarily by the surface reconstruction of the substrate or growth surface during deposition. Specifically, in a P-rich environment, a 2x1 surface reconstruction arises, consisting of P-dimers aligned along the  $[\bar{1}10]$ <sup>19,48</sup>. Due to the InGaP alloy size mismatch, the 2x1 reconstruction produces alternating compressed and dilated regions in the cation sublayer, as shown in Figure 3.21. This in turn promotes the alignment of In and Ga atoms in alternating  $[110]$ -oriented rows. This surface structure is propagated and metastably frozen into the bulk during subsequent deposition, yielding CuPt-B ordering domains throughout the bulk.

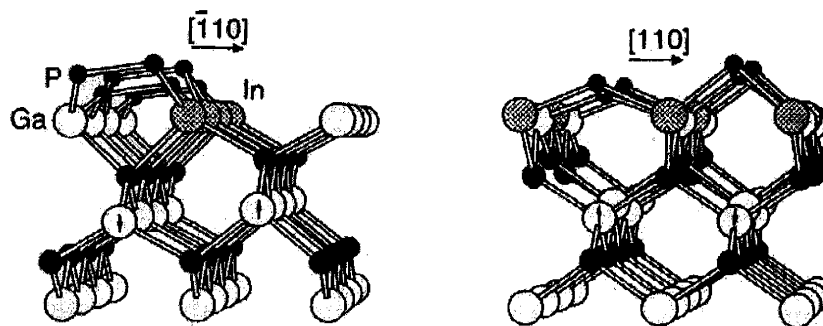


**Figure 3.21. P-rich 2x1 surface reconstruction in InGaP (reproduced from Zunger and Mahajan<sup>48</sup>).**

Ordering is found to depend on essentially all of the primary MOCVD growth parameters<sup>19,48,57-65</sup>. (It should be noted that the majority of studies reported in the literature deal with  $\text{In}_{0.5}\text{Ga}_{0.5}\text{P}$  lattice-matched to GaAs.) Zorn, *et al.*<sup>19</sup> found that ordering has a roughly parabolic dependence on temperature, with maximum ordering (minimum energy gap) at 660°C for  $V/\text{III} = 160$  and 650°C for  $V/\text{III} = 6$ . Ordering vanishes above 720°C, which is attributed to a destruction of the  $2 \times 1$  surface reconstruction. Ordering decreases below 660°C despite the surface reconstruction because suppressed adatom mobility limits the ability of In and Ga to relax to their ordered positions. Ordering decreases as  $V/\text{III}$  ratio decreases (surface becomes less P-rich). Finally, ordering is suppressed by doping, and vanishes for  $n > 6 \times 10^{18} \text{ cm}^{-3}$ . Zorn establishes a distinction, often confused in the literature, between the cation-rich  $2 \times 4$  reconstruction and the P-rich  $2 \times 1$  reconstruction, and confirms that ordering is favored only in the P-rich case<sup>19</sup>.

Kurtz, *et al.*<sup>63</sup> find similar dependences of ordering on growth temperature and  $V/\text{III}$  ratio. They also report an important relationship between ordering and growth rate. In general, a parabolic dependence of ordering on growth rate is found, in which the maximum degree of ordering is observed for a moderate growth rate. Kurtz observes that ordering is essentially a surface-diffusion-limited process, and proposes a two-step model of ordering to explain the dependence on growth rate and temperature. In this model, ordering is described as a competition between the ability of adatoms to assume the relaxed, ordered state, and a tendency for the subsequent destruction of ordering in a subsurface transition layer prior to complete “freezing” in the bulk. The residence time,  $t_s$ , of the cation is roughly the amount of time between adhesion and incorporation into the bulk. The cation relaxation time,  $\tau_s$ , reflects adatom diffusion to the ordered configuration. When  $t_s \gg \tau_s$ , the material will exhibit ordering. Similarly,  $t_t$  is the residence time of the alloy in the subsurface transition layer, while the relaxation time,  $\tau_t$ , reflects alloy interdiffusion to assume the disordered configuration. At a high growth rate, the ordered structure is never formed because  $t_s$  is too short. At a low growth rate,  $\tau_t \sim t_t$  and ordering is destroyed in the subsurface transition layer. Kurtz also reports a regime of low temperature and low growth rate where  $t_s > \tau_s$  and  $t_t < \tau_t$ , leading to a local

maximum of ordering and an energy gap decrease of roughly 50 meV. Control of ordering during MOCVD growth is critical, and will be discussed further in Chapter 7.

### 3.7.2 Microscopic Deviations

For an alloy  $A_{1-x}B_xC$ , five unique nearest-neighbor coordination arrangements about the common atom, C, are possible. These are noted as  $A_4$ ,  $A_3B$ ,  $A_2B_2$ ,  $AB_3$ , and  $B_4$ , or  $A_{4-n}B_n$  where n ranges from 0 to 4. In a random alloy, the probability of finding these cluster types in the alloy follows a standard binomial distribution<sup>48</sup>. The cases  $n=0$  and  $n=4$  correspond to the unmixed binaries and therefore are taken to be the zero of energy. Adapting the macroscopic energy formulation above, for a cluster  $n$  with composition  $X_n = \frac{1}{4}(4 - n)$ :

$$\Delta E^{(n)}(X_n) = \varepsilon^{(n)} + G(X_n), \quad \text{Equation 3.20}$$

where

$$\varepsilon^{(n)} = \Delta E_{CT}^{(n)} + \Delta E_{REL}^{(n)} \quad \text{Equation 3.21}$$

and

$$G(X_n) = \Delta E_{VD}^{(n)}. \quad \text{Equation 3.22}$$

Again,  $\varepsilon^{(n)}$  is the chemical energy of the cluster, while  $G(X_n)$  is the elastic deformation energy and is roughly equivalent for all cluster types. As such,  $G(x)$  impacts macroscopic phase separation, but does not contribute to microscopic deviations (short-range ordering, SRO).

The excess probability of finding a particular cluster type has been shown<sup>49</sup> to depend only on the chemical term  $\varepsilon^{(n)}$ . When  $\varepsilon^{(n)} < 0$ , cluster types  $n = 1$  through 3 are favored and anticlustering is expected. Conversely, when  $\varepsilon^{(n)} > 0$ , cluster types  $n = 0$  and 4 are favored and clustering is expected. Type-II lattice-mismatched alloys have positive  $G(x)$  and negative  $\varepsilon^{(n)}$ , so phase separation and anticlustering would be expected in the bulk. However, this formulation assumes coherency between the clusters and the matrix, which increases their predicted energy. As noted above, at a free surface, clusters are free to relax to a partially incoherent state. This will tend to lower the energy of

clustering relative to anticlustering. Therefore, the stability of clustering depends strongly on the deposition environment and may be enhanced for surface-governed processes such as MOCVD<sup>48</sup>.

### 3.7.2.1 Clustering

The precise nature of In “clustering” —really a local enrichment in In fraction—is dependent on factors such as alloy composition, substrate orientation, and MOCVD growth conditions, and the mechanism by which it occurs is not well defined. In general, its occurrence is believed to be related to size-mismatch driving forces similar to those that lead to spinodal decomposition and phase separation in the bulk. It is strongly favored under some deposition conditions, to the point that clustering is observed in samples with In fraction as low as 0.15, well away from the spinodal maximum. Feenstra, *et al.* have used scanning tunneling microscopy (STM) to directly observe alloy clustering in both AlGaAs and InGaAs<sup>66</sup>. The tendency of In to segregate to the growth surface during MBE, even through several In-free monolayers, has been established by Dehaese, *et al.*<sup>67</sup>. Wallart, *et al.*<sup>68</sup> propose a mechanism by which preexisting conditions of surface roughness drive In clustering in InGaP via strain relaxation considerations. In compression, In atoms tend to segregate to convex regions of the surface where their large size is more readily accommodated. Millunchick, *et al.*<sup>69</sup> describe a similar morphological instability mechanism and further note that the strain energy that drives In clustering is in competition with the resulting increase in surface energy, which would tend to stabilize a flat surface. This model is relatively simplistic, as it fails to consider key factors in surface-driven processes such as surface reconstruction, surface steps, etc. Work to clarify these points is ongoing.

From a properties standpoint, clustering has been observed to decrease the semiconductor bandgap, similar to ordering. The magnitude of this effect varies among the band transition types (e.g., X,  $\Gamma$ , L), to the point that clustering in Al<sub>0.5</sub>Ga<sub>0.5</sub>As can drive the alloy bandgap from indirect to direct character<sup>70</sup>. For In<sub>0.5</sub>Ga<sub>0.5</sub>P, wave-function calculations suggest that the conduction band maximum will localize on Ga<sub>4</sub> clusters, producing an impurity-like trap level in the energy gap<sup>70</sup>. Clustering will also introduce

local strain fields due the lattice mismatch between neighboring regions. The impact of In clustering on material quality will be further discussed in Chapter 6.

### 3.8 Device and Material Design Goals

#### 3.8.1 Quantum Efficiency and Device Performance

Optical efficiency is a key metric for light emitting device performance, as was briefly noted in Section 3.1. In the simplified case, device efficiency is taken to be the product of two factors: internal quantum efficiency and external quantum efficiency. Internal quantum efficiency refers to the ability of a material to convert electrical carriers to photons, while external quantum efficiency refers to the ability to extract these photons from the device.

Internal quantum efficiency has a complicated functional form depending on the properties of the band structure described in Figure 3.2. It can be expressed as<sup>4</sup>:

$$\eta_{\text{int}} = \left\{ 1 + \left( \frac{\tau_r}{\tau_{nr}} \right) \left[ 1 + \left( \frac{m_{eX}}{m_{e\Gamma}} \right)^{\frac{3}{2}} \exp\left( \frac{E_0 - E_X}{kT} \right) \right] \right\}^{-1}, \quad \text{Equation 3.23}$$

where  $\tau_r$  is the radiative recombination lifetime,  $\tau_{nr}$  is the nonradiative recombination lifetime,  $m_{eX}$  and  $m_{e\Gamma}$  are the electron effective masses at the X and  $\Gamma$  conduction band minima, respectively, and  $E_0 - E_X$  is the difference between the  $\Gamma$  and X energy gaps. This formulation ignores recombination by carriers in any other conduction band minima, as well as any possible radiative recombination from the X band, and assumes that  $\tau_{nr}$  is the same for X and  $\Gamma$  carriers. Qualitatively, Equation 3.23 suggests a number of criteria for the selection of an efficient light emitting material. As discussed above,  $E_0 - E_X$  should be as negative as possible. The ratio of electron effective masses in the X and  $\Gamma$  bands should be small, corresponding to a relatively small X density of states. Finally, the radiative/non-radiative lifetime ratio should be minimized, as shorter lifetime processes are more probable. Theoretical internal quantum efficiencies in the InGaP system are presented in Figure 3.22. Materials constants used in this calculation are given in Table 3.3.

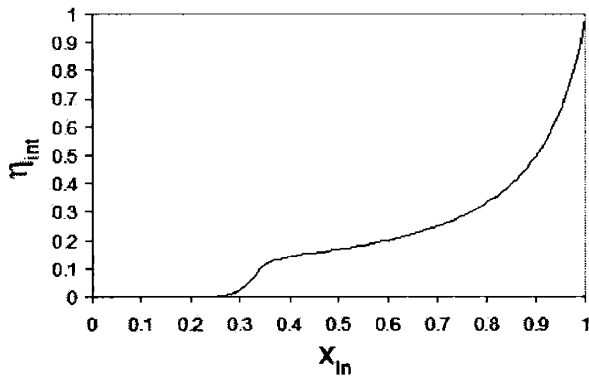


Figure 3.22. Variation of internal quantum efficiency with In fraction in  $\text{In}_x\text{Ga}_{1-x}\text{P}$ .

	$\tau_r/\tau_{nr}$	$m_{eX}/m_0$	$m_{e\Gamma}/m_0$	$E_0-E_X$
<b>GaP</b>	10 [after 26]	1.4 [24]	0.13 [24]	Equation 3.4
<b>InP</b>	0.01 [after 26]	0.88 [24]	0.08 [24]	Equation 3.4

Table 3.3. Constants used in Figure 3.21.

External quantum efficiency, or extraction efficiency, is primarily a geometrical factor. As a result of total internal reflection, light escaping from a point at the center of the active region is limited to a cone, as shown in Figure 3.23. The size of this cone is determined by Snell's Law for total internal reflection, wherein the critical angle varies inversely with the refractive index contrast at the interface. It is clear from Table 3.1 that the refractive index of a typical semiconductor is considerably larger than that of air, leading to a small critical angle on the order of  $17^\circ$ , or an azimuthal angle for the escape cone of  $34^\circ$ . The azimuthal angle of the escape cones can be increased to about  $52^\circ$  by encapsulating the device chip in an intermediate-index epoxy. The benefit of a transparent substrate is immediately obvious, as it roughly doubles the number of light cones escaping the device. If top and bottom contacts are present they will absorb emitted light, decreasing the extraction efficiency. External quantum efficiencies on the order of 0.3 have been achieved for shaped, transparent substrate InAlGaP devices<sup>7</sup>.



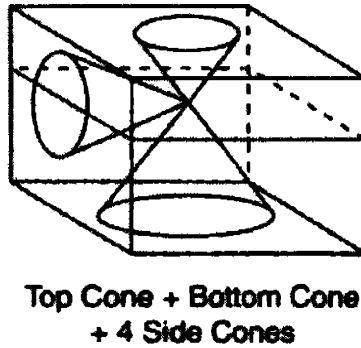


**Figure 3.23. Light escape cones in a transparent substrate device (reproduced from Kish<sup>4</sup>).**

Consider that we wish to fabricate an emitter operating near 555 nm with power conversion efficiency ( $P_E$ ) on the order of 0.2, as described in Figure 1.3. As shown in Figure 1.2, eye sensitivity reaches its maximum near 555 nm, where  $V(\lambda) = 1$ . Given<sup>2</sup> that Luminous Efficacy ( $\text{lm/W}$ ) =  $680V(\lambda)P_E \approx 680V(\lambda)C_{\text{ex}}\eta_{\text{int}}$  for an emitter with a narrow linewidth, then  $C_{\text{ex}}\eta_{\text{int}}$  must be approximately equal to 0.2 to satisfy this design goal. Higher  $P_E$  goals would demand even better quantum efficiencies. From this, we can quickly see that large internal quantum efficiencies and extraction efficiencies will be required to solve the green gap problem using a semiconductor LED. Chapter 7 will present one possible solution to coax InGaP to this performance level.

### 3.8.2 Emitter Designs

The simplest emitter configuration is a homojunction LED, shown in Figure 3.24. During forward bias operation of this device, electrons (holes) are injected into the p-type (n-type) material, where they recombine to produce a photon. Shortcomings of this design include the unconfined nature of the minority carrier injection, and the fact that absorption is likely to occur throughout the bulk. A single-heterostructure LED consists of a junction between a smaller bandgap material and a wider bandgap material. As illustrated in Figure 3.25, this bandgap difference is accommodated asymmetrically between the conduction and valence bands. For junctions between  $\text{In}_x(\text{Al}_y\text{Ga}_{1-y})_{1-x}\text{P}$  alloys of interest in this work ( $0 \leq x \leq 0.45$ ;  $0 \leq y \leq 0.2$ ), this ratio is approximately  $\Delta E_c:\Delta E_v::0.7:0.3$ , with a type-I band alignment<sup>71-73</sup>. The excess barrier in the valence band suppresses hole injection into the n-side, confining recombination to the smaller

bandgap region. This structure can be further improved by sandwiching the small bandgap material between two large bandgap regions, as shown in Figure 3.26. In this double heterostructure case, both electrons and holes are confined to the narrow-bandgap region. The probability of light absorption is decreased in the wide bandgap regions. The principles outlined above can be applied in more complicated configurations to produce additional device enhancements, as will be discussed in Chapter 7.

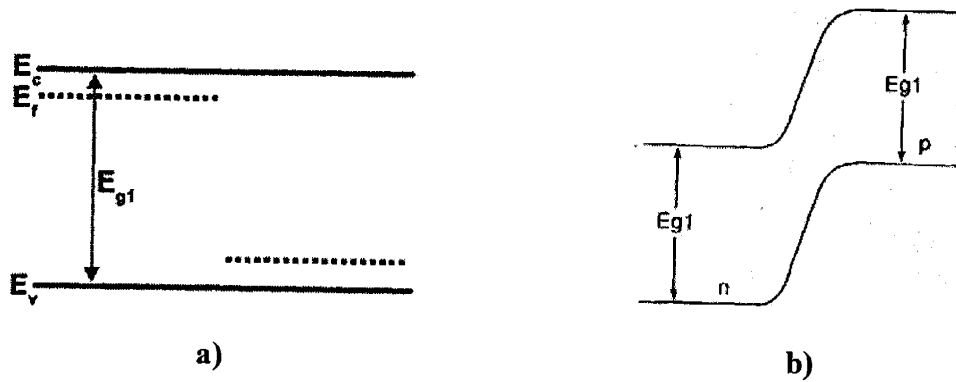


Figure 3.24. Energy band diagrams for a homojunction LED a) flat band, b) thermal equilibrium.

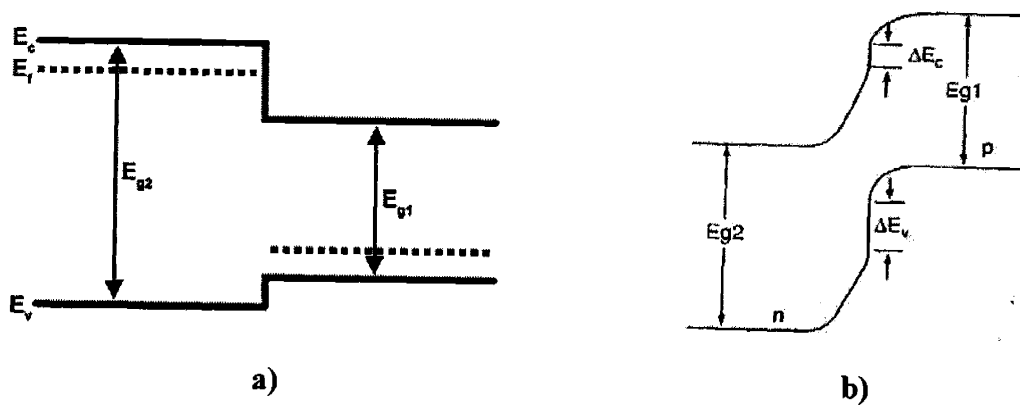


Figure 3.25. Energy band diagrams for a single heterojunction LED a) flat band, b) thermal equilibrium.

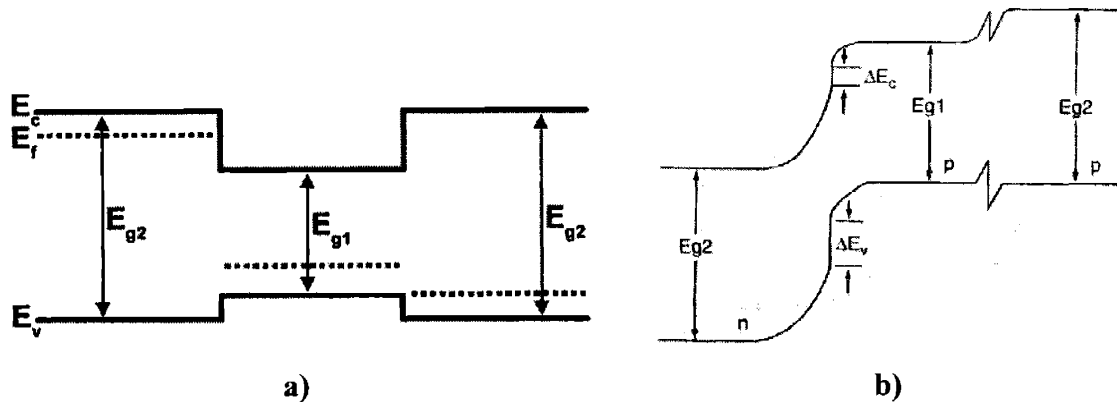


Figure 3.26. Energy band diagrams for a double heterojunction LED a) flat band, b) thermal equilibrium.

### 3.9 Summary

We have presented a review of the properties of InGaP and InAlGaP alloys as they pertain to the fabrication of interesting optical and electronic device materials.

These include:

- The reduction in internal quantum efficiency as the transition from direct bandgap to indirect bandgap is approached;
- The significance of dislocations arising from mismatched epitaxy, including enhanced nonradiative recombination at threading dislocations, and the reduction of threading dislocation density via the use of a relaxed, graded buffer;
- The occurrence of ordering and In clustering that occur under certain MOCVD conditions and lead to a degradation in device performance; and
- The large internal and external quantum efficiencies required to achieve a high-brightness LED that will fill the green gap.

For the reader interested in a more detailed exploration of these topics, we recommend High Brightness Light Emitting Diodes, Semiconductors and Semimetals, Volume 48, 1997, G.B. Stringfellow and M.G. Craford, editors; “Dislocations in strained-layer epitaxy: Theory, experiment, and applications,” E.A. Fitzgerald, *Materials Science Reports, Volume 7*, 1991; and “Atomic Ordering and Phase Separation in Epitaxial III-V Alloys,” A. Zunger and S. Mahajan, in Materials, Properties and Preparation, Handbook on Semiconductors, Volume 3b, 1994, T.S. Moss and S. Mahajan, editors.



## 4 MOCVD Conditions and Characterization Methods

### 4.1 Introduction

This section provides details of the MOCVD reactor chamber and growth conditions used to produce the material in this study. In addition, the various characterization techniques used to study these materials will be described.

### 4.2 MOCVD Reactor System

MOCVD growth, as described in Chapter 2, was carried out in a Thomas Swan 1” atmospheric pressure research reactor. A schematic of the reactor chamber is shown in Figure 4.1.

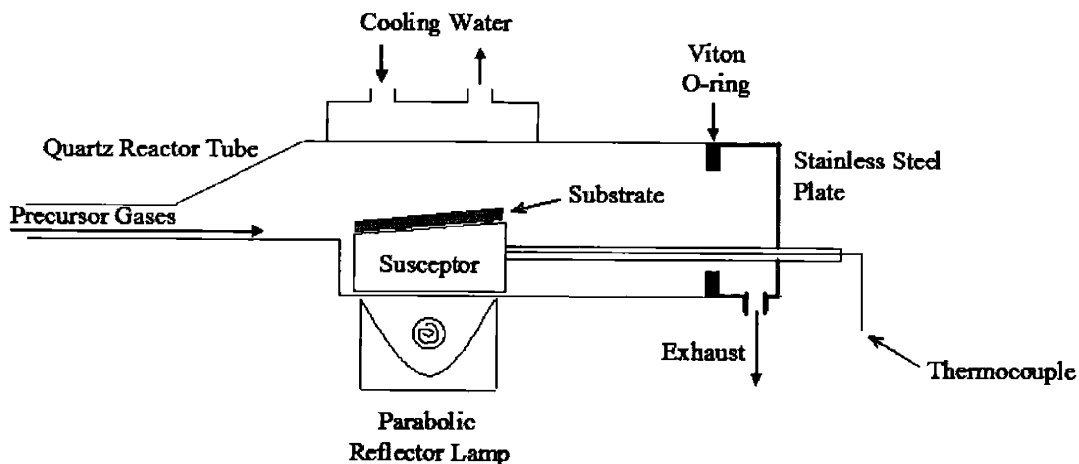


Figure 4.1. Thomas Swan MOCVD reactor chamber used to produce the samples in this study.

The reactor chamber consists of a quartz tube coupled at the nose to  $\frac{1}{4}$ " diameter stainless steel pipe and at the rear to a stainless steel platen. Quartz-to-steel seals are made with Viton O-rings to ensure that the system is leak tight. The graphite susceptor holds substrate pieces up to roughly one square inch in area and is heated via a parabolic reflector lamp. Substrate temperature is determined using a thermocouple enclosed in a

quartz sheath and inserted inside the susceptor. The top wall of the reactor is cooled via circulating water. This regulates the reactor temperature and creates a steep thermal gradient away from the substrate surface. Precursor gases are delivered from compressed hydride cylinders and from liquid organometallic bubblers.

N<sub>2</sub> gas, purified through a Nanochem filter, flows through the reactor chamber in standby purge. During growth, H<sub>2</sub> carrier gas is purified through a palladium diffuser before entering the reactor system. H<sub>2</sub> is bubbled through the liquid organometallic sources, TMI<sub>n</sub>, TMGa, TMAI, and DMZn, under the conditions described in Table 2.1. In addition, a constant total pressure of 1200 torr is maintained in each bubbler. PH<sub>3</sub> and dilute SiH<sub>4</sub> are supplied from compressed hydride gas cylinders. Flow rates of the carrier and precursors gases are controlled via high-precision mass flow controllers.

The reactor system is equipped with parallel reactor and vent lines operating up to 10 slpm. H<sub>2</sub> carrier flow is set to 5 slpm for all growth runs. Flow in the N<sub>2</sub>-purged vent line is determined by a differential pressure controller that maintains equilibrium between the reactor and vent lines. The reactor and vent lines meet at the gas-switching manifold, or epifold, where the precursor gases are mixed before being delivered to the reactor chamber. This configuration allows for the equilibration of precursor flows on the vent line, and minimizes the switching transient when precursors are sent to the reactor chamber. Flow rates for each of the precursor gases vary among experiments, but are always dictated by the mass transport limited growth model outlined in Chapter 2.

#### **4.2.1 Substrate Preparation**

InGaP and InAlGaP samples produced in this study were deposited on S-doped n-type (001) GaP substrates misoriented 10° toward the nearest <110>. This offset is illustrated in Figure 4.2.

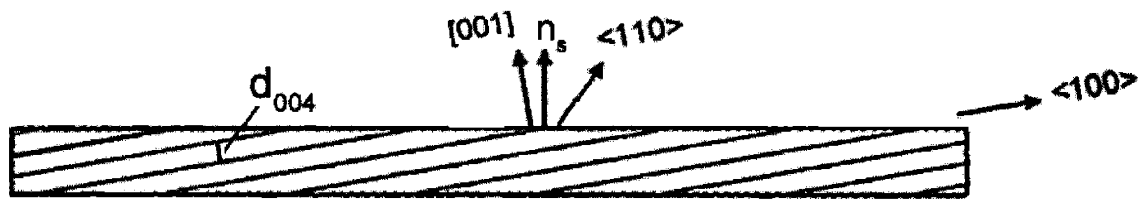


**Figure 4.2.** Orientation of (004) planes relative to the sample surface for 10° misorientation toward the nearest <110>;  $n_s$  refers to the sample surface normal.

Prior to growth, GaP wafers are cleaved into pieces with dimensions between 1 and 2.5 cm on a side. These pieces are removed to a Class 100 clean room, where they are etched for 75 sec in a solution of 15:1:1  $H_2SO_4:H_2O_2:H_2O$ . This etch removes 100 to 200 Å of GaP. The pieces are then rinsed in deionized water and blown dry with  $N_2$ . The substrate is loaded into the reactor chamber, where it is baked at 300°C under  $H_2$  for five to ten minutes to desorb water and organics from the surface. This is followed by baking at 800°C for ten to fifteen minutes to remove surface oxides. Finally, the substrate is brought to the growth temperature and allowed to equilibrate for five minutes before growth is initiated. A homoepitaxial GaP layer is deposited to create a high-quality surface, then growth proceeds according to the desired final structure.

For the experiments detailed in Chapter 5, InGaP was deposited on (001) GeSi/Si virtual substrates oriented 6° toward the nearest <111>. These substrates were cleaved in the same manner as the GaP substrates and removed to the clean room for pre-growth cleaning. GeSi substrates were etched in Piranha (3:1  $H_2SO_4:H_2O_2$ ) for varying amounts of time, as detailed in Chapter 5. A one minute HF dip was used to passivate the surface, and the substrate was immediately placed in the reactor chamber.

## 4.3 Characterization

### 4.3.1 Composition

#### 4.3.1.1 Triple Axis X-ray Diffraction

The composition of single crystal thin films was determined using triple axis x-ray diffraction (TAXRD). Single crystal XRD demands precise alignment, particularly for offcut substrates such as those employed in this work. In order to completely characterize the strain state of the epitaxial film, both symmetric (004) and asymmetric, glancing exit (224) scans are used. TAXRD is performed on a Bede D<sup>3</sup> diffractometer with a Rigaku RU-200 rotating copper anode source. Cu K $\alpha_1$  radiation from the rotating anode is conditioned using a collimating crystal prior to the sample. After the sample, the diffracted beam passes through two slits and an analyzer crystal before arriving at the detector.

Bragg's Law for diffraction<sup>74</sup> states that:

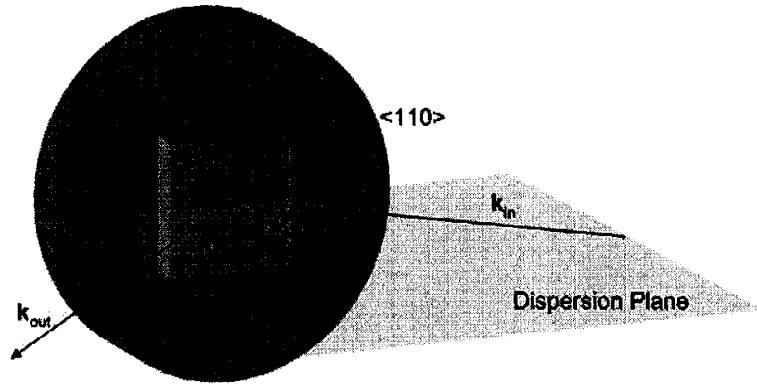
$$\lambda = 2d \sin \theta_B,$$

**Equation 4.1**

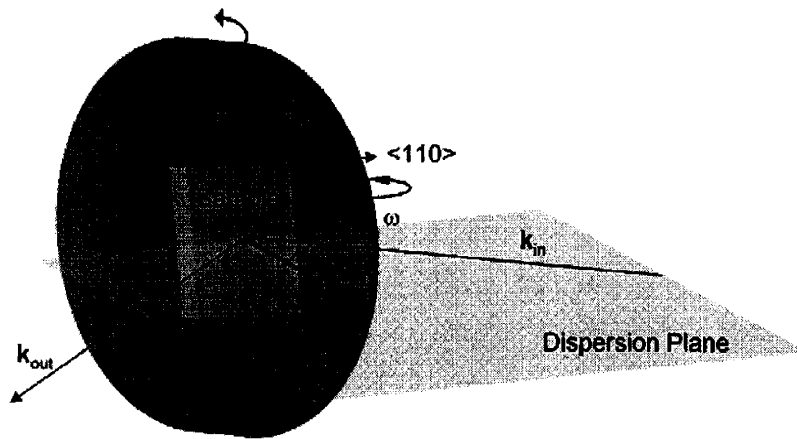
where  $\lambda$  is the wavelength of Cu K $\alpha_1$  radiation,  $d$  is the spacing between lattice planes of interest, and  $\theta_B$  is the Bragg angle associated with those lattice planes.

To illustrate XRD in our system, we represent the diffraction condition in reciprocal space using the diffraction vector,  $\mathbf{q}$ .  $\mathbf{q}$  equals  $\mathbf{k}_{\text{out}} - \mathbf{k}_{\text{in}}$  (where  $|\mathbf{k}| = 2\pi/\lambda$ ) and therefore  $\mathbf{q}$  is the perpendicular bisector of the incident ( $\mathbf{k}_{\text{in}}$ ) and diffracted ( $\mathbf{k}_{\text{out}}$ ) xray beams with  $|\mathbf{q}| = 4\pi \sin \theta_B / \lambda$ . The diffraction condition will be met when the normal vector,  $\mathbf{g}$ , for the atomic planes of interest equals  $\mathbf{q}$ .  $|\mathbf{g}|$  is defined as  $2\pi/d$ , where  $d$  is the spacing of the diffraction planes.  $\mathbf{g} = \mathbf{q}$  is a vector identity that satisfies Bragg's Law and contains additional information relating to proper sample alignment, as shown in Figure 4.3.





a)



b)

**Figure 4.3. Illustration of the single-crystal diffraction condition a) prior to alignment and b) with the plane normal of interest,  $g$ , aligned along the diffraction vector,  $q$ .**

Three axes of rotation are available to align the (004) or (224) substrate plane normal with the diffraction condition. These axes are illustrated in Figure 4.4. The sample is aligned with a  $\langle 110 \rangle$  direction parallel to the dispersion plane. This orientation is selected so that both (004) and (224) plane normals are simultaneously in the dispersion plane. In this geometry, only one sample orientation axis, Axis 2, must be altered to move between the (004) and (224) diffraction conditions.

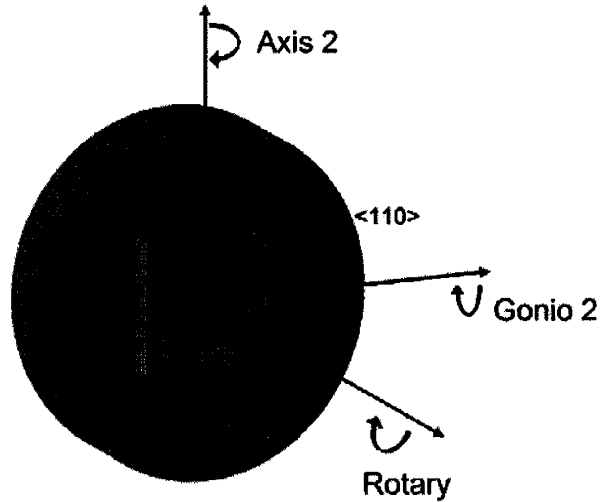


Figure 4.4. Axes of rotation available for sample alignment in TAXRD.

In the case of  $10^\circ$  substrate misorientation toward the nearest  $\langle 110 \rangle$ , the  $(004)$  plane normal lies  $10^\circ$  from the surface normal, toward an orthogonal  $\{100\}$  plane. This means that the offcut lies directly between the two in-plane  $\langle 110 \rangle$  directions. For the purposes of alignment, the  $10^\circ$  offcut is resolved into its  $7.1^\circ$  components along the in-plane  $\langle 110 \rangle$  directions, shown in Figure 4.5. This corresponds to  $7.1^\circ$  rotation on both Axis 2 and Gonio 2 to bring the substrate  $(004)$  plane normal into the diffraction condition, similar to the transition from Figure 4.3a to Figure 4.3b.

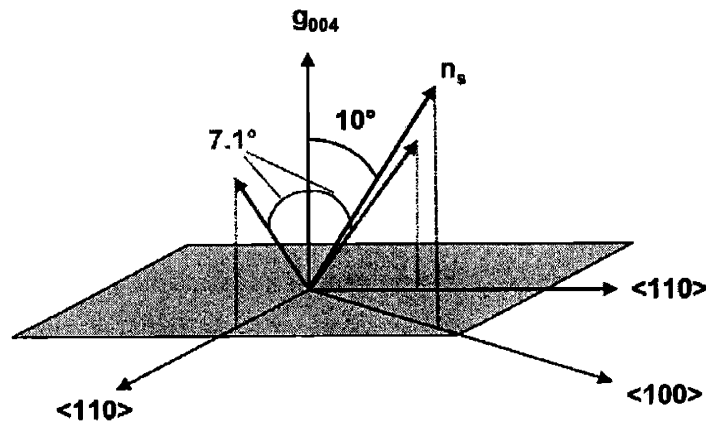


Figure 4.5. Resolution of substrate offcut into the perpendicular in-plane  $\langle 110 \rangle$  directions.  $g_{004}$  is the  $(004)$  plane normal;  $n_s$  is the sample surface normal.

An important outcome of this type of substrate misorientation is that the epitaxial film will tilt during growth to recover a (001) orientation, shown in Figure 4.6. Therefore, its plane normal will lie slightly out of the dispersion plane, as shown in Figure 4.7. This introduces a small but acceptable error to the diffraction calculations, since when  $\mathbf{g}_{\text{epi}}$  is aligned in the diffraction condition it will still lie at an angle to the idealized dispersion plane. The finite height of the detector accepts a wide enough range of  $\mathbf{q}$  values above and below the ideal dispersion plane that the diffraction peak of a tilted film is still detectable in this geometry. In principle, only the projection of  $\mathbf{g}_{\text{epi}}$  in the ideal dispersion plane is measured.

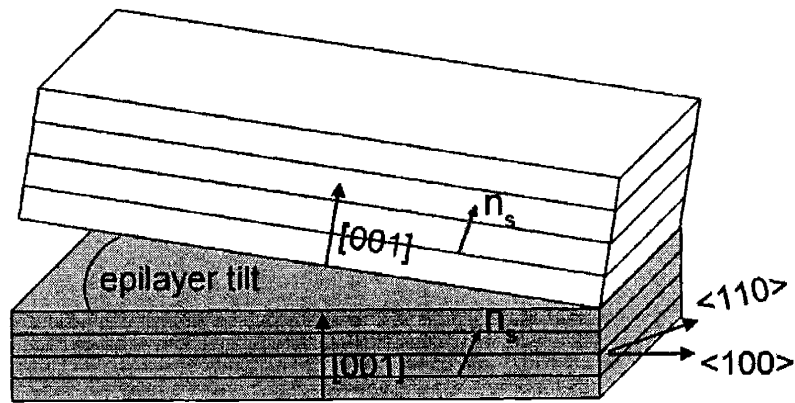


Figure 4.6. Tilt of epilayer (001) planes during growth on a misoriented substrate.

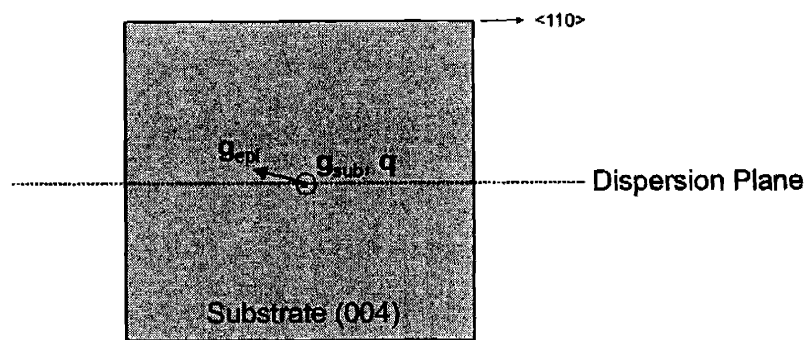


Figure 4.7. In the case of a tilted epilayer and  $\langle 110 \rangle$  sample alignment, the epitaxial plane normal of interest,  $\mathbf{g}_{\text{epi}}$ , does not lie completely in the dispersion plane.

The strain state in the film is fully characterized by 004 and 224 scans using a modification of the formulation of Matney and Goorski<sup>75</sup>. The 004 diffraction rocking

curve is symmetric; that is,  $\mathbf{g}$  is aligned with a unit cell axis, so the angle of incidence of the x-ray beam equals the angle of reflection relative to the unit cell. This measures the perpendicular lattice parameter in an epitaxial film, but cannot account for any distortion of the lattice, as the projection of the diffraction vector into the (004) plane is zero. This is illustrated in Figure 4.8.

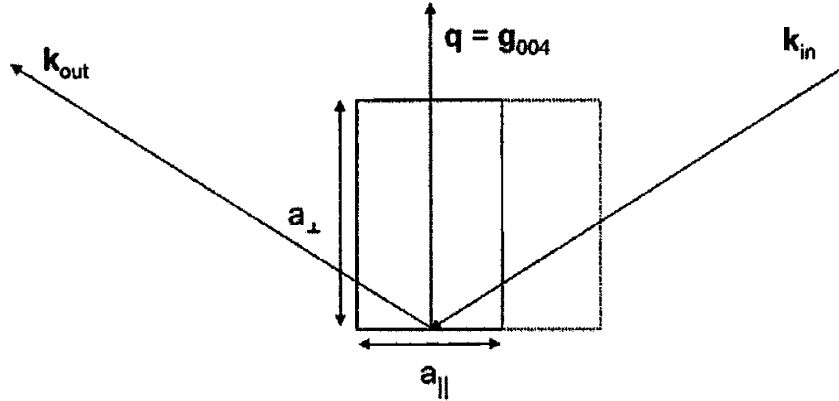


Figure 4.8. The 004 diffraction condition.

The perpendicular lattice constant,  $a_{\perp}$ , may be calculated from Bragg's Law:

$$a_{\perp} = \frac{2\lambda}{\sin(\theta_{B,004} + \Delta\theta_{004})}, \tag{Equation 4.2}$$

where  $\lambda$  is again the wavelength of Cu  $K\alpha_1$  x-rays,  $\theta_B$  is the substrate 004 Bragg angle, and  $\Delta\theta_{004}$  is the difference between the film and substrate 004 Bragg angles.

The 224 glancing exit diffraction rocking curve is asymmetric; that is, the angle of incidence of the xray beam is much larger than the angle of exit relative to the unit cell. In this configuration it is possible to measure a component of both the perpendicular and parallel film lattice constants, revealing the strain state of the film. The diffraction vectors in this geometry are defined as:

$$q_{\parallel} = \frac{2}{\lambda} \sin(\theta_{B,224} + \Delta\theta_{224}) \cdot \cos\left(\frac{\pi}{2} - (\phi + \Delta\omega_{224} - \Delta\omega_{004})\right) \tag{Equation 4.3}$$

$$q_{\perp} = \frac{2}{\lambda} \sin(\theta_{B,224} + \Delta\theta_{224}) \cdot \sin\left(\frac{\pi}{2} - (\phi + \Delta\omega_{224} - \Delta\omega_{004})\right) \quad \text{Equation 4.4}$$

where  $\theta_{B,224}$  is the substrate 224 Bragg angle,  $\Delta\theta_{224}$  is the difference between the film and substrate 224 Bragg angles,  $\phi$  is the angle between the substrate 004 plane normal and the substrate 224 plane normal ( $35.264^\circ$ ),  $\Delta\omega_{224}$  is the difference between the film and substrate  $\omega$  values for 224 diffraction, and  $\Delta\omega_{004}$  is the difference between the film and substrate  $\omega$  values for 004 diffraction. In this case,  $\omega$  refers to any rotation about Axis 2—independent of detector movement—that is required to bring the epilayer plane normal of interest into the diffraction condition. Physically,  $\Delta\omega_{004}$  can only arise from tilt between the substrate and epilayer 004 planes, as distortion is not detected.  $\Delta\omega_{224}$  includes any tilt of the epilayer, but also accounts for the tetrahedral distortion of the epilayer lattice, as illustrated in Figure 4.9.

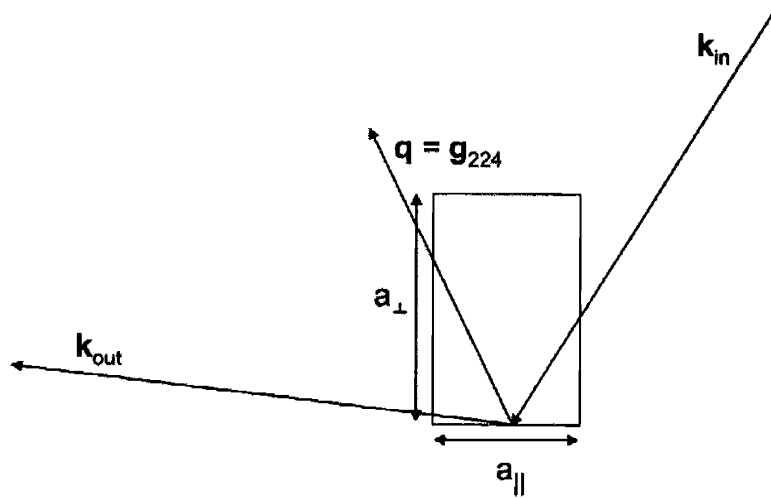


**Figure 4.9. The 224 diffraction condition.**

The reciprocal lattice vectors described above may be transformed into real space physical parameters through the following equations:

$$a_{\parallel} = 2\sqrt{2} / q_{\parallel} , \quad \text{Equation 4.5}$$

$$a_{\perp} = 4/q_{\perp}, \quad \text{Equation 4.6}$$

$$a_r = \frac{(-a_{\perp} - (\nu \cdot a_{\parallel}))}{-1 - \nu}, \quad \text{Equation 4.7}$$

$$\text{composition} = \frac{a_r - a_s}{a_f - a_s}, \quad \text{Equation 4.8}$$

$$\text{strain} = \frac{a_{\parallel} - a_r}{a_r}, \quad \text{Equation 4.9}$$

$$\text{misfit} = \frac{a_s - a_r}{a_r}, \quad \text{Equation 4.10}$$

$$\%relaxation = \left[1 - \frac{|\text{strain}|}{|\text{misfit}|}\right] \cdot 100, \quad \text{Equation 4.11}$$

where  $a_r$  is the lattice parameter of a fully relaxed film of the composition measured,  $\nu$  is Poisson's ration, and  $a_f$  is the lattice parameter the 100% alloy composition (e.g.  $a_f$  is the lattice parameter of pure InP when measuring In fraction in an InGaP film on a GaP substrate). As noted in Chapter 3, the asymmetric nature of dislocations in the zincblende lattice can produce asymmetric relaxation in the perpendicular in-plane  $\langle 110 \rangle$  directions. Therefore, diffraction must be performed in both in-plane  $\langle 110 \rangle$  directions to accurately determine average relaxation and any relaxation asymmetry.

#### 4.3.1.2 Cathodoluminescence

In some cases, composition was determined or confirmed using cathodoluminescence (CL). Cathodoluminescence is performed inside a scanning electron microscope (SEM). Bombardment by the electron beam promotes carriers across the semiconductor energy gap. Light produced by the recombination of these carriers is collected and the spectrum is analyzed. The resultant peak wavelength can be related to the bandgap of a relaxed film, and thus to its composition, via Equation 3.4 and Equation 3.5. The ballistic effects of the electron beam are sufficient to stimulate weak emission even in indirect bandgap materials. CL was performed in a JEOL 5300 SEM with a parabolic mirror, under typical operating conditions of 15 kV and 30 nA. Spectra were collected using a GaAs photomultiplier tube using lock-in techniques, and analyzed

with an Oxford Instruments spectrometer. The spectrum of a standard sample was obtained prior to each session to calibrate the spectral measurements.

#### 4.3.1.3 Secondary Ion Mass Spectroscopy

Doping levels in device structures were determined using secondary ion mass spectroscopy (SIMS). In this destructive technique, the film is sputtered away with a low-energy ion beam. The relative abundance of species in the sputtering yield is analyzed with a mass spectrometer to determine the material composition. As the film is sputtered away, a through-thickness composition profile is generated. SIMS is an extremely sensitive analysis technique, able to detect doping levels in the parts per million range.

#### 4.3.2 Microstructure and Defect Density

Transmission electron microscopy (TEM) is invaluable for the characterization of materials microstructure. In this technique, electrons are diffracted through a thin foil and may be viewed in reciprocal space or transformed into a real space image of the material. Because the electron wavelength is very short, TEM is capable of imaging on the scale of angstroms with acceptable resolution. Additionally, the short diffraction wavelength leads to a nearly flat Ewald sphere. As a result, the transmission electron diffraction pattern is essentially an image of the reciprocal lattice in and near the basal plane of the sample<sup>74,76</sup>. Figure 4.10 shows the predicted  $\langle 110 \rangle$  and  $\langle 100 \rangle$  electron diffraction patterns.

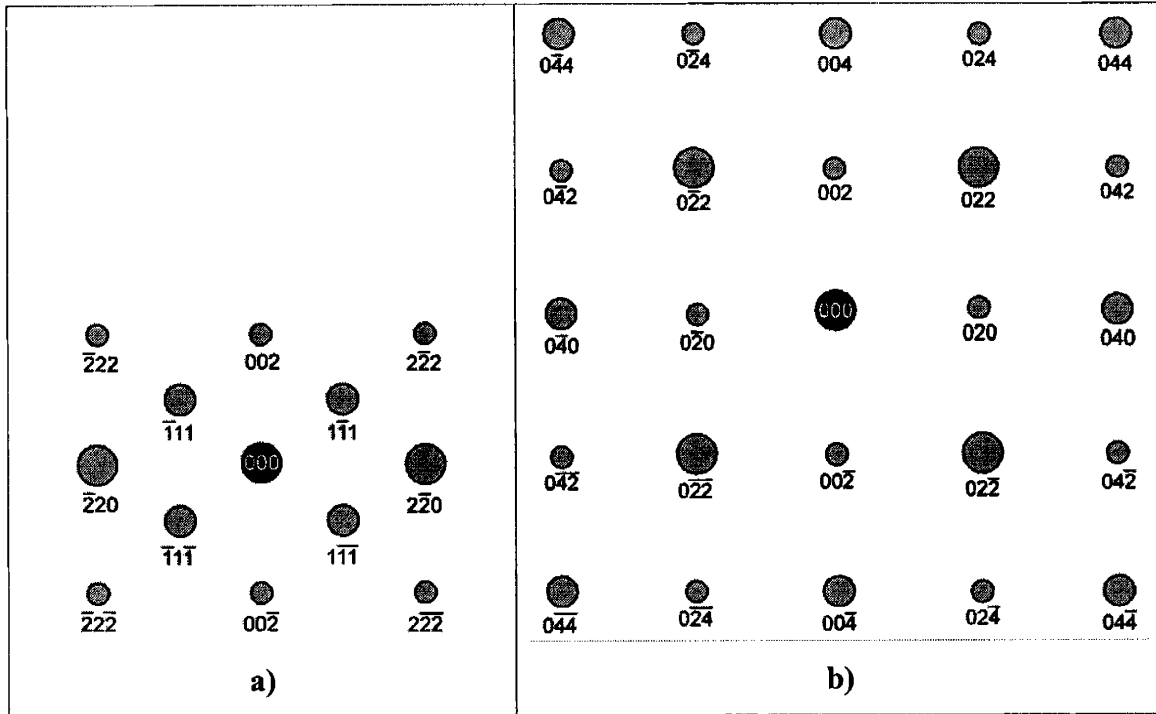


Figure 4.10. Predicted transmission electron diffraction patterns for a zincblende crystal. a)  $\langle 110 \rangle$  pole figure; b)  $\langle 100 \rangle$  pole figure.

TEM is utilized primarily to characterize defect microstructures. Due to their crystallographic nature, dislocations are clearly visible under certain diffraction conditions<sup>77</sup>. All threading dislocation densities in this study are measured by PVTEM. Contrast arising from strain modulations is also visible in the proper TEM diffraction condition<sup>77</sup>. Thus, both PVTEM and XTEM are well suited to the study of microstructures that result from compositional fluctuations.

TEM was performed using a JEOL 2000FX TEM operating at 200 kV and 110-120 mA. Both plan view (PVTEM) and cross-section (XTEM) sample foils were prepared. Foils were manually polished to approximately 10  $\mu\text{m}$  thick using SiC paper. Final thinning was accomplished in an  $\text{Ar}^+$  ion mill operating at 6 V at an incidence angle of 11.5°. A double-tilt holder was employed to ensure that all diffraction conditions of interest could be reached. Energy dispersive x-ray (EDX) studies and lattice imaging were carried out in a JEOL 2010 TEM with the help of Mr. Michael Frongillo of the MIT CMSE Electron Microscopy Shared Experimental Facility.



### 4.3.3 Surface Morphology

Tapping-mode atomic force microscopy (AFM) was employed to study sample surface morphology and surface roughness. In tapping-mode AFM, a sharp Si tip oscillates above the sample surface. Deflection of the tip via surface forces is measured by a piezoelectric crystal and transformed into a real-space map of the sample surface. Sample tips are calibrated prior to each session using a standard InGaP graded buffer sample. Surface roughness values reported in this work are for 10 micron by 10 micron scans, unless otherwise noted. Tapping-mode AFM was carried out on a Digital Instruments Nanoscope III AFM in the MIT CMSE Shared Surface Analysis Facility. Surface morphology was also studied using differential interference contrast, or Nomarski, microscopy.

### 4.3.4 Optical Performance

#### 4.3.4.1 Cathodoluminescence

Cathodoluminescence, described above, can also be used to determine the characteristic emission wavelength of unprocessed device structures. CL was systematically used to verify the performance of undoped device structures prior to processing their doped counterparts into light emitting diodes. However, because CL intensity is dependent on factors such as beam shape, beam focal depth, and SEM current and voltage, as illustrated in Figure 4.11, it is difficult to make quantitative intensity comparisons among samples.

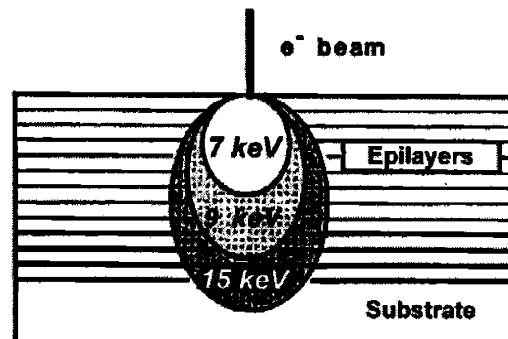


Figure 4.11. Schematic illustration of SEM beam shape variation with accelerating voltage (reproduced from Leon, *et al.*<sup>78</sup>)

#### 4.3.4.2 Electroluminescence

LED performance was characterized via electroluminescence (EL). To determine EL device characteristics, a forward current is applied to the processed device stack, creating excess carriers that recombine in the device active region. The variation in emission power with increasing operating current is measured using an integrating sphere. The pinhole aperture of the sphere is aligned with one face of the device, thus the measured performance represents roughly one-quarter to one-sixth of the total device output power. Characteristic device performance is reported for forward current operation at 20 mA. The emission spectrum is analyzed via a fiber-coupled spectrometer that is accurate to within 3 nm. EL was performed using a manual single probe station with an ILX-Lightwave integrating sphere in the lab of Prof. Rajeev Ram at MIT.

## 5 InGaP Heteroepitaxial Integration with GeSi

### 5.1 Introduction

Compound semiconductor optical devices, such as lasers and light-emitting diodes (LEDs), are essential components of many of the technologies we take for granted every day, from telecommunications to digital clocks. Compound semiconductors formed from Groups III and V of the periodic table, such as InGaP, mimic the crystal structure of silicon, but provide the higher bandgap energies and direct energy transition required for visible-wavelength devices. Because of fundamental problems with lattice mismatch, heterovalent-on-homovalent growth, and incompatible processing conditions, these visible optical devices have remained primarily separate and discrete from common silicon-based logic devices. The monolithic integration of visible optical materials on silicon-based technology would open a path for substantial advances in current technologies, from directly integrated and driven communications transceivers and LED displays, to the ambitious optoelectronic integrated circuit (OEIC). This section presents initial progress in the use of optimized, relaxed GeSi graded buffers as a lattice-matched virtual substrate for monolithic, epitaxial integration of InGaP-based light emitting devices on silicon.

### 5.2 Justification

Many paths to III-V on Si integration have been explored, falling generally into the categories of hybrid or monolithic integration. At the forefront of hybrid integration are various wafer-bonding techniques, which seek to mechanically join two dissimilar materials, particularly those that may not seem suited for epitaxial growth. Bonding of surfaces in intimate contact may be achieved at room temperature through van der Waals forces<sup>79</sup>, or at elevated temperatures through atomic rearrangement on the surface to form covalent bonds<sup>80</sup>. Though successful wafer-bonded devices have been demonstrated<sup>81,82,83</sup>, the process itself is not ideal for large-scale batch production. Scenarios in which the wafer-bonded structure can be inserted at the beginning of the

process are limited, and therefore the cost invariably approaches that of electronic packaging.

Monolithic integration involves the epitaxial growth of single-crystal III-V films directly on Si-based substrates with no external, mechanical steps. This type of integrated device structure is favorable because it would be compatible with standard integrated circuit processing<sup>84</sup>. Lattice-mismatched epitaxy is of primary interest in this field, as most useful III-V materials are not lattice-matched to silicon. There are a number of obstacles to the production of device-quality mismatched films; however, these obstacles are being addressed, and improved III-V films on Si have been demonstrated<sup>85</sup>. Monolithic integration offers superior fabrication and economics, and will therefore be the focus of our efforts to integrate InGaP on Si.

### 5.3 Early Growth Schemes

Initial attempts at monolithic InGaP integration on Si commonly utilized the “two-step” growth method, in which a thin, semi-amorphous GaAs buffer layer is deposited on Si, and then annealed to induce recrystallization<sup>86,87</sup>. These structures also often involved the growth of thick GaP, GaAs, GaAsP, or compositionally graded InGaP buffer layers, to isolate the device active region from the region of high mismatch and dislocation formation<sup>86,88,89,90,91</sup>. However, non-optimized growth of thick layers may have detrimental effects on film surface morphology<sup>84</sup>, and extremely thick films—which can be time-consuming and expensive to produce—may not be commercially viable. InGaP has also been shown to have an extremely low mismatch tolerance, with a degradation in film morphology for  $|f| > 0.1\%$ <sup>92</sup>, where  $f$  refers to lattice mismatch, as described in Chapter 3. This factor strongly motivates the development of closely lattice-matched substrates.

There have been reports of successful InGaP-on-Si device operation, including a 652 nm LED by Hu, *et al*<sup>86</sup> and a 605 nm LED by Kondo, *et al*<sup>91</sup>. However, in both cases, the device emission is weak and no threading dislocation density is reported. An efficient, reliable scheme for producing low-dislocation-density InGaP epitaxial films on Si has yet to be reported in the literature. We believe that optimized, relaxed GeSi graded buffer substrates are an ideal platform for monolithic InGaP/Si integration because of

their low threading dislocation densities ( $\sim 10^5 \text{ cm}^{-2}$ ) and the flexibility in virtual substrate lattice constant<sup>38</sup>.

## 5.4 Barriers to Heteroepitaxy

### 5.4.1 Lattice Mismatch

One of the major obstacles to monolithic integration of III-V devices on silicon is the large lattice mismatch that exists between the Si substrate and most of the III-V compounds of interest. Pertinent materials constants for III-V on IV epitaxy are given in Table 5.1.

	Si	Ge	GaP	InP
<b>a (Å)</b>	5.431 [26]	5.658 [26]	5.451 [17,25]	5.869 [24]
<b>E<sub>g</sub>(eV)</b>	1.12 [26]	0.661 [26]	2.26 [26]	1.35 [25]
<b>α (°C<sup>-1</sup>)</b>	2.6 x 10 <sup>-6</sup> [26]	5.9 x 10 <sup>-6</sup> [26]	5.91 x 10 <sup>-6</sup> [17]	4.75 x 10 <sup>-6</sup> [17]

**Table 5.1. Lattice parameters and bandgaps of semiconductors of interest.**

We opt to address the issue of lattice mismatch in this system through the use of optimized, relaxed GeSi graded buffer technology. Background information regarding lattice-mismatched epitaxy and graded buffer growth was presented in Chapter 3. Lattice constants available in the fully-miscible GeSi alloy system span a range from GaP to In<sub>0.5</sub>Ga<sub>0.5</sub>P. The simplest instance of lattice matching in this system involves the deposition of a binary III-P on a binary IV, GaP on Ge<sub>0.09</sub>Si<sub>0.91</sub>. In general, the growth of interesting compositions for optical devices will involve deposition of InGaP ternary alloys on GeSi. Of particular interest is the direct lattice-matched growth of In<sub>0.3</sub>Ga<sub>0.7</sub>P on Ge<sub>0.7</sub>Si<sub>0.3</sub>, as will be discussed below. The Ge<sub>0.7</sub>Si<sub>0.3</sub> virtual substrate is created via UHVCVD growth of a relaxed, graded GeSi buffer on Si, the details of which are presented elsewhere<sup>38</sup>. The best of these substrates have threading dislocation densities on the order of  $10^5 \text{ cm}^{-2}$ , sufficiently small to support the epitaxial integration of optical devices.

### 5.4.2 Thermal Mismatch

Another obstacle to monolithic heterointegration is thermal expansion mismatch between substrate and film, which will be dominated by the Si substrate. Table 5.1 lists the thermal expansion coefficients of the materials of interest in this project. Vapor deposition of compound semiconductors is generally performed at elevated temperatures, after which the final structure is cooled to room temperature. Furthermore, subsequent processing steps may subject the device structure to repeated thermal cycling. Given the disparate thermal expansion coefficients in Table 5.1, it is clear that substantial stresses may develop in the film, leading to strain damage and even cracking<sup>93</sup>. This thermal mismatch problem must be addressed and mitigated in the final device structures. In general, thermal mismatch is minimized through growth at low temperatures, with slow cooling to room temperature. It may also be partially offset through lattice-constant engineering—growing the film with an opposite sense of stress to that imposed by thermal contraction, so that a neutral state is achieved upon cooling<sup>38</sup>.

### 5.4.3 Heterovalent-on-Homovalent Epitaxy

Finally, in the case of III-V integration on a Group IV substrate, there is the problem of heterovalent-on-homovalent (polar-on-nonpolar) epitaxy. Group IV materials, being monatomic, possess a uniform charge distribution. This is referred to as being homovalent or nonpolar. Compound semiconductor materials, such as III-V compounds, form a zincblende structure that mimics the diamond cubic structure. The zincblende structure consists of interpenetrating FCC sublattices, one of which contains Group III atoms and the other Group V. A charge imbalance exists due to the differing valence states of the sublattices; this is referred to as heterovalent or polar. The primary difficulty in polar-on-nonpolar epitaxy is the formation of antiphase domains (APD) and associated antiphase boundaries (APB). APBs form in the epitaxial film due to misregistration of Group III and V sublattices in adjacent regions, shown in Figure 5.1.

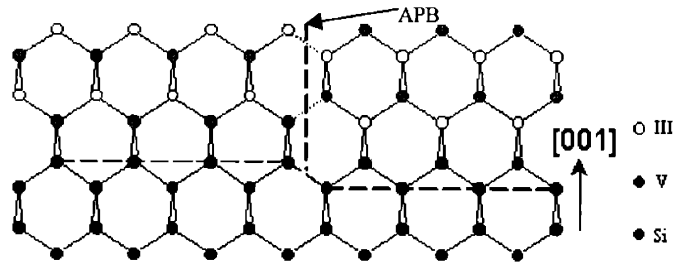


Figure 5.1. Anti-Phase Boundary ([110] projection)<sup>94</sup>.

Since III-V film growth is commonly initiated with a single layer of either Group III or Group V atoms, APBs are particularly likely to form on an odd-number-step-structure substrate. APBs act as nonradiative recombination centers and tend to produce a large leakage current in p-n diodes, so the growth of APB-free films for optical devices is especially important.

Antiphase disorder in heterovalent films may be eliminated using two complementary strategies of defect engineering, both of which involve growth on misoriented (001) substrates. The first strategy utilizes a high-temperature anneal of the offcut substrate, which tends to produce the double-atomic-layer step surface illustrated in Figure 5.2. This surface structure induces sublattice registration that helps to suppress APB formation<sup>95</sup>.

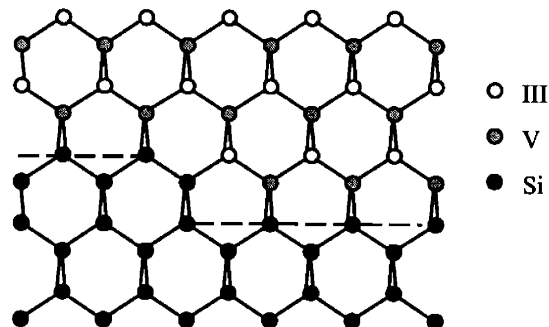


Figure 5.2. Double-atomic-step surface ([110] projection).

The second strategy takes advantage of the annihilating character of APBs; that is, when two APBs grow together, the lattice misregistration is eliminated and an enclosed domain forms, as shown in Figure 5.3.

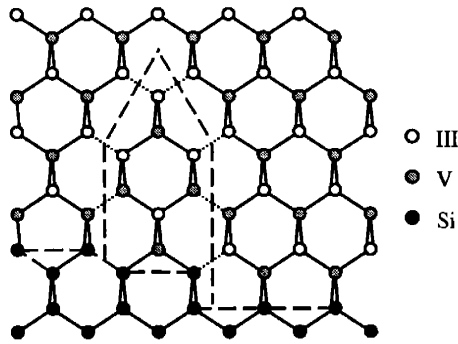


Figure 5.3. APB annihilation ([110] projection).

If a sufficient density of APBs is nucleated, they will be more likely to interact and may annihilate within a boundary layer near the interface, leaving a single-domain active region. A relatively high substrate offcut angle will produce a large surface step density, and any APBs that nucleate on remnant odd-number-steps will be likely to annihilate<sup>95</sup>. APB formation is a well-known complication in III-V on IV epitaxy, and the method to suppress it is reasonably well-understood. However, it is possible that the complexity of the interface chemistry in the InGaP/GeSi system will present additional problems.

## 5.5 The Device Material

The sensitivity of the human eye increases dramatically as wavelength shortens from 700 nm to 555 nm, where it peaks<sup>86</sup>. Consequently, for visible applications we seek a III-V compound with emission wavelengths near 555 nm. Figure 5.4 illustrates that InGaP compositions near the direct-indirect gap crossover ( $x_{In} = 0.27$ ) will emit at wavelengths as short as 570 nm. However, radiative recombination decreases close to this crossover point, leading to a trade-off between increased efficiency and shorter wavelengths. With this in mind, we have selected  $In_{0.3}Ga_{0.7}P$  for our device layer composition.



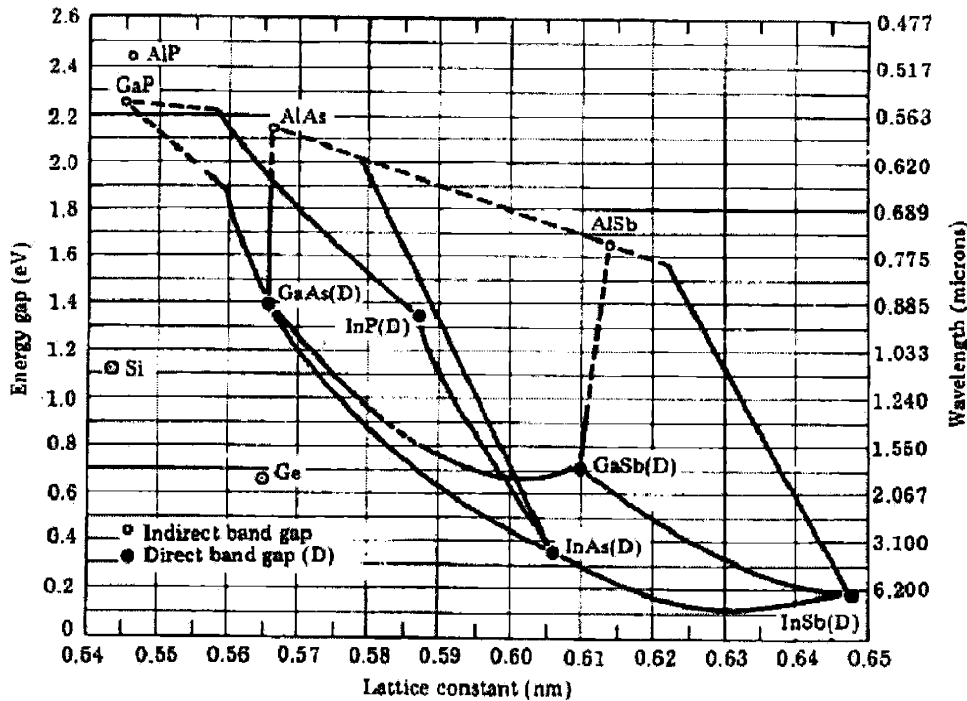


Figure 5.4. Bandgap vs. lattice constant of common III-V and IV semiconductors. (—: Direct bandgap; ---: Indirect bandgap)

## 5.6 Growth Conditions

In this study, III-V growth was carried out in a Thomas Swan metalorganic chemical vapor deposition (MOCVD) reactor, using H<sub>2</sub>-bubbled trimethylindium, H<sub>2</sub>-bubbled trimethylgallium, arsine and phosphine as gaseous precursors carried in a H<sub>2</sub> ambient. MOCVD growth of InGaP, GaP and InP has been extensively investigated, and our specific growth system and apparatus have been well documented<sup>40,92,94</sup>. A complete overview of MOCVD is given in Chapter 2. GeSi substrates are prepared as detailed in Chapter 4.

Prior to film deposition, the GeSi substrate is annealed at 750°C to induce the desired double-step surface morphology. Ideally, film growth proceeds in two stages:

### 1. Low-temperature initiation

The first few hundred angstroms of III-V film are deposited at a slow growth rate and low temperature. This is designed to limit adatom mobility and produce two-dimensional growth. However, the necessity of precursor pyrolysis in MOCVD growth places a lower limit on the initiation temperature. Past studies have found that

GaAs initiation at 400°C produces good quality films. Because phosphine cracks at a higher temperature than arsine,<sup>16</sup> we have chosen 500°C as the InGaP initiation temperature. It is hoped that this temperature will provide an adequate compromise between growth morphology and sufficient phosphine cracking and overpressure.

## 2. High-temperature growth

If two-dimensional growth is established, subsequent deposition may be carried out at high temperature and growth rates. Optimal InGaP growth has been observed between 600°C and 750°C, with degradation at higher and lower temperatures<sup>16,86</sup>. This may be related to the cracking of PH<sub>3</sub> and adsorption of P, which has been found to achieve maximum surface coverage at about 625°C<sup>96</sup>.

Growth rates on the order of 1 μm/hour or higher are common, making thick and/or complex structures practical for commercial production.

## 5.7 Results and Discussion

To investigate the lattice-matched integration of In<sub>0.3</sub>Ga<sub>0.7</sub>P directly on Ge<sub>0.7</sub>Si<sub>0.3</sub>, approximately thirty samples were prepared, grouped into the following categories:

### 1. Initiation Studies

In this section, we examine the slow deposition of an initial thin InGaP buffer on the GeSi substrate. A range of MOCVD conditions are explored to determine their impact on film quality.

### 2. Substrate Studies

In this section, GeSi substrate surface degradation prior to InGaP deposition is studied. The substrate is exposed to the ambient gases and thermal cycle of InGaP film initiation, without actual InGaP deposition. In this way, we are able to characterize the substrate surface morphology as it exists immediately to InGaP initiation.

### 3. Luminescence Studies

Finally, we characterize the visible wavelength luminescence of three-dimensional InGaP islands deposited on GeSi. Given the appropriate deposition conditions, we believe these islands may be scaled to a suitable size for use as quantum dot emitters.

### 5.7.1 Initiation Studies

Preliminary to the growth of InGaP device structures, we attempted to deposit high-quality, thin ( $\sim 500\text{\AA}$ ) InGaP buffers lattice-matched to GeSi. GeSi substrates are cleaned prior to deposition using a five-minute piranha clean followed by a one-minute HF dip. Accuracy of lattice-matching for all samples was confirmed via TAXRD calibrations of the GeSi substrate and of InGaP graded buffer samples on GaP. Initiation conditions and results are summarized in Table 5.2.

V/III ratio / Initiation Temperature	Low V/III Ratio ( $\sim 200$ )	High V/III Ratio ( $\sim 1000$ )
400°C	No deposition	No deposition
500°C	$\rho = 0.012 \mu\text{m}^{-2}$ $r \approx 3 \mu\text{m}$ Narrow distribution in island size	$\rho = 0.067 \mu\text{m}^{-2}$ $r \approx 1 \mu\text{m}$ Narrow distribution in island size
700°C	$\rho = 2.44 \mu\text{m}^{-2}$ $r \approx 0.1\text{-}0.25 \mu\text{m}$ Wide distribution in island size	$\rho = 2.66 \mu\text{m}^{-2}$ $r \approx 0.2\text{-}0.5 \mu\text{m}$ Wide distribution in island size

**Table 5.2. Nucleation of  $\text{In}_{0.3}\text{Ga}_{0.7}\text{P}$  on  $\text{Ge}_{0.7}\text{Si}_{0.3}$  by MOCVD.**

Volmer-Webber-type three-dimensional growth, as shown in Figure 5.5, was observed for all nucleation conditions. For low-temperature initiation, InGaP island formation shows a strong dependence on V/III ratio, with a tight distribution in island size. Island density increased with V/III ratio, while the typical island radius decreased. This is probably the result of suppression by the large Group V overpressure of the already low adatom mobility at the surface, leading to a smaller nucleus size<sup>97,98</sup>. High-temperature initiation produced a dense array of small islands over a range of V/III ratios; however, the size distribution broadened considerably. The observation of smaller islands at a higher growth temperature is unexpected, since an island formation process governed by adatom mobility would produce larger islands as temperature and mobility increase. However, more frequent In adsorption/desorption events at high temperature, resulting from a lower In sticking coefficient, provide an alternative path for adatom redistribution<sup>14</sup>. The results in Table 5.2 indicate that this phenomenon dominates over surface diffusion at high initiation temperature. This conclusion is supported by the

observation that island density and size are nearly independent of V/III ratio at high deposition temperature.

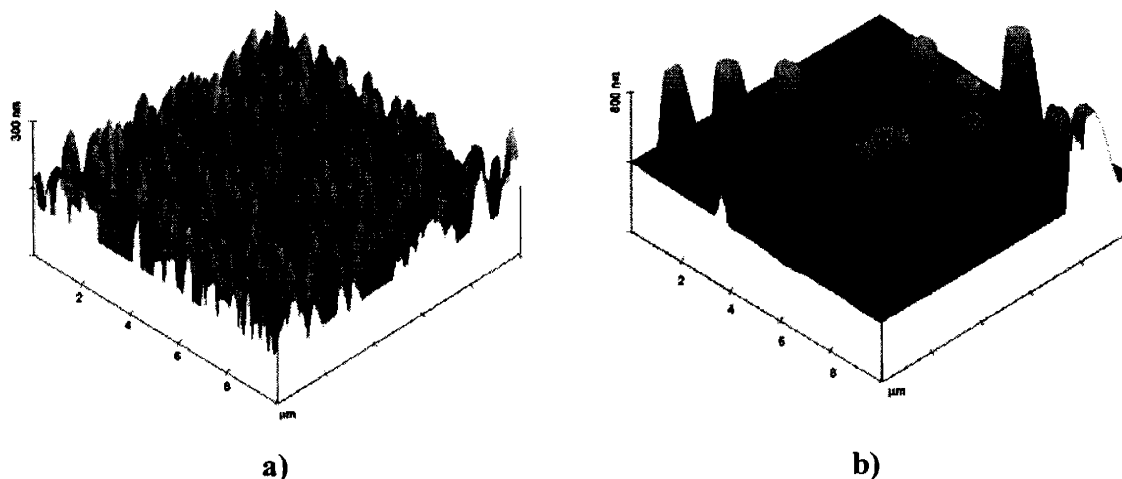


**Figure 5.5.** a) PV-AFM image of  $\text{In}_{0.3}\text{Ga}_{0.7}\text{P}$  on  $\text{Ge}_{0.7}\text{Si}_{0.3}$ , initiated at  $T=700^\circ\text{C}$  and  $V/\text{III} = 1000$ . Target InGaP thickness =  $500\text{\AA}$ . Maximum island height = 300 nm; b) PV-AFM image of  $\text{In}_{0.3}\text{Ga}_{0.7}\text{P}$  on  $\text{Ge}_{0.7}\text{Si}_{0.3}$ , initiated at  $T=500^\circ\text{C}$  and  $V/\text{III} = 1000$ . Target InGaP thickness =  $500\text{\AA}$ . Maximum island height = 675 nm.

Given longer initiation times, the InGaP film does coalesce, but forms a poor-quality polycrystalline film not suitable for optical device growth, shown in Figure 5.6.

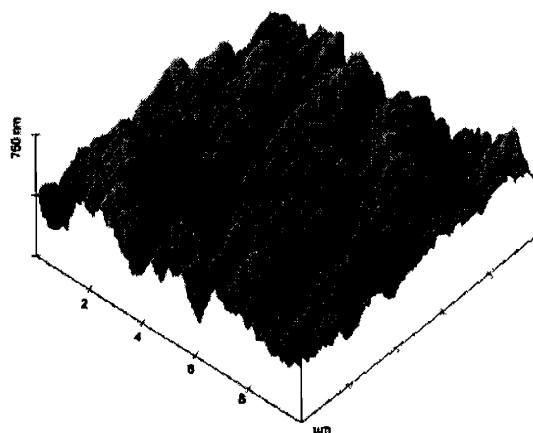


**Figure 5.6.** PV-AFM image of  $\text{In}_{0.3}\text{Ga}_{0.7}\text{P}$  on  $\text{Ge}_{0.7}\text{Si}_{0.3}$ , initiated at  $T=500^\circ\text{C}$  and  $V/\text{III} = 1000$ . Target InGaP thickness = 500nm, RMS = 167 nm.

## 5.7.2 Substrate Studies

We would like to identify or eliminate the GeSi substrate surface as the source of 3-D nucleation and of the discouraging results described above. Non-uniformities in the mixed  $\text{Ge}_{0.7}\text{Si}_{0.3}$  surface may arise, particularly at the high Ge fractions required for this study. Degradation of the GeSi surface may arise from non-uniform etching during pre-deposition cleaning or from in situ thermal cycling and etching during MOCVD growth in a  $\text{H}_2$  or  $\text{H}_2$  plus  $\text{PH}_3$  ambient.

### 5.7.2.1 Pre-deposition Cleaning

As previously described,  $\text{Ge}_{0.7}\text{Si}_{0.3}$  substrates were prepared for MOCVD growth by cleaning with a standard Piranha etch followed by a one minute dilute HF dip. The Piranha etch time was varied from five minutes to fifteen minutes. A standard Ge etch was also examined. Thin InGaP films were deposited using high temperature and high V/III ratio initiation conditions.

All resulting films exhibit three-dimensional growth and are extremely rough, as shown in Figure 5.7 for two of the cases examined.

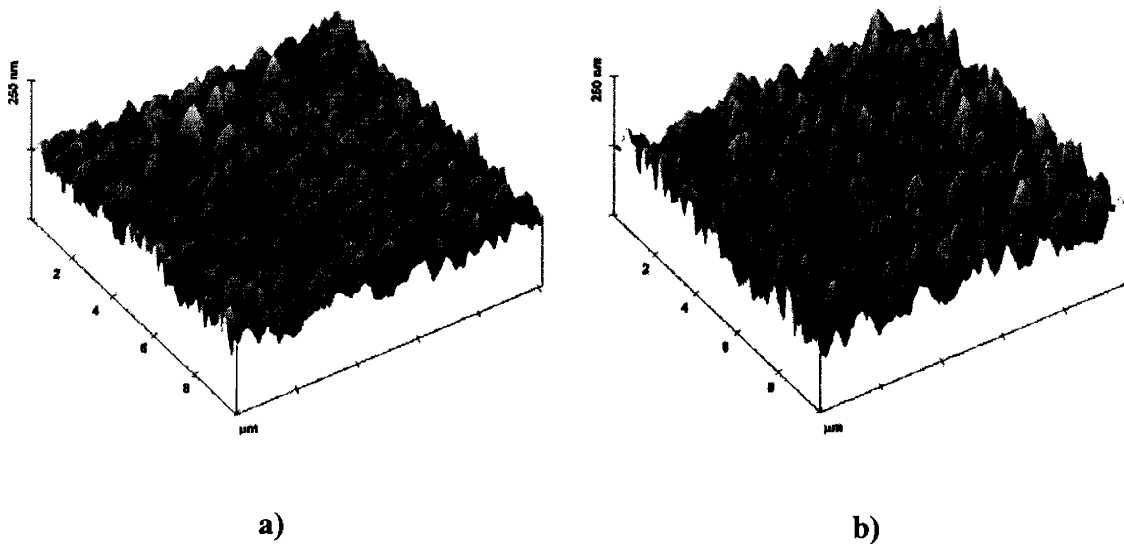


**Figure 5.7. PV-AFM images of  $\text{In}_{0.3}\text{Ga}_{0.7}\text{P}$  on  $\text{Ge}_{0.7}\text{Si}_{0.3}$ , initiated at  $T=700^\circ\text{C}$  and  $V/\text{III} = 1000$ . Target InGaP thickness = 300nm. a) 5 min Piranha clean; RMS = 28 nm, and b) 10 min Piranha clean; RMS = 32 nm.**

These results suggest that the quality of InGaP growth is not strongly affected by the GeSi cleaning method. This conclusion is supported by AFM scans of the bare GeSi substrate before and after cleaning, which show negligible change in surface structure and roughness.

As a final test for the effect of substrate cleaning,  $\text{In}_{0.22}\text{Ga}_{0.78}\text{P}$  was deposited lattice-matched to  $\text{Ge}_{0.5}\text{Si}_{0.5}$ . High-quality regrowth of GeSi on CMPed  $\text{Ge}_{0.5}\text{Si}_{0.5}$  is commonly achieved<sup>38</sup>, so we would expect no surface degradation to arise from cleaning. As shown below in Figure 5.8, poor InGaP film quality results even for deposition on  $\text{Si}_{0.5}\text{Ge}_{0.5}$ .

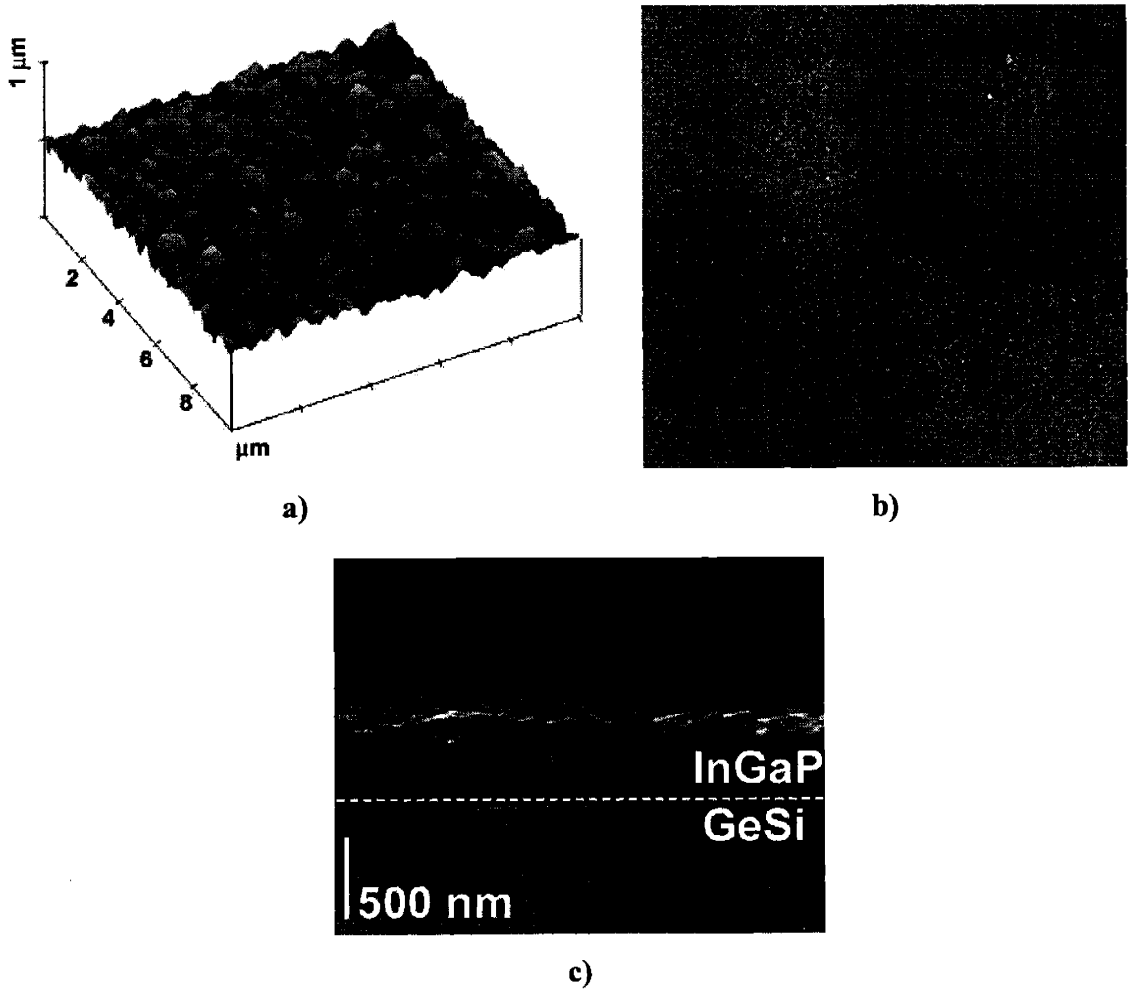


**Figure 5.8.**  $\text{In}_{0.22}\text{Ga}_{0.78}\text{P}$  on  $\text{Ge}_{0.5}\text{Si}_{0.5}$ , initiated at  $T=700^\circ\text{C}$  and  $V/\text{III} = 1000$ . Target InGaP thickness = 800nm; RMS = 58nm. a) PV-AFM; b) Nomarski; c) cross-section SEM.

As confirmed via TAXRD of the substrate and of a thick  $\text{In}_{0.22}\text{Ga}_{0.78}\text{P}$  calibration layer deposited on  $\text{V}_x[\text{In}_x\text{Ga}_{1-x}\text{P}]/\text{GaP}$ , we expect the InGaP film and GeSi substrate to have a lattice mismatch of less than 0.05%. Despite this precise lattice-matching and the expectation of a high-quality substrate surface, the three-dimensional growth morphology shown in Figure 5.8 is clearly undesirable. The composition of the coalesced polycrystalline InGaP film was approximately determined using SIMS, shown in Figure 5.9. The accuracy of the SIMS measurement will be greatly reduced due to the roughness of the film; however, the SIMS profile may suggest one source for the observed difficulties with monolayer growth. While the desired InGaP composition is achieved near the sample surface, In fraction appears to decrease sharply near the interface with GeSi. This would lead to a tensile strain of roughly 0.12% at the interface. Any initial wetting layer would subsequently experience nearly 0.17% compressive strain during the next 100 nm to 200 nm of deposition. While the magnitudes of these stresses are relatively small, it is sufficient to lead to InGaP film degradation, as noted above. It is also unknown precisely how any stresses will be accommodated at the heterovalent interface. However, given the rough film, it must be noted that the apparent suppression of indium incorporation at the GeSi substrate, shown in Figure 5.9, may simply be a measurement artifact, and further confirmation of this effect is required.

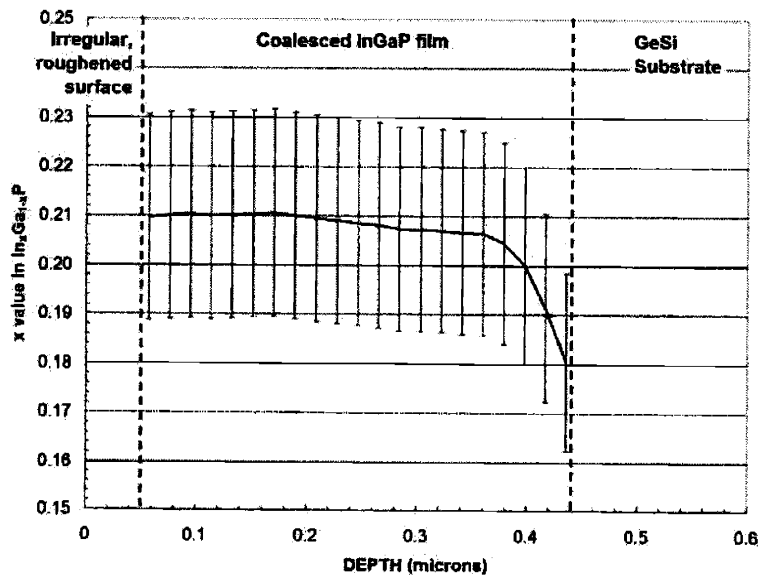
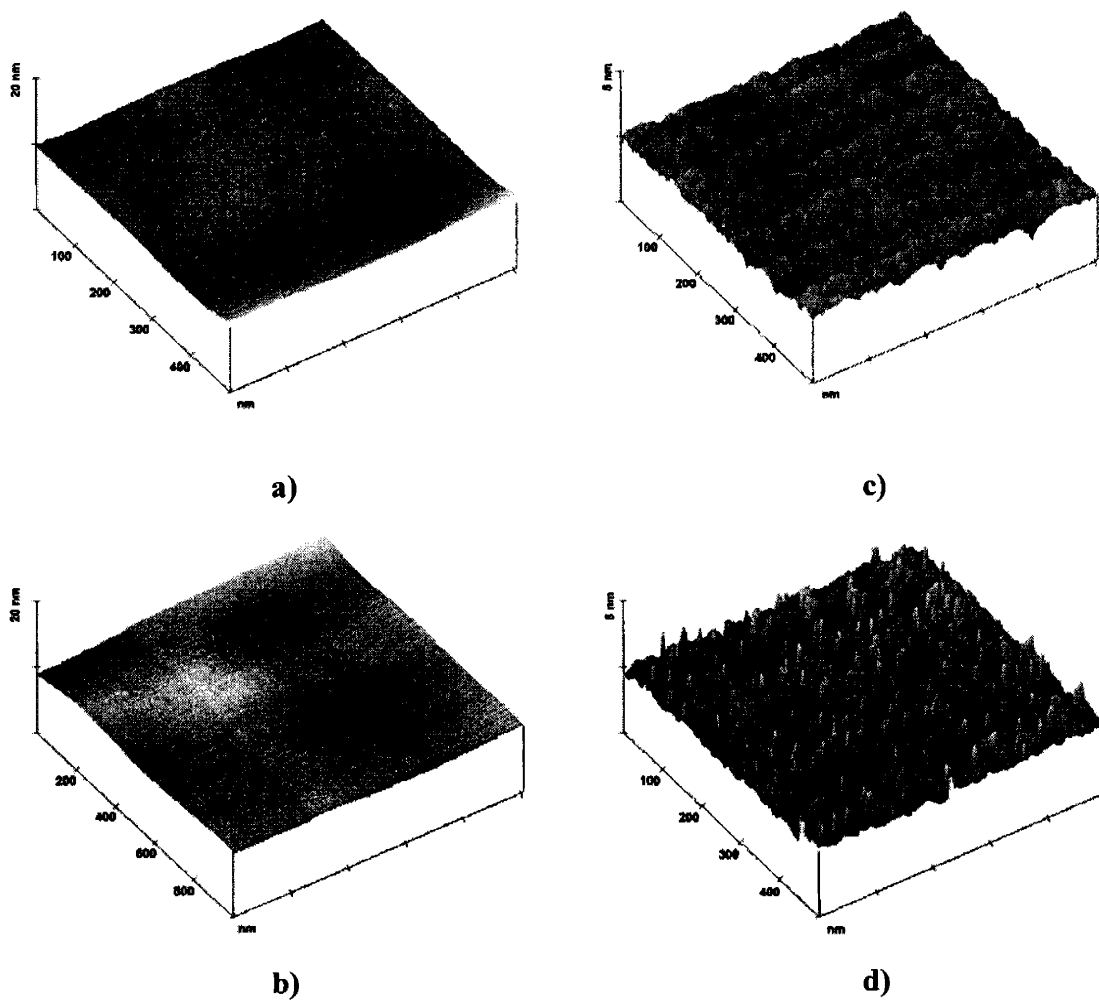


Figure 5.9. SIMS analysis of  $\text{In}_{0.22}\text{Ga}_{0.78}\text{P}$  on  $\text{Ge}_{0.5}\text{Si}_{0.5}$ ; images of this sample shown in Figure 5.8.

### 5.7.2.2 *In-situ* Surface Degradation

Bare GeSi substrates were taken through the thermal cycle of a standard 500°C InGaP initiation in the presence of N<sub>2</sub> only, H<sub>2</sub> only, and H<sub>2</sub> plus PH<sub>3</sub>. Substrates are annealed for 5 minutes at 350°C to remove water vapor and organics, followed by annealing at 750°C for 10 minutes to desorb surface oxides and produce the desired surface-step reconstruction, before being brought to the InGaP initiation temperature. AFM images of these samples are shown in Figure 5.10.



**Figure 5.10.** PV-AFM images of Ge<sub>0.7</sub>Si<sub>0.3</sub> before and after thermal cycling in MOCVD hydride ambient. a) Before thermal cycling, RMS ~ 0.17 nm, b) After cycling in N<sub>2</sub> only, RMS ~ 0.2 nm (note change in image scale), c) After cycling in H<sub>2</sub> only, RMS = 0.25 nm and d) After cycling in H<sub>2</sub> plus PH<sub>3</sub>, RMS = 0.88 nm.



In the case of annealing in a N<sub>2</sub> ambient, AFM reveals negligible change in the surface structure and roughness. After annealing in H<sub>2</sub> only, surface roughness increases only slightly. However, annealing in a H<sub>2</sub> plus PH<sub>3</sub> ambient produces 5 nm x 5 nm x 2.5 nm mesas at a density of 900 μm<sup>-2</sup>. These features may be P clustering on the substrate surface, or a GeP compound formed in conjunction with preferential etching of GeSi by H<sub>2</sub>, as discussed below. They may also reflect the formation of surface oxides as a result of water vapor in the deposition system. If these features form prior to the initial deposition of InGaP, they will provide heterogeneous nucleation sites that would disrupt monolayer growth. This may be an important source of poor epitaxial film quality.

Thermodynamic simulations, while not an accurate representation of the surface-driven processes that dominate in MOCVD, can hint at origins of the behavior illustrated above. For the purposes of thermodynamic analysis, using the Thermocalc software package, we considered a closed system at equilibrium containing the volume of gas introduced into the reactor in one minute. To approximate the dynamic system in the reactor, it was assumed that this volume of gas reaches equilibrium instantaneously in the closed system and is removed after one minute and replaced by a new volume of gas. In our system, the H<sub>2</sub> carrier is always present in excess; therefore, the overall quantity of gas in the system was approximated by the volume of H<sub>2</sub>, disregarding the presence of any Group V hydrides. Initial conditions for gas flow rates were 5000 sccm for H<sub>2</sub> and 5-100 sccm of PH<sub>3</sub>. The initial substrate quantity was taken to be 0.025 moles, equivalent to a 1 cm x 1 cm x 2 mm piece of GeSi.

Etch gas speciation for H<sub>2</sub>(g) over Ge<sub>0.7</sub>Si<sub>0.3</sub>(s) is illustrated in Figure 5.11.

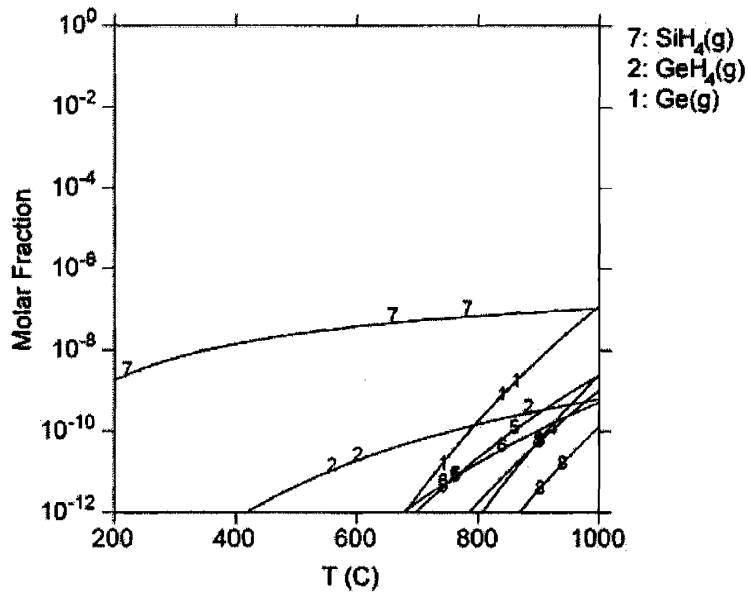


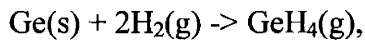
Figure 5.11. Thermodynamically predicted gas-phase etch products for  $H_2(g)$  over  $Ge_{0.7}Si_{0.3}$ .

The important overall etching reactions in this system appear to be:



with a small contribution from

$$\text{Equation 5.3}$$



below  $800^\circ C$ .

Silane production is significant above about  $\sim 400^\circ C$ , while Ge sublimation becomes important only above  $\sim 900^\circ C$ . The total outcome of etching occurring in this system is best illustrated in Figure 5.12, which gives the moles of atomic constituents in each phase.

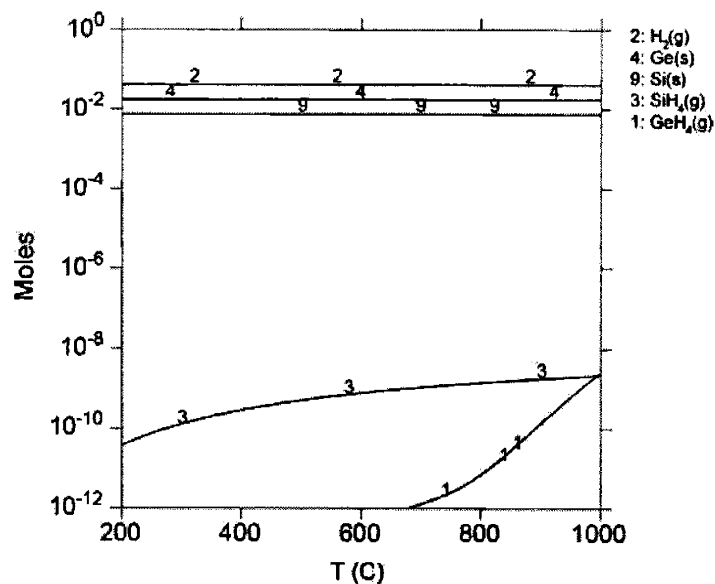


Figure 5.12. Thermodynamically predicted gas- and solid-phase etch products for  $H_2(g)$  over  $Ge_{0.7}Si_{0.3}$ .

The total amount of substrate material in the equilibrium gas phase is equivalent to the net etching in the system. Therefore, the curves that represent the quantities of Si and Ge in the gas give the dependence of etch rate on temperature. The etch data taken from Figure 5.12 are summarized in Table 5.3.

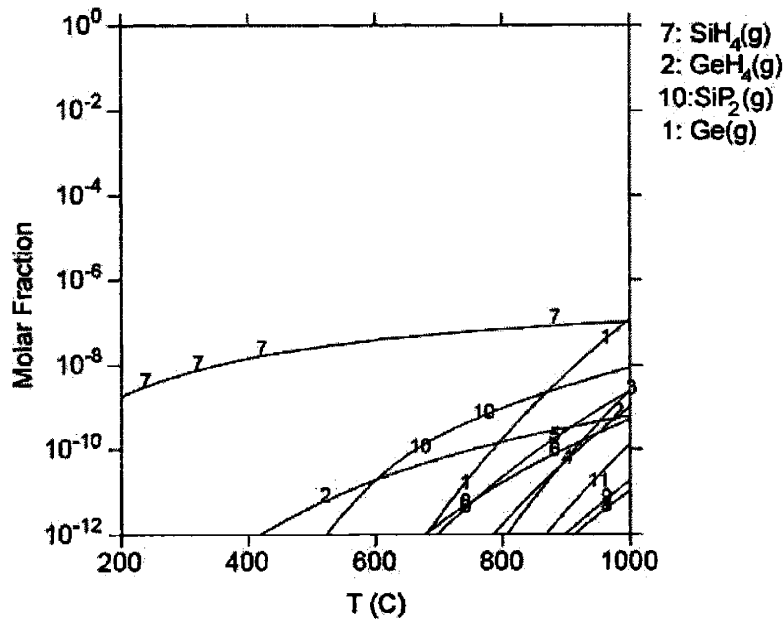
Temperature (°C)	400	600	800
Moles of Si in gas	$\sim 5 \times 10^{-10}$	$\sim 10^{-9}$	$\sim 5 \times 10^{-9}$
Etch rate of Si (monolayers/min)	0.5	1	5
Moles of Ge in gas	$\sim 10^{-15}$	$\sim 10^{-13}$	$\sim 10^{-11}$
Etch rate of Ge (monolayers/min)	$10^{-6}$	$10^{-4}$	0.01

Table 5.3. Thermodynamically predicted etch rates for  $H_2$  over  $Ge_{0.7}Si_{0.3}$ .

Silicon etching becomes important above  $400^\circ C$ , while Ge is never etched to a significant degree. Thermodynamic simulations of this process indicate the potential for preferential removal of Si atoms from the alloy surface in the form of  $SiH_4$ , as shown in Figure 5.12. This will lead to an excess concentration of Ge on the surface and an

increase in surface roughness. Similar results have been reported by Segala, et al<sup>99</sup>. The data indicate that it would be advisable to initiate H<sub>2</sub>(g) flow at low temperatures, while N<sub>2</sub> could be used as the carrier at higher temperatures.

Etch gas speciation for H<sub>2</sub>(g) + PH<sub>3</sub>(g) over Si<sub>0.3</sub>Ge<sub>0.7</sub> is shown in Figure 5.13.



**Figure 5.13. Thermodynamically predicted gas-phase etch products for H<sub>2</sub>(g) plus PH<sub>3</sub>(g) over Ge<sub>0.7</sub>Si<sub>0.3</sub>.**

Comparison of Figure 5.13 and Figure 5.11 underscores the production of an additional etch gas phase, SiP<sub>2</sub>, in the presence of PH<sub>3</sub>, and the additional reaction:



SiP<sub>2</sub> is present in substantial quantities for elevated PH<sub>3</sub> flow rates (P mole fraction) and temperature, as indicated in Figure 5.14.

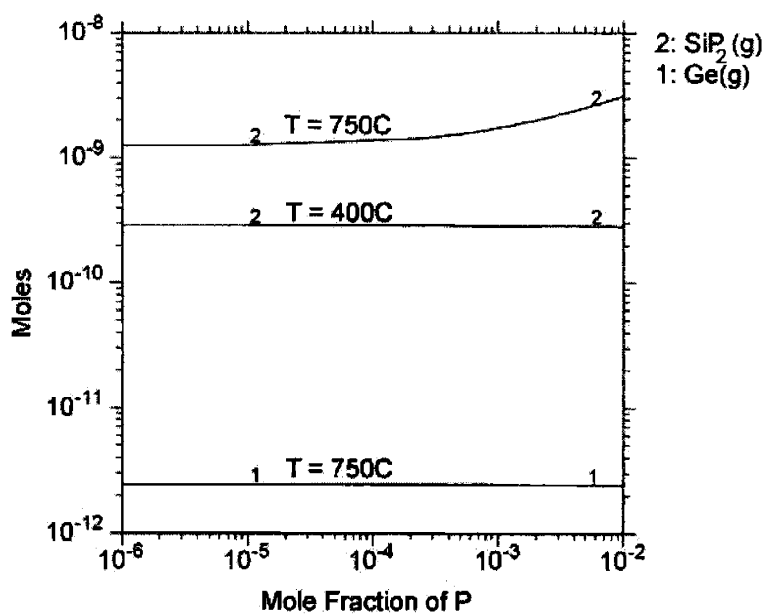


**Figure 5.14. Variation of  $\text{SiP}_2(\text{g})$  production with temperature and P for  $\text{H}_2(\text{g})$  plus  $\text{PH}_3(\text{g})$  over  $\text{Ge}_{0.7}\text{Si}_{0.3}$ .**

The total production of etching in this system is given by Figure 5.15. Comparison of Figure 5.15 and Figure 5.12 indicates that a low P content has little or no effect on the etch rates in the system, and the etching conditions are again those established by the  $\text{H}_2(\text{g})$  in the system. However, Figure 5.14 shows that high P content combined with high temperature may increase Si etching by a few monolayers per minute. This effect increases the disparity between Si and Ge etching, leading to further detrimental effects on the surface morphology. Thus, large  $\text{PH}_3(\text{g})$  flows and high temperatures should be avoided until after a film has nucleated and coated the substrate surface, protecting it from further interaction with the precursor gases.

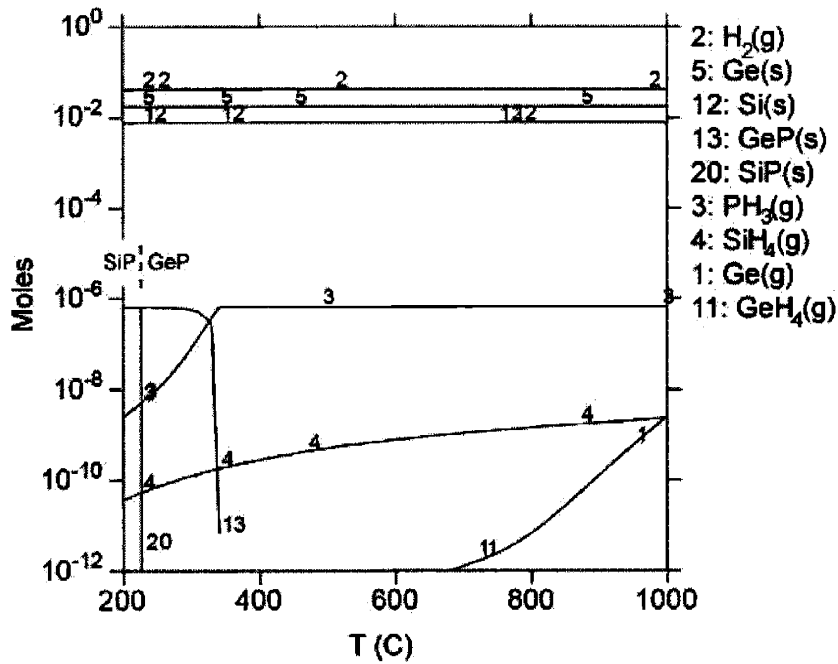
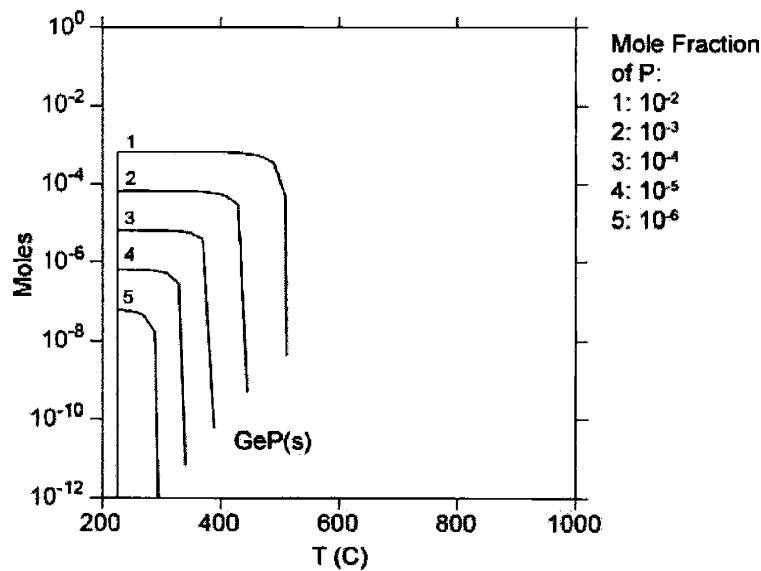


Figure 5.15. Thermodynamically predicted gas- and solid-phase etch products for  $H_2(g)$  plus  $PH_3(g)$  over  $Ge_{0.7}Si_{0.3}$ .

The creation of surface alloys in the  $H_2(g)$  plus  $PH_3(g)$  system is apparent in Figure 5.15. In this system, both  $SiP(s)$  and  $GeP(s)$  alloys are created. However, these phases are in direct competition with one another, as shown by the disappearance of  $SiP(s)$  at  $\sim 230^\circ C$  and the appearance of an equal quantity of  $GeP(s)$  at that temperature. Under real growth conditions, temperatures above  $500^\circ C$  are required for significant decomposition of  $PH_3(g)$ ; thus, this  $SiP(s)$  phase likely never forms. The dependence of  $GeP(s)$  nucleation on temperature and quantity of P is given in Figure 5.16. The P is completely incorporated in the  $GeP(s)$  alloy up to a certain temperature, above which  $GeP$  nucleation ceases.



**Figure 5.16. Thermodynamically predicted GeP(s) formation for  $H_2(g)$  plus  $PH_3(g)$  over  $Ge_{0.7}Si_{0.3}$ , illustrating complete consumption of available P.**

It should be noted that the validity of thermodynamic predictions as applied to MOCVD growth conditions is limited, and the processes described above are simply suggestive of what may be occurring at the film/substrate interface during deposition. The presence of water vapor and organic contaminants in the MOCVD chamber may result in oxide- or organic-GeSi complexes, particularly germanium oxides, that could also lead to the observed surface degradation. A scanning surface analysis technique, such as STM, could possibly identify the mesas observed in Figure 5.10d and suggest the necessary means to eliminate them.

Standard polar-on-non-polar epitaxy is initiated under a Group V ambient in order to create a uniform surface layer and suppress APB formation, as discussed above. It may be that, in the case of a mixed GeSi surface, suppression of anti-phase boundaries and establishment of monolayer growth demand conflicting initiation conditions. Single-crystal epitaxy of InGaP on GeSi will require us to map a complex initiation phase space. We must deconvolve the factors that may be inhibiting monolayer growth, including polar-on-non-polar epitaxy, and the effects on MOCVD growth of interface chemistry between the ternary III-V and Ge-rich GeSi.

### 5.7.3 Luminescence Studies

While undesirable from the standpoint of thin-film device growth, the three-dimensional nucleation observed for InGaP/GeSi epitaxy may present interesting opportunities for quantum dot emitters. The inherent tendency of lattice-mismatched III-V semiconductors toward self-assembled Stranski-Krastinov (SK) growth has generated interest in their potential quantum dot applications<sup>97</sup>. The use of quantum dot active layers is not simply a means to overcome the difficulties attached to mismatched and polar-on-nonpolar epitaxy. The effects of quantum confinement are expected to be quite favorable, particularly in quantum dot lasers, leading to a low threshold current, high characteristic temperature, and high differential gain<sup>100</sup>. For LED applications, quantum confinement can be expected to increase the emission energy gap, providing access to shorter wavelengths than in conventional bulk growth<sup>101,102</sup>. Efficient quantum dot emitters on Si could provide an alternate path to OEIC heterointegration.

Micic, *et al.*<sup>102</sup> fabricated GaP and In<sub>0.5</sub>Ga<sub>0.5</sub>P quantum dots in colloidal suspension with diameters of 2 nm to 8 nm. As a result of quantum confinement, the GaP bandgap becomes direct for dot diameters less than 2 nm, and relatively strong PL at 520 nm is observed. For 2.5 nm In<sub>0.5</sub>Ga<sub>0.5</sub>P dots, emission at 540 nm is observed; this is a blueshift of more than 0.7 eV from the predicted bulk emission. Lee, *et al.*<sup>101</sup> fabricated an SK In<sub>0.5</sub>Ga<sub>0.5</sub>P quantum dot active layer on a Si substrate, using a GaP wetting layer and a GaP upper clad. They report emission at 630 nm, a blueshift of roughly 0.1 eV from the bulk energy gap. Finally, Walter, *et al.*<sup>103</sup> coupled an InGaP quantum well carrier confinement layer to an InP quantum dot active layer, achieving 300K continuous wave laser operation with wavelengths between 656 nm and 670 nm.

In an effort to nucleate InGaP quantum dots on GeSi, approximately 50 nm of In<sub>0.42</sub>Ga<sub>0.58</sub>P is deposited on Ge<sub>0.7</sub>Si<sub>0.3</sub> at a relatively low temperature of 500°C and high V/III ratio of 1000. The low growth temperature and high V/III ratio are chosen to produce islands with a narrow distribution in size, while the larger In fraction should improve the internal quantum efficiency of the luminescent dots. A narrow distribution is desirable for light emitter applications, as it reduces spectral broadening<sup>104</sup>. Cathodoluminescence (CL) of In<sub>0.42</sub>Ga<sub>0.58</sub>P islands on GeSi reveals several emission peaks, the largest at 618 nm, while a bare GeSi substrate shows no emission, as shown in



Figure 5.17. Assuming fully relaxed InGaP islands, the predominant 618 nm emission in Figure 5.17a is consistent with  $\text{In}_{0.41}\text{Ga}_{0.59}\text{P}$ . Other peaks roughly correspond to relaxed  $\text{In}_{0.32}\text{Ga}_{0.68}\text{P}$ ,  $\text{In}_{0.34}\text{Ga}_{0.66}\text{P}$ , and  $\text{In}_{0.39}\text{Ga}_{0.61}\text{P}$ . The presence of phases with lower In fraction suggests that the phenomenon observed in Figure 5.9 for the deposition of  $\text{In}_{0.22}\text{Ga}_{0.78}\text{P}$  on  $\text{Ge}_{0.5}\text{Si}_{0.5}$  is also occurring here. The weak, shorter-wavelength peaks may originate from the In-poor regions near the InGaP/GeSi interface. The run-to-run reproducibility of this lineshape when V/III ratio is varied suggests a consistent indium incorporation profile among samples.

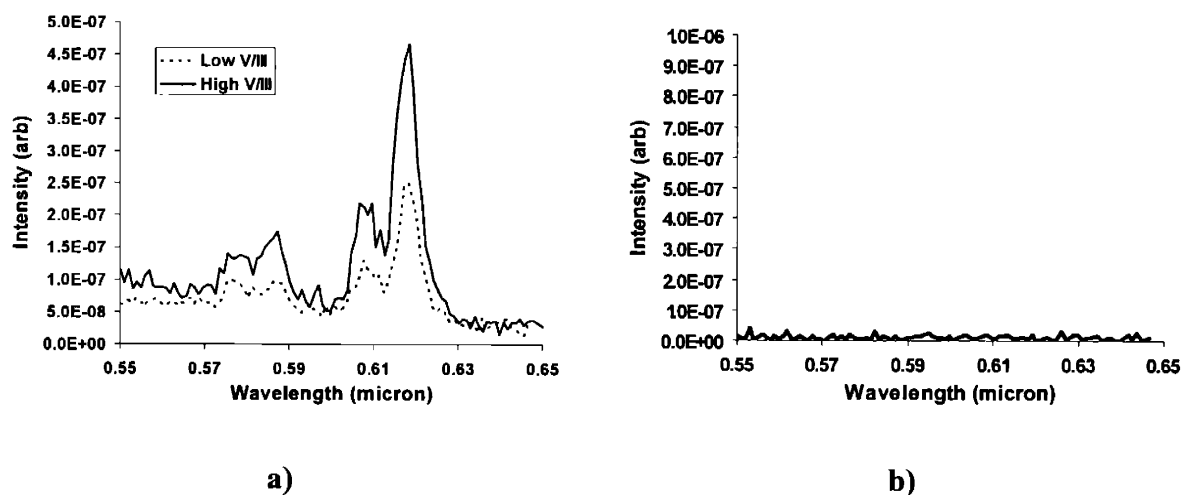


Figure 5.17. CL emission from a) InGaP islands and b) bare GeSi substrate.

The three-dimensional island growth shows a distinctive radial growth habit, indicating point-like nucleation at the center of each island, as shown in Figure 5.18. AFM and TEM images indicate an island density of about  $0.1 \mu\text{m}^{-2}$ , with a radius of  $1 \mu\text{m}$  and a 1:1 aspect ratio. This is volumetrically equivalent to the deposition of a 140 nm thick InGaP thin film, nearly three times greater than anticipated, probably the result of inaccurate growth rate projections for the growth temperature. However, given the observed point-like nucleation, and assuming island size scales with growth rate and time, future studies may demonstrate the ability to produce true InGaP quantum dots on GeSi. The dramatic increase in island density and decrease in size observed at higher

temperatures may prove useful for the production of quantum dot emitters, assuming that the size distribution issues can be addressed.

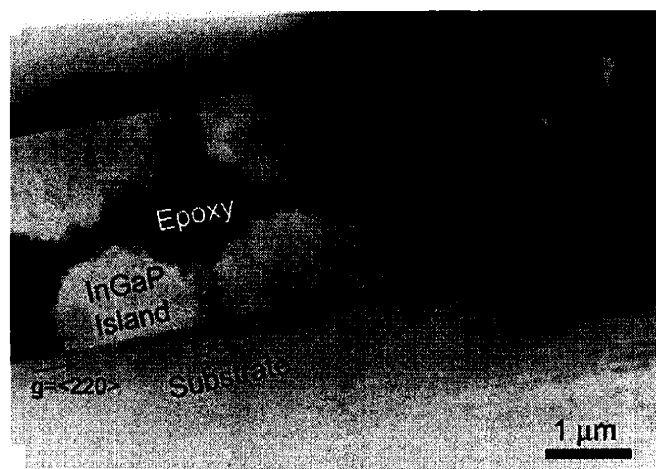


Figure 5.18. XTEM of  $\text{In}_{0.42}\text{Ga}_{0.58}\text{P}$  islands on  $\text{Ge}_{0.7}\text{Si}_{0.3}$ , initiated at  $T=500^\circ\text{C}$  and  $V/\text{III} = 1000$ .

## 5.8 Conclusions

Initial modes of InGaP lattice-matched epitaxy on GeSi are described above. Three-dimensional growth is observed under all MOCVD conditions, comprising temperatures from  $400^\circ\text{C}$  to  $700^\circ\text{C}$  and  $V/\text{III}$  ratios from 200 to 1000. Island nucleation density was found to vary directly with  $V/\text{III}$  ratio at low growth temperature, while island radius shows a concomitant inverse relationship. Island density and size were relatively independent of  $V/\text{III}$  ratio at high growth temperature. Island size distribution is reduced at low growth temperatures. Pre-growth substrate cleaning led to no degradation of the surface morphology, so inhomogeneities arising from preferential wet etching were eliminated as a source of three-dimensional nucleation.

The effects of substrate thermal cycling in  $\text{N}_2$ ,  $\text{H}_2$ , and  $\text{H}_2$  plus  $\text{PH}_3$  were examined. No surface degradation was observed for a  $\text{N}_2$  ambient, while a slight increase in surface roughness occurred for a  $\text{H}_2$  ambient. Thermal cycling in  $\text{H}_2$  plus  $\text{PH}_3$  led to a large increase in surface roughness and the formation of surface mesas. Thermodynamic calculations suggest that these mesas may be P clusters or GeP solid complexes. They may also be surface oxides. The creation of such a rough surface prior to the initiation of epitaxy would certainly interfere with monolayer growth. It is possible that this effect

could be mitigated by a modified gas switching sequence and/or the use of N<sub>2</sub> as the carrier. In addition, SIMS and CL data indicate that the incorporation of In into the InGaP film may be suppressed at the GeSi interface relative to incorporation rates observed for InGaP homoepitaxy, leading to a compositional gradient in the film and strain levels capable of disrupting epitaxy.

Finally, the luminescent properties of the observed InGaP islands are examined with an eye to creating InGaP quantum dot emitters on GeSi. Emission from the islands is clearly observed; however, compositional variations in the InGaP islands lead to extremely poor color purity. The observed initial growth modes and island distributions show promise for implementation in quantum dot emitters; however, to date no semiconductor quantum dot emitters have proven to be competitive with established thin-film LED technologies.



## 6 Mechanisms of Branch Defect Formation

### 6.1 Introduction

Indium aluminum gallium phosphide (InAlGaP) is currently the material of choice for light emitting diodes (LEDs) operating in the wavelength range of 590 nm (amber) to 630 nm (red). Intensities of industrially produced InAlGaP-based LEDs range from 63-24100 mcd @ 20 mA for amber devices and from 40-31000 mcd @ 20 mA for red devices<sup>105,106</sup>. (Candela, or cd, is a common measure of device intensity, where one candela equals one lumen per steradian. That is, the total flux of a uniform one candela source is  $4\pi$  lumens. The lumen, a measure of luminous flux, should not be confused with lumens/watt, a measure of luminous efficiency or efficacy.) To satisfy lattice-matching constraints, illustrated in Figure 3.3, devices have historically consisted of  $\text{In}_{0.5}(\text{Al}_y\text{Ga}_{1-y})_{0.5}\text{P}$  devices deposited on GaAs substrates<sup>5</sup>. Though considered unavoidable, this constraint led to large extraction losses due to absorption by the GaAs substrate. Recently, this problem has been addressed by etching away the GaAs substrate after LED growth, followed by wafer bonding of the device to a transparent GaP substrate<sup>7,107,108</sup>. This technology produces large gains in luminous intensity; however, substrate removal and wafer bonding can be cumbersome and detrimental to overall device economy.

Another solution to the absorbing-substrate problem is lattice-mismatched epitaxy. Using relaxed, compositionally graded buffer technology, we can bridge the gap between the lattice constant of a GaP substrate and that of the InGaP or InAlGaP active region<sup>37,40,43</sup>. Beginning with a GaP substrate, a  $\nabla_x[\text{In}_x\text{Ga}_{1-x}\text{P}]$  buffer is deposited in thin layers of increasing indium fraction. Misfit dislocations are nucleated at the first mismatched interface to relieve strain and are then recycled throughout the buffer, obviating the need for further dislocation nucleation. InGaP buffers grown in this manner in our 1"-substrate research reactor have threading dislocation densities on the order of  $10^6 \text{ cm}^{-2}$ , low enough for good light-emitting devices<sup>40,43</sup>. When the desired final

composition is reached, a thick constant composition cap layer is grown, as shown in Figure 6.1; device layers may be grown on top of this cap.

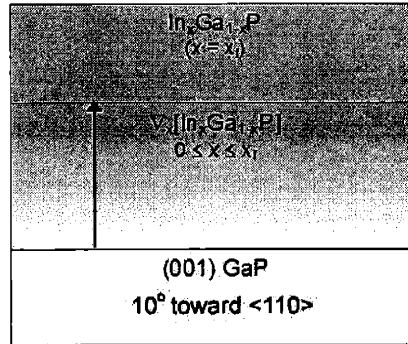


**Figure 6.1. Schematic of the InGaP relaxed, graded buffer deposited via MOCVD.**

Work in the GaAs system indicates that carrier diffusion length approaches defect spacing at a threading dislocation density of around  $1 \times 10^6 \text{ cm}^{-2}$ <sup>109</sup>. This suggests that an InGaP or InAlGaP visible device may be deposited on a  $\nabla_x[\text{In}_x\text{Ga}_{1-x}\text{P}]/\text{GaP}$  platform to yield a high-quality emitter that is epitaxially integrated on a transparent substrate. The work presented here seeks to optimize the microstructural properties of the relaxed, graded-InGaP buffer to further improve epitaxial transparent substrate-LEDs (ETS-LEDs).

## 6.2 Branch Defects in InGaP

Previous work by Kim<sup>40</sup> examined the “branch defect” in the InGaP system. Microstructures resembling branch defects have also been observed in the InGaAs system<sup>110</sup>, but the origins of this phenomenon have not been extensively examined. Kim maps out a branch defect “phase diagram”, shown in Figure 6.2, in which the indium fraction in the film at the onset of defect formation varies with growth temperature.

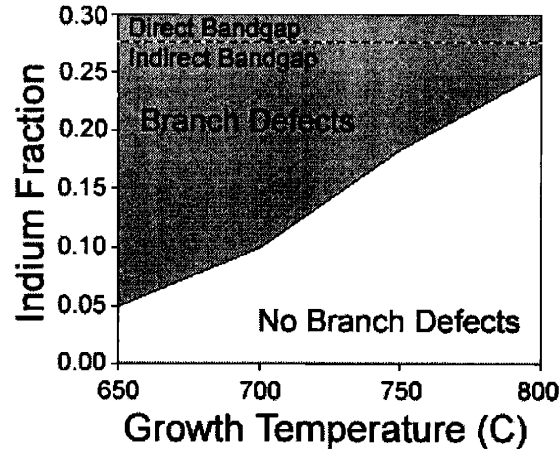


**Figure 6.2. Branch defect formation regimes for MOCVD grown InGaP<sup>40</sup>. Note that the direct bandgap to indirect bandgap crossover for InGaP lies within the branch defect regime.**

The ability of existing branch defects to pin dislocations, termed their “strength”, is found to depend on the indium fraction at which the branch defects nucleate. At high growth temperatures and small indium fraction, the nucleation of branch defects is suppressed. However, when a sufficiently large indium fraction is reached at high growth temperatures, branch defect formation becomes favorable. Branch defects that form under high temperature conditions tend to be widely spaced and to strongly pin threading dislocations. Conversely, low growth temperatures favor the formation branch defects at a smaller indium fraction. In the low temperature case, the density of branch defects increases, but their interaction with threading dislocations is weak. Empirical evidence shows that the presence of these defects in InGaP- and InAlGaP-based visible light emitting diodes leads to a decrease in device intensity<sup>40</sup>. Branch defects are observed to pin gliding threads, as seen in Figure 6.3, leading to threading dislocation multiplication and an increase in potential non-radiative recombination sites. Similar dislocation pileup mechanisms have been identified in the  $\nabla_x[\text{Ge}_x\text{Si}_{1-x}]$  system<sup>38,39</sup>. The detrimental effects described above prompt our interest in characterizing and eliminating this microstructural defect.



PVTEM

800°C, 2° Offcut,  $x_{In}=0.15$

Figure 6.3. Threading dislocations pinned on a branch defect.

## 6.3 InGaP Graded Buffers Produced using an Industrial MOCVD Reactor

### 6.3.1 Background

In collaboration with Lumileds Lighting, LLC, we have been able to compare branch defect characteristics of material grown at MIT<sup>40</sup> with those of material grown in an industrial system. Four InGaP graded buffer samples were produced under various deposition conditions, summarized in Table 6.1, in a Lumileds LP-MOCVD reactor.

Sample ID	Substrate Offcut (° towards <110>)	Growth Temperature (°C)	$x_{In}$ in Cap
LL2	2	800	0.15
LL8	2	650	0.14
LL5	10	800	0.16
LL11	10	650	0.14

Table 6.1. Description of samples provided by Lumileds Lighting.



The primary variables for sample deposition were growth temperature and substrate offcut. The substrate material was (001) GaP misoriented  $10^\circ$  toward the nearest  $\langle 110 \rangle$ . All InGaP buffers were nominally graded to and capped with a layer of  $\text{In}_{0.15}\text{Ga}_{0.85}\text{P}$ . A summary of the data extracted from the Lumileds  $\text{InGaP}/\nabla_x[\text{In}_x\text{Ga}_{1-x}\text{P}]/\text{GaP}$  samples is presented in Table 6.2. To compare phenomena observed in a commercial reactor setting to the MIT research reactor and environment, data from comparable samples grown by atmospheric-pressure MOCVD at MIT<sup>40</sup> is summarized in Table 6.3.

Sample ID	Branch Defects ( $\mu\text{m}^{-1}$ )	$\rho_{\text{TD}}$ ( $\text{cm}^{-2}$ )	RMS (nm, 10 $\mu\text{m}$ scan)	Relaxation (%)
LL2	0.35	$0.5 \times 10^6 - 10^6$	$12.12 \pm 5.05$	76
LL8	0.28/5.37	$(< 10^5)$	$17.50 \pm 14.70$	79
LL5	$< 0.01$	$3 \times 10^6 - 7 \times 10^6$	$7.52 \pm 1.77$	83
LL11	1.5	$(< 10^5)$	$5.03 \pm 1.59$	80

Table 6.2. Data from Lumileds  $\nabla_x[\text{In}_x\text{Ga}_{1-x}\text{P}]$  MOCVD samples.

Substrate Offcut ( $^\circ$ toward $\langle 110 \rangle$ )	Growth Temperature ( $^\circ\text{C}$ )	Branch Defects ( $\mu\text{m}^{-1}$ )	$\rho_{\text{TD}}$ ( $\text{cm}^{-2}$ )	RMS (10 $\mu\text{m}$ scan)	$x_{\text{In}}$ in cap
10	800	$< 0.01$	$4.0 \times 10^5$	4.9	0.12
10	650	26	$1.2 \times 10^7$	8.5	0.15

Table 6.3. Data from MIT  $\nabla_x[\text{In}_x\text{Ga}_{1-x}\text{P}]$  MOCVD samples<sup>11</sup> (compare to LL5 and LL11).

To characterize the Lumileds samples, film composition, relaxation, and substrate offcut were confirmed using triple-axis x-ray diffraction (TAXRD) on a Bede D3 diffractometer. To improve accuracy, (004) and (224) TAXRD reciprocal space maps were taken. The  $\langle 110 \rangle$  alignment was consistent among samples. Threading dislocation density and branch defect density were obtained via plan view transmission electron microscopy (PVTEM) using a JEOL 2000FX microscope. Cross-section TEM (XTEM) images were also obtained. Surface roughness values refer to 10  $\mu\text{m}$  by 10  $\mu\text{m}$  scans obtained by tapping-mode atomic force microscopy (AFM) on a DI Nanoscope III. The most generally significant result is the observation of branch defects in industrially-

produced  $\text{InGaP}/\nabla_x[\text{In}_x\text{Ga}_{1-x}\text{P}]/\text{GaP}$ , which suggests that they are an intrinsic feature of MOCVD-grown InGaP and not an artifact of the particular reactor.

### 6.3.2 Threading Dislocation Density and Surface Structure

Trends in threading dislocation density and surface roughness in the Lumileds samples, shown in Table 6.2, do not entirely conform to our previous observations. In general, we would expect the higher growth temperature to enhance relaxation via dislocation glide and lead to a lower overall threading density<sup>39</sup>. For these mismatched samples, we do observe that a higher threading density is associated with greater strain relaxation in the cap layer, as expected. However, samples LL2 and LL5, grown at 800°C, are observed to have larger dislocation densities than samples LL8 and LL11, grown at 650°C. This is counter to previous observations<sup>39,40</sup> of efficient strain relief via dislocation glide at high temperatures. In the 800°C samples, we observe a relatively high RMS surface roughness. Dislocation pinning on surface topography and subsequent multiplication may account in part for the larger-than-expected threading dislocation densities in these 800°C samples<sup>38</sup>. However, the high RMS roughness of LL8 does not appear to produce the same effect.

In the GeSi system, it has been observed<sup>39</sup> that threading density is larger for high-temperature graded buffer deposition on an offcut substrate than on an on-axis substrate. A similar behavior is observed here, with an approximately seven-fold increase in threading density as substrate offcut increases from 2° to 10° toward the nearest  $\langle 110 \rangle$ . This has been attributed to a saturation in dislocation reduction reactions with greater offcut<sup>39</sup>. Threading dislocation densities in samples LL8 and LL11 appear to be below the detection limit for PVTEM, less than around  $10^6 \text{ cm}^{-2}$ . This contradicts observations of MOCVD-grown InGaP graded buffers deposited at MIT, which show an increase in threading density at lower growth temperatures. The apparent, unexpected increase in threading dislocation density may occur because PVTEM contrast arising from branch defects and supersteps in LL8 and LL11 masks the appearance of existing threading dislocations in the field. It may also be an accurate measurement, and therefore would be due to differences in growth conditions such as V/III ratio, background

pressure, partial pressures, and growth rate, the values of which differ between the commercial and research reactors.

The evolution of surface structure and roughness in these samples also proves to be complicated, as shown in Figure 6.4. In LL8, a bimodal surface RMS is observed, with a slightly lower overall roughness in the regions between branch defects than in regions that include branch defects; however, exclusion of branch defects from the roughness calculation lowers the RMS by only about 1 nm. The distinctive branch defects present in Figure 6.4d suggest that surface topography is affected by branch defect formation.

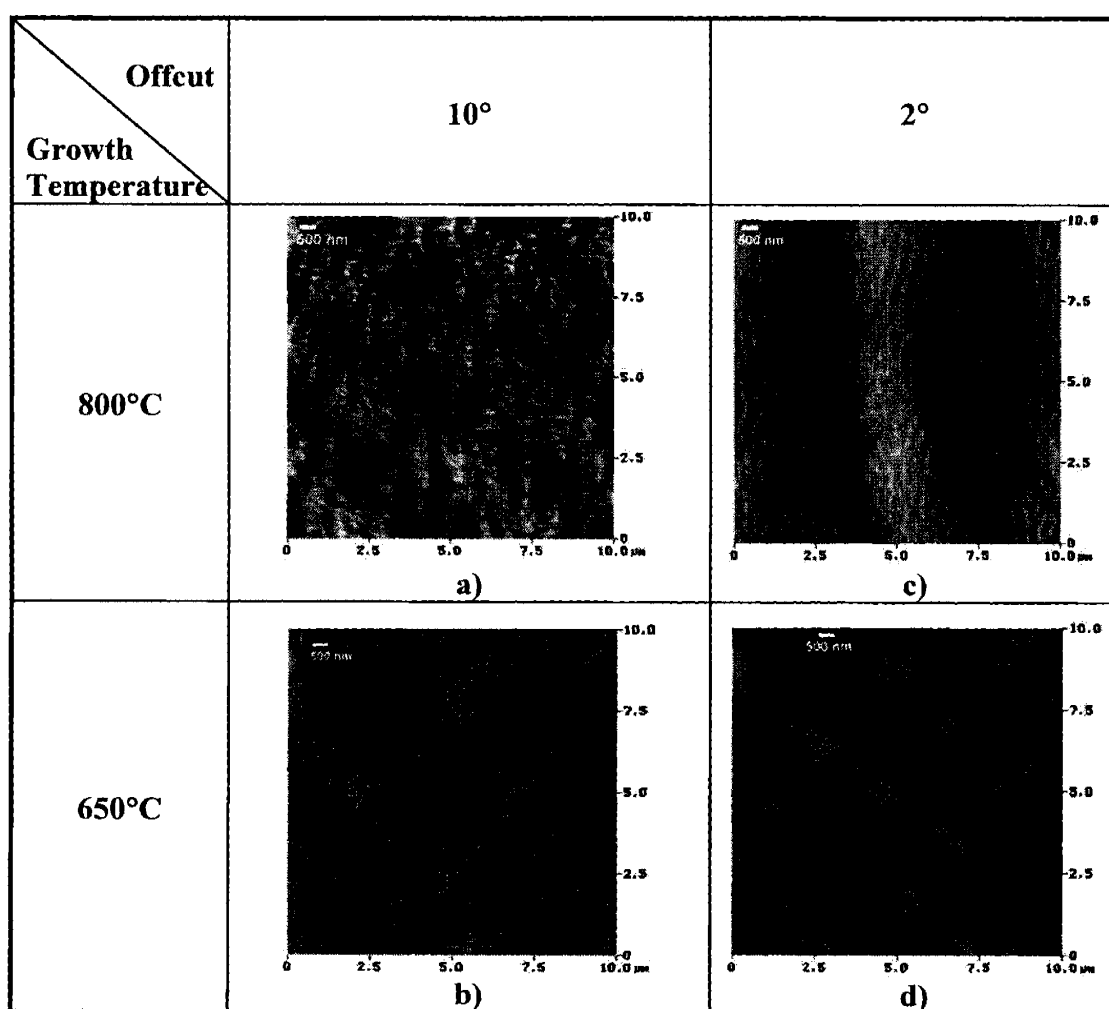


Figure 6.4. AFM of Lumileds samples: a) LL5, b) LL11, c) LL2, d) LL8.

LL11 has a low RMS, lower than that of LL5, which has the same substrate offcut. Conversely, the RMS of LL8 is higher than that of LL2. The trend for 10° offcut samples contradicts observations of materials grown at MIT. As stated above, we would expect enhanced dislocation glide at high temperatures to produce better overall strain relief and therefore a reduction in surface roughness arising from crosshatch. However, a low growth temperature is known to suppress adatom mobility at the growth front and may promote flatness in the deposition of thin layers. In general, there is an optimal temperature window wherein both the kinetic roughening that occurs at low temperatures and the strain roughening that occurs at high temperature are minimized<sup>111-113</sup>. It may be that the Lumileds samples were deposited in a different region of this window than the MIT samples.

The partially relaxed cap layers of LL8 and LL11 have a higher average relaxation than that of LL2, despite having a lower indium fraction. Indeed, in these samples, relaxation seems to trend with the surface roughness while showing no clear relation to the threading dislocation density. For 800°C deposition, we observe a lower RMS roughness with higher threading density and greater relaxation. These factors suggest that other sources of surface roughness—for example, roughening from superstep formation<sup>46,61</sup>—dominate over crosshatch-induced roughening in these samples.

Substrate offcut appears to play an important role in surface morphology. Samples grown on 10° offcut substrates have a cellular morphology suggestive of superstep formation. Supersteps are less pronounced in the 2° offcut samples. This is consistent with previous observations by Hotta, *et al.*<sup>114</sup> the In<sub>0.5</sub>Ga<sub>0.5</sub>P/GaAs system, in which maximum superstep formation was observed for substrate offcuts ranging from 6° to 10°. The detrimental effect of supersteps on surface roughness appears to be suppressed at lower growth temperature, and the characteristic wavelength of the supersteps is shorter. Dislocation interactions with supersteps may contribute to the higher threading density observed for LL5<sup>38</sup>.

### 6.3.3 Branch Defects

Trends in branch defects for 10° offcut Lumileds samples are in relatively good agreement with values measured in MIT samples. To within the resolution of PVTEM,

branch defect formation is not observed for 10° substrate offcut and high growth temperature, as shown in Figure 6.5. In Figure 6.5, we see that branch defects appear as expected at lower growth temperature, though a relatively lower density is observed in the industrially produced samples.

As noted above, branch defects present in the 2° offcut samples have a unique habit, reminiscent of railroad tracks. At high temperature, shown in Figure 6.5c, these defect bands are diffuse and widely spaced. At low temperature, similar defect bands appear, but they have evolved a sharp internal fine structure visible in Figure 6.5d. This may be a localized manifestation of the expected increase in branch defect density at low growth temperatures.

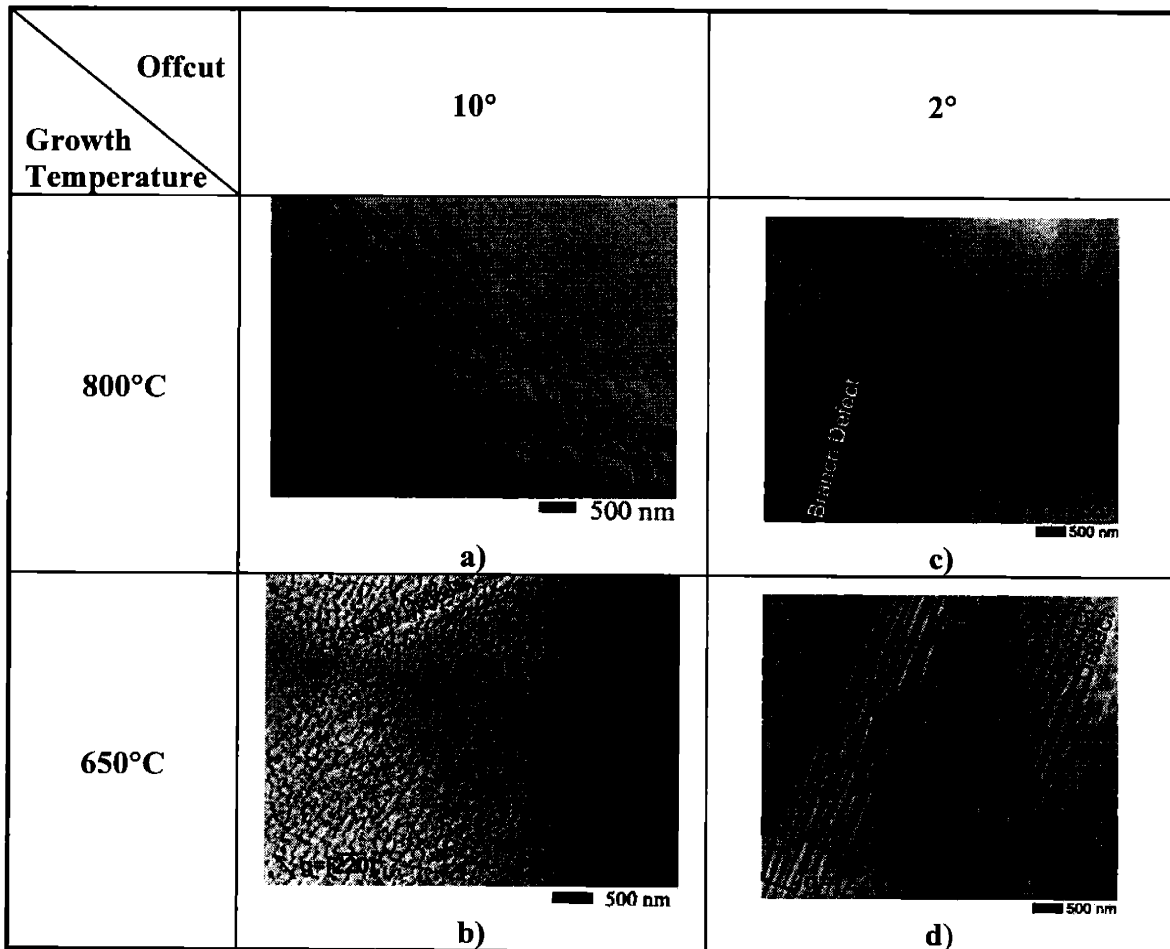
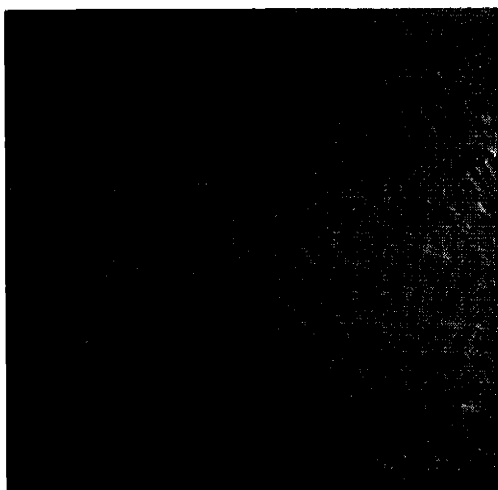
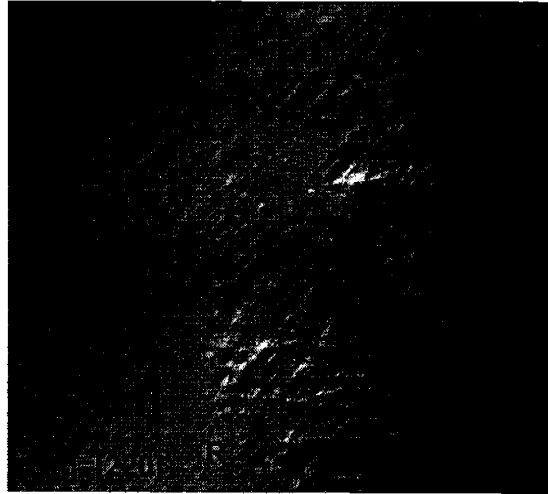


Figure 6.5. PVTEM of Lumileds samples: a) LL5, b) LL11, c) LL2, d) LL8.

Differences in branch defect structure between samples grown on  $10^\circ$  offcut substrates and those grown on  $2^\circ$  offcut substrates likely arise from changes in misorientation-governed properties such as anisotropic diffusion rates and surface reconstruction. The railroad track-like defect structure is clearly visible via AFM in Figure 6.4d; however, TEM analysis indicates that these defects are not purely a surface feature. In PVTEM, strong defect contrast in the  $[2\bar{2}0]$  beam condition nearly vanishes in the perpendicular  $[220]$  condition, leaving behind a ghostly shadow, illustrated in Figure 6.6 and Figure 6.7. In two-beam electron microscopy of a strained feature, contrast vanishes for  $\mathbf{g}\cdot\mathbf{R}=0$ , where  $\mathbf{g}$  is the diffraction vector and  $\mathbf{R}$  is the displacement of the atom from its site in a perfect crystal<sup>77</sup>. Therefore, Figure 6.7 indicates that branch defect strain contrast arises from a displacement field oriented roughly perpendicular to the long axis of the defect. For  $10^\circ$  offcut substrates, branch defects consistently lie about  $10^\circ$  from the  $[110]$ , so this displacement occurs roughly along the  $[1\bar{1}0]$  direction.



**Figure 6.6. PVTEM of sample LL8.**



**Figure 6.7. PVTEM of sample LL8,  $g \cdot R \approx 0$ .**

XTEM, shown in Figure 6.8, reveals that the strong defect contrast observed in PVTEM penetrates deep into the InGaP cap.

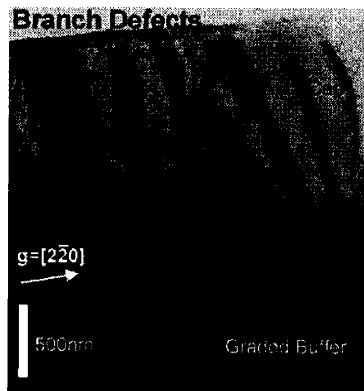


**Figure 6.8. XTEM of sample LL8.**

Finally, branch defects observed in TEM are not always detected in AFM. These factors indicate a crystallographic as well as topographic origin.

The contrast observed in TEM suggests the presence of strain fields around branch defects. Figure 6.9 and Figure 6.10 show TEM images of the “railroad tracks” optimized for dislocation contrast. Misfit dislocations have formed below the branch defects, suggesting that the observed branch defects are an area of high lattice mismatch.

This is strong evidence that branch defects originate from compositional fluctuations, specifically from the uphill diffusion of indium.



**Figure 6.9. PVTEM of sample LL8.**



**Figure 6.10. PVTEM of sample LL8, in the same area as Figure 6.9. Note misfit dislocations that underlie regions of branch defect contrast in Figure 6.9.**

#### 6.3.3.1 EDX Analysis

The distinct bright and dark defect fringes of LL8 were probed using energy dispersive x-ray spectroscopy (EDX) on a JEOL 2010 high resolution TEM, as reported in Table 6.4. While suggestive of a compositional difference between bright and dark defect fringes, the results are not entirely conclusive. The values in Table 6.4 do indicate that Group III quantities consistent with the bulk composition are conserved within a given defect. The defect fringes appear to arise from local segregation of Group III



atoms. Assuming an average difference in indium fraction of 0.01 across fringes, the magnitude of strain between bright and dark fringes would be approximately 0.07%. This represents, for example, a branch defect consisting of  $\text{In}_{0.13}\text{Ga}_{0.87}\text{P}$  and  $\text{In}_{0.12}\text{Ga}_{0.88}\text{P}$  regions within an  $\text{In}_{0.125}\text{Ga}_{0.875}\text{P}$  matrix. However, given the spatial and compositional resolution limits of EDX in comparison to branch defect size, it would be desirable to verify these measurements with a higher resolution technique. The scanning tunneling microscopy (STM) techniques developed by Feenstra<sup>66,115</sup> could prove useful for such a direct examination of branch defects.

Indium Fraction	High Magnification			Low Magnification	
	Field	Dark Fringe	Bright Fringe	Field	Entire Defect
Defect 1	0.121	0.126	0.122	0.115	0.115
Defect 2	0.140	0.145	0.128	0.135	0.132

Table 6.4. Energy dispersive x-ray (EDX) measurements of lateral fluctuations in indium fraction within a branch defect.

### 6.3.3.2 High Resolution Lattice Image Analysis

High resolution transmission electron microscopy (HRTEM) lattice images of branch defect regions confirm that these regions retain their crystalline nature, as shown in Figure 6.11.

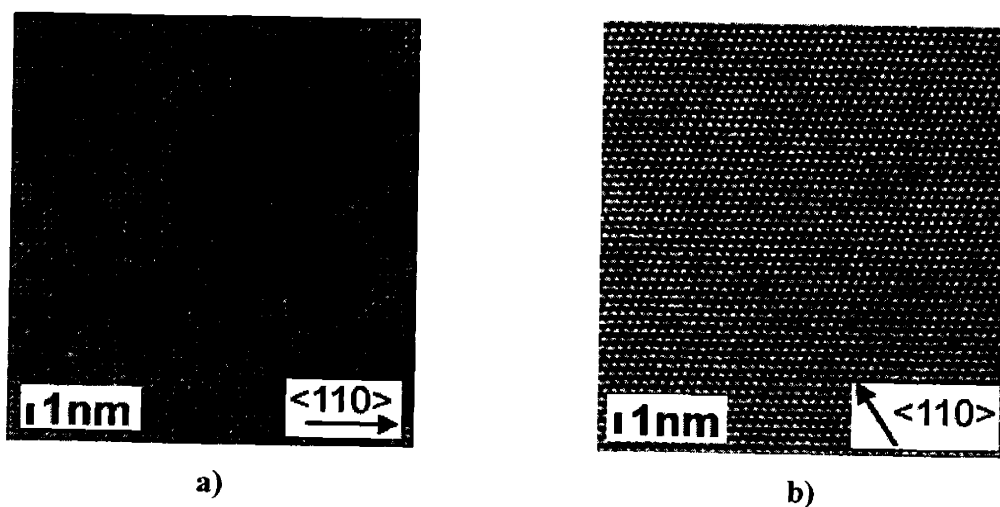
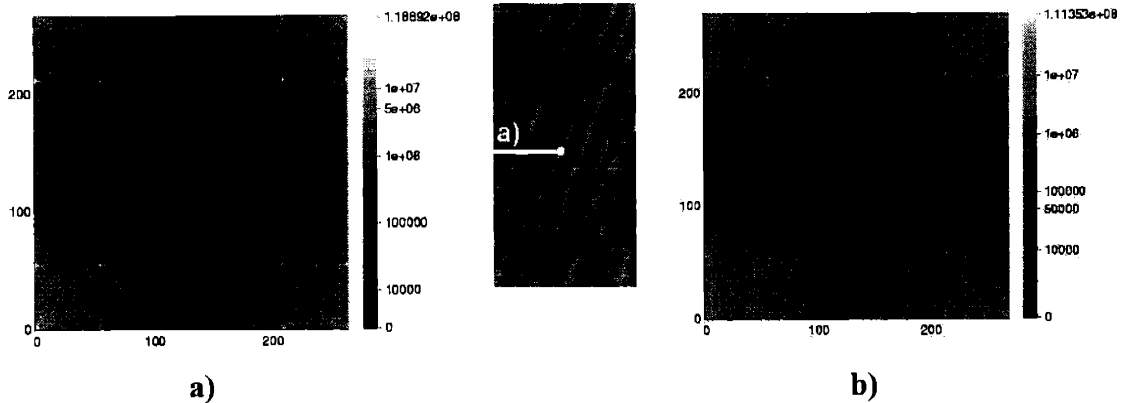


Figure 6.11. HRTEM lattice image of a branch defect region: a) plan view and b) cross section.

Fourier analysis of such images provides the periodicity of the {111} lattice fringes. From the lattice fringe spacing, it is straightforward to extract the lattice constant of the material. Fast Fourier transforms of plan-view lattice images taken on bright and dark branch defect fringes are shown in Figure 6.12.



**Figure 6.12.** Fast Fourier transforms of plan view lattice images from a) a bright fringe and b) a dark fringe of a branch defect.

From Figure 6.12a, we determine a lattice constant of  $5.497 \pm 0.073 \text{ \AA}$  for the bright fringe of the branch defect. Figure 6.12b gives a lattice constant of  $5.503 \pm 0.062 \text{ \AA}$  for the dark fringe, which is  $0.006 \text{ \AA}$  larger than that of the bright fringe. Additionally, Figure 6.12b indicates that the lattice fringe spacing differs in the two perpendicular  $\langle 110 \rangle$  directions, which would result from an in-plane rhombohedral distortion—or shearing—of the lattice. The magnitude of this distortion, as given by Figure 6.12b, is a relatively small  $1.3^\circ$ ; that is, an  $88.7^\circ$  angle between the  $[100]$  and  $[010]$  directions. The  $0.006 \text{ \AA}$  difference in lattice constant between the branch defect fringes corresponds to an increase in indium fraction of nearly 0.015. However, while consistent with the EDX results presented above, this result is also within the error of the measurement and is suggestive rather than conclusive.

### 6.3.4 Summary

Branch defect formation in industrially-grown  $\text{In}_{0.15}\text{Ga}_{0.85}\text{P}/\nabla_x[\text{In}_x\text{Ga}_{1-x}\text{P}]/\text{GaP}$  is found to depend strongly on growth temperature and substrate offcut. Higher growth temperatures shift branch defect onset to higher indium fractions. Similarly, increasing

substrate misorientation angle tends to suppress defect formation. Branch defects in samples deposited on 2° offcut substrates exhibit a distinctive habit and are present at both high and low growth temperatures. Widely spaced defect bands form at high temperature; similar bands form at low temperature but acquire an internal, short-wavelength defect structure. These defect bands lead to a small increase in overall RMS surface roughness, as the field regions between defects display an RMS approximately 1 nm lower than the overall RMS.

For deposition on a 10° offcut substrate, branch defects are nominally eliminated for growth at 800°C, while a high density of weakly interacting defects form during growth at 650°C. This is in relatively good agreement with previous observations of comparable samples grown at MIT<sup>40</sup>. However, trends in surface roughness and threading density are not consistent with past observations; specifically, a comparison of LL5 and LL11 shows that RMS roughness and threading density do not appear to increase in the presence of branch defects. Possible explanations for this discrepancy include differences in growth conditions such as reactor pressure, precursor partial pressures, and growth rate, but at present the cause is unclear.

#### **6.4 *In-situ* Annealing and Branch Defect Evolution**

In an effort to further understand the origins of branch defect-like microstructures, we have explored the effects on their evolution of *in-situ* annealing during MOCVD growth. In particular, we wish to determine whether growth interruption and annealing at an elevated temperature will enhance or suppress branch defect formation. Given a thermodynamically unstable defect, we would expect branch defect density and strength to decrease under annealing. Likewise, a kinetically limited branch defect formation process would be enhanced at high temperatures, particularly if it is related to In surface diffusion.

Samples examined in these annealing experiments were deposited in a Thomas Swan 1” research reactor located at MIT, described in Chapter 4. A schematic of the two annealing procedures utilized for this study are presented in Figure 6.13, for “uncapped” anneals, and Figure 6.14, for “capped” anneals.

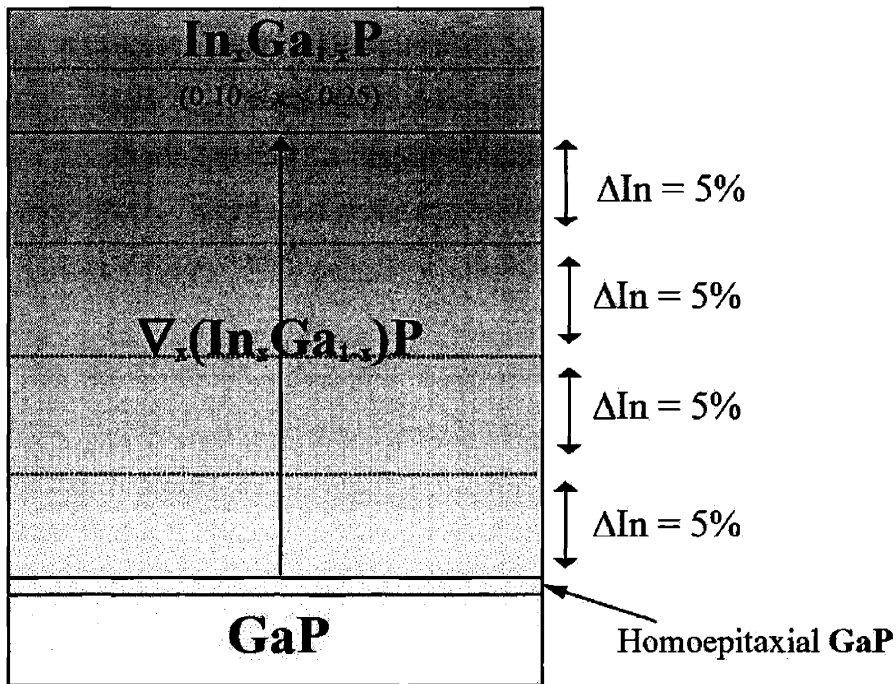


Figure 6.13. Uncapped *in-situ* annealing procedure for InGaP graded buffer. Dashed lines indicate an interruption in 725°C growth to perform a 10 minute anneal at 775°C in a PH<sub>3</sub> ambient.

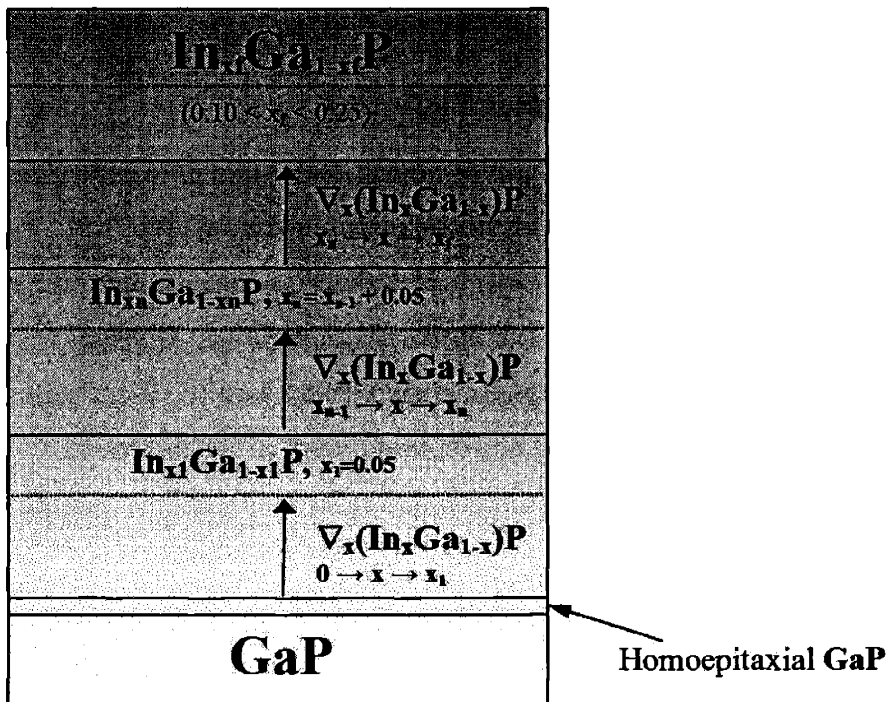


Figure 6.14. Capped *in-situ* annealing procedure for InGaP graded buffer. Dashed lines indicate an interruption in 725°C growth to perform a 10 minute anneal at 775°C in a PH<sub>3</sub> ambient.

Regular graded buffer growth was carried out at 725°C, with a grading rate of -0.4% strain/μm, and a growth rate of 4-6 μm/hr. V/III ratio during growth and final indium composition were varied. The substrate was (001) GaP offcut 10° to the nearest <110>. For each  $\Delta x_{In} = 0.05$ , growth was interrupted and the sample was annealed *in situ* under a H<sub>2</sub> plus PH<sub>3</sub> ambient at 775°C for 10 minutes. The sample was then returned to 725°C. For uncapped anneals, growth resumed with the next graded buffer step. For capped anneals, growth resumed with a 500 nm thick constant-composition layer, followed by subsequent grading. In both cases, an additional annealing step was inserted in the middle of the constant-composition cap layer. A summary of these annealing samples is given in Table 6.5.

<b>Sample ID</b>	<b>10-1</b>	<b>10-2</b>	<b>10-3</b>	<b>10-5</b>	<b>10-6</b>	<b>10-7</b>	<b>10-A</b>
Annealing Sequence	Uncapped	No annealing	Uncapped	Uncapped	Uncapped	Uncapped	Post-growth
Final $x_{In}$ (target/actual)	0.25/0.21	0.25/0.21	0.10/0.08	0.15/0.13	0.20/0.19	0.10/0.08	0.25/0.21
V/III ratio	150	150	150	150	150	50	H <sub>2</sub> + PH <sub>3</sub> ambient
<b>Sample ID</b>	<b>11-2</b>	<b>11-3</b>	<b>11-4</b>	<b>11-8</b>			
Annealing Sequence	Capped	No annealing	Capped	No annealing			
Final $x_{In}$ (target/actual)	0.10/0.12	0.10/0.12	0.20/0.15	0.20/0.19			
V/III ratio	150	150	150	150			

**Table 6.5. Summary of Samples in Annealing Series**

#### 6.4.1 Uncapped Anneals

In general for these samples, branch defect onset and development was enhanced by prolonged annealing steps and decreased Group V overpressure. Figure 6.15 shows the pronounced effect of *in-situ* annealing on graded buffer growth. For the case of uninterrupted graded buffer growth to  $x_{In} = 0.25$ , Figure 6.15a, no unusual defect contrast is observed. Conversely, in the case of interrupted, annealed graded buffer growth, Figure 6.15b, branch-like defects begin to appear around the  $x_{In} = 0.15$  annealed interface and extend toward the surface of the sample. The most dramatic effect, illustrated in

Figure 6.15b, occurs when annealing is followed by growth at the same composition and no misfits are present, as for annealing and regrowth within the cap layer.

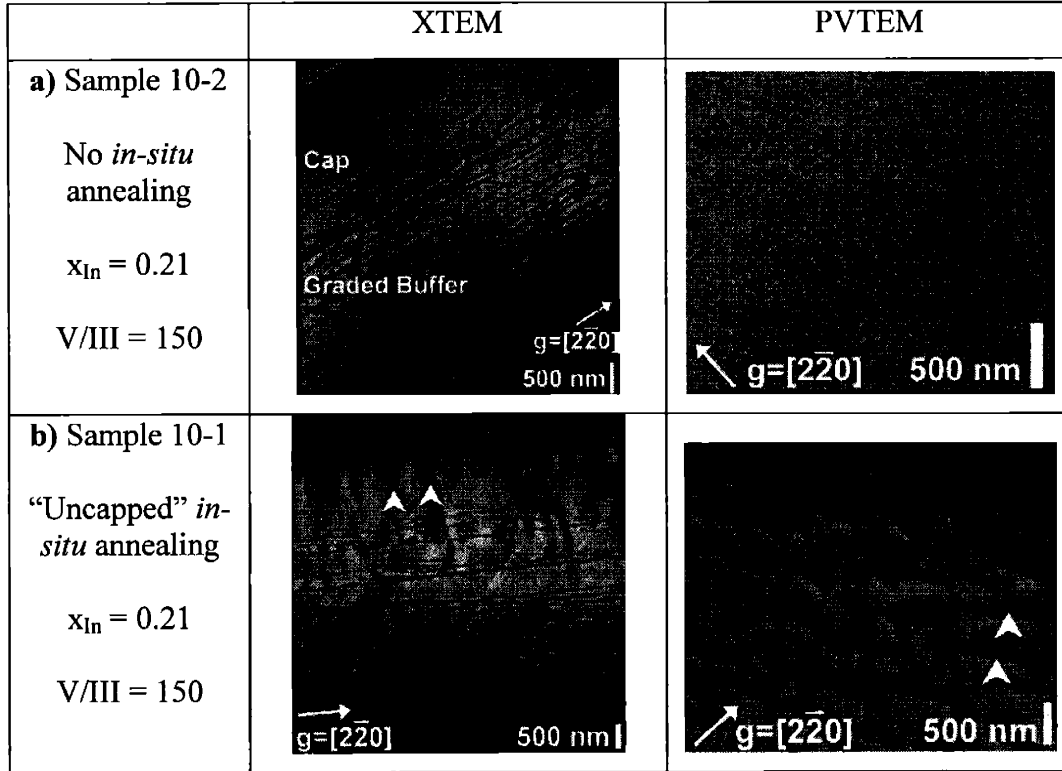


**Figure 6.15. TEM of a) unannealed and b) *in-situ* annealed  $\nabla_x[In_xGa_{1-x}P]$  graded buffer, where  $x_{In} = 0.21$  in the cap layer. Typical branch defects indicated by ▲.**

Annealing does not produce this defect structure for all indium compositions. Figure 6.16 shows the gradual onset of branch defect formation as the indium fraction in the cap layer increases from  $x_{In} = 0.08$  to  $x_{In} = 0.19$ . For  $x_{In} = 0.08$ , extremely weak or no branch defect formation is observed. For  $x_{In} = 0.13$ , moderate defect contrast is observed at the annealed interface in the cap layer. PVTEM of this sample reveals a strong anisotropy in branch defect habit, again aligned roughly  $10^\circ$  from  $\langle 110 \rangle$ . For  $x_{In} = 0.19$  in the cap, contrast is observed at all annealing interfaces where  $x_{In} \geq 0.15$ , but is again strongest in the cap layer. In plan view, a transition from a one-dimensional to two-dimensional structure is apparent. The dependence of branch defect formation on indium fraction at the annealed interface is consistent with the observations of Kim, et al<sup>40</sup>.

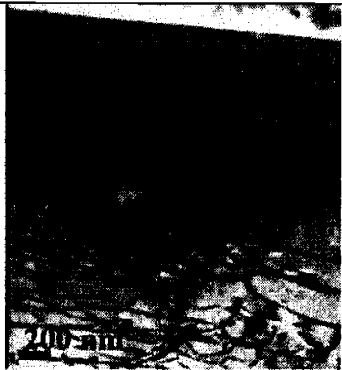
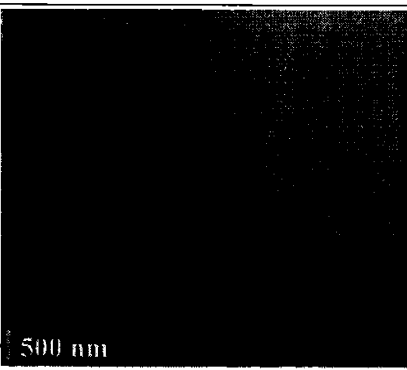
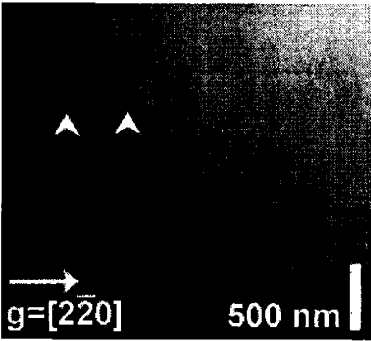
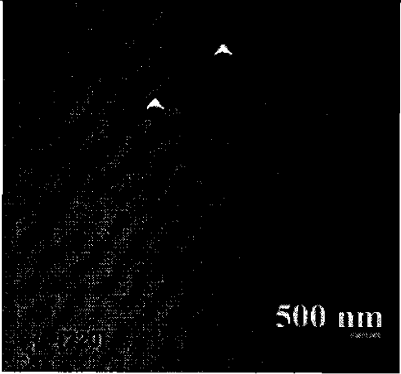
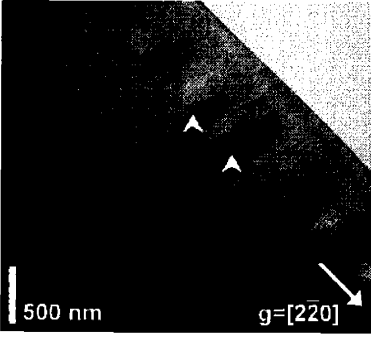
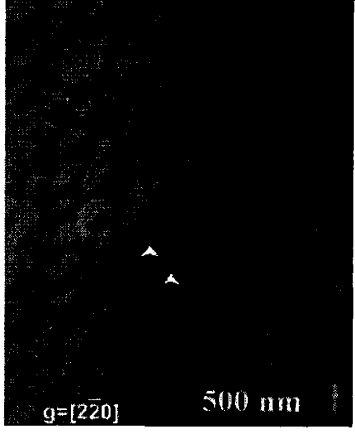
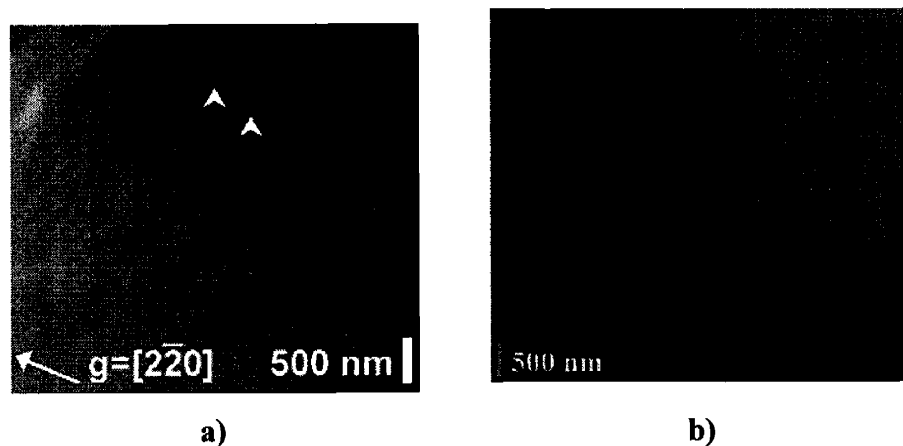
	XTEM	PVTEM
<p>a) Sample 10-3</p> <p>“Uncapped” <i>in-situ</i> annealing</p> <p><math>x_{\text{In}} = 0.08</math></p> <p>V/III = 150</p>		
<p>b) Sample 10-5</p> <p>“Uncapped” <i>in-situ</i> annealing</p> <p><math>x_{\text{In}} = 0.13</math></p> <p>V/III = 150</p>		
<p>c) Sample 10-6</p> <p>“Uncapped” <i>in-situ</i> annealing</p> <p><math>x_{\text{In}} = 0.19</math></p> <p>V/III = 150</p>		

Figure 6.16. TEM of *in-situ* annealed  $\nabla_x[\text{In}_x\text{Ga}_{1-x}\text{P}]$  graded buffers with a)  $x_{\text{In}} = 0.08$ , b)  $x_{\text{In}} = 0.13$ , and c)  $x_{\text{In}} = 0.19$  in the cap layer. Typical branch defects indicated by  $\blacktriangle$ .

The effect of V/III ratio on branch defect formation is illustrated in Figure 6.17. For a lower V/III ratio of 50, branch defects appear for  $x_{\text{In}} = 0.10$ , whereas they are absent at this composition for V/III = 150. Comparison to other *in-situ* annealed samples shows that the branch defect density and habit observed for  $x_{\text{In}} = 0.10$  and V/III = 50 are similar

to that for  $x_{In} = 0.15$  and  $V/III = 150$ . This indicates that an increased Group V overpressure acts to suppress the mechanism of branch defect formation.



**Figure 6.17. PVTEM of annealed samples with  $x_{In} = 0.10$ , deposited with V/III ratio of a) 50, and b) 150. Typical branch defects indicated by  $\blacktriangle$ . Note the lack of branch defect development in b).**

#### 6.4.2 Capped Anneals

The growth process outlined above and in Chapter 3 leads to an inevitable connection between the final composition of the graded buffer and its total thickness. This tends to confuse the role of overall composition on branch defect formation with that of overall strain. In an attempt to disentangle these two factors, we have deposited a thick, constant-composition layer atop each annealed interface, as shown in Figure 6.14. In this way, we can determine any change in branch defect behavior arising from augmented relaxation in the thick cap layers.

To understand the results of these experiments, we first consider samples 11-2 and 11-3, shown in Figure 6.18 and detailed in Table 6.5. Sample 11-2 was graded to  $x_{In} = 0.05$ , annealed and capped, then further graded to  $x_{In} = 0.12$ , annealed and capped. Sample 11-3 is a typical relaxed, graded buffer. TAXRD confirms that the addition of the buried  $x_{In} = 0.05$  cap layer increased strain relaxation from 58.8% (sample 11-3) to 88.2% (sample 11-2). Weak branch defect-like contrast is visible at the  $x_{In} = 0.12$  annealed interface of sample 11-2, shown in Figure 6.18b. It is clear that the branch defect regime has been reached at this composition via annealing, despite additional



relaxation arising from the buried cap layer. Sample 11-3, shown in Figure 6.18a, exhibits no branch defect contrast, confirming that branch defects do not form under these conditions in the absence of annealing.

Next, we compare “capped” sample 11-4 to “uncapped” sample, 10-6. Figure 6.18c illustrates branch defect-like contrast present at the  $x_{\text{In}} = 0.15$  annealing interface of sample 11-4. In sample 10-6, such contrast is absent at the  $x_{\text{In}} = 0.15$  interface, which is buried in the misfit array of the relaxed, graded buffer. This indicates that the presence of the graded buffer acts to suppress or reverse the mechanism of branch defect formation. Conversely, the deposition of a lattice-matched cap acts to “freeze in” defects that have formed during annealing. We also observe the association of perpendicular misfits with the areas of branch defect-like contrast, further evidence for the existence of a local strain field.

Finally, we compare the  $x_{\text{In}} = 0.15$  annealed interfaces of sample 11-4 and sample 10-5. While the linear density of contrast fringes visible in XTEM is roughly the same for both samples, the magnitude of contrast is slightly less for sample 11-4, despite its higher indium fraction. It would seem that while the onset of branch defect formation is primarily dictated by indium fraction, the properties of the defects may be modified by the amount of strain in the lattice.

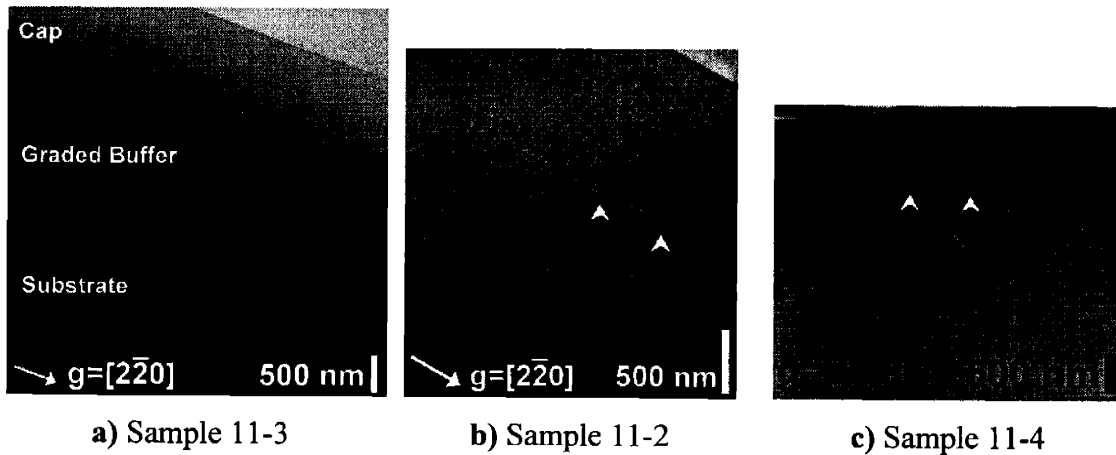


**Figure 6.18.** XTEM of  $\nabla_x[\text{In}_x\text{Ga}_{1-x}\text{P}]$  graded buffers a) unannealed,  $x_{\text{In}} = 0.12$ , b) capped anneal,  $x_{\text{In}} = 0.12$ , and c) capped anneal,  $x_{\text{In}} = 0.15$ . Typical branch defects are denoted by  $\blacktriangle$ .  $V/\text{III}=150$  for all.

### 6.4.3 Post-growth Annealing

Finally, we wish to compare the effect of *in-situ* annealing of the InGaP graded buffer with that of post-growth annealing. When a sample with  $x_{\text{In}} = 0.21$  in the cap is subjected to post-growth annealing at 775°C, branch defect-like contrast does not arise throughout the thickness. The surface of the sample alone degrades, becoming heavily islanded and consuming part of the cap region, while the remainder of the cap and buffer are unaffected, as shown in Figure 6.19. This is reasonable given that semiconductor surface diffusivity is generally orders of magnitude larger than bulk diffusivity, and it suggests a surface-driven defect formation mechanism.

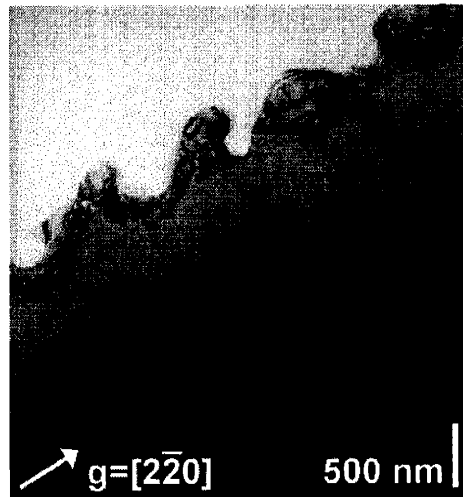


Figure 6.19. Surface degradation in sample 10-2 (see Figure 6.15) after post-growth annealing.

## 6.5 Defect Formation Mechanism

The results presented above for the InGaP system point to a complex mechanism for the formation of the various branch defect-like structures described; however, indium clustering on the growth surface, possibly governed by local changes in surface reconstruction and diffusivity, would account for the various observations. For MOCVD growth, dependencies on substrate offcut, growth temperature, V/III ratio, composition, and strain are observed. Though the phase space for branch defect formation is complicated, we believe that the various defects described may be attributed to indium

clustering at the growth surface. Indium segregation and clustering in InGaP is a much-studied phenomenon<sup>68,116,117</sup>. Indium clustering is related to the miscibility gap that exists at low temperatures in the InGaP system. The differing bond lengths of In and Ga in the zincblende structure lead to a distortion of the bonded tetrahedron<sup>118</sup>. Under certain conditions, it becomes thermodynamically favorable for In atoms on the group III sublattice to congregate in order to relieve the bonding strain, as described in Chapter 3. In thermodynamic equilibrium, spinodal decomposition is maximized near  $\text{In}_{0.5}\text{Ga}_{0.5}\text{P}$ . MOCVD growth is a non-equilibrium process; however, certain driving forces for decomposition remain. In particular, high adatom mobilities enable a redistribution of In on the surface that could not occur via lattice diffusion in the bulk. In fact, we have observed that localized In segregation at the surface is favored even for compositions outside the thermodynamically predicted range. The results presented above, along with the treatment of deviations from randomness given in Chapter 3, allow us to develop a qualitative model for the formation of branch defects.

### 6.5.1 Spinodal Decomposition

As described in Chapter 3, spinodal decomposition of an alloy occurs at temperatures where entropic effects no longer dominate over differences in bond energies. As temperature decreases, it becomes favorable to nucleate clusters of like atoms or molecules, locally relieving distortion in the lattice. For our purposes, the important characteristics of spinodal decomposition are<sup>50</sup>:

1. For an alloy  $A_xB_{1-x}$  that exhibits spinodal decomposition,  $x$  at the onset of decomposition is directly proportional to  $T$ . Stated another way, for a given  $x$ , decomposition is enhanced at lower temperatures.
2. In the case of coherent spinodal decomposition, the minimum decomposition wavelength is inversely proportional to the overall undercooling.

This behavior is precisely consistent with the relationship between indium fraction and branch defect formation found in the samples presented above as well as by Kim, *et al.*<sup>40</sup> At high temperatures, the onset of branch defect formation is shifted to higher indium fractions, and the wavelength of the defect structure is longer.

However, we observe branch defect formation well outside the compositional bounds that the coherent spinodal would dictate. This apparent discrepancy may arise because MOCVD is a non-equilibrium process and because branch defect formation occurs at the growth surface—not in the bulk—and is governed by surface processes. EDX analysis and lattice imaging of branch defect fringes suggests that the magnitude of the compositional fluctuation is approximately 1.5%, as we might expect for a relatively small driving force.

### 6.5.2 Nucleation and Growth

In the case of a metastable alloy, the development of surface compositional fluctuations may proceed via nucleation and growth. For MOCVD deposition, it is likely that the nucleation and growth of branch defects will be related to the step-flow mechanism of epilayer nucleation and growth. Indeed, the clear dependence of branch defect habit on substrate offcut, growth temperature, and V/III ratio is highly suggestive of a dependence on the surface reconstruction at the growth front. Although a detailed treatment of the effects of surface reconstruction and step flow on branch defect formation is beyond the scope of this study, we can draw some general conclusions.

Branch defect formation is dictated primarily by the kinetics of indium diffusion at the surface during deposition. While there is negligible bulk driving force for clustering, it may be energetically favorable to generate localized, partially incoherent GaP-GaP and InP-InP regions at the surface. Such clustering tends to locally decrease bonding distortions in the epilayer, as well as to create regions that are better matched to the underlying, compressively strained lattice. In general for surface nucleation and growth of In clusters, we would expect the critical radius of the cluster to be larger at higher temperatures<sup>50</sup>. That is, a larger number of In atoms must find one another to form a stable cluster, and the overall size of the cluster will be greater. Clustering would therefore be enhanced under conditions of increased Group III adatom mobility. Again, this is consistent with the observations described above.

#### 6.5.2.1 Growth Temperature

Elevated deposition temperature will contribute in two ways to the effective diffusivity of In atoms. Increased thermal energy will of course enhance the diffusivity

of In atoms adhered to the growth surface. Additionally, the In sticking coefficient will decrease as temperature increases, leading to an increased rate of adsorption/desorption events<sup>13</sup>. This augmented gas/solid exchange will create a greater dynamic range of In attachment at surface sites. We do observe that branch defects formed in samples grown at a high temperature tend to be more widely spaced and to generate larger strain fields than their low temperature counterparts. This is well described by high temperature nucleation and growth, wherein enhanced diffusivity permits the formation of larger In clusters. During annealing, we would expect both increased thermal energy and the absence of new material deposition to increase In adatom diffusivity. Indeed, TEM strain contrast from branch defects at the annealed interface is greatly enhanced, illustrating the expected augmentation of In clustering.

#### 6.5.2.2 V/III Ratio

During MOCVD growth, a large Group V overpressure will suppress adatom mobility and, subsequently, In clustering<sup>12</sup>. If branch defects are the result of indium clustering, we would expect to find enhanced branch defect formation at lower V/III ratios. We have some evidence to support this in Figure 6.17, which illustrates the formation of branch defects during low V/III deposition at a composition where branch defect formation does not occur for high V/III deposition. In the case where branch defects are present at a given composition for both low V/III and high V/III growth, we would expect to see greater dislocation pinning in the low V/III sample; however, at this time such behavior has not been directly observed.

#### 6.5.2.3 Strain

The role of lattice strain in branch defect formation is somewhat less clear. Samples that have nearly identical strain relaxation arising from misfit dislocations can nonetheless have vastly different branch defect properties<sup>40</sup>. We therefore cannot point to misfit strain fields as a primary influence on surface In clustering. As described above, increased lattice relaxation with all other factors being equal is not sufficient to prevent In clustering during annealing. This further suggests that branch defect formation is a surface phenomenon that is only secondarily affected by lattice strain.

#### 6.5.2.4 Dislocation Diffusion

The annealing results presented in Section 6.4 provide some evidence that the dislocation array formed in the relaxed, graded buffer provides a pathway for In diffusion. Clustering is observed at capped, annealed interfaces of a given composition, while no clustering is observed at the uncapped, annealed interface of the same composition. This suggests that although clustering does occur during annealing in both cases, the fluctuations are consumed and redistributed by dislocation pipe diffusion in the uncapped sample. In addition to redistribution via pipe diffusion, the bulk indium self-diffusivity will increase as a result of vacancies left in the wake of gliding dislocations. In this way, dislocation-enhanced diffusion provides a limited pathway to relieve local strains that arise from In clustering. However, as indium fraction and decomposition driving force increase, dislocation diffusivity becomes insufficient and the clustering persists even within the graded buffer.

#### 6.5.3 Relaxation Anisotropy

The zincblende structure of III-V semiconductors leads to an anisotropy in materials properties along the perpendicular in-plane  $\langle 110 \rangle$  directions. During the deposition of a compressively strained layer, misfit dislocations form below the epilayer to relieve strain. Matragrano, *et al.*<sup>30</sup> have demonstrated for this situation that  $\alpha$ -type dislocations have a  $[1\bar{1}0]$  line direction, while  $\beta$ -type dislocations have a  $[110]$  line direction, shown in Figure 3.6. Both are  $60^\circ$  dislocations having mixed character; however, only the edge component of the Burger's vector is available to relieve strain. For this reason,  $\alpha$  dislocations provide strain relief in the  $[110]$  direction, while  $\beta$  dislocations provide strain relief in the  $[1\bar{1}0]$  direction. In general for InGaP,  $\alpha$  dislocations have a higher glide velocity and would be expected to dominate strain relief. However, it has been postulated<sup>30</sup> that in the case of an offcut substrate, a large number of  $\alpha$  dislocations with Burger's vector that increases strain may nucleate to reduce tilt and rotation in the film. In this case, strain relief by  $\beta$  dislocations would be expected to play a more equitable role.

The final piece of evidence to consider in identifying In clustering as the mechanism behind branch defect formation relates to the unusual strain relaxation

characteristics of uncapped, annealed samples, summarized in Table 6.6. Previous TAXRD diffraction analysis of relaxed, graded InGaP buffers produced in the MIT system found negligible anisotropy in strain relaxation<sup>11</sup>. This is consistent with the enhanced role of  $\beta$  dislocations in strain relief described above. Similarly, as shown in Table 6.6, typical graded buffer samples produced in this study show isotropic strain relaxation. On the other hand, relaxation becomes anisotropic when uncapped anneals are introduced to the growth sequence. This sheds interesting light on the nature of branch defects.

<b>Annealed Sample ID</b>	<b>10-3</b>		<b>10-1</b>	
<b>Orientation</b>	[110]	[1 $\bar{1}$ 0]	[110]	[1 $\bar{1}$ 0]
$x_{In}$	0.083	0.085	0.208	0.215
<b>Relaxation</b>	63.4%	68.6%	71.1%	77.8%
<b>Relaxation Anisotropy</b>	0.92		0.91	
<b>Unannealed Sample ID</b>	<b>11-3</b>		<b>11-8</b>	
<b>Orientation</b>	[110]	[1 $\bar{1}$ 0]	[110]	[1 $\bar{1}$ 0]
$x_{In}$	0.112	0.110	0.191	0.198
<b>Relaxation</b>	58.8%	59.6%	77.0%	77.6%
<b>Relaxation Anisotropy</b>	0.99		0.99	

**Table 6.6. Strain relaxation for uncapped, annealed samples compared to strain relaxation for standard relaxed, graded buffers grown at 725°C.**

Consider first the comparison between samples 10-3 (annealed) and 11-3 (unannealed). Sample 10-3 exhibits extremely weak branch defect formation elongated along [110]. Sample 11-3 shows no branch defect formation. The annealed sample shows a greater average relaxation than the unannealed sample, as expected from the thermal activation of dislocation glide during annealing. However, a relaxation anisotropy of 0.92 arises in the case of annealing. The primary difference between the samples is indium clustering at the annealed interface, which would indicate that the compositional fluctuation contributes a dislocation blocking mechanism. Strain relief is

inhibited in the  $[110]$  direction, consistent with suppressed  $\alpha$  dislocation glide. We have observed that the one-dimensional branch defect mode in the annealed samples has a near- $[110]$  alignment, and so could reasonably be expected to block dislocations gliding in the  $[1\bar{1}0]$  direction.

Next we compare samples 10-1 (annealed) and 11-8 (unannealed). Again we observe isotropic relaxation for standard graded buffer growth, while relaxation is anisotropic for annealed growth. However, we find in this case that annealing at an elevated temperature has not led to enhanced dislocation glide. Indeed,  $[1\bar{1}0]$  relaxation for both the annealed and unannealed samples is effectively identical. The key to this behavior lies in the transition to a two-dimensional defect habit observed for sample 10-1. The two-dimensional character of the branch defects leads to dislocation blocking for both  $\alpha$  and  $\beta$  dislocations, suppressing enhanced relaxation during annealing. The explanation for this augmented dislocation blocking provides us with the last piece of the branch defect puzzle. Gliding dislocations are commonly blocked by interactions with strain fields in the crystal<sup>38</sup>. Geometrically, as illustrated in Figure 6.20, we would expect strain fields of the elongated branch defects to preferentially block dislocations gliding in the perpendicular direction. Compositional fluctuation is a straightforward explanation for the origin of dislocation-pinning strain fields emanating from branch defects. Given the size mismatch between InP and GaP, local distortion of the lattice to accommodate a nonrandom atomic arrangement will lead to local strain fields, as discussed in Chapter 3, and discussed above in reference to Figure 6.6 and Figure 6.7. Similarly, as the branch defect geometry transitions from one-dimensional to two-dimensional, the influence of their strain fields extends to dislocations gliding in both directions. This dislocation blocking behavior in the annealed samples suggests that branch defects do indeed form via indium clustering.



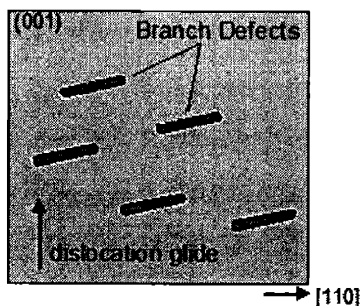


Figure 6.20. Schematic crystallographic geometry of branch defects and dislocation blocking.

## 6.6 Conclusions

We have characterized in the detail the formation of branch defects in relaxed, graded InGaP buffers produced using both industrial and research MOCVD reactors. Differences in surface roughness and threading density between industrially produced graded buffers and those deposited at MIT may arise from variations in unknown parameters such as reactor pressure, growth rate, and V/III ratio. However, the formation phase space for branch defects is consistent among industrial and research samples. In particular, branch defect formation is shifted to higher indium fraction and lower density at high growth temperatures. To further characterize branch defects, interrupted graded buffer growth including *in-situ* annealing at high temperature was carried out. In general, annealing leads to enhanced branch defect-like contrast at the annealed interfaces. This contrast is especially visible when the annealing interface is outside the relaxed, graded buffer region. The relationship between deposition temperature and composition at the onset of branch defect formation follows that predicted by spinodal decomposition, the driving force that has been related to In clustering. Branch defect formation is enhanced under conditions where the diffusivity of In adatoms is maximized. We believe that these results are consistent with the identification of In clustering at the MOCVD growth surface as the mechanism for branch defect formation. Finally, we demonstrate that dislocations gliding in the  $[1\bar{1}0]$  direction are preferentially blocked by nearly- $[110]$ -oriented branch defects. This is further evidence for the association between branch defects and In clustering.

Ultimately, branch defects result from the propagation of indium clustering at the growth front. They arise at the surface, but can become a metastable bulk defect as each growth surface is covered by the next and the compositional fluctuation is frozen in place. Local strain fields arising from the branch defects produce a rough self-alignment of the defects along the direction of growth, as shown in Figure 6.8. A similar effect is utilized in the production of vertically aligned quantum dot arrays<sup>119,120</sup>. The independence of branch defect characteristics from misfit dislocation density suggests that misfit strain fields do not drive branch defect formation. Given the characteristics detailed above, a surface reconstruction-driven mechanism for branch defect formation, similar to that described for ordering in Figure 3.21 but resulting in a different microstructure, seems reasonable. The dependence of branch defect properties on substrate offset supports this interpretation. The precise nature of branch defect formation and interaction with dislocations depends on an extensive suite of growth conditions. From a practical standpoint, perhaps the most important information we can take away from these studies is how to avoid branch defects. By understanding the conditions under which branch defects form, we can engineer graded buffers that have zero or weakly interacting branch defects and decreased threading dislocation densities. These graded buffers can be used as high-quality virtual substrates for a range of InGaP devices.

## 7 Yellow-green Strained-InGaP Quantum Well LEDs

### 7.1 Introduction

Light emitting-diode (LED) devices are a natural replacement for common incandescent lights and indicators. LEDs are efficient, intense, long-lived and produce little heat. In the development of solid state lighting, the ultimate goal of red-green-blue LED mixing for full-color and white applications has been hindered by the lack of an appropriate green light source<sup>2</sup>, as discussed in Chapter 1. While intense red and blue LEDs are available, various materials issues have prevented the development of a similarly intense green source. These same materials issues limit even more strongly the production of solid-state laser diodes at these wavelengths. We present a solution, based on the InAlGaP semiconductor system, for laser and LED devices operating in the wavelength range of 540 nm-600 nm.

The  $\text{In}_x\text{Ga}_{1-x}\text{P}$  alloy system has a maximum direct energy gap of 2.24 eV at  $x = 0.27$ <sup>121</sup>, corresponding to 554 nm emission. However, because this maximum direct energy gap occurs near the indirect bandgap-to-direct bandgap crossover, the ability of the material to efficiently convert carriers to photons is reduced. We believe that confinement in a strained- $\text{In}_x\text{Ga}_{1-x}\text{P}$  quantum-well active layer with  $x \geq 0.32$ , in conjunction with a fully transparent substrate, will compensate for this inherent inefficiency. This structure also offers promise for incorporation into semiconductor laser diodes with yellow emission. The fact that InGaP alloys in this composition range are not lattice-matched to any traditional substrate material has historically hindered their implementation. Through the use of optimized, relaxed, graded buffer virtual substrate technology<sup>43</sup>, we have lifted the lattice-matching constraint. Previous work in our group has produced  $\nabla_x[\text{In}_x\text{Ga}_{1-x}\text{P}]$  relaxed, graded buffers, where  $x$  grades from 0 to 0.2, with threading dislocation densities on the order of  $1 \times 10^6 \text{ cm}^{-2}$ , low enough for good light emitting devices<sup>40</sup>. These buffers allow us to integrate the strained-InGaP active region on a fully transparent GaP substrate. Similar structures have previously been examined by Bi, *et al.*<sup>122</sup> and Chin, *et al.*<sup>123</sup> Additionally, InGaP/InAlGaP heterostructures

integrated on absorbing GaAs substrates via graded GaAsP have been studied by Tanaka, *et al.*<sup>124</sup>, Lin *et al.*<sup>125</sup>, and Jou, *et al.*<sup>126</sup>

## 7.2 Materials Issues in Device Design

$\text{In}_x(\text{Al}_y\text{Ga}_{1-y})_{1-x}\text{P}$ , a common visible-light-emitting device material composed of alloys in the fully-miscible AlP-GaP-InP system, is utilized in varying proportions in this design. Using Equations 3.1-5 and the constants in Table 3.1, we can generate a contour plot of lattice constant and bandgap for any  $\text{In}_x(\text{Al}_y\text{Ga}_{1-y})_{1-x}\text{P}$  alloy, as shown in Figure 7.1 and detailed in Appendix C. The plot illustrates energy gap and lattice constant contours for the entire  $\text{In}_x(\text{Al}_y\text{Ga}_{1-y})_{1-x}\text{P}$  composition space as well as the boundary between indirect and direct bandgap regimes. This plot is a convenient reference for engineering a device with a transparent, indirect bandgap substrate and cladding that will interact minimally with light emitted by the strained-InGaP active region.

Of particular importance to this device structure is the behavior of the semiconductor bandgap; carrier recombination across the bandgap—when permitted—results in light emission. It is important to distinguish between bandgap,  $E_g$ , and direct ( $k=0$ ) energy gap,  $E_0$ . In a direct bandgap material,  $E_g$  and  $E_0$  coincide in wavevector; that is, the conduction band minimum directly overlies the valence band maximum in momentum space. In an indirect bandgap material, on the other hand, carriers at the conduction band minimum have a different wave vector than those at the valence band maximum. Direct bandgap materials readily convert electrically generated carriers into photons, while indirect bandgap materials require a phonon interaction that makes light emission improbable. However, an indirect material may absorb light across its direct energy gap,  $E_0$ , and this must be considered in the device design. Wavelengths of light that have a higher energy than the direct energy gap will be absorbed, while those with lower energy will be relatively unimpeded.

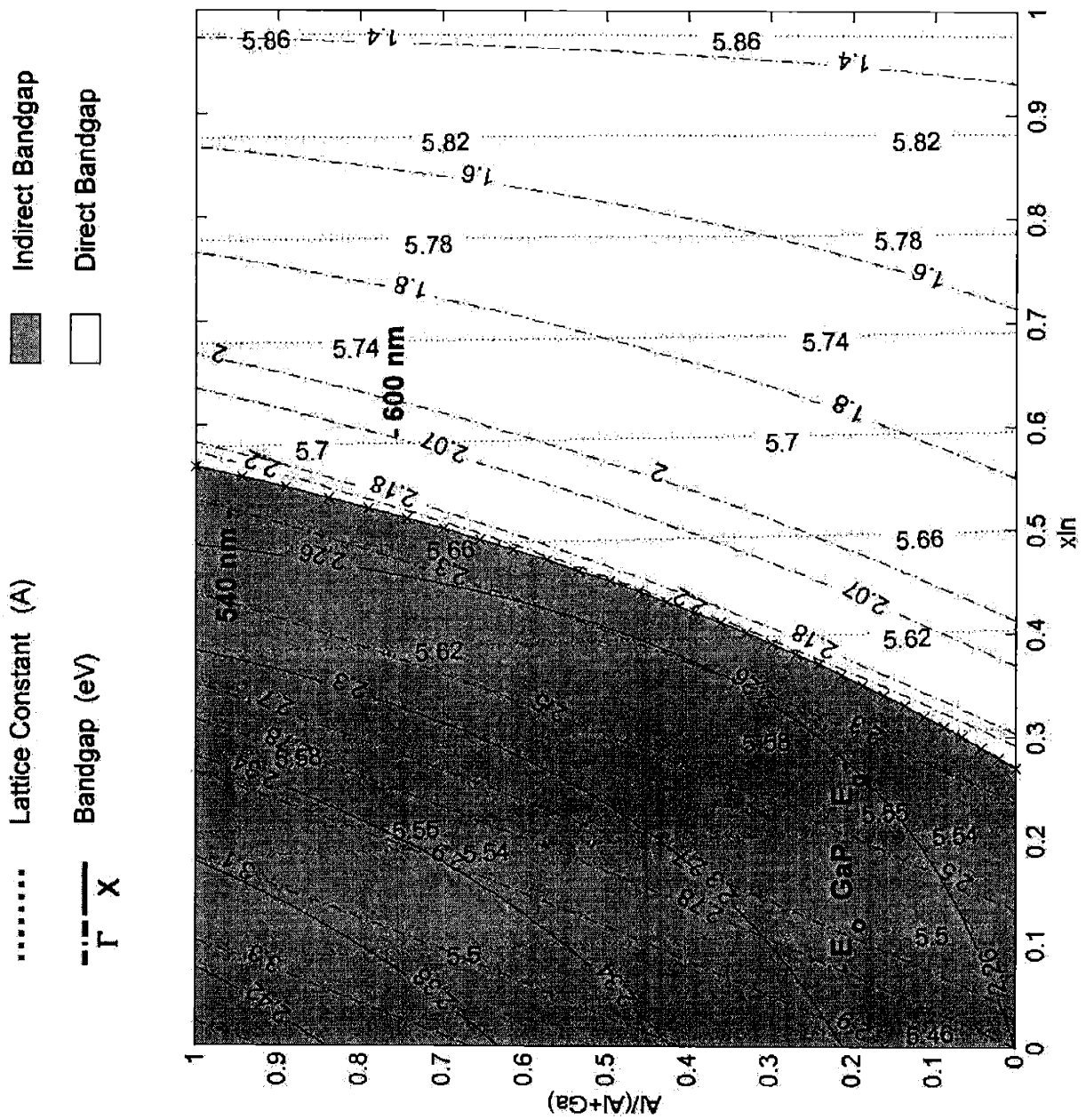


Figure 7.1.  $E_g$ ,  $E_o$  and lattice constant contours for the InAlGaP system.  $\Gamma$  refers to direct ( $k=0$ ) transitions, while X refers to indirect ( $k \neq 0$ ) transitions from the conduction band.

The indirect-direct bandgap crossover illustrated in Figure 7.1 is vital to the device design. As described in Chapter 3, the transition from indirect to direct is gradual. For  $\text{In}_{0.49}(\text{Al}_y\text{Ga}_{1-y})_{0.51}\text{P}$ , which crosses from direct to indirect at  $y \approx 0.53$ <sup>17</sup>, Cao, *et al*<sup>10</sup> measure a decrease in photoluminescence (PL) emission beginning near  $y = 0.35$ , as shown in Figure 7.2. PL intensity decreases by nearly an order of magnitude by the time  $y \approx 0.43$  is reached. Our device structure incorporates a strained- $\text{In}_x\text{Ga}_{1-x}\text{P}$  quantum-well active layer with  $x \geq 0.32$ . We believe that quantum confinement, in conjunction with a fully transparent substrate, will help compensate for the unavoidable loss of quantum efficiency near the indirect-direct crossover. In addition, compressively-strained InGaP quantum wells are predicted to have a low ground state density of states in the conduction band, leading to a reduced threshold current for lasing operation<sup>127</sup>.

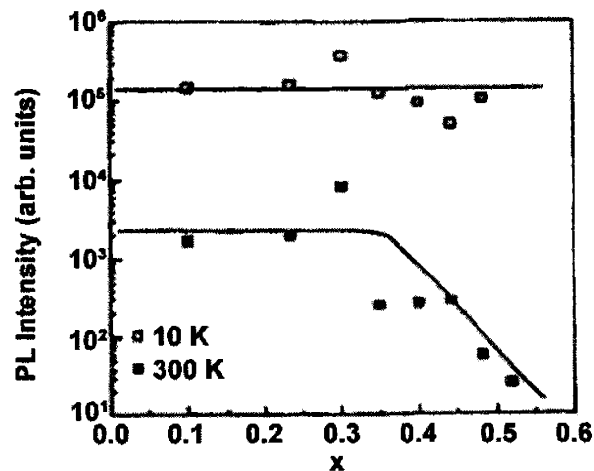


Figure 7.2. Decline in internal quantum efficiency with increasing Al fraction in  $\text{In}_{0.5}(\text{Al}_x\text{Ga}_{1-x})_{0.5}\text{P}$  (reproduced from Cao, *et al*<sup>10</sup>).

### 7.2.1 Relaxed Graded Buffer Epitaxial Transparent Substrate

$\text{In}_x(\text{Al}_y\text{Ga}_{1-y})_{1-x}\text{P}$  LED device fabrication has historically been constrained to deposition on substrates with the same lattice constant as the desired LED composition, usually GaAs<sup>2,4,17</sup>. Since GaAs absorbs visible wavelengths, the substrate is subsequently removed and the device is wafer bonded to transparent GaP<sup>4</sup>. A monolithically integrated

transparent substrate that eliminates the wafer bonding step would improve the economy of the fabrication process.

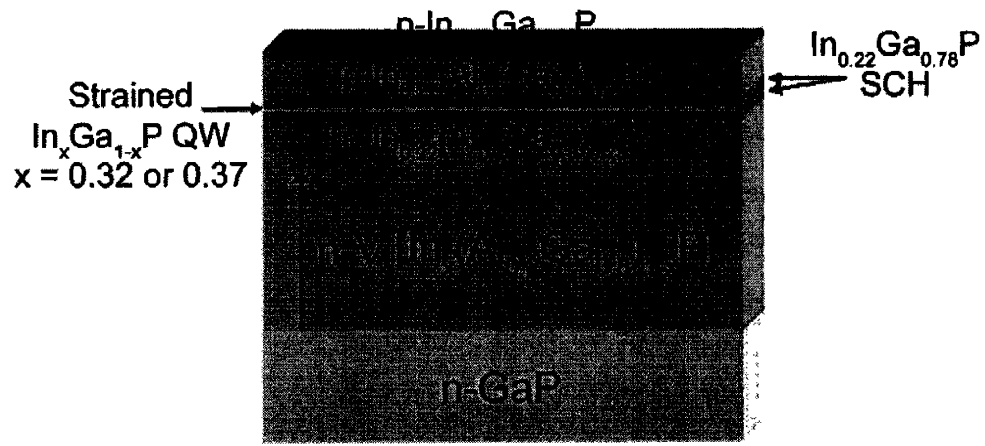
While GaP and AlP have nearly identical lattice constants, the lattice constant of InP is considerably larger. Any composition of AlGaP may be grown on a GaP substrate without introducing significant strain, but the introduction of In to the alloy will cause compressive strain to build in the epitaxial overlayer. Above a critical thickness, an array of misfit dislocations will nucleate to relieve this strain. Because a dislocation cannot terminate within a crystal, each misfit will be associated with two threading dislocations that travel from the mismatched interface to the film surface, passing through any overlying device region. Since dislocations act as non-radiative recombination sites, a high threading dislocation density in the active region may catastrophically reduce radiative recombination in the light-emitting device. Through the use of relaxed, graded buffer technology<sup>43</sup>, we can avoid the lattice-matching constraint.

### 7.2.2 Device Structure

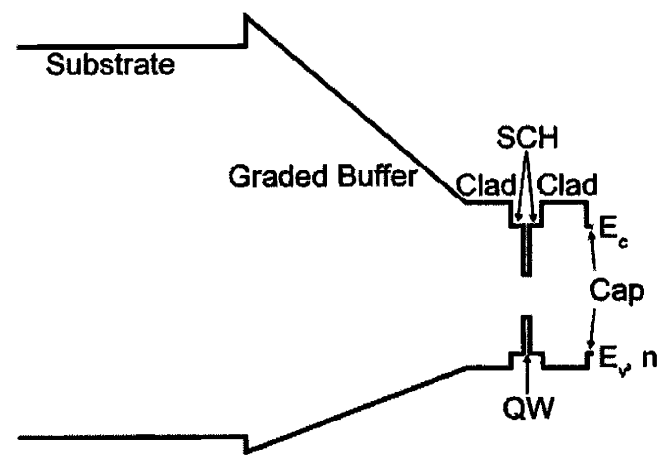
Device fabrication begins with MOCVD deposition of a 2  $\mu\text{m}$  or 4  $\mu\text{m}$  thick (-0.8% strain/ $\mu\text{m}$  or -0.4% strain/ $\mu\text{m}$ , respectively) n-type  $\nabla_x[\text{In}_x(\text{Al}_{0.2}\text{Ga}_{0.8})_{1-x}\text{P}]$  graded buffer, where  $x$  increases from 0 to 0.22, atop an n-type GaP substrate. The relaxed buffer is grown at 760°C, and the grading rate is chosen to be -0.8% strain/ $\mu\text{m}$  or -0.4% strain/ $\mu\text{m}$ , depending on the desired final threading dislocation density ( $\rho_{\text{TD}}$ ). The more conservative grading rate reproducibly yields a threading density on the order of  $7 \times 10^6 \text{ cm}^{-2}$ , while the faster rate produces approximately  $5 \times 10^7 \text{ cm}^{-2}$  threading dislocations, as measured by PVTEM. The buffer is doped with Si at  $1 \times 10^{18} \text{ cm}^{-3}$ .

The upper region of the  $\text{In}_{0.22}(\text{Al}_{0.2}\text{Ga}_{0.8})_{0.78}\text{P}$  cap layer serves as the lower, 400 nm-thick n-clad region of the device stack. The n-clad region is also grown at 760°C and is Si doped at  $3 \times 10^{18} \text{ cm}^{-3}$ . An undoped, aluminum-free 40 nm-thick  $\text{In}_{0.22}\text{Ga}_{0.78}\text{P}$  separate confinement heterostructure (SCH), lattice-matched to the clad, surrounds the device active region. The strained-quantum well active region consists of undoped  $\text{In}_x\text{Ga}_{1-x}\text{P}$ , where  $0.32 \leq x \leq 0.42$ , and is nominally 100 Å thick. The SCH and quantum well are grown at 650°C or 575°C. Depositing the SCH and quantum well at the same temperature leads to a continuous gas switching sequence, which greatly improves the

quality of the well, while the lower temperature is chosen to promote a planar quantum well. A p-type  $\text{In}_{0.22}(\text{Al}_{0.2}\text{Ga}_{0.8})_{0.78}\text{P}$  upper clad, of the same thickness as the lower n-clad and grown at  $760^\circ\text{C}$ , tops the device. The p-clad is doped with Zn at  $3 \times 10^{18} \text{ cm}^{-3}$ . The structure is capped with a thin, lattice-matched layer of heavily p-doped  $\text{In}_{0.22}\text{Ga}_{0.78}\text{P}$  to prevent oxidation of the aluminum-containing top clad. Schematics of this device structure, assuming an asymmetric type-I band offset<sup>4,72,128</sup>, are shown in Figure 7.3.



a)



b)



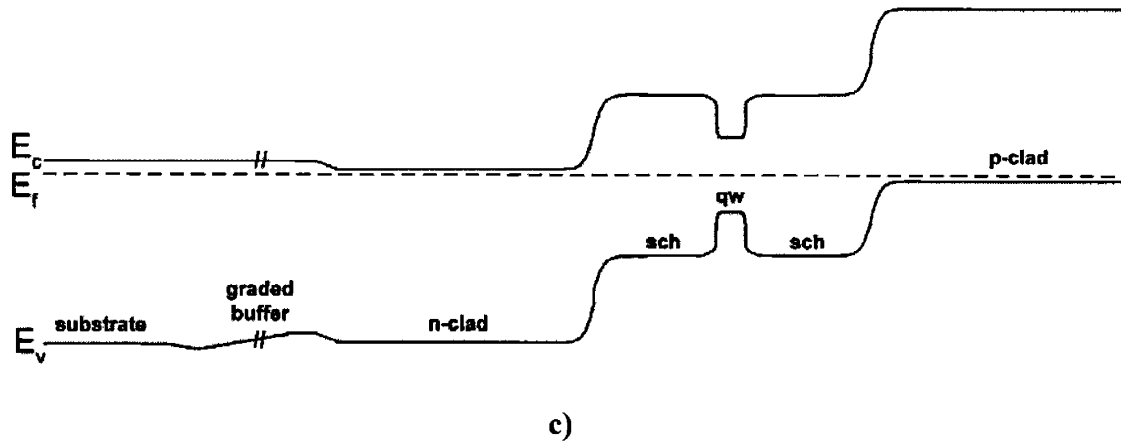


**Figure 7.3. Schematic of a) the device structure, b)  $E_c$ ,  $E_v$ , and refractive index variation in the device structure, c) the device energy levels in thermal equilibrium (not to scale).**

The indium fraction in the graded buffer increases as we approach the active region, with the highest indium fraction in the quantum well itself, leading to transparent virtual substrate and clad regions. Furthermore, the quantum well is the only layer with a direct bandgap, minimizing extraneous emission from or detrimental absorption in the surrounding material. Quantum confinement and compressive strain in the active region are expected to increase recombination energy and lead to shorter emission wavelengths and narrower linewidths than those accessible in the bulk<sup>129,130</sup>; additionally, compressive strain in the quantum well will improve carrier confinement and light output<sup>131,132</sup>. By using a direct bandgap, strained-InGaP quantum-well active region deposited on the virtual substrate described, we are in principle<sup>129</sup> able to produce wavelengths in the range of 540 nm-600 nm, as shown in Figure 7.4. The ability to create extremely thin quantum wells would enable even lower emission wavelengths, but an 80 Å thick quantum well is taken to be the practical lower limit for our deposition system.

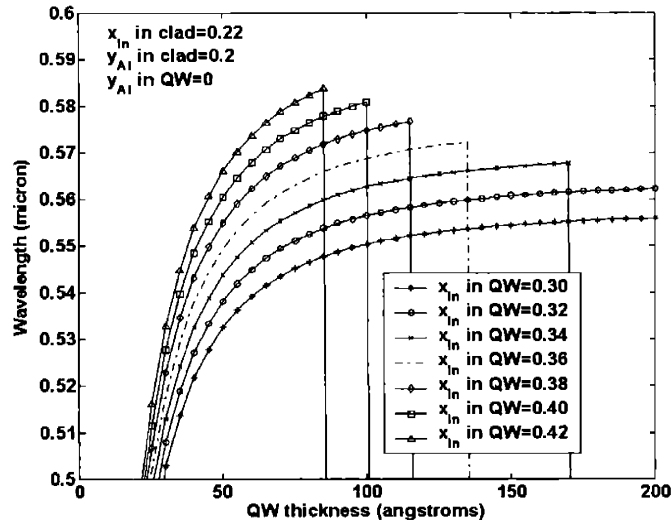


Figure 7.4. Predicted emission for sub-critical-thickness quantum well devices with  $\text{In}_{0.22}(\text{Al}_{0.2}\text{Ga}_{0.8})_{0.78}\text{P}$  clads and an aluminum-free strained quantum well.

### 7.2.3 Thermal Expansion

Thermal expansion mismatch is another source of strain that is often a concern for thin film epitaxy. Because the epitaxial film(s) and the substrate material often have different coefficients of thermal expansion, an alloy composition that would be lattice-matched to the substrate at room temperature will not necessarily be lattice-matched at growth temperature. For the LED structure described above, the film and substrate are intentionally mismatched at both room and growth temperatures, so it is more useful to think in terms of strain contributed by thermal expansion mismatch. We can see in Figure 7.5 that in our system thermal mismatch is expected to contribute an excess compressive strain of 0.04% between the GaP substrate and the  $\text{In}_{0.22}(\text{Al}_{0.2}\text{Ga}_{0.8})_{0.78}\text{P}$  clads, and an excess compressive strain of 0.03% between the GaP substrate and an  $\text{In}_{0.32}\text{Ga}_{0.68}\text{P}$  quantum well. Because this perturbation amounts to less than 2.5% and 1.5% of the overall strain, respectively, it is ignored in subsequent device design.

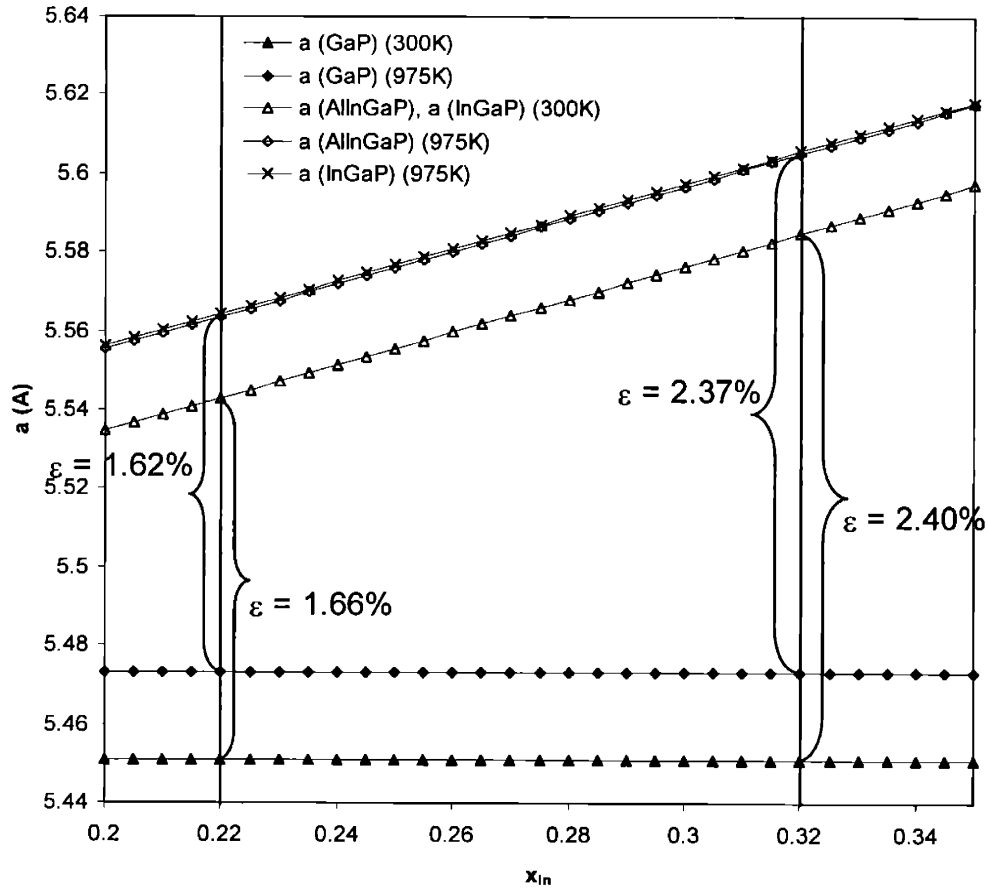


Figure 7.5. Strain contributed by thermal expansion mismatch between GaP and  $\text{In}_x(\text{Al}_{0.2}\text{Ga}_{0.8})_{1-x}\text{P}$ , and between GaP and  $\text{In}_{0.32}\text{Ga}_{0.68}\text{P}$ .

#### 7.2.4 Quantum Well Emission Model

To predict the wavelengths we can expect from the described device structure, as in Figure 7.4, we have adapted a model from Coldren and Corzine<sup>129</sup> that accounts for both quantum size effects and strain effects in the quantum well active region. Details of the simulation may be found in Appendix D; pertinent points are summarized below. We first determine the Matthews-Blakeslee critical thickness of the quantum well and set this as the upper limit of quantum well thickness. Because of the thermodynamic nature of the critical thickness model, it is likely that somewhat thicker quantum wells can be grown without misfit nucleation.

Next, we calculate the change in bulk energy gap,  $E_g$ , resulting from quantum size effects in the well. The unstrained band offsets,  $V_b$ , for the clad/well heterojunction are calculated assuming that the offset is taken up 70% in the conduction band and 30% in the valence band<sup>72,73</sup>. The ground state energy,  $E_b$ , for each carrier type in an infinite well is calculated as:

$$E_b \text{ (eV)} = \frac{3.76}{m_b} \cdot \frac{(100/l)^2}{1000}, \quad \text{Equation 7.1}$$

where subscript  $b$  refers to the electron, light hole, or heavy hole values,  $m_b$  is the effective mass of carrier  $b$  in the quantum well, and  $l$  is the quantum well thickness in Angstroms. These values are used to find the maximum quantum number,  $N_{max,b}$ , of the system:

$$N_{max,b} = \sqrt{\frac{V_b}{E_b}}, \quad \text{Equation 7.2}$$

The symmetric normalized quantum number in the well,  $N_b$ , is defined by the transcendental equation:

$$N_b = \frac{2}{\pi} \cdot \tan^{-1} \left( \frac{\sqrt{N_{max}^2 - N_b^2}}{N_b} \right), \quad \text{Equation 7.3}$$

and is used in conjunction with the ground state energy to determine the quantum well energy gap adjusted for quantum size effects,  $E_g'$ :

$$E_g' \text{ (eV)} = E_{g, \text{ bulk}} + \sum_b E_b \cdot N_b^2, \quad \text{Equation 7.4}$$

where, in this case,  $b$  refers to the electron or appropriate (higher energy) hole level.

Next, the effects of hydrostatic and shear strain in the quantum well are considered. The hydrostatic strain energy shift is defined as:

$$H \text{ (eV)} = -a_d \cdot 2 \cdot \frac{C_{11} - C_{12}}{C_{11} \cdot f}, \quad \text{Equation 7.5}$$

where  $a_d$  is the effective hydrostatic deformation potential in the quantum well,  $C_{11}$  and  $C_{12}$  are elastic constants of the quantum well, and  $f$  is the mismatch strain. We have assumed a fully-strained quantum well:

$$f = \varepsilon = \frac{a_{\text{clad}} - a_{\text{qw}}}{a_{\text{qw}}}, \quad \text{Equation 7.6}$$

where  $a_{\text{clad}}$  and  $a_{\text{qw}}$  refer to the lattice constants of the quantum well and clad layers. The shear strain energy shift is given by:

$$S \text{ (eV)} = -b_d \cdot \frac{C_{11} + 2C_{12}}{C_{11} \cdot f}, \quad \text{Equation 7.7}$$

where  $b_d$  is the effective shear deformation potential in the quantum well. Finally, the overall quantum well energy gap,  $E_g''$ , accounting for both quantum size and strain effects, is given by:

$$E_g'' \text{ (eV)} = E_g' + H + S. \quad \text{Equation 7.8}$$

Solutions to Equation 7.8 utilizing various combinations of clad and quantum well compositions demonstrate the flexibility in emission wavelength of this device design, as shown in Figure 7.6. If we elect to move closer to the direct bandgap region in the clad, as in Figure 7.7, wavelengths longer than 600 nm are obtainable. Because many of the materials constants assumed in the model, particularly the deformation potentials, are not

well known at these compositions, the output of the model must be taken as an approximate guide and not an exact prediction.

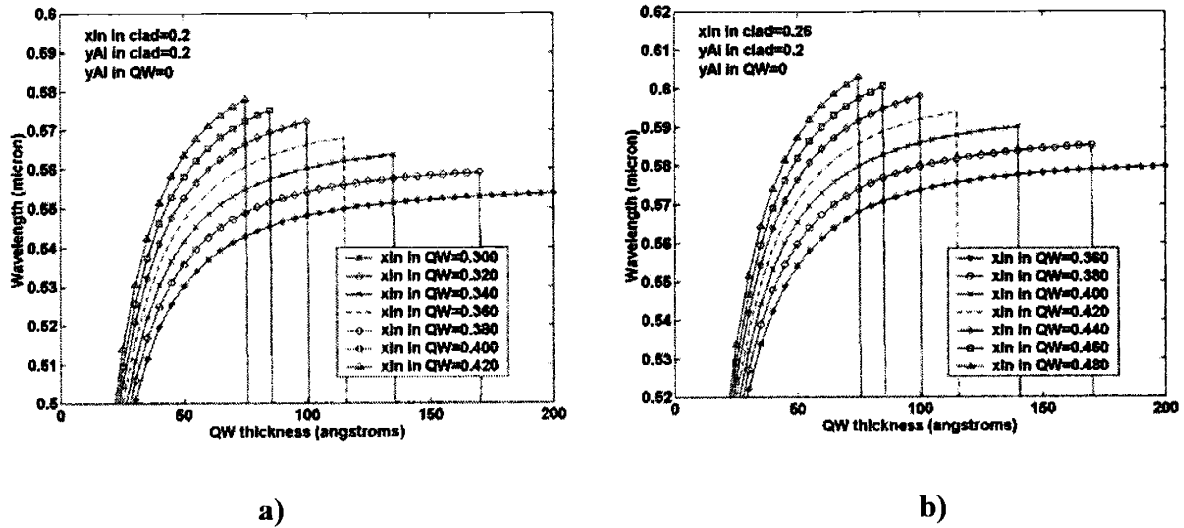


Figure 7.6. Predicted emission for sub-critical-thickness quantum well devices with a)  $In_{0.2}(Al_{0.2}Ga_{0.8})_{0.8}P$  clads and an aluminum-free strained quantum well, and b)  $In_{0.26}(Al_{0.2}Ga_{0.8})_{0.74}P$  clads and an aluminum-free strained quantum well.

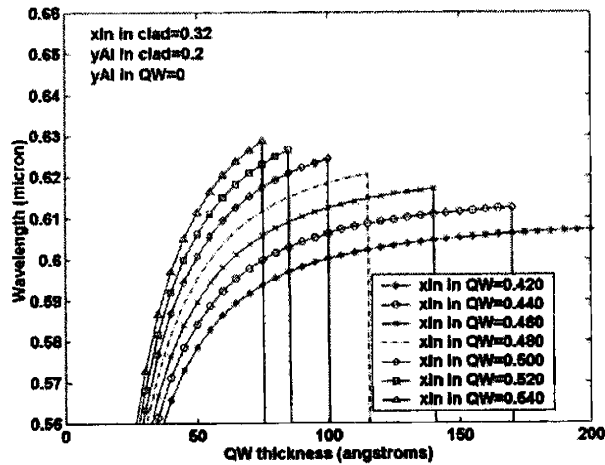
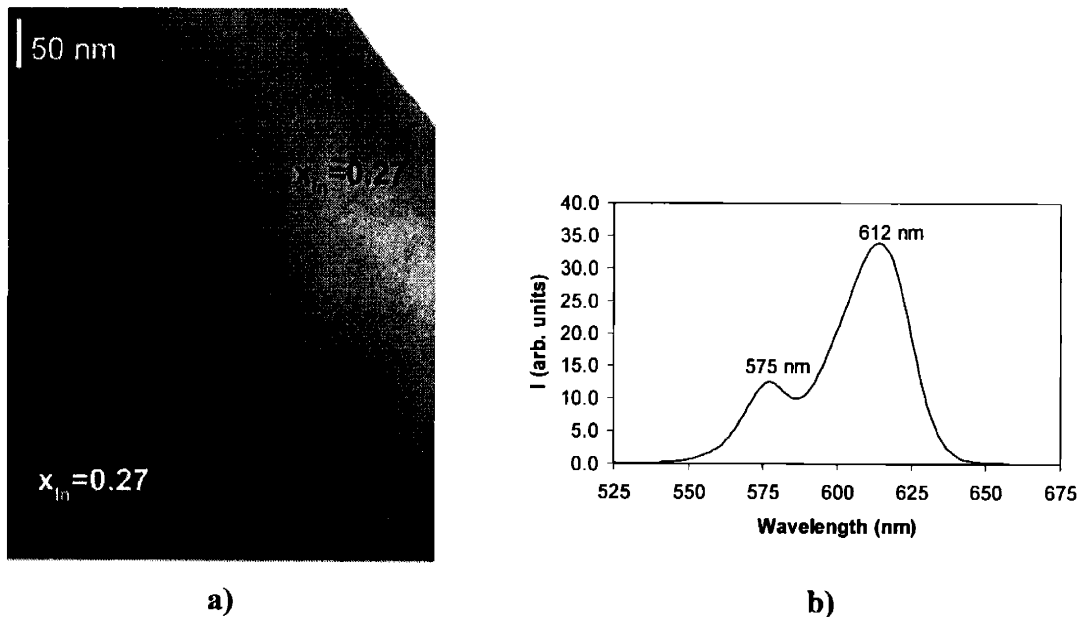


Figure 7.7. Predicted emission for sub-critical-thickness quantum well devices with  $In_{0.32}(Al_{0.2}Ga_{0.8})_{0.78}P$  clads and an aluminum-free strained quantum well.

### 7.3 Initial Results

The first generation of device structures in this study were deposited without the SCH described above. This proved to be deleterious for several reasons. First, the absence of an SCH leads to a decrease in carrier confinement in the active region. Second, and perhaps more importantly, in the absence of an SCH there must be a growth interruption both before and after quantum well deposition. During such interruptions, Group III precursor flow is halted, and the sample temperature is equilibrated. For this time, the sample surface is effectively subjected to annealing in the absence of deposition. This results in surface roughening which severely disrupts the morphology of the thin quantum well; many samples deposited in this manner failed to emit at all.

Emission was first observed in a sample with  $\text{In}_{0.27}\text{Ga}_{0.73}\text{P}$  clads and an  $\text{In}_{0.4}\text{Ga}_{0.6}\text{P}$  active layer, shown in Figure 7.8.



**Figure 7.8.** a) XTEM of a device structure with an undoped  $\text{In}_{0.4}\text{Ga}_{0.6}\text{P}$  active layer and undoped  $\text{In}_{0.27}\text{Ga}_{0.73}\text{P}$  clads. b) Cathodoluminescence emission from the active layer, at 612 nm, and from the clads, at 575 nm.

Figure 7.8a illustrates the poor quality of the quantum well for this growth sequence. The active layer is not a quantum well, but rather discontinuous platelets. This led to weak

active region emission, on the same order of magnitude as emission from the nearly-indirect clads, as shown in Figure 7.8b.

In light of these results, the device structure was altered to include a SCH deposited at the same temperature as the quantum well. In this way, the unavoidable growth interruptions associated with temperature equilibration are buried between the SCH and the clad regions, minimizing detrimental effects on the quantum well. Additionally, Al was introduced to the graded buffer and clads, as described above, to maximize transparency. Cathodoluminescence of undoped device structures, presented in Figure 7.9, shows strong emission at 570 nm for a quantum well composition of  $\text{In}_{0.35}\text{Ga}_{0.65}\text{P}$ . This is in reasonable agreement with the predicted 565 nm emission wavelength, and considerably shorter than the 590 nm emission expected<sup>28</sup> from bulk  $\text{In}_{0.35}\text{Ga}_{0.65}\text{P}$ . The improvement in performance with the introduction of the SCH and Al in the clad is evident.

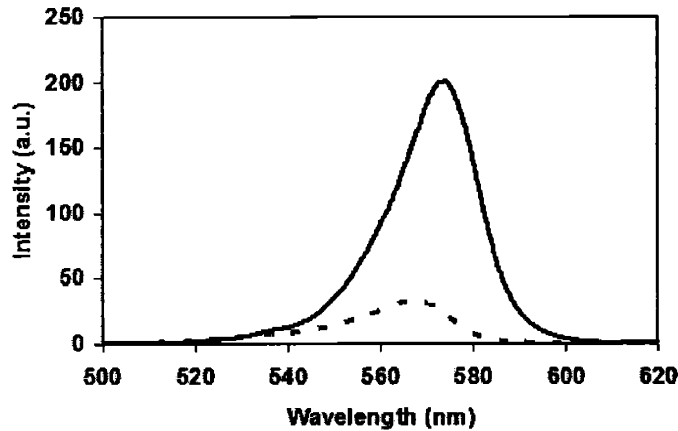


**Figure 7.9.** Cathodoluminescence emission from undoped, strained  $\text{In}_{0.35}\text{Ga}_{0.65}\text{P}$  quantum well device structures. —:  $\text{In}_{0.24}(\text{Al}_{0.2}\text{Ga}_{0.8})_{0.76}\text{P}$  clads and  $\text{In}_{0.24}\text{Ga}_{0.76}\text{P}$  SCH. - - -:  $\text{In}_{0.24}\text{Ga}_{0.76}\text{P}$  clads and no SCH.

In order to eliminate the  $\text{In}_{0.24}(\text{Al}_{0.2}\text{Ga}_{0.8})_{0.76}\text{P}$  clads and the  $\text{In}_{0.24}\text{Ga}_{0.76}\text{P}$  SCH as possible sources of the 570 nm emission seen in Figure 7.9, we have examined a device structure identical in all ways to the better emitter in Figure 7.9, with the exception that no quantum well is deposited. CL emission from this structure is shown in Figure 7.10.



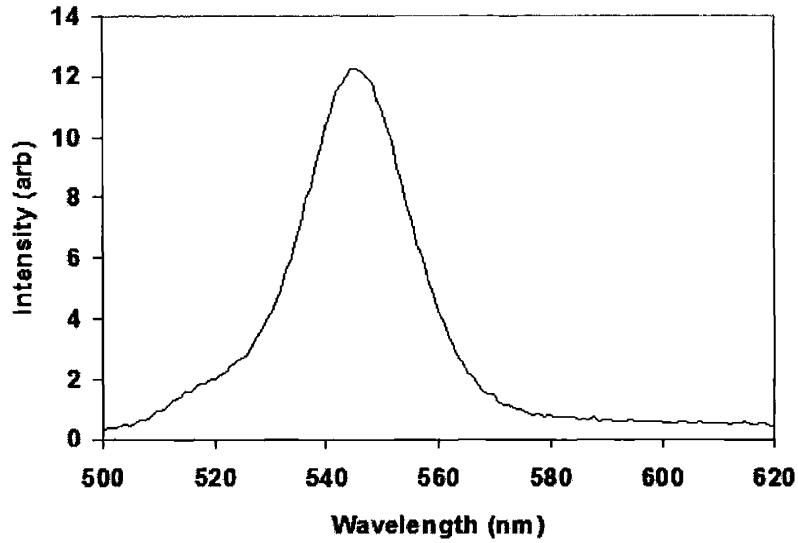


**Figure 7.10.** Cathodoluminescence emission from undoped device structure with  $\text{In}_{0.24}(\text{Al}_{0.2}\text{Ga}_{0.8})_{0.76}\text{P}$  clads and  $\text{In}_{0.24}\text{Ga}_{0.76}\text{P}$  SCH, but no quantum well.

We see that the device structure without a quantum well does emit light in CL, but at about 545 nm. The spectral shape in Figure 7.10 can be modeled extremely well as the sum of three Gaussians, shown in Figure 7.11.

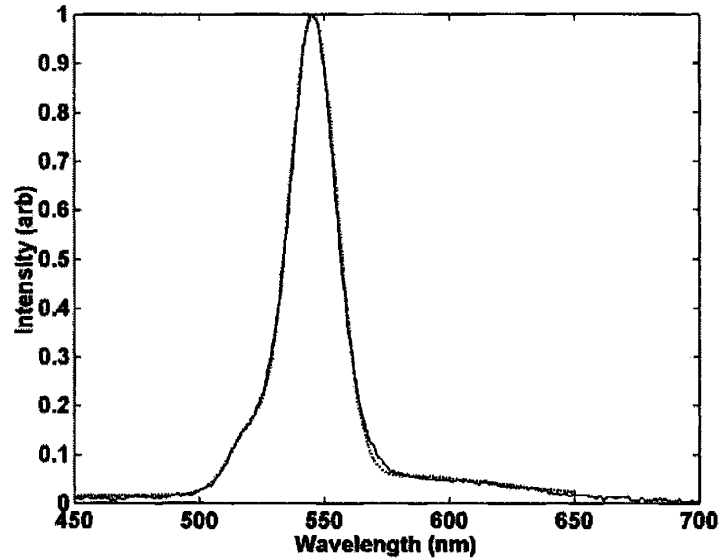


**Figure 7.11.** —: CL emission from sample shown in Figure 7.10, ---: Sum of Gaussian functions defined below in Table 7.1.

The individual contributions to the simulated spectrum are defined by:

$$I(\lambda) = \frac{P}{\sigma\sqrt{2\pi}} \cdot e^{-(\lambda-\lambda_{\mu})^2/2\sigma^2}, \quad \text{Equation 7.9}$$

where  $P$  is the relative magnitude,  $\sigma$  is the standard deviation, and  $\lambda_{\mu}$  is the peak wavelength. Coefficients for the Gaussian sum in Figure 7.11 are given in Table 7.1.

	<b>P</b>	<b><math>\sigma</math></b>	<b><math>\lambda_{\mu}</math></b>
<b>I<sub>1</sub></b>	1.2	9.5	545.5
<b>I<sub>2</sub></b>	0.12	8	519.5
<b>I<sub>3</sub></b>	0.2	38	582

**Table 7.1. Coefficients of Gaussian functions in Figure 7.11. I<sub>1</sub> represents  $\Gamma$  emission from the SCH, I<sub>2</sub> represents  $\Gamma$  emission from the clad, and I<sub>3</sub> is a broad background.**

The emission lineshape in Figure 7.9 may subsequently be reproduced with the addition of a Gaussian quantum well peak with  $P = 25$ ,  $\sigma = 7.5$ , and  $\lambda_{\mu} = 573.5$ , as shown in Figure 7.12.

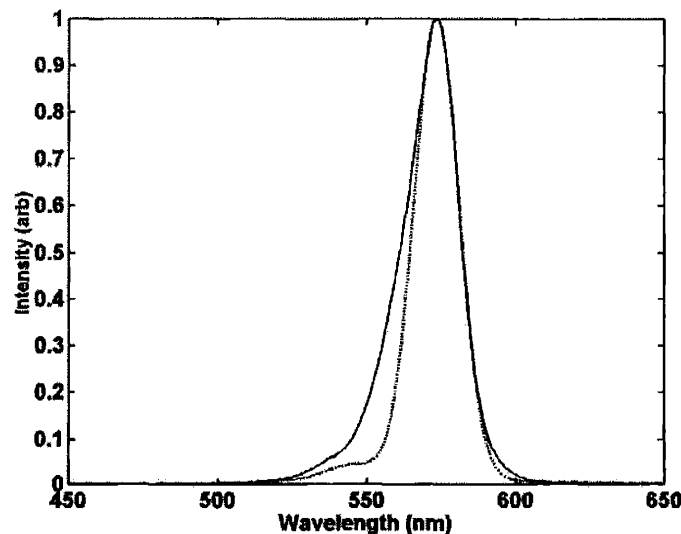


**Figure 7.12. —: CL emission from sample shown in Figure 7.9, ---: Sum of Gaussian functions representing all emission sources.**

Due to inhomogeneous broadening of the quantum well emission, the Gaussian model does not perfectly reproduce the emission lineshape of the device structure. However, Figure 7.12 strongly suggests that emission from sources other than the quantum well is limited to the weak shoulder present near 545 nm, while emission from the active region has a peak wavelength of about 573 nm and a FWHM of 18 nm.

## 7.4 Device Performance

Several of these device structures were deposited and good material quality was achieved. Cross-section transmission electron microscopy (XTEM) shows a continuous, planar quantum well region surrounded by clads that are free of microstructural defects, as shown in Figure 7.13.

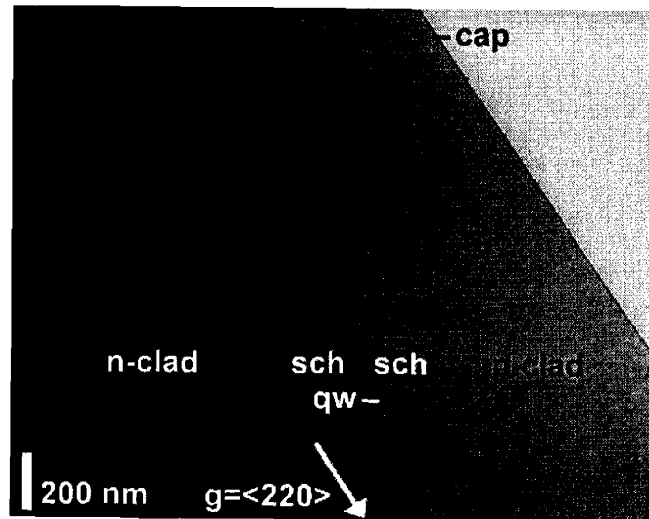


Figure 7.13. XTEM of device structure with  $\text{In}_{0.24}(\text{Al}_{0.2}\text{Ga}_{0.8})_{0.76}\text{P}$  clads,  $\text{In}_{0.24}\text{Ga}_{0.76}\text{P}$  SCH, and  $\text{In}_{0.35}\text{Ga}_{0.65}\text{P}$  quantum well. Emission from this structure is shown in Figure 7.9.

We have fabricated LEDs based on this device structure using a simple contacting scheme, shown in Figure 7.14. LED processing began with deposition of a thin Ti wetting layer followed by a 200 nm Au p-type contact on the front side of the device structure. The device was then manually thinned from the back side to a total thickness of 200  $\mu\text{m}$ , followed by deposition of a 350 nm Ni/AuGe/Ni n-type contact on the back side. To accommodate our LED testing apparatus, the chip was die-sawed to create

individual 300  $\mu\text{m}$  by 300  $\mu\text{m}$  dice. Electrical and radiometric characteristics of each device were obtained on a manual single-probe station under forward current operation.

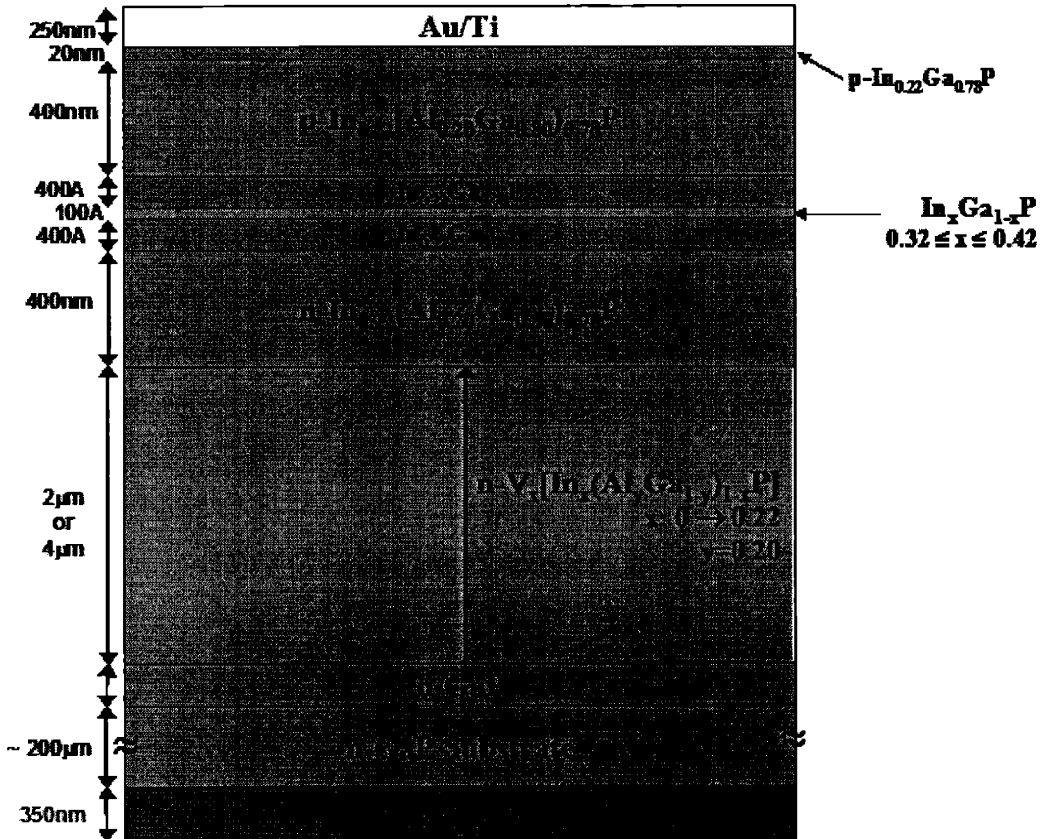


Figure 7.14. Schematic of the processed LED.

#### 7.4.1 Performance Variation with Threading Dislocation Density

By altering the strain rate in the graded buffer, devices were fabricated with different threading dislocation densities. Figure 7.15 shows a comparison of the spectral and power characteristics of devices grown at 650°C with an In<sub>0.32</sub>Ga<sub>0.68</sub>P quantum well. Device output power at 20 mA increased from 0.08  $\mu\text{W}$  per facet to 0.18  $\mu\text{W}$  per facet as threading dislocation density decreased from  $5 \times 10^7 \text{ cm}^{-2}$  to  $7 \times 10^6 \text{ cm}^{-2}$ . This dependence is expected, as threading dislocations are known to act as dark recombination centers. However, the relatively small increase in efficiency for such a large decrease in dislocation density suggests that the internal quantum efficiency is nearing the point at

which dislocation density is not limiting internal quantum efficiency. This transition from dislocation-dominated recombination to other recombination mechanisms has been modeled by Yamaguchi<sup>133</sup> and observed in GaAs on Si for solar cell applications<sup>109</sup>.

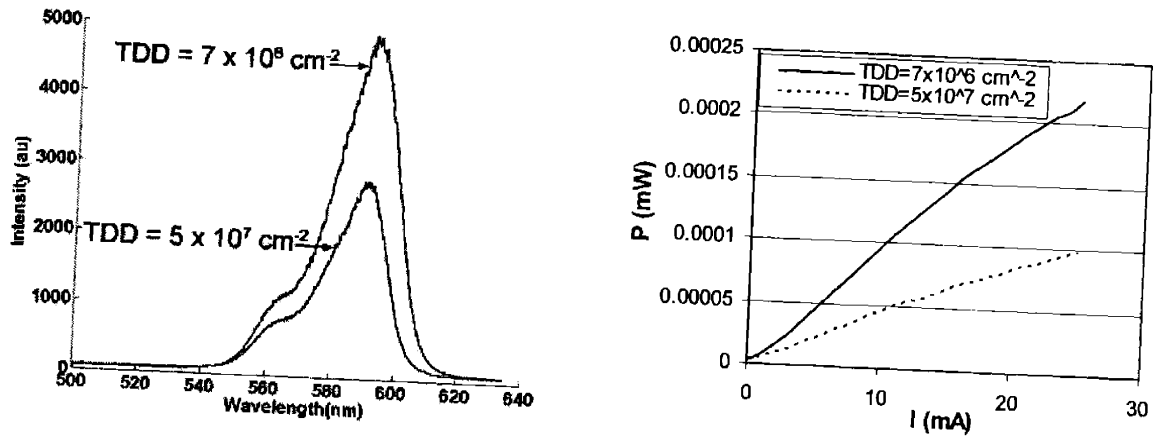
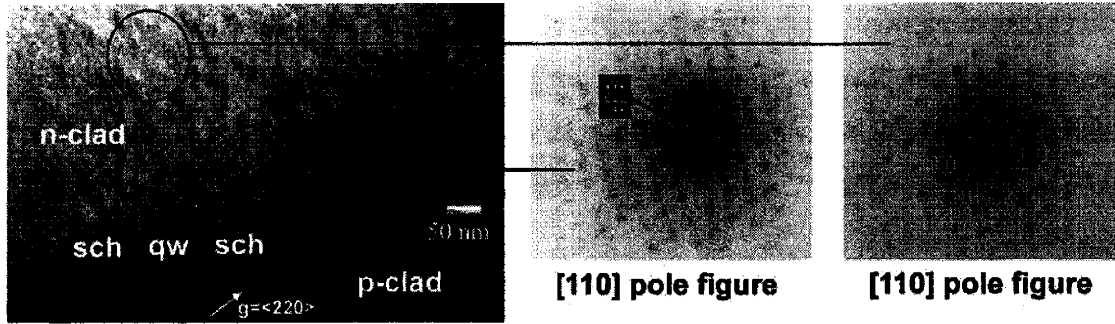


Figure 7.15. Spectral and optical power per facet characteristics of devices with the structure illustrated in Figure 7.14, grown at 650°C with an  $\text{In}_{0.32}\text{Ga}_{0.68}\text{P}$  quantum well active region and varying  $\rho_{\text{TD}}$ .

The spectral behavior of these  $\text{In}_{0.32}\text{Ga}_{0.68}\text{P}$  quantum well devices is noteworthy because emission at the predicted wavelength of 560 nm was weak and the devices emitted primarily at 590 nm. This lineshape was observed for both threading dislocation densities. Transmission electron diffraction reveals a probable mechanism for this deviation from the predicted wavelength. Diffraction superspots indicative of CuPt-B-type ordering are visible in electron diffraction from the quantum well, as shown in Figure 7.16. Such ordering is known to decrease the bandgap and thereby increase the emission wavelength of direct materials<sup>17,134</sup>. Emission may originate from both ordered and disordered domains in the quantum well, producing the two observed peaks.



**Figure 7.16. XTEM of a device with an  $\text{In}_{0.32}\text{Ga}_{0.68}\text{P}$  quantum well. Electron diffraction of the quantum well (center) shows ordering superspots, while the clad (right) does not.**

Yellow-green emission from both devices was clearly visible to the unaided eye in ambient room light. Emission from the quantum well was observed to escape throughout the thickness of the device stack, confirming the expected transparency of the virtual substrate and clads. Although the measurement system was not designed for the determination of luminous performance, we may approximate this important metric through the relations<sup>2</sup>:

$$\text{Luminous Efficacy (lm/W)} = \varphi_p / (I_f \cdot V_f), \text{ and} \tag{Equation 7.10}$$

$$\varphi_p = 683 \int_{\lambda} \varphi_e(\lambda) V(\lambda) d\lambda, \tag{Equation 7.11}$$

where  $\varphi_p$  is the photometric flux in lumens,  $\varphi_e$  is the radiometric flux in watts,  $V(\lambda)$  is the eye sensitivity curve shown in Figure 1.2,  $I_f$  is the device drive current, and  $V_f$  is the operating voltage. The approximation given in Chapter 3 is not valid here, due to the broadening of the device emission. Because there were discrete components for spectral and power measurement in the manual system that was used to characterize the devices, we must normalize Equation 7.11 by the arbitrary spectral intensity:

$$\varphi_p = \frac{683 P_0}{\int_{\lambda} I(\lambda) d\lambda} \cdot \int_{\lambda} I(\lambda) V(\lambda) d\lambda, \tag{Equation 7.12}$$

where  $P_0$  is the measured radiometric power and  $I(\lambda)$  is the device emission spectrum (like those shown in Figure 7.15) for a given  $I_f$ . Given these relations, and assuming good manual sample alignment during device testing, numerical integration allows us to determine that the  $0.18 \mu\text{W}$  per facet performance of the best device is approximately equivalent to a luminous efficacy of  $0.01 \text{ lm/W}$ . This is at best an order-of-magnitude calculation; however, it does demonstrate that the luminous efficacy of the device is three or four orders of magnitude lower than our goal. Factors that may have been detrimental to device performance will be discussed below.

#### 7.4.2 Performance Variation with Quantum Well Composition

Spectral and power characteristics for devices grown at  $650^\circ\text{C}$  with a threading dislocation density of  $5 \times 10^7 \text{ cm}^{-2}$  are shown in Figure 7.17. Device output power at  $20 \text{ mA}$  increased from  $0.06 \mu\text{W}$  per facet to  $0.08 \mu\text{W}$  per facet as indium fraction in the quantum well decreased from  $0.37$  to  $0.32$ . This power difference falls within the error in the measurement apparatus, indicating that changes in quantum well composition in this range do not strongly impact device power. This is promising in the sense that the use of  $\text{In}_{0.32}\text{Ga}_{0.68}\text{P}$  for the device quantum well does not lead to any degradation in performance, despite the fact that  $\text{In}_{0.32}\text{Ga}_{0.68}\text{P}$  lies closer to the indirect-direct bandgap transition than  $\text{In}_{0.37}\text{Ga}_{0.63}\text{P}$ .

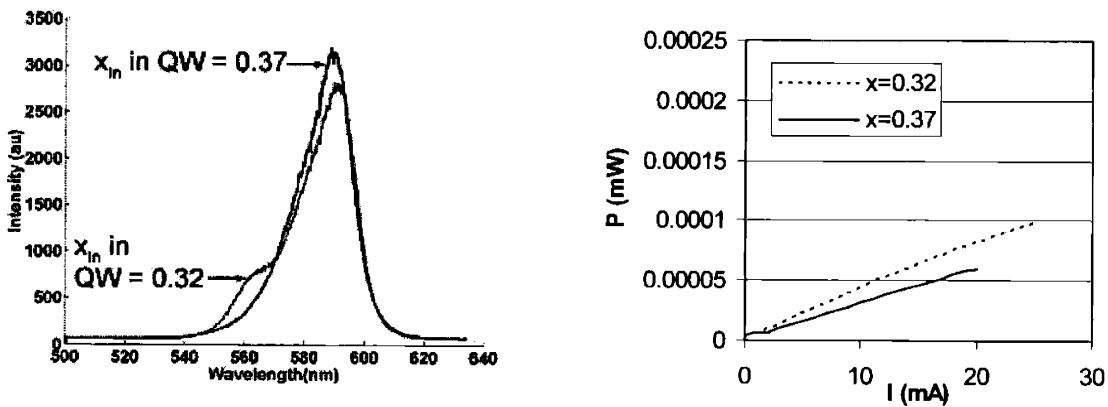
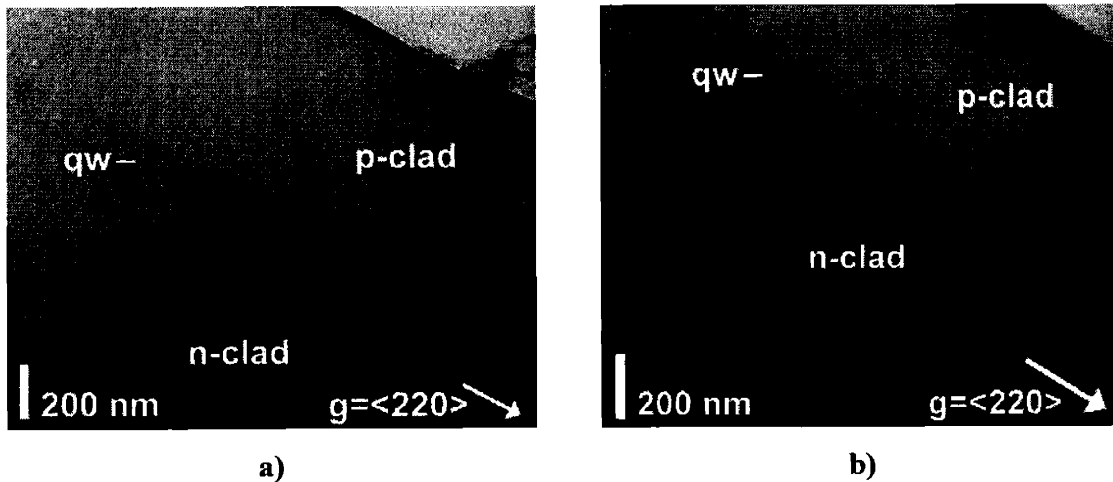


Figure 7.17. Spectral and optical power per facet characteristics of devices grown at  $650^\circ\text{C}$  with  $\rho_{\text{TD}} = 5 \times 10^7 \text{ cm}^{-2}$  and varying  $x_{\text{in}}$  in the quantum well.

For the device with  $x_{\text{In}} = 0.37$  in the quantum well, the primary emission wavelength of 588 nm is larger than the predicted 575 nm wavelength, again influenced by ordering and by a thicker than expected quantum well. The spectrum for this device does not exhibit the pronounced short-wavelength shoulder observed for the  $x_{\text{In}} = 0.32$  device. It is likely that the decreased V/III ratio during deposition, resulting from the increase in quantum well indium fraction, led to a decrease in the degree of ordering in the quantum well as measured by the change in bandgap. A small shoulder is present near 580 nm; however, the ordered and disordered emission peaks almost completely overlap. A similar result is observed in the  $\text{In}_{0.35}\text{Ga}_{0.65}\text{P}$  quantum well characterized via CL in Figure 7.9; however, the red shift in CL emission is less pronounced since the excited carriers are not preferentially channeled into the ordered regions.

#### 7.4.3 Performance Variation with Quantum Well Growth Temperature

We have also studied the effects of growth temperature on quantum well morphology and emission. Figure 7.18 shows XTEM micrographs of samples with active layer growth temperatures of 650°C and 575°C, both with  $x_{\text{In}} = 0.37$  in the quantum well and  $\rho_{\text{TD}} = 5 \times 10^7 \text{ cm}^{-2}$ .



**Figure 7.18.** XTEM of a device with an  $\text{In}_{0.37}\text{Ga}_{0.63}\text{P}$  quantum well and  $\rho_{\text{TD}} = 5 \times 10^7 \text{ cm}^{-2}$ . a) 650°C quantum well growth, b) 575°C quantum well growth. The ripple pattern in b) is an artifact of TEM foil preparation.



We can see from these images that the 650°C quantum well, Figure 7.18a, is slightly undulated, while the 575°C quantum well, Figure 7.18b, is relatively flat. This is consistent with kinetic considerations of adatom mobility during deposition, as mobility and therefore strain undulation are suppressed at lower growth temperatures. Spectral and power characteristics for these devices are shown in Figure 7.19.

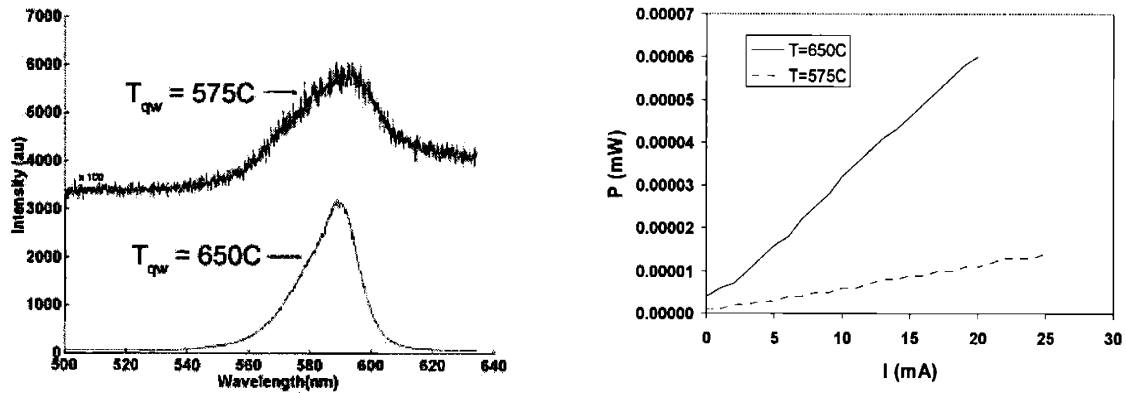


**Figure 7.19. Spectral and optical power per facet characteristics of devices grown with an  $\text{In}_{0.37}\text{Ga}_{0.63}\text{P}$  active layer,  $\rho_{TD} = 5 \times 10^7 \text{ cm}^{-2}$ , and varying quantum well growth temperatures.**

These devices emit at roughly the same wavelength, consistent with having the same quantum well composition. Despite undulation in the quantum well, the emitter grown at 650°C clearly outperforms the emitter grown at 575°C. One possible explanation for this is that while lower growth temperatures yield flatter interfaces, they also reduce the crystalline perfection of the film<sup>19</sup>. Because the adatoms have less ability to assume their ideal positions in the lattice before being buried, the overall quality of the film may be diminished, degrading device performance. Alternately, it may be that the quantum well undulation localizes carrier recombination within relaxed, smaller bandgap regions, making the effective carrier diffusion length shorter than the threading dislocation spacing. This would limit non-radiative carrier recombination at threading dislocations and improve the light output. A similar effect is believed to occur in III-Nitride light emitters.

#### 7.4.4 Longer-Wavelength Operation

Finally, in Figure 7.20, we compare the performance of an  $\text{In}_{0.42}\text{Ga}_{0.58}\text{P}$ -quantum well device grown at  $650^\circ\text{C}$  with  $\rho_{\text{TD}} = 5 \times 10^7 \text{ cm}^{-2}$  to similar devices shown in Figure 7.17.

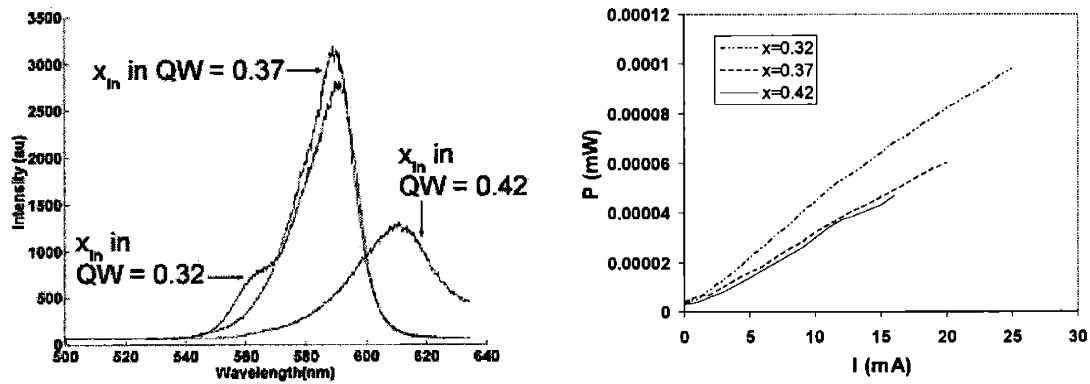


Figure 7.20. Spectral and optical power per facet characteristics of devices grown at  $650^\circ\text{C}$  with  $\rho_{\text{TD}} = 5 \times 10^7 \text{ cm}^{-2}$  and varying  $x_{\text{In}}$  in the quantum well.

While the peak performance of the  $\text{In}_{0.42}\text{Ga}_{0.58}\text{P}$  quantum well is relatively poor, its integrated power is comparable to the  $\text{In}_{0.37}\text{Ga}_{0.63}\text{P}$  quantum well as a result of broadening. Such broadening is undesirable, as it reduces color purity and is generally indicative of poor active layer quality. However, the spectral comparison allows us to reiterate that the lack of any consistent spectral features among these samples—in which only the quantum well properties vary—confirms that the distinctive emission of each device must originate from within the quantum well.

Characteristics of the devices detailed above are summarized in Table 7.2.

$x_{\text{qw}}$	$T_{\text{qw}}$ ( $^\circ\text{C}$ )	$\rho_{\text{TD}}$ ( $\text{cm}^{-2}$ )	Peak $\lambda$ (nm)	Secondary $\lambda$ (nm)	Power per facet @ 20mA ( $\mu\text{W}$ )
0.32	650	$7 \times 10^6$	590	560	0.18*
0.32	650	$5 \times 10^7$	590	560	0.08
0.37	650	$5 \times 10^7$	588	--	0.06
0.37	575	$5 \times 10^7$	588	--	0.013
0.42	650	$5 \times 10^7$	610	--	0.06

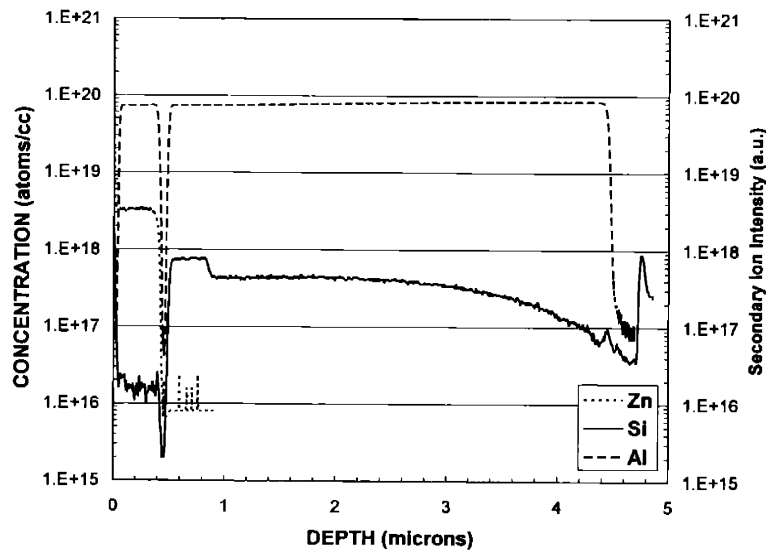
\*( $\sim 0.01 \text{ ImW}$ )

Table 7.2. Summary of LED results.

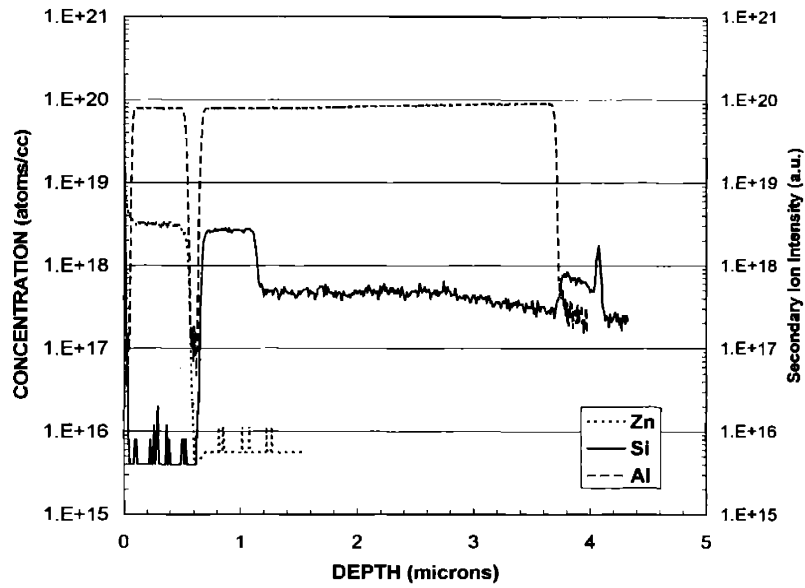
## 7.5 Non-idealities in Device Performance

### 7.5.1 Doping Control

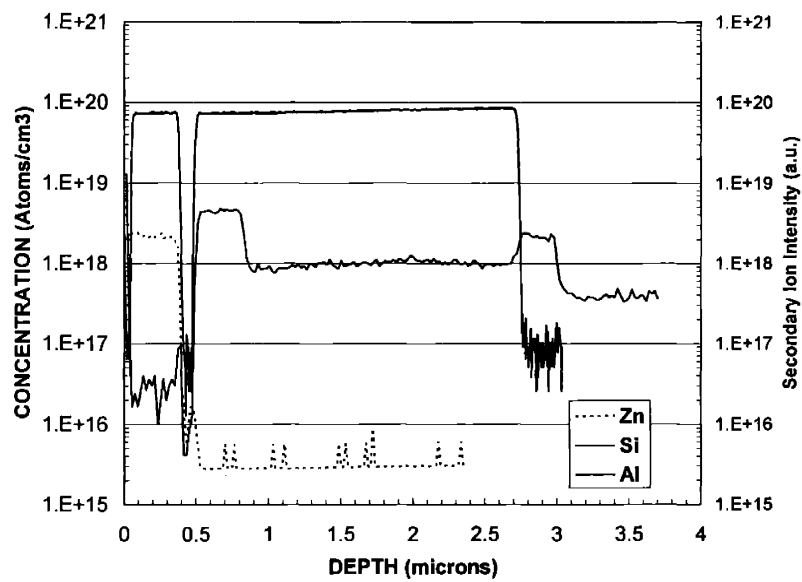
Precise control of doping in MOCVD-grown InAlGaP is difficult to achieve, particularly for the p-type Zn dopant<sup>12</sup>. Non-idealities in doping levels can severely degrade electrical, and consequently optical, device performance. An examination of drift in doping levels among different structures grown in our MOCVD system, Figure 7.21, illustrates this problem. All samples in Figure 7.21 were grown within two months of each other, and were nominally calibrated to produce identical doping levels. In Figure 7.21a, we can see that the n-type doping in the graded buffer, indicated by the introduction of Al, follows a smooth profile. However, the doping in the clad layers is quite asymmetric. In Figure 7.21b, the doping asymmetry in the clads has been resolved, but an unintended weak bipolar junction has appeared at the substrate/graded buffer interface. This junction may act as a barrier to current flow and diminish light output. Finally, in Figure 7.21c, the doping asymmetry in the clad layers has returned, and the weak bipolar junction in the backside is still present. Such unpredictable variations in device doping levels may lead to unexpected performance losses.



a)



b)



c)

Figure 7.21. Doping fluctuations via SIMS analysis of three quantum well device structures. a) and b) were deposited 2 months apart, while b) and c) were deposited one week apart.

### 7.5.2 Ordering

As discussed above and in Chapter 3, ordering in the active region is detrimental to the production of short-wavelength devices, since it has been observed to decrease the semiconductor bandgap by as much as 160 meV<sup>134</sup>. In an attempt to define the regimes of ordered and disordered quantum well growth in our system, bulk In<sub>0.32</sub>Ga<sub>0.68</sub>P samples were deposited at 650°C using various growth rates and V/III ratios, summarized in Table 7.3.

Growth Rate (Å/min)	V/III Ratio
515	15, 85, 150
131	85, 300, 500

**Table 7.3. Summary of growth conditions for In<sub>0.32</sub>Ga<sub>0.68</sub>P samples in the ordering study.**

Based on previous observations of In<sub>0.5</sub>Ga<sub>0.5</sub>P ordering made by Kurtz, *et al.*<sup>63</sup> and others<sup>17,19,134-136</sup>, we would expect ordering to disappear as V/III ratio is decreased or as growth rate is decreased. However, electron diffraction reveals the presence of ordering in all samples from Table 7.3. Two typical examples are shown in Figure 7.22. The appearance of pronounced streaks between superspots in Figure 7.22b is evidence of the degradation in crystalline perfection of the ordered domains given the higher growth rate<sup>48</sup>.

The observation of ordering over the range of growth rates and V/III ratios listed in Table 7.3 suggests that temperature is a dominant factor in ordering in our system, and a different quantum well growth temperature may be required to suppress the formation of ordered domains. Based on the observations of Zorn, *et al.*<sup>19</sup>, higher growth temperatures would be most favorable for the elimination of ordering; however, this may lead to undesirable degradation in the strained quantum well morphology.

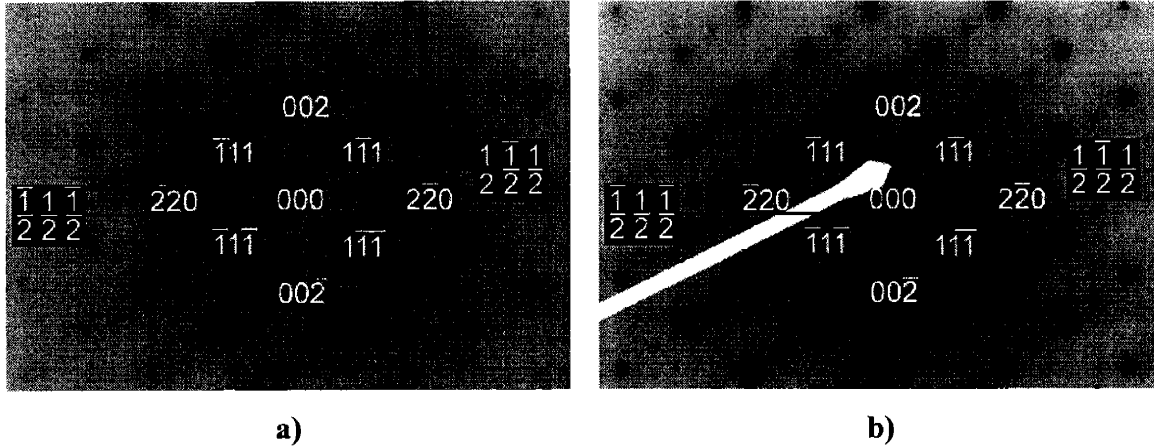


**Figure 7.22.** [110] Transmission Electron Diffraction of InGaP for V/III = 85 and a) Growth Rate = 131 Å/min, b) Growth Rate = 515 Å/min.

The marked dependence of ordering on growth conditions and the observed occurrence of ordering across the range of conditions studied above suggest that the reproducible elimination of ordering in the quantum well is not a trivial matter. However, an ordering-free regime of quantum well deposition must be unambiguously defined in order to achieve devices emitting at the shortest possible wavelengths.

## 7.6 Conclusions

A novel, visible LED based on the InAlGaP system was epitaxially integrated on a fully transparent substrate via MOCVD, fabricated using simple top and bottom contacts, and tested on a manual single-probe station. The LED structure is theoretically capable of emitting wavelengths from 540 nm (green) to 600 nm (amber). The best devices had  $\rho_{TD} = 7 \times 10^6 \text{ cm}^{-2}$  and an  $\text{In}_{0.32}\text{Ga}_{0.68}\text{P}$  quantum well active region. These devices operated at 0.18  $\mu\text{W}$  per facet at 20 mA, corresponding to a luminous efficacy of approximately 0.01 lm/W, with a primary wavelength of 590 nm and a secondary wavelength of 560 nm. Theory predicts a dominant emission wavelength near 560 nm. We believe that the observed spectral lineshape arises primarily from ordering in the quantum well active region, as observed by electron diffraction. Modification of the MOCVD growth conditions during quantum well deposition should suppress this ordering and allow us to recover the desired 560 nm emission. In addition, the use of

thinner quantum wells should substantially decrease the emission wavelength of future devices. While the output power of these emitters is relatively low, large increases in device power can likely be achieved with improved doping and contacting of the devices. Furthermore, the observed threading dislocation density of  $7 \times 10^6 \text{ cm}^{-2}$  from the graded buffer is higher than that of our best material and can be reduced.

Emission power decreases by nearly a factor of two for devices intentionally grown with an order-of-magnitude higher threading dislocation density of  $5 \times 10^7 \text{ cm}^{-2}$ . This behavior is consistent with the tendency of carriers to recombine nonradiatively at threading dislocations. Devices with  $\rho_{\text{TD}} = 5 \times 10^7 \text{ cm}^{-2}$  and an  $\text{In}_{0.32}\text{Ga}_{0.68}\text{P}$  quantum well active region operated at  $0.08 \mu\text{W}$  per facet, but exhibited the same 590 nm and 560 nm peaks and spectral lineshape as their counterparts with lower threading densities. Devices with  $\rho_{\text{TD}} = 5 \times 10^7 \text{ cm}^{-2}$  and an  $\text{In}_{0.37}\text{Ga}_{0.63}\text{P}$  quantum well operated at  $0.06 \mu\text{W}$  per facet at peak wavelength of 588 nm. The degree of ordering in devices with an  $\text{In}_{0.37}\text{Ga}_{0.63}\text{P}$  quantum well was reduced due to a decrease in V/III ratio during deposition, leading to a large overlap between ordered and disordered emission peaks. These device results confirm that the described LED structure enables us to fabricate devices emitting over a range of green-yellow wavelengths, and in the future may lead to high-brightness green LEDs and solid-state yellow laser diodes.





## 8 Summary of Results and Suggestions for Future Work

### 8.1 Overview

This work utilized the versatile MOCVD growth technique to fabricate and explore a range of InGaP- and InAlGaP-based heterostructures for optical device applications. The unifying ideology of the approach taken in this study is a vertical integration of basic materials research with novel device design and applications. Each experimental path sought to identify new or improved platforms for the integration of InGaP alloy compositions that are not lattice-matched to any common substrate materials. Lattice-mismatched integration of InGaP on GaP was achieved using  $\nabla_x[\text{In}_x\text{Ga}_{1-x}\text{P}]$  and  $\nabla_x[\text{In}_x(\text{Al}_y\text{Ga}_{1-y})_{1-x}\text{P}]$  relaxed graded buffers. In addition, initial modes of InGaP epitaxy on relaxed, graded  $\nabla_x[\text{Ge}_x\text{Si}_{1-x}]/\text{Si}$  virtual substrates were studied for the eventual monolithic integration of InGaP on Si. A central result was the identification of a mechanism for the formation of “branch defects”, a microstructure identified in InGaP that is detrimental to device performance. The formation of branch defects during MOCVD growth was attributed to surface-driven In clustering at the growth front. Finally, a novel strained-InGaP SCH quantum well ETS-LED device was designed and fabricated. This device design provides access to the 540 nm to 600 nm region of the visible spectrum using an Al-free InGaP active layer. Processed devices operated with emission near 560 nm and 590 nm and were clearly visible in ambient room light, despite non-idealities in processing. This is the first report of yellow LED emission from a strained-InGaP quantum well ETS-LED. In this chapter, the major results in each of these areas are reviewed. Finally, suggestions for future expansion upon these studies are discussed.

## 8.2 Summary of Results

### 8.2.1 InGaP Monolithic Integration with GeSi

Initial modes of InGaP epitaxy lattice-matched on GeSi were studied. Three-dimensional growth was observed under all MOCVD conditions, comprising a wide range of temperatures and V/III ratios. Island nucleation density was found to vary directly with V/III ratio and growth temperature. Pre-growth substrate cleaning produced no detrimental effects on the surface morphology, so wet etching inhomogeneities were eliminated as a source of three-dimensional growth. The effects of substrate thermal cycling in N<sub>2</sub>, H<sub>2</sub>, and H<sub>2</sub> plus PH<sub>3</sub> were examined. No surface degradation was observed for a N<sub>2</sub> ambient, while a slight increase in surface roughness occurred for a H<sub>2</sub> ambient. Thermal cycling in H<sub>2</sub> plus PH<sub>3</sub> led to a large increase in surface roughness and the formation of surface mesas. Thermodynamic calculations suggested that these mesas may be P clusters or GeP solid complexes. They may also be surface oxides formed in conjunction with water vapor in the growth chamber. Their presence prior to the initiation of epitaxy would disrupt monolayer growth, and a window wherein P coverage can be established without surface degradation must be identified. In addition, SIMS and CL data tentatively indicated that the incorporation of In into the InGaP film was suppressed at the GeSi interface, leading to a compositional gradient in the film and strain levels that could disrupt epitaxy. Finally, the luminescent properties of the observed InGaP islands were studied for potential InGaP quantum dot emitters on GeSi.

### 8.2.2 Microstructural Studies

In parallel with studies of InGaP integration on GeSi, investigations were continued into the microstructure and device properties of InGaP integrated on GaP substrates using a relaxed, graded InGaP buffer. The branch defect microstructure in InGaP was recently identified<sup>40</sup> and found to degrade LED performance. In this work, the properties of branch defects in InGaP graded buffers deposited on GaP were examined for a large number of growth and annealing conditions. Branch defects were observed in material produced by Lumileds in an industrial reactor. Branch defect properties in these samples correspond well to observations of similar samples produced at MIT; however, trends in surface roughness and threading dislocation density were

inconsistent with previous samples. This may be the result of unknown differences in MOCVD conditions such as reactor pressure, growth rate, or V/III ratio.

To explore the surface and/or bulk processes at work in branch defect formation, an *in-situ* annealing procedure was developed. Two types of *in-situ* anneals were performed. In the first, graded buffer deposition was interrupted for every 5% change in In fraction and the sample was annealed at elevated temperature before resuming growth. In the second, each of these annealed surfaces was capped with a thick constant-composition layer before resumption of graded buffer growth. In both cases, a final *in-situ* anneal was performed in the middle of the constant composition cap layer.

These studies confirmed that branch defect formation is driven by surface, and not bulk, processes. Subsurface branch defects are surface features that are “frozen” in by subsequent deposition and propagate through the thickness of the sample. Based upon the nucleation phase space of branch defects, wherein a larger compositional driving force is required at higher temperatures, we conclude that local clustering of In atoms is the mechanism for branch defect formation. This was corroborated by the suppression of branch defect formation under conditions of reduced adatom mobility, including low growth temperature and high V/III ratio. Finally, we demonstrate that dislocations gliding in the  $[1\bar{1}0]$  direction are preferentially blocked by strain fields arising from nearly- $[110]$ -oriented branch defects. This is further evidence for the link between branch defects and In clustering.

Once formed, In cluster size increases via surface diffusion-assisted nucleation and growth. Branch defects that are formed in the graded buffer are observed to diminish as a result of dislocation pipe diffusion. However, once a sufficient driving force for compositional fluctuation is established, the clustering has no path for redistribution and the defect becomes frozen in the bulk. With an understanding of these branch defect formation mechanisms, the development of branch defects in InGaP graded-buffer virtual substrates can be suppressed. This will improve the performance of devices integrated on InGaP graded buffer platforms.

### 8.2.3 Strained-InGaP Quantum Well ETS-LEDs

Low-threading-dislocation-density mismatched epitaxy makes available a nearly unlimited range of InGaP alloy compositions for device layers, an advantage utilized in this work for the design and fabrication of a novel strained-InGaP quantum well LED. This device design makes it possible to achieve yellow and green light emission without the incorporation of Al into the active region. In addition, the device virtual substrate and clads were selected to be inherently transparent to the quantum well emission for improved light extraction. The best devices had  $\rho_{TD} = 7 \times 10^6 \text{ cm}^{-2}$  and an  $\text{In}_{0.32}\text{Ga}_{0.68}\text{P}$  quantum well active region. These devices operated at  $0.18 \mu\text{W}$  per facet at 20 mA, corresponding to a luminous efficacy of approximately  $0.01 \text{ lm/W}$ , with a primary wavelength of 590 nm and a secondary wavelength of 560 nm. Electron diffraction studies showed that this spectral lineshape is a result of emission from ordered and disordered domains in the quantum well. Emission power decreased by about a factor of two in devices intentionally grown with an order-of-magnitude higher threading dislocation density of  $5 \times 10^7 \text{ cm}^{-2}$ . Such behavior is consistent with the tendency of carriers to recombine nonradiatively at threading dislocations. Devices with  $\rho_{TD} = 5 \times 10^7 \text{ cm}^{-2}$  and an  $\text{In}_{0.32}\text{Ga}_{0.68}\text{P}$  quantum well active region operated at  $0.08 \mu\text{W}$  per facet, but exhibited the same 590 nm and 560 nm peaks and spectral lineshape as their counterparts with lower threading densities. Devices with  $\rho_{TD} = 5 \times 10^7 \text{ cm}^{-2}$  and an  $\text{In}_{0.37}\text{Ga}_{0.63}\text{P}$  quantum well operated at  $0.06 \mu\text{W}$  per facet at peak wavelength of 588 nm. The degree of ordering in devices with an  $\text{In}_{0.37}\text{Ga}_{0.63}\text{P}$  quantum well was reduced due to an increase in V/III ratio during deposition, leading to a nearly complete overlap between ordered and disordered emission peaks. These results confirm that the device structure developed in this work fulfills our design goal; namely, an ETS-LED with an Al-free active region that emits over a range of yellow to green wavelengths.

## 8.3 Suggestions for Future Work

### 8.3.1 InGaP Monolithic Integration with GeSi

This work identified two primary obstacles to single-crystal epitaxy of InGaP on GeSi: substrate surface degradation from H<sub>2</sub> and PH<sub>3</sub> etching prior to epitaxy, and potential inaccuracies in lattice-matching arising from anomalously low In incorporation at the GeSi substrate surface. Future work in this area must develop an accurate calibration of In incorporation near the substrate to establish a constant, lattice-matched composition profile. Perhaps more difficult will be the definition of a window in which gas-phase etching of the substrate is suppressed while still establishing the proper V surface coverage for III-V epitaxy. The use of N<sub>2</sub> as the carrier gas during initiation may suppress catalysis of surface roughening reactions and improve growth morphology. In addition, it may be necessary to identify the shortest required exposure time for PH<sub>3</sub>, or to explore alternative P precursors. The phase space for initial epitaxy is tremendously complicated, including variables such as carrier gas and precursor selection, pre-deposition baking procedures, gas switching sequences, flow velocity, growth temperature, and V/III ratio. Identification of conditions that promote monolayer epitaxy of InGaP on GeSi is likely to be challenging, but will enable proportionally large advances in semiconductor technology.

### 8.3.2 Microstructural Studies

An important aspect of branch defect microstructure that remains to be understood is their evolution in Al-containing  $\nabla_x[\text{In}_x(\text{Al}_y\text{Ga}_{1-y})_{1-x}\text{P}]$  relaxed graded buffers. The incorporation of Al into the graded buffer is desirable for the maximization of LED substrate transparency. However, preliminary results suggest that the introduction of Al early in the graded buffer sequence augments branch defect formation and enhances dislocation blocking. In order to produce the best possible  $\nabla_x[\text{In}_x(\text{Al}_y\text{Ga}_{1-y})_{1-x}\text{P}]/\text{GaP}$  virtual substrates for InGaP LEDs, the Al profile in the graded buffer must be optimized with respect to transparency and defect evolution.

A direct confirmation of compositional fluctuation within branch defects would confirm the basic mechanism suggested by the results presented in this work. Such small

variations in In fraction are challenging to measure directly; however, the STM techniques reported by Feenstra<sup>66,115</sup> for the study of In clustering appear promising. Finally, it would be informative to study the occurrence of branch defect-like structures in other III-V systems, such as InGaAs, and compare their properties to those of branch defects in InGaP.

### **8.3.3 Strained-InGaP Quantum Well ETS-LEDs**

Perhaps the most vital improvement to the strained-InGaP quantum-well LED structure presented in this work will be the elimination of CuPt-B ordering from the quantum well active region. As long as ordering persists the shortest emission wavelengths will remain inaccessible. The mechanism of ordering is not fully understood, but it is believed to be driven by surface diffusion and related to P surface reconstruction during epitaxy. Under typical quantum well growth conditions in our system, ordering was observed over a wide range of V/III ratios and growth rates. The phase space for ordering must be mapped out to identify reproducible disordered quantum well growth conditions.

Defect densities in these devices were higher than expected. This is probably the result of the branch defect enhancement from Al in the graded buffer, as discussed above. Optimization of the InAlGaP graded buffer deposition sequence should allow us to recover the lower defect densities found in InGaP graded buffers having the same In fraction, improving internal device efficiency. Carrier confinement in the active region could be improved by increasing the Al content of the clad layers, so the flexibility to increase the amount of Al in the clad layers without incurring further defect multiplication would lead to improved device performance.

There is also a great deal of room for improvement on the processing side of the device design. Non-ideal doping profiles led to poor diode behavior in the devices, in many cases creating voltage overloads that prevented the devices from operating. Gains in device performance can be realized simply by eliminating these doping artifacts. Simple full-area top and bottom contacts were employed, blocking emission from the top and bottom faces. Insulator stripe and double-top contact configurations, illustrated in Figure 8.1, are currently being developed. These contacts should be implemented to

improve device extraction efficiency. Finally, structures utilizing thinner quantum wells and multiple quantum wells may lead to improvements in emission wavelength and power.

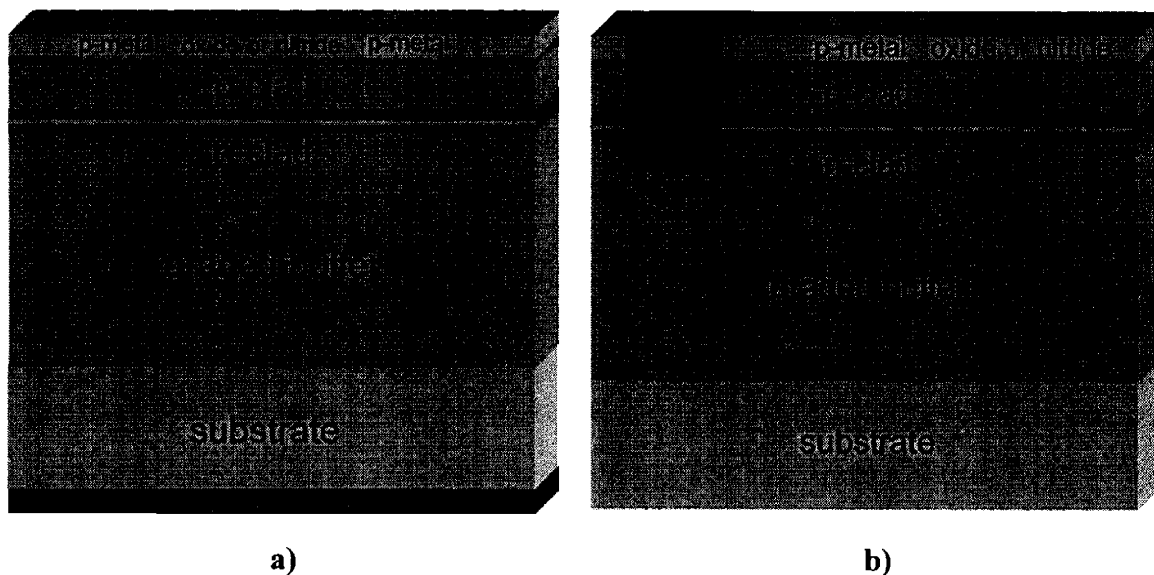


**Figure 8.1. Schematic of a) insulator-stripe contacts; b) double top contacts.**

The fundamental limiting factors in the development of high-brightness green LEDs in the InAlGaP system are the direct-to-indirect bandgap crossover problem and the O-related defects that are associated with high Al content in the active region. We believe that confinement within the Al-free InGaP quantum well active region, in conjunction with increased extraction due to the relaxed, graded buffer transparent substrate, will compensate for the reduction in internal efficiency expected at the compositions of interest for green LEDs, thus allowing for the production of a bright device. It is likely that the overall material quality and design of these devices can be improved to the extent that they are a viable option both for high-brightness green and yellow LEDs and for yellow lasers.





## Appendix A. Critical Thickness Calculation

```
%CRITHICQW.M
%Calculates the critical thickness of an InGaP thin film on an InGaP
cap layer.
%Can be modified for a GeSi cap layer.

%clear variables
clear

%Materials Parameters
ASi=5.431;
AGe=5.658;
AGaP=5.4505;
AInP=5.869;
C11Si=16.577e11;
C12Si=6.393e11;
C44Si=7.962e11;
C11Ge=12.60e11;
C12Ge=4.40e11;
C44Ge=6.77e11;
C11GaP=14.05e11;
C12GaP=6.20e11;
C44GaP=7.03e11;
C11InP=10.11e11
C12InP=5.61e11
C44InP=4.56e11

%In in the substrate
xIns=0.22;
%In in the film
xIno=0.42;

%Interpolated materials properties
C11o=(xIno*C11InP)+((1-xIno)*C11GaP);
C12o=(xIno*C12InP)+((1-xIno)*C12GaP);
C44o=(xIno*C44InP)+((1-xIno)*C44GaP);
C11s=(xIns*C11InP)+((1-xIns)*C11GaP);
C12s=(xIns*C12InP)+((1-xIns)*C12GaP);
C44s=(xIns*C44InP)+((1-xIns)*C44GaP);
Go=C44o-(2*C44o+C12o-C11o)/2;
Gs=C44s-(2*C44s+C12s-C11s)/2;
Y=C11o+C12o-2*C12o^2/C11o;
nu=C12o/(C12o+C11o);

%constants
A=(xIno*AInP)+((1-xIno)*AGaP);
As=(xIns*AInP)+((1-xIns)*AGaP);
b=2^.5/2*A;
beff=b/2;
D=(Go*Gs*b)/(3.1428*(Go+Gs)*(1-nu));
alph=60/180*3.1428;
f=abs((As-A)/A);

%initial guesses
```

```
hc1=0;
hc2=50;

%Iterate to find critical thickness
while(abs(hc1-hc2)>1)
    hc1=hc2;
    hc2=D*(1-nu*cos(alph)^2)*(log(hc1/b)+1)/(Y*f)
end

%prints answer
hc2
```

## Appendix B. Sample MOCVD Growth Sheets

Reactor Parameters	
Temperature	760°C
Temperature	1033K
Flow Rate	50.0
Flow Rate	5000 sccm
Time	20.00 min
Time	1200 sec

Gas Control Settings					
DMGa	10.0	30.0	26.0	2.35E-01	84.20%
DMGa			10.2	4.41E-02	15.80%
TGA			0.0	0.00E+00	0.00%
AsH3	100.0	0.0	0.0	0.00E+00	0.00%
PH3			100.0	1.38E+02	100.00%
DMZn	15.0	0.0	0.0	0.00E+00	0.00%
SiH4	15.0	0.0	0.0	0.00E+00	0.00%

Calibration					
	23.17	24.40			20.54
	0.694693	0.6000			1.1000
	1.3367	1.2316			1.5620

# AlInGaP Epitaxy

Element	Gas Molar	R Factor	Calculated
Al	0.00%	1.5620	0.00%
Ga	84.20%	1.0000	90.03%
In	15.80%	0.5900	9.97%
Zn	0.00%	0.0001	0.0E+00
Si	0.00%	0.0000	0.0E+00

<b>494</b>	
6168 $\mu\text{M}/\text{min}$	2.6E-2 atm
12 $\mu\text{M}/\text{min}$	2.8E-1 sccm
234485.6211	5.2E+3 sccm

<b>736 A/min</b>	4.41 $\mu\text{m}/\text{hr}$
<b>14715 A</b>	1.47 $\mu\text{m}$

<b>6.49219 A</b>
2.931%
1.596%
-0.759%
0.000%

2.567 eV	<b>483.6 nm</b>
0 meV	0.0 nm
0.00% Al	100.00% Ga

		-0.4%		0.2316051		5.7		31483 A						
1.9	2.0%	8	5200 A	0.59	650 A/min	8.13E-03	5.4589 A	650 A/min	4.00E-07	5.4505	0.41825	-2.2798	2.2773	-0.0309
2.8	2.7%	4	2685 A	0.59	650 A/min	1.10E-02	5.4618 A	668 A/min	-4.00E-07	5.4505	0.41825	-2.2798	2.3241	-0.0610
3.2	3.4%	2	1344 A	0.59	650 A/min	1.40E-02	5.4647 A	676 A/min	-4.00E-07	5.4505	0.41825	-2.2798	2.3400	-0.0770
3.9	4.1%	2	1356 A	0.59	650 A/min	1.71E-02	5.4677 A	684 A/min	-4.00E-07	5.4505	0.41825	-2.2798	2.3560	-0.0930
4.7	4.8%	2	1381 A	0.59	650 A/min	2.02E-02	5.4707 A	691 A/min	-4.00E-07	5.4505	0.41825	-2.2798	2.3722	-0.1091
5.4	5.5%	2	1394 A	0.59	650 A/min	2.34E-02	5.4737 A	697 A/min	-4.00E-07	5.4505	0.41825	-2.2798	2.3885	-0.1254
6.2	6.3%	2	1407 A	0.59	650 A/min	2.67E-02	5.4767 A	704 A/min	-4.00E-07	5.4505	0.41825	-2.2798	2.4049	-0.1419
7.7	7.7%	2	1421 A	0.59	650 A/min	3.00E-02	5.4798 A	710 A/min	-4.00E-07	5.4505	0.41825	-2.2798	2.4215	-0.1584
8.5	8.5%	2	1434 A	0.59	650 A/min	3.34E-02	5.4829 A	717 A/min	-4.00E-07	5.4505	0.41825	-2.2798	2.4382	-0.1751
9.4	9.2%	2	1449 A	0.59	650 A/min	3.70E-02	5.4860 A	724 A/min	-4.00E-07	5.4505	0.41825	-2.2798	2.4550	-0.1920
10.2	10.0%	20	14780 A	0.59	650 A/min	4.08E-02	5.4891 A	732 A/min	-4.00E-07	5.4505	0.41825	-2.2798	2.4720	-0.2090
							5.4923 A	739 A/min	-4.00E-07	5.4505	0.41825	-2.2806	2.4785	-0.2851



## Appendix C. Calculation of Figure 7.1: InAlGaP Properties

```

%alingap.m
%Generates a plot of lattice constant, Eo, and Eg contours with x(In)
as the x axis and y(Al) as the y axis.

%lattice constants of InP, GaP, AlP
aInP=5.8697;
aGaP=5.4505;
aAlP=5.4672;

%generate arrays, x=x(In), y=y(Al)=Al/Al+Ga, q=compositions for
indirect-direct boundary calculation
x=0:.01:1;
y=0:.01:1;
q=0.27:.01:0.56;

%Calculate Direct/Indirect Boundary
p=zeros(1,30);
for k=1:length(q)
    p(k)=0.44*((q(k)-0.27)/(0.29-.29*q(k))); %linear interpolation
between 27%In InGaP and 56%In InAlP
end

% Calculate lattice constants and bandgaps over mesh region (x,y)
% Bandgap models from H. C. Casey and M. B. Panish, Heterostructure
Lasers Pt. B., and
% D. P. Bour, J. R. Shealy, G. W. Wicks, and W. J. Schaff, Applied
Physics Letters 50, 615-17 (1987).

m=length(x);
n=length(y);
eg=zeros(101,101);
a=zeros(101,101);
egi=zeros(101,101);
for i=1:m
    for j=1:n
        eg(j,i) = ((1.351+1.83*(1-x(i))+0.38*(1-x(i))*(1-
x(i)))*y(j))+((1.351+0.643*(1-x(i))+0.786*(1-x(i))*(1-x(i)))*(1-y(j)));
        a(j,i) = (x(i)*aInP)+((y(j)-x(i))*y(j))*aAlP+((1-x(i)-
y(j)+x(i)*y(j))*aGaP);
        egi(j,i) = (((2.45-2.058)*(1-x(i)))+2.058)*y(j)+(((2.26-
2.183)*(1-x(i)))+2.183)*(1-y(j)); %continuous with direct at
crossover
    end
end

%generate intervals for contour plotting
t=[2.3:.2:3.5,2.78];
u=[2.26:.04:2.44];
v=[1.351,1.4:.2:2.2,2.07,2.18];
w=[5.46:.04:5.88,5.55];
z=[2.07:0.01:2.3];

```

```

%Shade indirect region
q2=cat(2,[0,0],q);
p2=cat(2,[1,0],p);

fill(q2,p2,[.8 .8 .8])

hold on

% Shade QW wavelengths
[B,j] = contour(x,y,eg,z,'g');

hold off

hold on

% Plot direct gap contours
[B,j] = contour(x,y,eg,v,'c');
clabel(B,j);

% Plot Eo contours
[C,h] = contour(x,y,eg,t,'--c');
clabel(C,h);

% Plot indirect gap contours
[E,f] = contour(x,y,egi,u,'w');
clabel(E,f);

% Plot lattice constant contours
[D,g] = contour(x,y,a,w,'r');
clabel(D,g);

%Plot indirect/direct boundary
plot(q,p,'x k')

hold off

%set plot styles
axis([0 1 0 1])
xlabel('xIn')
ylabel('Al/(Al+Ga)')

```



## Appendix D. Calculation of Predicted InGaP Strained Quantum Well Emission

```

%QWModel.m
%Predicts emission wavelengths for a strained InGaP quantum well (based
on Coldren and Corzine)

clear all

%calls materials data file and parameters of device structure
materialfile
parameterfile

%percent In in QW
xIn = [0.42:.02:0.54];
NumIn = length(xIn);

%quantum well thickness (in Angstroms)
l = [200:-5:20];
Numl = length(l);

for (m=1:NumIn)                                %iterates over xIn values
    for (n=1:Numl)                                %iterates over thickness(l)
        values
            if (l(n) < 1.5*Crithicqw(xIn(m)) & yf < indirect(xIn(m)))
%checks for direct bandgap and subcritical thickness
                Eg(m,n) = QWEnergy(xIn(m), l(n));
%calculates deltaEg due to QW effects
                EgQW(m,n) = QWStrain(Eg(m,n), xIn(m));
%adds deltaEg due to strain effects
                Wavelength(m,n) = 1.24/EgQW(m,n);
            end
        end
    end

%Sets plot style options
figure('DefaultAxesColorOrder',[0 0 0],'DefaultAxesLineStyleOrder','-
*|-o|-x|-.|-d|-s|^')
%, 'LineStyleOrder', '-*|-+|-s|-d|-v')
%set(gca,'LineStyleOrder', '-*|-+|-s|-d|-v')
plot(l,Wavelength)
axis([0 200 0.56 0.66])
myticks=.56:.01:.66;
set(gca,'YTick',myticks)
ylabel('Wavelength (micron)')
xlabel('QW thickness (angstroms)')

%automatically generates a legend of QW compositions
legarr=[];
for (m=1:NumIn);                                %iterates over xIn values
    if (yf < indirect(xIn(m)));
        double(xIn(m));
    end
end

```

```
        leg1= strcat('xIn in QW=',num2str(double(xIn(m)),'%1.3f'));
        legarr=[legarr;leg1];
    end
end
legend(legarr);

%generates a second legend with device parameters
xc
txt1=strcat('xIn in clad=',num2str(xc));
txt2=strcat('yAl in clad=',num2str(yc));
txt3=strcat('yAl in QW=',num2str(yf));

text(10,.655,txt1);
text(10,.65,txt2);
text(10,.645,txt3);

fprintf('done\n')
```

```

%Materialfile.m

%Physical constants for materials used in the device structure (Ga=GaP,
In=InP, Al=AlP)

%lattice constants
Aga = 5.4505;           %GaP lattice constant
Ain = 5.8697;          %InP lattice constant
Aal = 5.4672;          %AlP lattice constant

%mechanical constants
C11ga = 14.05e11;      %GaP mechanical constants
C12ga = 6.20e11;
C44ga = 7.03e11;
C11in = 10.11e11;     %InP mechanical constants
C12in = 5.61e11;
C44in = 4.56e11;
C11al = 13.30e11;     %AlP mechanical constants
C12al = 6.3e11;
C44al = 6.15e11;

%effective masses (* rest mass)
meGa = 0.13;           % transverse
mhhGa = 0.79;
mlhGa = 0.14;
meIn = 0.08;
mhhIn = 0.85;
mlhIn = 0.089;
meAl = 0.22;
mhhAl = 0.8;          %This is a guess, no reference
mlhAl = 0.155;

%Bandgaps (in eV at 300K)
EgGa = 2.26;
EgIn = 1.35;
EgAl = 2.45;

%deformation potentials (in eV) from Adachi
aGa = -3.0;
bGa = -1.5;
aIn = -2.9;
bIn = -2.0;
aAl = -3.0;
bAl = -1.5;

```



```
%parameterfile.m
%Assigns Al and In content to clad and Al content to QW
xc = 0.32;      %In in clad
yc = 0.2;      %Al/Al+Ga in clad
yf = 0;        %Al/Al+Ga in film
```



```

%CRITHICQW.M
%Calculates the critical thickness of an InGaP thin film on an InGaP
cap layer.
%Can be modified for a GeSi cap layer.

%clear variables
clear

%Materials Parameters
ASi=5.431;
AGe=5.658;
AGaP=5.4505;
AInP=5.869;
C11Si=16.577e11;
C12Si=6.393e11;
C44Si=7.962e11;
C11Ge=12.60e11;
C12Ge=4.40e11;
C44Ge=6.77e11;
C11GaP=14.05e11;
C12GaP=6.20e11;
C44GaP=7.03e11;
C11InP=10.11e11
C12InP=5.61e11
C44InP=4.56e11

%In in the substrate
xIns=0.22;
%In in the film
xIno=0.42;

%Interpolated materials properties
C11o=(xIno*C11InP)+((1-xIno)*C11GaP);
C12o=(xIno*C12InP)+((1-xIno)*C12GaP);
C44o=(xIno*C44InP)+((1-xIno)*C44GaP);
C11s=(xIns*C11InP)+((1-xIns)*C11GaP);
C12s=(xIns*C12InP)+((1-xIns)*C12GaP);
C44s=(xIns*C44InP)+((1-xIns)*C44GaP);
Go=C44o-(2*C44o+C12o-C11o)/2;
Gs=C44s-(2*C44s+C12s-C11s)/2;
Y=C11o+C12o-2*C12o^2/C11o;
nu=C12o/(C12o+C11o);

%constants
A=(xIno*AInP)+((1-xIno)*AGaP);
As=(xIns*AInP)+((1-xIns)*AGaP);
b=2^.5/2*A;
beff=b/2;
D=(Go*Gs*b)/(3.1428*(Go+Gs)*(1-nu));
alph=60/180*3.1428;
f=abs((As-A)/A);

%initial guesses
hc1=0;
hc2=50;

%Iterate to find critical thickness

```

```
while(abs(hc1-hc2)>1)
    hc1=hc2;
    hc2=D*(1-nu*cos(alph)^2)*(log(hc1/b)+1)/(Y*f)
end

%prints answer
hc2
```



```

%QWEnergy.m

function Eg = QWEnergy(xIn, l)
%calculates effective bandgap for a QW given the Indium concentration
and well thickness

%calls materials data file and parameters of device structure
MATERIALFILE
parameterfile

%effective masses of electrons and holes in QW
mefInAlP = (xIn*meIn)+((1-xIn)*meAl);
mefInGaP = (xIn*meIn)+((1-xIn)*meGa);
mef=(yf*mefInAlP)+((1-yf)*mefInGaP);

mlhfInAlP = (xIn*mlhIn)+((1-xIn)*mlhAl);
mlhfInGaP = (xIn*mlhIn)+((1-xIn)*mlhGa);
mlhf=(yf*mlhfInAlP)+((1-yf)*mlhfInGaP);

mhhfInAlP = (xIn*mhhIn)+((1-xIn)*mhhAl);
mhhfInGaP = (xIn*mhhIn)+((1-xIn)*mhhGa);
mhhf=(yf*mhhfInAlP)+((1-yf)*mhhfInGaP);

%potential barrier for electrons and holes in QW in eV
QWEgInAlP = 1.351 + 1.83*(1-xIn) + 0.38*((1-xIn)^2);
QWEgInGaP = 1.351 + 0.643*(1-xIn) + 0.786*((1-xIn)^2);
%from Casey and Panish
BulkQWEg = (yf*QWEgInAlP) + ((1-yf)*QWEgInGaP);
Ve = BulkQWEg*0.67; %unstrained bandgap offsets from Arent
Vh = BulkQWEg*0.33;

%ground state in infinite well in eV (from Coldren & Corzine p. 396)
Ee = (3.76/mef)*((100/l)^2)/1000;
%distance from E = 0 at bottom of well
Ehh = (3.76/mhhf)*((100/l)^2)/1000;
Elh = (3.76/mlhf)*((100/l)^2)/1000;

%calculates max quantum number (most allowed bound states)
nme = sqrt(Ve/Ee);
nmhh = sqrt(Vh/Ehh);
nmlh = sqrt(Vh/Elh);

%calculates adjusted energy levels using effectiveQW function
Eqwe = Ee*(effectiveQW(nme))^2;
Eqwhh = Ehh*(effectiveQW(nmhh))^2;
Eqwlh = Elh*(effectiveQW(nmlh))^2;
if (Eqwhh < Eqwlh) %checks which hole level is lower
    Eqwh = Eqwhh;
else
    Eqwh = Eqwlh;
end

%calculates adjusted QW bandgap
Eg = BulkQWEg + Eqwe + Eqwh;

```



```

%EffectiveQW.m

function nqw = effectiveQW(nmax)
%given the max quant. number (nmax), iterates to find nqw, the
normalized quant. numb.

    %guess starting values (nqwy must be < nqwx)
    nqwx = 2;
    nqwy = .1;
    %iterate to find correct nqw
    while (abs(nqwy - nqwx)>=0.001)
        nqwx = nqwy;
        nqwy = (2/pi)*atan((1/nqwx)*sqrt(nmax^2 - nqwx^2));
%formula for symmetric solutions from Coldren & Corzine
    end
    nqw = nqwy;

```



```

%QWStrain.m

function EgQW = QWStrain(Eg, xIn)
%calculates the strain shift in energy bandgap given the initial
bandgap and xIn

%calls materials data file and parameters of device structure
MATERIALFILE
parameterfile

%calculates clad lattice constant
AcInAlP=(xc*Ain)+(1-xc)*Aal;
AcInGaP=(xc*Ain)+(1-xc)*Aga;
Ac=(yc*AcInAlP)+(1-yc)*AcInGaP;

%calculates QW lattice constant
AfInAlP=(xIn*Ain)+(1-xIn)*Aal;
AfInGaP=(xIn*Ain)+(1-xIn)*Aga;
Af=(yf*AfInAlP)+(1-yf)*AfInGaP;

%calculates mismatch strain
fin = (Af - Ac)/Af;

%calculates QW mechanical constants
C11fInAlP=(xIn*C11in)+(1-xIn)*C11al;
C12fInAlP=(xIn*C12in)+(1-xIn)*C12al;
C44fInAlP=(xIn*C44in)+(1-xIn)*C44al;

C11fInGaP=(xIn*C11in)+(1-xIn)*C11ga;
C12fInGaP=(xIn*C12in)+(1-xIn)*C12ga;
C44fInGaP=(xIn*C44in)+(1-xIn)*C44ga;

C11f=(yf*C11fInAlP)+(1-yf)*C11fInGaP;
C12f=(yf*C12fInAlP)+(1-yf)*C12fInGaP;
C44f=(yf*C44fInAlP)+(1-yf)*C44fInGaP;

afInAlP=(xIn*aIn)+(1-xIn)*aAl;
%hydrostatic deformation potential of InGaP
afInGaP=(xIn*aIn)+(1-xIn)*aGa;
adefeff=(yf*afInAlP)+(1-yf)*afInGaP;

bfInAlP=(xIn*bIn)+(1-xIn)*bAl;
%shear deformation potential of InGaP
bfInGaP=(xIn*bIn)+(1-xIn)*bGa;
bdeff=(yf*bfInAlP)+(1-yf)*bfInGaP;

H = (-adefeff)*2*(C11f - C12f)/C11f*fin;
%Hydrostatic strain energy shift
S = (-bdeff)*(C11f + 2*C12f)/C11f*fin;
%Shear strain energy shift

deltaEg = H + S; %Total Energy shift (+ for compressive strain)

EgQW = Eg + deltaEg; %adjusted bandgap energy (larger for compressive)

```



## References

- 1 N. Holonyak and S. F. Bevaqua, *Applied Physics Letters* **1**, 82-83 (1962).
- 2 M. G. Craford, in *High Brightness Light Emitting Diodes, Semiconductors and Semimetals, Vol. 48*, edited by M. G. Craford (Academic Press, San Diego, CA, 1997), p. 47-63.
- 3 A. H. Herzog, W. O. Groves, and M. G. Craford, *Applied Physics Letters* **40**, 1830-1833 (1969).
- 4 F. A. Kish and R. M. Fletcher, in *High Brightness Light Emitting Diodes, Semiconductors and Semimetals, Vol. 48*, edited by M. G. Craford (Academic Press, San Diego, CA, 1997), p. 149-220.
- 5 C. Kuo, R. Fletcher, T. Osentowski, M. Lardizbal, M. Craford, and V. Robbins, *Applied Physics Letters* **57**, 2937-2939 (1990).
- 6 H. Sugawara, M. Ishikawa, and G. Hatakoshi, *Applied Physics Letters* **58**, 1010-1012 (1991).
- 7 F. A. Kish, F. M. Steranka, D. C. DeFevere, D. A. Vanderwater, K. G. Park, C. P. Kuo, T. D. Osentowski, M. J. Peanasky, J. G. Yu, R. M. Fletcher, D. A. Steigerwald, M. G. Craford, and V. M. Robbins, *Applied Physics Letters* **64**, 2839-2841 (1994).
- 8 M. R. Krames, M. Ochiai-Holcomb, G. E. Hofler, C. Carter-Coman, E. I. Chen, I.-H. Tan, P. Grillot, N. F. Gardner, H. C. Chui, J.-W. Huang, S. A. Stockman, F. A. Kish, M. G. Craford, T. S. Tan, C. P. Kocot, M. Hueschen, J. Posselt, B. Loh, G. Sasser, and D. Collins, *Applied Physics Letters* **75**, 2365-7 (1999).
- 9 OIDA, (2002).
- 10 D. S. Cao, A. W. Kimball, and G. B. Stringfellow, *Journal of Applied Physics* **67**, 739-44 (1990).
- 11 A. Y. Kim, Ph.D. Thesis, MIT, 2000.
- 12 G. B. Stringfellow, in *High Brightness Light Emitting Diodes, Semiconductors and Semimetals, Vol. 48*, edited by M. G. Craford (Academic Press, San Diego, CA, 1997), p. 1-41.
- 13 G. B. Stringfellow, *Organometallic Vapor-Phase Epitaxy: Theory and Practice* (Academic Press, San Diego, CA, 1989).
- 14 J. A. McCaulley and V. M. Donnelly, *Journal of Chemical Physics* **91**, 4330-7 (1989).
- 15 J. G. Cederberg, B. Bieg, J.-W. Huang, S. A. Stockman, M. J. Peanasky, and T. F. Kuech, *Journal of Crystal Growth* **195**, 63-8 (1998).
- 16 J. S. Yuan, M. T. Tsai, C. H. Chen, R. M. Cohen, and G. B. Stringfellow, *Journal of Applied Physics* **60**, 1346-1351 (1986).
- 17 C. H. Chen, S. A. Stockman, M. J. Peanasky, and C. P. Kuo, in *High Brightness Light Emitting Diodes, Semiconductors and Semimetals, Vol. 48*, edited by M. G. Craford (Academic Press, San Diego, CA, 1997), p. 97-144.
- 18 A. Zunger, *MRS Bulletin* (1997).
- 19 M. Zorn, P. Kurpas, A. I. Shkrebti, B. Junno, A. Bhattacharya, K. Knorr, M. Weyers, L. Samuelson, J. T. Zettler, and W. Richter, *Physical Review B (Condensed Matter)* **60**, 8185-90 (1999).

- 20 D. W. Shaw, *Journal of Crystal Growth* **31**, 130-41 (1975).
- 21 K. Jensen, F., in *MODELLING OF CHEMICAL VAPOR DEPOSITION REACTORS.*, Cincinnati, OH, Engl, 1984 (Electrochemical Soc Inc, Pennington, NJ, USA), p. 233.
- 22 K. F. Jensen, (Publ by ACS, Washington, DC, USA, 1989), p. 199-263.
- 23 K. F. Jensen, D. I. Fotiadis, T. J. Mountziaris, E. O. Einset, and T. F. Kuech, in *Models of chemical kinetics and transport phenomena in chemical vapor deposition systems*, Montreal, Que, Can, 1991 (Publ by Electrochemical Soc Inc, Manchester, NH, USA), p. 142-160.
- 24 I. Vurgaftman, J. R. Meyer, and L. R. Ram-Mohan, *Journal of Applied Physics* **89**, 5815-75 (2001).
- 25 S. Adachi, *Journal of Applied Physics* **53**, 8775-92 (1982).
- 26 M. Levinshtein, S. Rumyantsev, and M. Shur, *Handbook series on semiconductor parameters. Vol.1* (World Scientific, 1996).
- 27 K. Asami, H. Asahi, T. Watanabe, M. Enokida, S. Gonda, and S. Fujita, *Applied Physics Letters* **62**, 81-3 (1993).
- 28 H. C. Casey and M. B. Panish, *Heterostructure Lasers Pt. B.--Materials and operating characteristics* (Academic Press, New York, 1978).
- 29 D. P. Bour, J. R. Shealy, G. W. Wicks, and W. J. Schaff, *Applied Physics Letters* **50**, 615-17 (1987).
- 30 J. Matragrano, D. G. Ast, J. R. Shealy, and V. Krishnamoorthy, *Journal of Applied Physics* **79**, 8371-8 (1996).
- 31 E. A. Fitzgerald, *JOM* **41**, 20-24 (1989).
- 32 J. W. Matthews and A. E. Blakeslee, *Journal of Crystal Growth* **27**, 118-125 (1974).
- 33 J. W. Matthews and A. E. Blakeslee, *Journal of Crystal Growth* **29**, 273-280 (1975).
- 34 J. W. Matthews, S. Mader, and T. B. Light, *Journal of Applied Physics* **41**, 3800 (1970).
- 35 E. A. Fitzgerald, *Materials Science Reports* **7**, 87-142 (1991).
- 36 J. W. Matthews, *Epitaxial Growth: Part B* (Academic Press, New York, 1975).
- 37 E. A. Fitzgerald, Y.-H. Xie, M. L. Green, D. Brasen, A. R. Kortan, J. Michel, Y.-J. Mii, and B. E. Weir, *Applied Physics Letters* **59**, 811-13 (1991).
- 38 M. T. Currie, S. B. Samavedam, T. A. Langdo, C. W. Leitz, and E. A. Fitzgerald, *Applied Physics Letters* **72**, 1718 (1998).
- 39 C. W. Leitz, M. T. Currie, A. Y. Kim, J. Lai, E. Robbins, E. A. Fitzgerald, and M. T. Bulsara, *Journal of Applied Physics* **90**, 2730 (2001).
- 40 A. Y. Kim, W. S. McCullough, and E. Fitzgerald, *Journal of Vacuum Science & Technology B (Microelectronics and Nanometer Structures)* **17**, 1485-501 (1999).
- 41 T. P. Chin, J. C. P. Chang, K. L. Kavanagh, C. W. Tu, P. D. Kirchner, and J. M. Woodall, *Applied Physics Letters* **62**, 2369-71 (1993).
- 42 M. S. Abrahams, L. R. Weisberg, C. J. Buiochi, and J. Blanc, *Journal of Materials Science* **4**, 223-35 (1969).
- 43 E. A. Fitzgerald, Y.-H. Xie, D. Monroe, P. J. Silverman, J. M. Kuo, A. R. Kortan, F. A. Thiel, and B. E. Weir, *Journal of Vacuum Science & Technology B: Microelectronics Processing and Phenomena* **10**, 1807 (1992).



- 44 M. Ohring, *The Materials Science of Thin Films* (Academic Press, Boston, 1992).  
45 J. Ishizaki, S. Goto, M. Kishida, F. Takashi, and H. Hasegawa, *Japanese Journal of Applied Physics, Part 1 (Regular Papers, Short Notes & Review Papers)* **33**, 721-726 (1994).
- 46 M. Shinohara and N. Inoue, *Applied Physics Letters* **66**, 1936-8 (1995).  
47 R. Tycko, G. Dabbagh, S. R. Kurtz, and J. P. Goral, *Physical Review B (Condensed Matter)* **45**, 13452 (1992).
- 48 A. Zunger and S. Mahajan, in *Handbook on Semiconductors; Vol. 3b*, edited by S. Mahajan (Elsevier, Amsterdam, 1994), p. 1402-1507.  
49 L. G. Ferreira, A. A. Mbaye, and A. Zunger, *Physical Review B (Condensed Matter)* **37**, 10547-70 (1988).
- 50 D. A. Porter and K. E. Easterling, *Phase Transformations in Metals and Alloys* (Chapman & Hall, London, England, 1992).  
51 N. Marzari, S. de Gironcoli, and S. Baroni, *Physical Review Letters* **72**, 4001-4 (1994).
- 52 S. Mahajan and M. A. Shahid, in *Advances in Materials, Processing, and Devices on III-V Compound Semiconductors*, 1989, p. 169.  
53 O. Ueda, T. Fujii, Y. Nakada, H. Yamada, and I. Umebu, *Journal of Crystal Growth* **95**, 38-42 (1989).
- 54 O. Ueda, T. Fujii, Y. Nakada, H. Yamada, and I. Umebu, *Applied Physics Letters* **54**, 2312 (1989).  
55 T. L. McDevitt, S. Mahajan, and D. E. Laughlin, *Physical Review B (Condensed Matter)* **45**, 6614-22 (1992).
- 56 A. Gomyo, T. Suzuki, K. Kobayashi, S. Kawata, I. Hino, and T. Yuasa, *Applied Physics Letters* **50**, 673-5 (1987).  
57 G. W. 't Hooft, C. J. B. Riviere, M. P. C. M. Krijn, C. T. H. F. Liedenbaum, and A. Valster, *Applied Physics Letters* **61**, 3169-71 (1992).
- 58 R. P. Schneider, Jr., E. D. Jones, J. A. Lott, and R. P. Bryan, *Journal of Applied Physics* **72**, 5397-400 (1992).  
59 S. H. Lee, T. C. Hsu, and G. B. Stringfellow, *Journal of Applied Physics* **84**, 2618-23 (1998).
- 60 Y. S. Chun, H. Murata, S. H. Lee, I. H. Ho, T. C. Hsu, G. B. Stringfellow, C. E. Inglefield, M. C. DeLong, P. C. Taylor, J. H. Kim, and T.-Y. Seong, *Journal of Applied Physics* **81**, 7778 (1997).  
61 G. B. Stringfellow and L. C. Su, *Journal of Crystal Growth* **163**, 128-134 (1996).  
62 H. Murata, S. H. Lee, I. H. Ho, and G. B. Stringfellow, *Journal of Vacuum Science & Technology B (Microelectronics and Nanometer Structures)* **14**, 3013-18 (1996).
- 63 S. R. Kurtz, J. M. Olson, and A. Kibbler, *Applied Physics Letters* **57**, 1922-4 (1990).  
64 S. Hasenohrl, J. Novak, R. Kudela, J. Betko, M. Morvic, and J. Fedor, *Journal of Crystal Growth* **248**, 369-74 (2003).
- 65 M. Longo, A. Parisini, L. Tarricone, L. Toni, and R. Kudela, *Materials Science and Engineering B: Solid-State Materials for Advanced Technology* **86**, 157-164 (2001).  
66 R. M. Feenstra, *Semiconductor Science and Technology* **9**, 2157-68 (1994).

- 67 O. Dehaese, X. Wallart, and F. Mollot, *Applied Physics Letters* **66**, 52 (1995).  
68 X. Wallart, C. Priester, D. Deresmes, and F. Mollot, *Applied Physics Letters* **77**,  
253-5 (2000).
- 69 J. M. Millunchick, R. Twesten, S. R. Lee, D. M. Follstaedt, E. D. Jones, S.  
Ahrenkiel, Y. Zhang, H. Cheong, and A. Mascarenhas, *MRS Bulletin*, 38-43  
(1997).
- 70 K. Mader and A. Zunger, *Applied Physics Letters* **64**, 2882 (1994).  
71 T. M. Ritter, B. A. Weinstein, R. E. Viturro, and D. P. Bour, *Physica Status Solidi*  
**B 211**, 869-83 (1999).
- 72 M. D. Dawson and G. Duggan, *Applied Physics Letters* **64**, 892-4 (1994).  
73 D. J. Arent, M. W. Peterson, C. Kramer, K. A. Bertness, and J. A. Turner, *Journal*  
*of Electronic Materials* **25**, 1633-6 (1996).
- 74 B. D. Cullity, *Elements of X-ray Diffraction* (Addison-Wesley, 1978).  
75 K. M. Matney and M. S. Goorsky, in *New approach for determining epilayer*  
*strain relaxation and composition through high resolution x-ray diffraction*, San  
Francisco, CA, USA, 1995 (Materials Research Society, Pittsburgh, PA, USA), p.  
257-262.
- 76 C. Kittel, *Introduction to Solid State Physics* (Wiley, New York, 1986).  
77 D. B. Williams and C. B. Carter, *Transmission Electron Microscopy: a textbook*  
*for materials science* (Plenum Press, New York, 1996).
- 78 R. Leon, J. O. Okuno, R. A. Lawton, M. Stevens-Kalceff, M. R. Phillips, J. Zou,  
D. J. H. Cockayne, and C. Lobo, *Applied Physics Letters* **74**, 2301 (1999).
- 79 U. Gosele and Q. Y. Tong, *Annual Review of Materials Science*, 215-241 (1998).  
80 Z. L. Liau and D. E. Mull, *Applied Physics Letters* **56**, 737-9 (1990).  
81 Y. C. Zhou, Z. H. Zhu, D. Crouse, and Y. H. Lo, *Applied Physics Letters* **73**,  
2337-9 (1998).
- 82 F. E. Ejeckam, C. L. Chua, Z. H. Zhu, Y. H. Lo, M. Hong, and R. Bhat, *Applied*  
*Physics Letters* **67**, 3936-8 (1995).  
83 Y. H. Lo, R. Bhat, D. M. Hwang, C. Chua, and C. H. Lin, *Applied Physics Letters*  
**62**, 1038-40 (1993).
- 84 J.-W. Lee, A. T. Schremer, J. R. Shealy, and J. M. Ballantyne, in *Proceedings of*  
*the SPIE - The International Society for Optical Engineering*, San Jose, CA, USA,  
1997, p. 20-31.
- 85 S. M. Ting, S. B. Samavedam, M. T. Currie, T. A. Langdo, and E. A. Fitzgerald,  
in *Proceedings of the MRS*, San Francisco, CA, USA, 1998 (Mater. Res. Soc), p.  
107-12.
- 86 C. C. Hu, C. S. Sheu, and M. K. Lee, *Materials Chemistry and Physics* **48**, 17-20  
(1997).
- 87 K. Akahori, G. Wang, K. Okumura, T. Soga, T. Jimbo, and M. Umeno, *Solar*  
*Energy Materials and Solar Cells* **66**, 593-8 (2001).  
88 H. Kawanami, *Solar Energy Materials and Solar Cells* **66**, 479-86 (2001).  
89 T. Egawa, T. Jimbo, J. Dong, K. Matsumoto, and M. Umeno, *Applied Physics*  
*Letters* **67**, 3605-7 (1995).
- 90 Y. Komatsu, K. Hosotani, T. Fuyuki, and H. Matsunami, *Japanese Journal of*  
*Applied Physics, Part 1 (Regular Papers, Short Notes & Review Papers)* **36**, 5425-  
30 (1997).

- 91 S. Kondo, H. Nagai, Y. Itoh, and M. Yamaguchi, *Applied Physics Letters* **55**,  
1981-3 (1989).
- 92 S. Makan, M.S. Thesis, MIT, 1997.
- 93 V. Yang, M. Groenert, C. W. Leitz, A. Pitera, M. Currie, and E. A. Fitzgerald,  
*Journal of Applied Physics* **93**, 3859-3865 (2003).
- 94 S. M. Ting, Ph.D. Thesis, MIT, 1999.
- 95 S. M. Ting, E. A. Fitzgerald, R. M. Sieg, and S. A. Ringel, *Journal of Electronic  
Materials* **27**, 451-61 (1998).
- 96 L. Kipp, R. D. Bringans, D. K. Biegelsen, J. E. Northrup, A. Garcia, and L. E.  
Swartz, *Physical Review B (Condensed Matter)* **52**, 5843-5850 (1995).
- 97 H.-W. Ren, M. Sugisaki, J.-S. Lee, S. Suguu, and Y. Masumoto, *Japanese Journal  
of Applied Physics, Part 1 (Regular Papers, Short Notes & Review Papers)* **38**,  
507-10 (1999).
- 98 R. Leon, C. Lobo, A. Clark, R. Bozek, A. Wysmolek, A. Kurpiewski, and M.  
Kaminska, *Journal of Applied Physics* **84**, 248-54 (1998).
- 99 A. S. Segala, S. Y. Karpov, A. P. Sid'ko, and Y. N. Makarov, *Journal of Crystal  
Growth* **225**, 268-73 (2001).
- 100 R. Mirin, A. Gossard, and J. Bowers, *Electronics Letters* **32**, 1732-1734 (1996).
- 101 J. W. Lee, A. T. Schremer, J. R. Shealy, and J. M. Ballantyne, *SPIE* **3290**, 20-31  
(1997).
- 102 O. I. Micic and A. J. Nozik, *Journal of Luminescence* **70**, 95-107 (1996).
- 103 G. Walter, N. Holonyak, J. H. Ryou, and R. D. Dupuis, *Applied Physics Letters*  
**79**, 1956-8 (2001).
- 104 D. Gammon, *MRS Bulletin*, 44-48 (1998).
- 105 Agilent, "SunPower Series Data Sheet," (2001).
- 106 Agilent, "HSM Series Surface Mount LED Data Sheet," (2003).
- 107 F. A. Kish, D. A. DeFevere, D. A. Vanderwater, G. R. Trott, R. J. Weiss, and J. S.  
J. Major, *Electronics Letters* **30**, 1790-1792 (1994).
- 108 S.-J. Chang, J.-K. Sheu, Y.-K. Su, M.-J. Jou, and G.-C. Chi, *Japanese Journal of  
Applied Physics, Part 1: Regular Papers & Short Notes & Review Papers* **35**,  
4199-4202 (1996).
- 109 R. M. Sieg, J. A. Carlin, J. J. Boeckl, S. A. Ringel, M. T. Currie, S. M. Ting, T. A.  
Langdo, G. Taraschi, E. A. Fitzgerald, and B. M. Keyes, *Applied Physics Letters*  
**73**, 3111 (1998).
- 110 M. T. Bulsara, Ph.D. Thesis, MIT, 1998.
- 111 J. Chevrier, A. Cruz, N. Pinto, I. Berbezier, and J. Derrien, *Journal De Physique*,  
III **4**, 1309-1324 (1994).
- 112 M. A. Cotta, R. A. Hamm, S. N. G. Chu, R. Hull, L. R. Harriott, and H. Temkin,  
*Materials Science & Engineering B: Solid-State Materials for Advanced  
Technology* **B30**, 137-142 (1995).
- 113 N.-E. Lee, D. G. Cahill, and J. E. Greene, *Journal of Applied Physics* **80**, 2199-  
2210 (1996).
- 114 H. Hotta, A. Gomyo, F. Miyasaka, K. Tada, T. Suzuki, and K. Kobayashi, in  
*Anomalous photoluminescence behaviour for GaInP/AlGaInP quantum wells  
grown by MOVPE on misoriented (001) substrates*, Freiburg, Germany, 1994  
(IOP Publishing), p. 631-6.

- 115 R. M. Feenstra, AIP Conference Proceedings, 131-2 (1990).
- 116 A. Dieguez, F. Peiro, A. Cornet, J. R. Morante, F. Alsina, and J. Pascual, Journal  
of Applied Physics **80**, 3798-803 (1996).
- 117 X. Wallart, D. Deresmes, and F. Molloy, Applied Physics Letters **78**, 2961-3  
(2001).
- 118 K. Lee, B. A. Philips, R. S. McFadden, and S. Mahajan, Materials Science &  
Engineering B (Solid-State Materials for Advanced Technology) **32**, 231-7  
(1995).
- 119 G. S. Solomon, J. A. Trezza, A. F. Marshall, and J. S. Harris, Jr., Journal of  
Vacuum Science & Technology B (Microelectronics and Nanometer Structures)  
**14**, 2208-11 (1996).
- 120 M. K. Zundel, A. P. Specht, K. Eberl, N. Y. Jin-Phillip, and F. Phillipp, Applied  
Physics Letters **71**, 2972-4 (1997).
- 121 L. P. Fu, D. G. Chtchekine, G. D. Gilliland, H. Lee, H. P. Hjalmarson, J. G. Yu,  
M. G. Craford, and D. J. Wolford, IEEE Journal of Quantum Electronics **33**,  
1123-31 (1997).
- 122 W. G. Bi and C. W. Tu, Journal of Crystal Growth **165**, 210-14 (1996).
- 123 T. P. Chin, J. C. P. Chang, K. L. Kavanagh, C. W. Tu, P. D. Kirchner, and J. M.  
Woodall, in *Growth and characterization of In/sub x/Ga/sub 1-x/P (x<or=0.38)  
on GaP(100) with a linearly graded buffer layer by gas-source molecular beam  
epitaxy*, Boston, MA, USA, 1993 (Mater. Res. Soc), p. 227-32.
- 124 T. Tanaka, K. Uchida, Y. Ishitani, and S. Minagawa, Applied Physics Letters **66**,  
783-5 (1995).
- 125 J.-F. Lin, M.-C. Wu, M.-J. Jou, C.-M. Chang, and B.-J. Lee, Journal of Crystal  
Growth **137**, 400-4 (1994).
- 126 M.-J. Jou, J.-F. Lin, C.-M. Chang, C.-H. Lin, M.-C. Wu, and B.-J. Lee, Japanese  
Journal of Applied Physics, Part 1: Regular Papers & Short Notes & Review  
Papers **32**, 4460-4466 (1993).
- 127 D. Ahn, Applied Physics Letters **66**, 628-30 (1995).
- 128 C. S. Menoni, D. Patel, M. J. Hafich, and G. Y. Robinson, AIP Conference  
Proceedings, High-Pressure Science and Technology - 1993 **309**, 589-92 (1994).
- 129 L. A. Coldren and S. W. Corzine, *Diode lasers and photonic integrated circuits*  
(Wiley, New York, 1995).
- 130 S.-H. Wei, L. G. Ferreira, and A. Zunger, Physical Review B (Condensed Matter)  
**41**, 8240-69 (1990).
- 131 S. Kamiyama, M. Monnoh, K. Ohnaka, and T. Uenoyama, Journal of Applied  
Physics **75**, 8201-3 (1994).
- 132 S.-J. Chang and C.-S. Chang, Japanese Journal of Applied Physics, Part 2  
(Letters) **37**, 653-5 (1998).
- 133 M. Yamaguchi, C. Amano, and Y. Itoh, Journal of Applied Physics **66**, 915-19  
(1989).
- 134 L. C. Su, S. T. Pu, G. B. Stringfellow, J. Christen, H. Selber, and D. Bimberg,  
Applied Physics Letters **62**, 3496-8 (1993).
- 135 C. Geng, M. Moser, R. Winterhoff, E. Lux, J. Hommel, B. Hohing, H. Schweizer,  
and F. Scholz, Journal of Crystal Growth **145**, 740-5 (1994).

<sup>136</sup> R. Osorio, J. E. Bernard, S. Froyen, and A. Zunger, *Physical Review B (Condensed Matter)* **45**, 11173-91 (1992).